SOFT-SWITCHED MULTI-INPUT CONVERTER FOR RENEWABLE ENERGY SYSTEMS

SANJIDA MOURY

A DISSERTATION SUBMITTED TO THE FACULTY OF GRADUATE STUDIES IN PARTIAL FULFILMENT OF THE REQUIREMENTS FOR THE DEGREE OF DOCTOR OF PHILOSOPHY

GRADUATE PROGRAM IN ELECTRICAL ENGINEERING AND COMPUTER SCIENCE

YORK UNIVERSITY

TORONTO, ONTARIO

May, 2020

Abstract

In a renewable energy system, multiple energy sources (such as combining renewable energy and energy storage) are utilized together to enhance the overall energy conversion reliability since renewable energy, such as wind and solar, are intermittent in nature. In conventional power architecture, each energy source requires a dedicated individual power converter to perform specific control or power management function. To reduce the overall number of circuit components, multi-input converter (MIC) configuration provides a cost effective power architecture when multiple energy sources are utilized, as they can use fewer filter circuit components and utilize smaller system space. To maximize the features offered by MICs, a truly power efficient and compact MIC should utilize minimal number of active switching components with soft-switching features, while at the same time, assist each energy power interface to achieve all the required control functions.

In the first part of this thesis, a class of several soft-switched DC-DC MICs is proposed, where each input module of the devised MICs utilizes only a single switch. Each of the presented MIC circuits can also be integrated with a front-end (either single phase or three phase) AC-DC stage without adding additional switches to interface with renewable energy generation unit that outputs an AC voltage. In addition, input power factor correction is also provided.

The second part of this thesis investigates the use of the devised DC-DC MIC circuit to improve the double power conversion steps typically seen in a solar-battery energy conversion system with a common DC grid that utilizes a bi-directional energy storage power converter. This chapter focuses on the development of a soft-switched MIC circuit that

consists of integrated unidirectional energy storage (i.e. battery) power interface, for use in module-connected solar energy power optimizer system with distributed energy storage. In the proposed circuit, the storage charging (storage absorbs power) circuit is integrated with the input stage of the main converter via high frequency AC link, whereas the storage discharging (storage delivers power) circuit is connected to the output stage of MIC. As a result, energy is directed from the input to the battery and from the battery to the load through a single power conversion step.

The third part of this thesis utilizes the circuit concepts devised previously to develop a new soft-switched MIC configuration that consists of an integrated unidirectional energy storage power interface, as well as to provide output voltage regulation. Hence, the proposed MIC is applicable for both regulated and unregulated grids. The control mechanism of the proposed system is presented. The operating principles and characteristics of each proposed converter topology are provided in detail. Simulation and experimental results on proof-of-concept prototypes are provided to demonstrate the functionalities of each devised MIC topology.

Acknowledgement

I would like to thank everyone who has supported me in the completion of this paper. To my supervisor, Dr. John Lam for his patience, motivation, and guidance. To my supervisory committee: Dr. Hany Farag and Dr. Ali Hooshyar for their continuous support and encouragement. To the faculty and staff members of the Electrical Engineering and Computer Science (EECS) department, especially the graduate program directors, graduate program assistants, and the IT team. To my colleague, Kajanan who helped me whenever needed. To Xingkai who assisted me during the toughest time of this journey. To Jennifer who was always by my side and listened to me in my bad days and good days. To all my family members and friends who were by my side to encourage me. To my parents and my sister, who made the fine balance of supporting me and leaving me alone when required. Finally, to Arafat, whose strength and love have changed my life. This paper is for Owais who was the biggest support and encouragement of this journey.

Table of Contents

List of Tables

List of Figures

List of Acronyms

AC	Alternate Current
BSS	Battery Storage System
CAES	Compressed Air Energy Storage
CC	Constant Current
CC	Constant Current
CV	Constant Voltage
CV	Constant Voltage
DAB	Dual Active Bridge
DC	Direct Current
DCM	Discontinuous Current Mode
DCM	Discontinuous Current Mode
DG	Distributed Generation
DHB	Dual Half-Bridge Converter
ESS	Energy Storage Systems
MIC	Multi-Input Converter
MOSFET	Metal Oxide Silicon Field Effect Transistor
MPP	Maximum Power Point
MPPT	Maximum Power Point Tracking
MR	Multi- Resonant
P2G	Power to Gas
PEI	Power Electronics Interface
PF	Power Factor

PFC	Power Factor Correction
PHS	Pumped Hydro Storage
PV	Photovoltaic
PWM	Pulse Width Modulation
QRC	Quasi Resonant Converters
RES	Renewable Energy System
rms	Root Mean Square
T&D	Transmission and Distribution
THD	Total Harmonic Distortion
VA	Volt-Ampere
WECS	Wind Energy Conversion System
ZCS	Zero-Current Switching
ZVS	Zero-Voltage Switching

List of Symbols

R_{sh}	shunt resistance
R_s	series resistance
I	PV terminal current
V	PV terminal voltage
I_{d0}	diode reverse saturation current
q	electronic charge
K	Boltzmann's constant
n	diode ideality factor
T	absolute temperature
V_w	wind speed
ρ	air density
R	blade radius
C_p	wind turbine power coefficient
ω_r	wind turbines angular speed
λ	tip speed ratio
β	pitch angle
I_{cond}	current through the component
$R_{parasitic}$	parasitic resistive element
R_{ds_on}	resistance between drain and source
P_{sw_loss}	switching loss
P_{on}	turn on loss

P_{off}	turn off loss
f_s	switching frequency
P	real power
S	apparent power
K_θ	distortion power factor
K_d	displacement power factor
$I_{rms,1}$	fundamental root-mean-square (rms) current
I_{rms}	total rms current
θ	phase difference between the fundamental input current and the input line voltage
φ	phase difference between the voltage across the primary and secondary side of the isolation transformer
R_L	Output load resistance
t_{ri}	current rising time
t_{fv}	voltage falling time
t_{rv}	voltage rising time
t_{fi}	current falling time
d	Duty ratio of converter
M_v	Voltage gain of converter
V_0	Output voltage
I_0	Output current
V_{bat}	Battery voltage
V_{PV}	PV voltage

V_{wind}	Wind turbine voltage
f_s	Switching frequency
f_r	Resonant frequency
ω_r	Angular resonant frequency
L_r	Resonant inductor
C_r	Resonant capacitor
Z	Characteristic impedance
T_s	Switching time period
R_n	Normalized load resistance
N	Turns ratio
L_m	Magnetizing inductance
f_N	Normalized frequency
γ	Ripple factor
λ	percentage of voltage ripple
C_e	Effective capacitance of capacitor
L_e	Effective inductance of inductance
v_{ds}	Voltage across MOSFET
i_s	Current through MOSFET
V_{gs}	Gate signal of MOSFET
i_{pri}	Primary side current of transformer
i_{sec}	Secondary side current of transformer

Chapter 1 Introduction

As of 2018, global energy demand reached 26589TWh [1]. 74% of today's global energy [1] is generated from fossil fuel resources. These resources are limited and power generation from these resources results in global warming due to greenhouse gas emissions. Therefore, renewable resources such as wind, solar, hydro, ocean waves and tides, biomass, and geothermal have attracted attention to meet the growing energy demand and to reduce greenhouse gas emissions.

Power generation from renewable resources has been growing rapidly over the past decade. According to the Renewable Energy Statistics 2019 [2], power generation from such sources reached 2356GW by the end of 2018 (Figure 1-1). The percentage growth rates of the power generation from different renewable resources in the past decade (from 2009 to 2018) are shown in Figure 1-2. The global total installed capacity has increased from 23.5GW to 486GW for solar and from 150GW to 563GW for wind in the last decade [2]. This rapid growth has been largely driven by factors including the cost-competitiveness and technological improvement, governments' policies, better access to financing, energy security and environmental concerns, and growing demand for energy in developing and emerging economies [3]. The global weighted average levelized cost of electricity has dropped (2010-2018) from 0.37USD/kW to 0.09USD/kW for solar, from 0.34USD/kW to 0.19USD/kW for offshore wind, and from 0.08USD/kW to 0.06USD/kW for onshore wind [4]. Therefore, wind and solar energy have become the most promising among renewable energy resources.

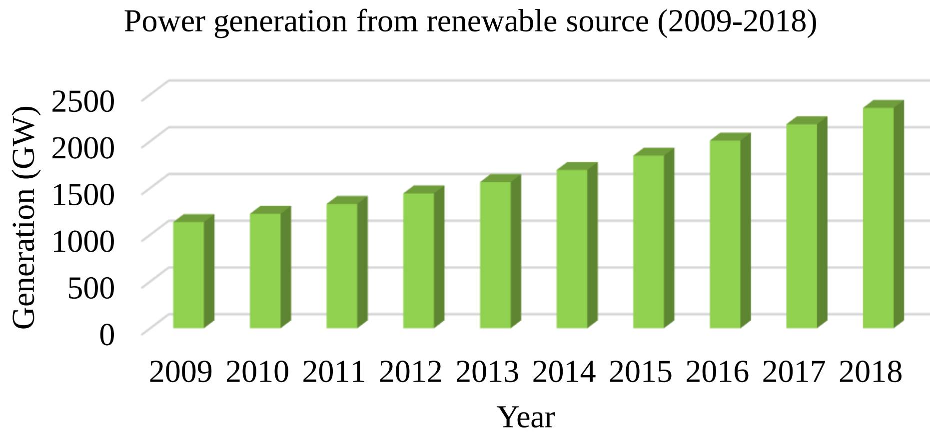

Figure 1-1 Power generation from renewable sources in the past decade [2]

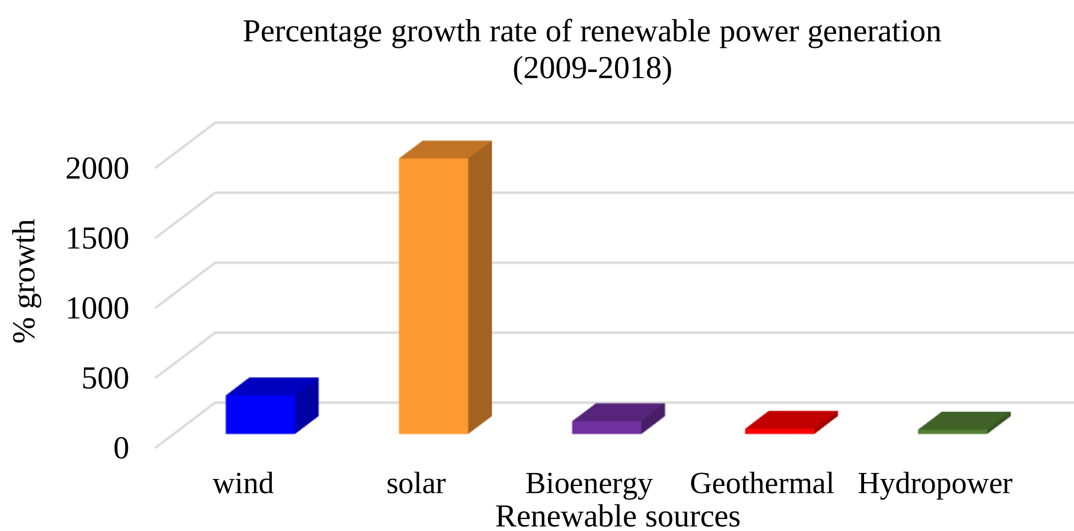

Figure 1-2 Percentage growth rate of renewable power generation by source type [2]

1.1 Power Generation from Renewable Resources

1.1.1 Solar Energy

The solar photovoltaic (PV) module converts the solar energy to direct current (DC) electrical energy. A PV module comprises of PV cells. In a typical commercial PV module, 60 or 72 PV cells are connected in series and parallel to achieve certain voltage and power levels. PV modules connected in series to achieve further higher voltage level are termed as

PV string. PV strings are connected in parallel to form PV array to attain higher power level. Figure 1-3 shows the photographs of PV cell, module, string, and array.

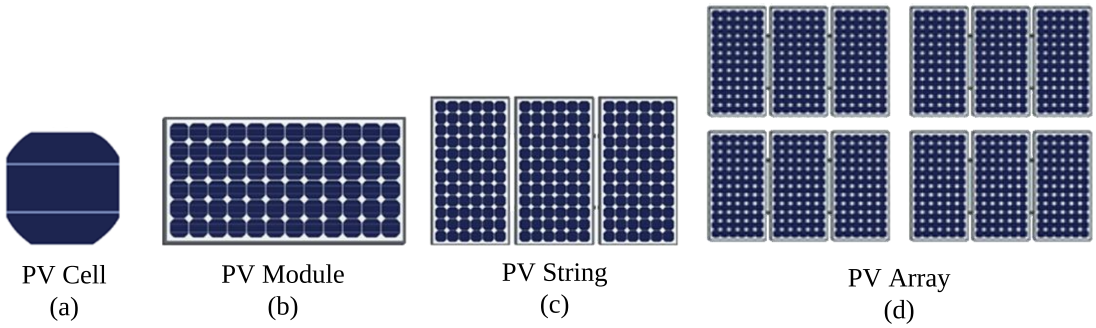

Figure 1-3 (a) PV cell (b) PV module (c) PV string, and (d) PV array [5]

The equivalent circuit model of a PV module consists of a diode in parallel with an ideal current source and the resistive loss elements as shown in Figure 1-4. The ideal current source delivers current, I_{pv} in proportion to the solar irradiance to which it is exposed. The shunt resistance, R_{sh} is the leakage resistance and the series resistance, R_s represents the resistance between the cell and its wire lead, and the resistance of the semiconductor itself. The output current of the PV module is governed by Eq. 1-1 where I is the terminal current, V is the terminal voltage, I_{d0} the diode reverse saturation current, q is the electronic charge, K is the Boltzmann's constant, n is the diode ideality factor, and T is the absolute temperature.

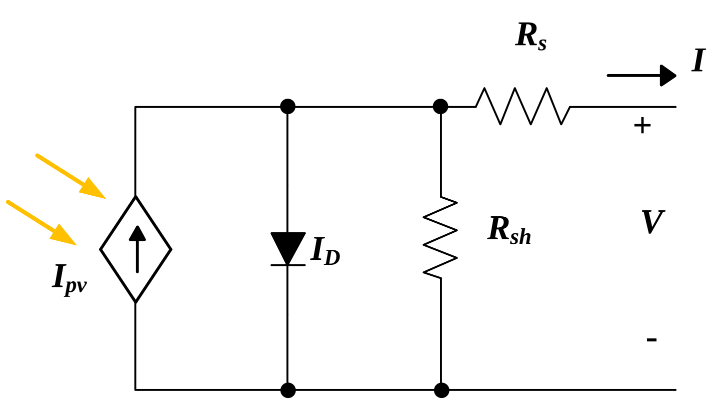

Figure 1-4 Equivalent circuit of a PV module

$$I = I_{pv} - I_{d0}\left[e^{\left(\frac{q(V+IR_s)}{nkT}\right)} - 1\right] - \frac{V + IR_s}{R_{sh}} \qquad \text{Eq. 1-1}$$

The V-I characteristic of PV module is nonlinear and changes with light intensity and temperature. In general, there is only one point on each V-I or V-P curve, called the Maximum Power Point (MPP), at which the PV module operates with maximum efficiency and produces maximum power at a fixed temperature and light intensity. The PV module characteristic curves for different light intensity are shown in Figure 1-5. With the change of the light intensity, the power generated by the PV panel changes. The change in MPP voltage is not significant. However, a significant change happens in PV current as well as in PV power. The impedance seen by the PV panel determines the operating point.

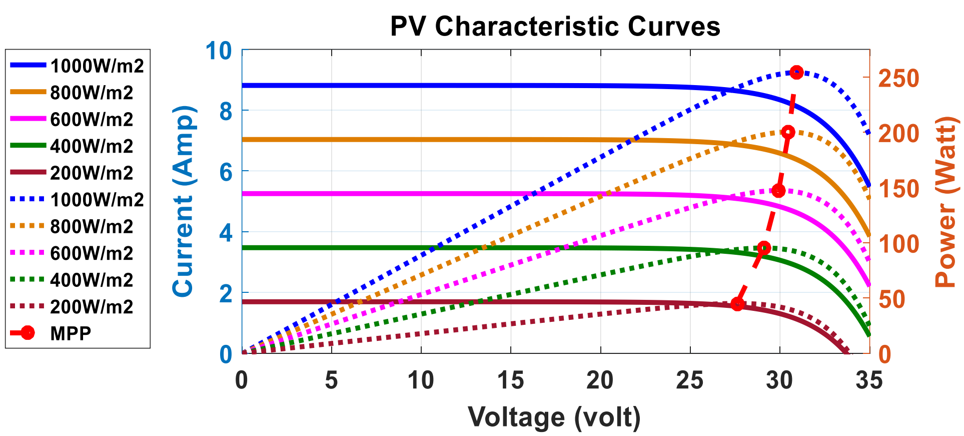

Figure 1-5 PV characteristic curves (V-I and V-P) at different solar irradiances

The power captured by the PV system cannot be directly used by the load. Therefore, the power electronics interface (PEI) is required to convert the captured power to the usable electrical power as shown in Figure 1-6. Other than conditioning power, PEI is also responsible for tracking the MPP of the PV system.

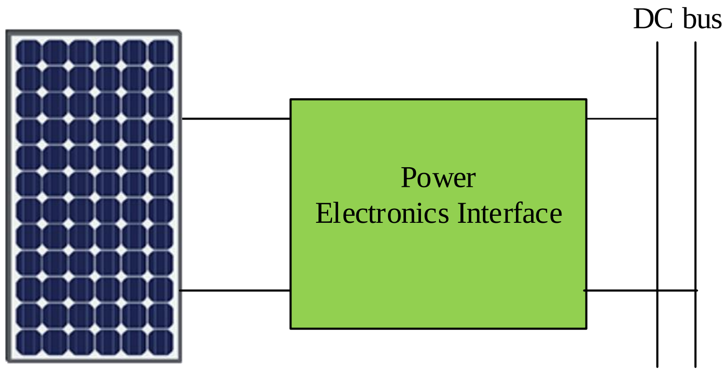

Figure 1-6 PV power conversion system

1.1.2 Wind Energy

Wind turbines convert the kinetic energy in the wind into rotational mechanical power. A generator is used to convert this mechanical power to electrical power. The block diagram of a wind energy conversion system (WECS) is shown in Figure 1-7. The purpose of the PEI required for WECS is same as the PV system. It is needed to capture the maximum amount of power and convert it to usable electrical power. Unlike PV system, as the output of the generator is alternate current (AC), the WECS requires a front end AC-DC conversion. Moreover, a high quality balanced 3-phase current is required to be drawn from the generator to optimize the lifetime of the generator.

The three main factors that influence the captured power of a wind turbine are wind speed (V_w), air density (ρ), and blade radius (R). The output power of a wind turbine is defined as Eq. 1-2 where C_p is the power coefficient [6]. The maximum value of C_p is 0.59. λ is the tip speed ratio and β is the pitch angle. The tip speed ratio λ is given by Eq. 1-3 where ω_r is the turbines angular speed.

$$P = \frac{1}{2}\rho\pi R^2 V_w^{\ 3} C_p(\lambda, \beta) \qquad \text{Eq. 1-2}$$

$$\lambda = \frac{\omega_r R}{V_w} \qquad \text{Eq. 1-3}$$

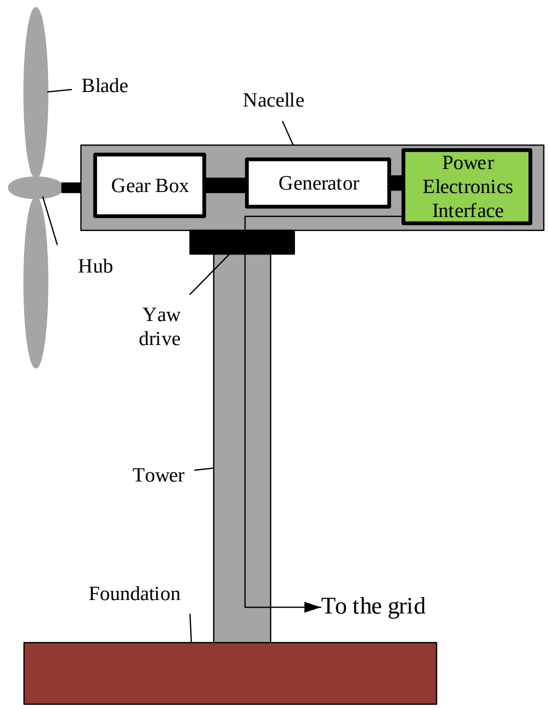

Figure 1-7 Block diagram of a wind energy conversion system (WECS)

The power generated by the wind turbine largely depends on the wind speed (Eq. 1-2). Higher wind speed results in higher rotational speed and ultimately higher electrical power. However, turbines are designed to operate within specific wind speeds. The wind speed at which the turbine starts to generate power is called cut-in speed and the wind speed at which the turbine shuts down is called the cut-out speed. At rated speed the turbine starts generating maximum power and continues till the cut-out speed. Between the cut-in and rated speed, the output power cubically depends on the wind speed as of Eq. 1-2.

The wind speed is always changing and thus the power generation from the wind. At different wind speeds, the maximum power can be captured by changing the turbines angular speed, ω_r. The variation of mechanical power with the change of the turbines angular speed ω_r, is shown in Figure 1-8 for different wind speeds. Therefore, the maximum power from the wind turbine can be captured by controlling the angular speed ω_r of the turbine.

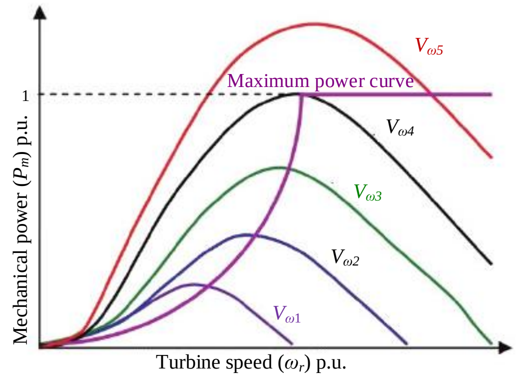

Figure 1-8 wind turbine mechanical power as a function of rotor speed for various wind speed [7]

1.2 Energy Storage System

Though renewable resources (such as wind and solar) abound in nature, they are volatile and intermittent. Therefore, renewable energy systems are typically combined with energy storage systems to provide dispatchable energy (that is, energy on demand) and reliable capacity (that is, grid stability). Numerous energy storage systems have been developed over the last century. Early large scale systems such as pumped hydro storage (PHS), compressed air energy storage (CAES), and power to gas (P2G) utilized physical or thermal media for storage. However, the use of such systems is limited by cost, energy density, and siting disadvantage. The capacity requirement, discharge duration requirement, and the application of energy storage systems have changed with the growth of the power generation from renewable sources. Figure 1-9 shows different energy storage systems categorized as application, system rating, and the discharge time [8]. Among the energy storage systems, battery storage system can be used in a wide range of applications, available in a wide range of system capacity and can be used for the discharge time from few minutes to several hours. Among the battery storages, Li-ion battery possesses several favorable performances such as lightweight, higher energy density, high round trip efficiency, and longer life. Therefore, the global annual capacity of Li-ion has been increased significantly in the past decade [3].

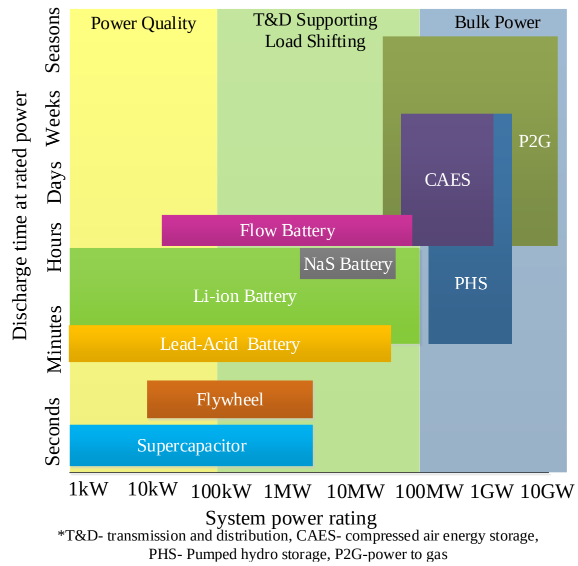

Figure 1-9 Comparison of various energy storage systems in terms of application, system power rating and discharge time [8]

In a battery, several battery cells are connected in series and several batteries are connected in parallel to form a battery pack [9]. Figure 1-10 shows a simplified battery power conversion system. The PEI needs to be capable of bidirectional power flow to charge and discharge the battery. The simplified Li-Ion battery charging profile is illustrated in Figure 1-11. It has two distinct operating modes: i) constant current (CC) mode and ii) constant voltage (CV) mode. In CC mode, the charging circuit supplies preset maximum allowable charging current until battery voltage reaches floating voltage. During CV mode, the battery voltage is regulated at the float voltage until the charging current drops to a certain value (e.g. 3%-5% of rated current) [10]. The life and capacity of the battery storage depend on several factors including cycle count, depth of discharge, charging modes, maintenance, temperature and age [11]. Among these factors, charging modes are maintained by the charging circuit and controller.

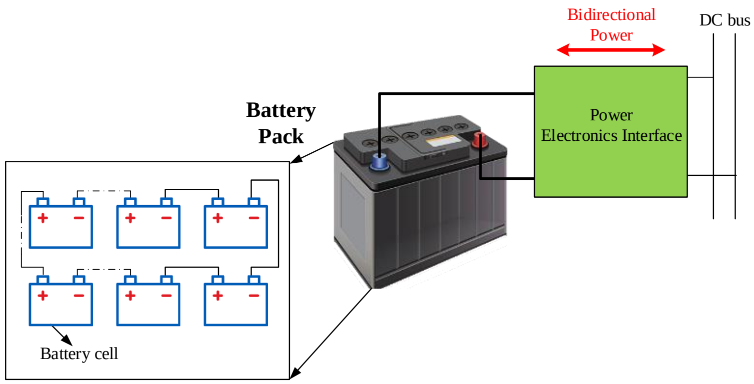

Figure 1-10 Battery power conversion system

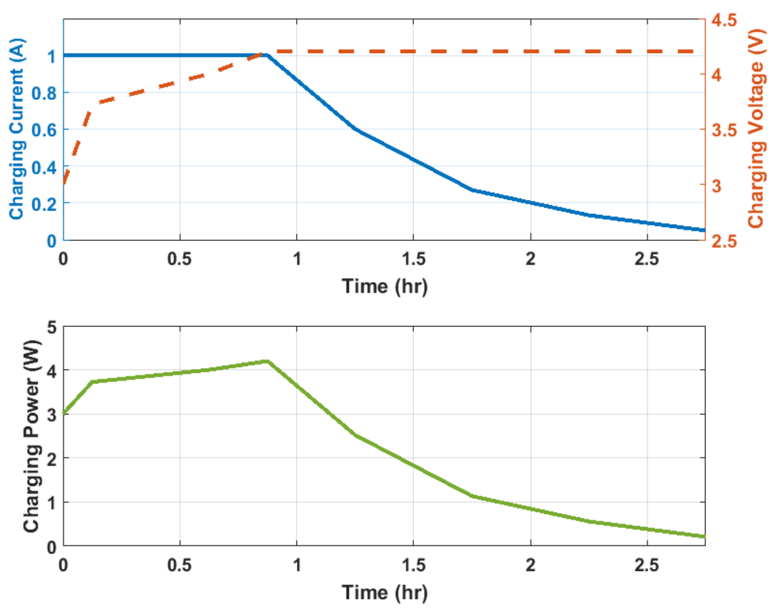

Figure 1-11 simplified charging profile of Li-Ion battery for a single battery cell (HE-4813)

Maintaining CC and CV mode is required to avoid overcharging and/or losing capacity. However, the battery capacity depends on the charging rate, C. For example, charging at 0.7 C results in a capacity of 50% to 70% when 4.1 or 4.2 V is reached, whereas charging at less than 0.2 C can result in a full battery as soon as the voltage reaches 4.1 or 4.2 V. The decreased charging current does not result in losing the capacity of the battery, rather it decreases the CV mode charging time [12].

1.3 Power Electronics Interface for the Renewable Energy System

The power captured by the renewable energy systems cannot be used directly by the load. The power electronics interface (PEI) is required to convert and control the captured power into usable electric power. This energy is then provided to the load or to the grid. The energy sources (wind, PV, and battery) can be integrated at the AC grid (AC-coupled) or at the DC link (DC-coupled) as shown in Figure 1-12 and Figure 1-13 respectively. These energy sources are typically compatible with the DC distribution system. Therefore, for each source one extra conversion step (DC-AC) is required for AC coupled system. Hence, DC networks require a reduced number of conversion stages to accommodate energy transfer between renewable sources and loads, leading to lower capital cost and higher efficiency.

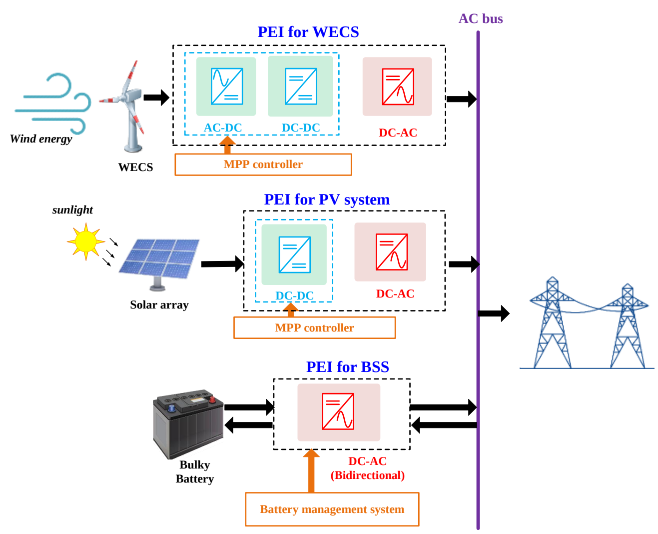

Figure 1-12 Conventional AC-coupled renewable energy system

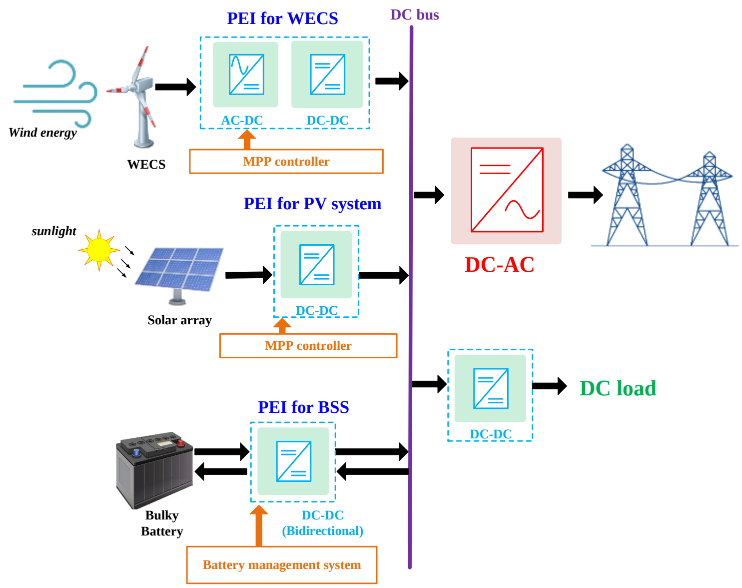

Figure 1-13 Conventional DC-coupled renewable energy system

The battery storage system can be co-located (on the same site) or in different locations with the renewable energy systems. The co-located system can reduce soft costs (site preparation, land acquisition, installation labor, permitting, interconnection, and EPC (engineering, procurement, and construction) [3]. Figure 1-14 shows the DC-coupled co-located system costs the lowest among the DC-coupled and AC coupled (co-located and in different sites) PV-battery systems.

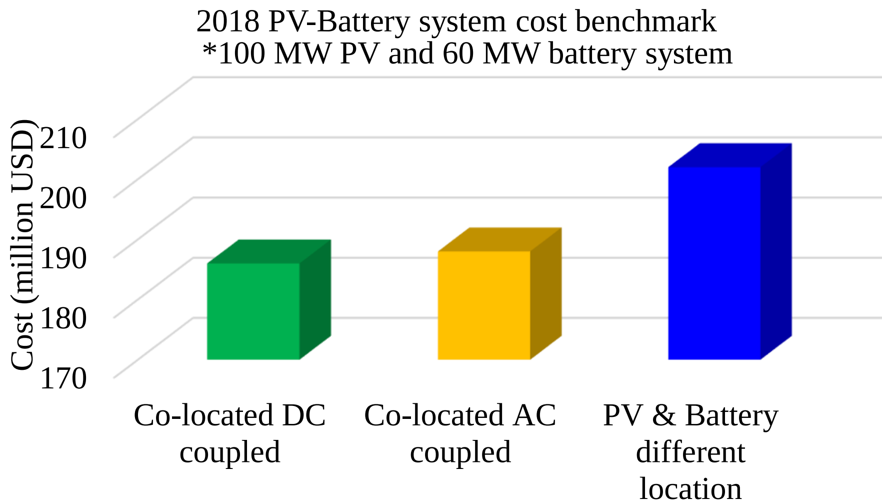

Figure 1-14 2018 cost benchmark for PV-battery system (4-hour duration) in co-located and in different sites (DC- coupled and AC coupled)

1.3.1 Power Electronics Interface for PV System

The output voltage of a PV module is low. Therefore, several PV modules are connected in series to achieve higher voltage and in parallel to achieve higher power level. Depending on the arrangement of PV modules and power electronic interfaces, PV PEIs are categorized as centralized, string/ multi-string type and module integrated type [13] as shown in Figure 1-15. The centralized converter is a single, high voltage, and high power converter and is connected with the PV array. The centralized converter (Figure 1-15.a) suffers from several issues including 1) each module may not operate at maximum power point (MPP), therefore maximum energy harvesting is challenging, 2) power degradation due to mismatch between PV panels caused by partial shading, dissimilar aging of PV panels, manufacturing imperfections, and dirt accumulation, and 3) losses in string diode and junction box [13]. The multi-string and string technologies (Figure 1-15.b) are the modified version of the centralized technology and overcome partially disadvantages of centralized technology [14]. Module integrated technology (Figure 1-15.c and Figure 1-15.d) has been proposed to overcome the aforementioned disadvantages suffered by centralized, string and multi-string technologies. It also offers advantages such as maximum energy harvest, improved safety, increased lifetime and reliability, enhanced performance monitoring, and flexible PV array design and installation [14].

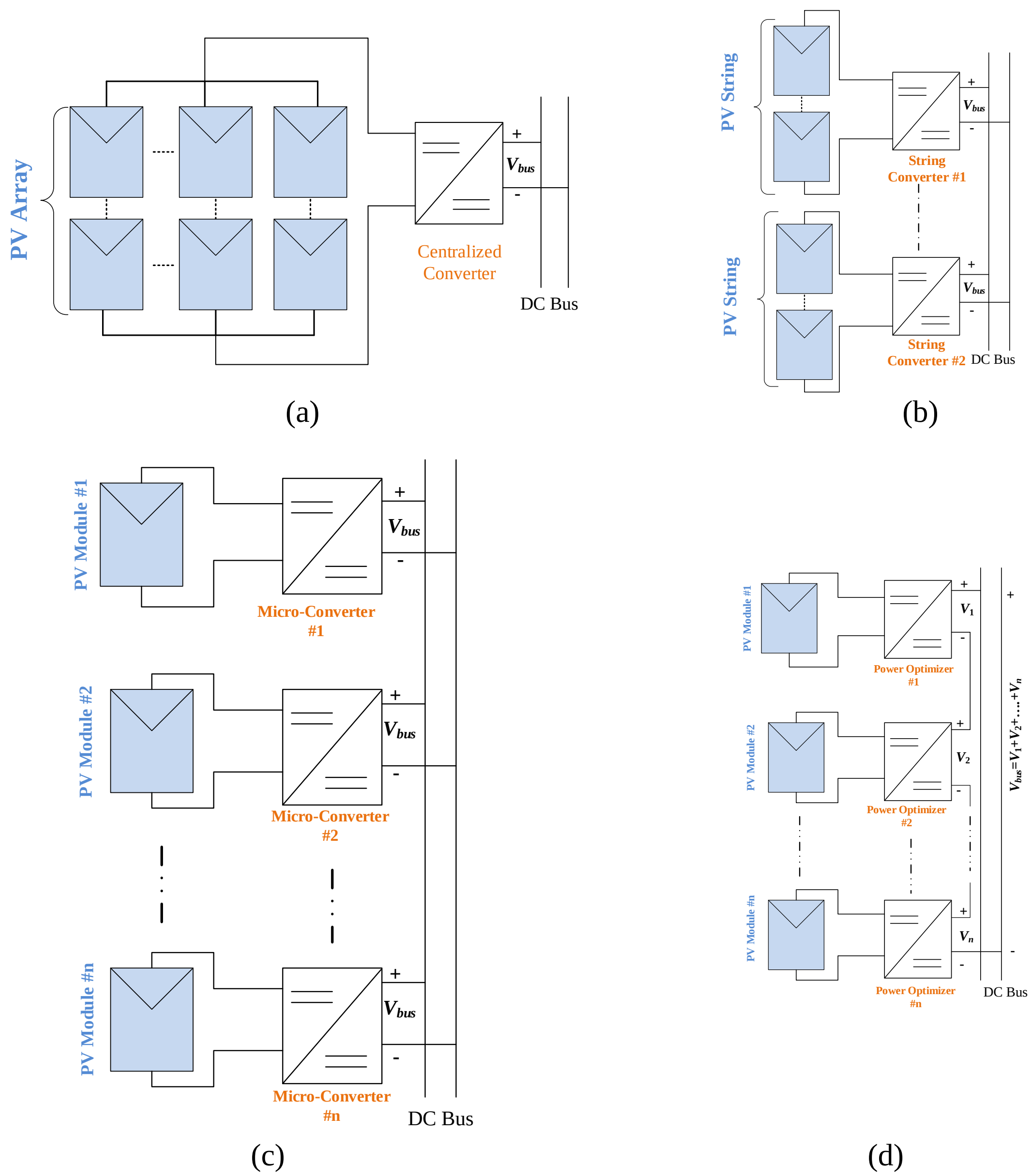

Figure 1-15 PV power electronics interface (a) centralized, (b) string/multistring, (c) micro-converter, and (d) power optimizer

There are two types of module integrated converters for DC integration: the power optimizer and the micro-converter. The micro-converter offers maximum power point tracking (MPPT) and high step up conversion with galvanic isolation. Therefore, the system becomes complex and it requires a complicated control system. On the other hand, the power optimizer is a non-isolated converter with MPPT and performs pre-regulating of the fluctuating voltage of the PV panel to some desired DC voltage level (typically up to 100V) [15]. Therefore, the power optimizer is simple and cost effective. The input and output voltage and current rating of power optimizer are low. Therefore, low rating components can be used in power optimizer. Typically, several PV panels combined with power optimizer are then connected in series to achieve desired high DC voltage level [16]. The series configuration of the power optimizer can be extended to *i* modules to meet different power and voltage levels.

In case of partial shading, the power harvesting by series connected power optimizer will not be affected. The PV module under the shading generates lower current. The unequal current generated by PV modules connected in series forces all panels to carry the lowest current generated by the shaded panel. However, the output side components of the power optimizers carry the output current, not the current generated by the respective PV panel. Therefore, partial shading will not affect other modules. With the module integrated power optimizer, 36% of the power lost from partial shading can be recovered as MPP tracking of each module is separate from each other [17].

1.3.2 Power Electronics Interface for Battery Storage System

In conventional DC-coupled PV-battery system, a bidirectional converter is used for the bulky centralized battery system as shown in Figure 1-13. In case of centralized battery system, if one or several cells fail, the entire battery system has to stop working or works with degraded performance such as voltage drop. Therefore, the system becomes less reliable. Moreover, the centralized battery system is less efficient and requires a larger system to support the same load [18]. To overcome these drawbacks, the decentralized battery system (Figure 1-16) is introduced [19]. The decentralized system offers easy assembly and customization (in terms of voltage and power). Moreover, in the decentralized battery system, battery cells do not have to be of the same brand or series. This feature is beneficial, especially during battery replacement. Better thermal balancing is achievable by assigning less power to the high thermal stressed cell in case of the decentralized system. There are further advantages of the decentralized battery system in power electronics point of view such as 1) cell equalizer is not required and 2) reduced power and voltage stress of the power electronics.

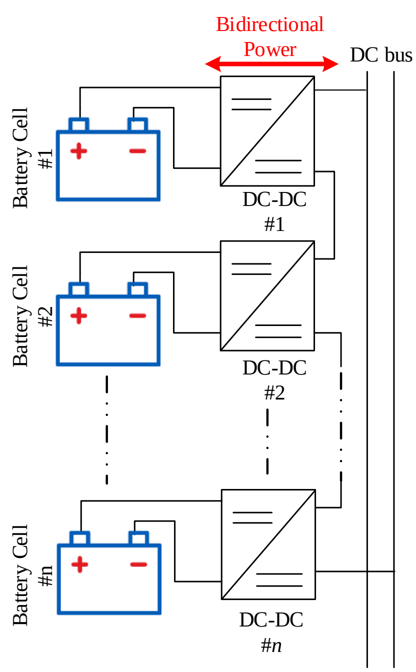

Figure 1-16 Block diagram of decentralized battery system

Conventionally the centralized battery system is connected with the renewable energy systems at the DC link through a bidirectional converter. Therefore, the battery charging power is processed twice and the battery charging efficiency suffers. DC link integration of the PV-battery system is shown Figure 1-17 (a). The battery charging power is processed first by the DC-DC converter#1 (PV to DC bus) and then by the DC-DC bidirectional converter#2 (DC bus to battery). Similarly, if the battery is connected with the PV system at the front end as shown in Figure 1-17 (b) through a bidirectional converter, the discharge power will process twice; first by the DC-DC bidirectional converter#2 and then by the DC-DC converter#1. Assume, the efficiency of both converters is 97% and battery charging power from PV is 100W. Therefore, power at DC link is 97W (97% PV to DC link converter efficiency) and the power to the battery is 94.1W (97% DC link to battery converter efficiency). Ultimately, battery charging efficiency becomes 97%*97% = 94.1%. The same efficiency loss happens in case of front end integration with bidirectional converter. Therefore, using a bidirectional converter affect the system efficiency. However, using separate unidirectional converter for charging and discharging requires more components and makes the system bulky.

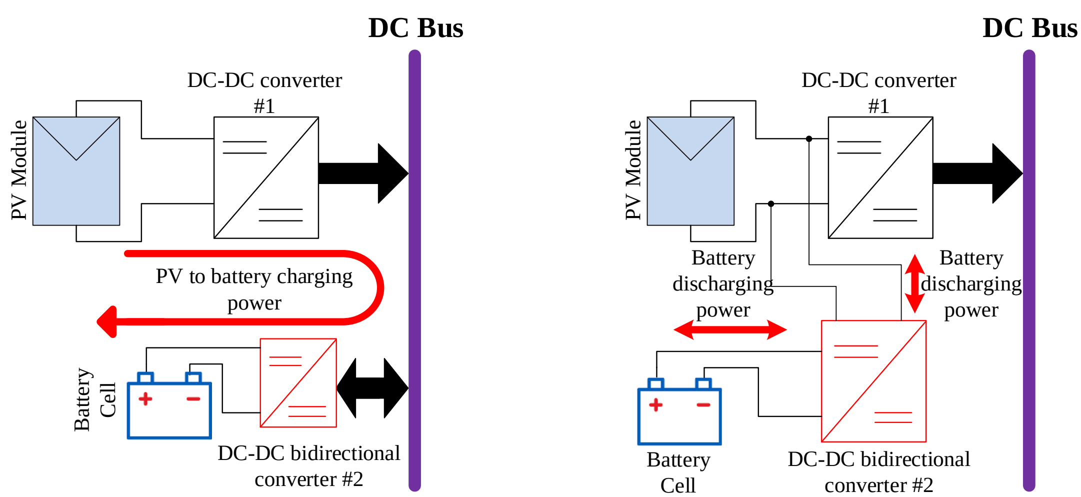

(a) DC link integration (b) Front end integration

Figure 1-17 Battery integration with PV system using bidirectional converter

1.4 Performance Characteristics of the Power Converter

Power converter is essential for power conversion and control of renewable energy system and battery storage system. Power converters typically consist of passive circuit components such as inductors (*L*) and capacitors (*C*), and active components (that is, power switches). Among the power switches, diodes are not controllable; that means the turn on and turn off of the diode cannot be controlled. However, power switches such as MOSFET (Metal Oxide Silicon Field Effect Transistors) and IGBT (Insulated Gate Bipolar Transistors) are controllable. The circuit components (active and passive) used in power converters are not ideal and are a source of energy losses. The main losses that are associated with these components are conduction losses (active and passive components) and switching losses (active component).

1.4.1 Conduction and Switching Losses

Conduction loss happens in both active and passive components of the power converters due to the non-ideal characteristics. In practical, components have the parasitic resistive element in series of components. Therefore, when current flows through the components, the resistive loss happens. This loss is termed as conduction loss. The parasitic resistors (ESR-effective series resistor of the capacitor, DCR-DC resistor of the inductor, and R_{ds_on}- resistance between drain and source in case of MOSFET) are responsible for the conduction loss. The conduction loss, P_D is shown in Eq. 1-4 where I_{cond} is the current through the component and $R_{parasitic}$ is the parasitic resistive element of the component.

$$P_D = I_{cond}^2 \times R_{parasitic} \qquad \text{Eq. 1-4}$$

Switching loss happens during any switching transition (that is, switch turn on and turn off). In practical, the switch voltage or switch current does not go to zero instantaneously at the instant of turn on or turn off. Therefore, for a period of time, there is an overlap of switch voltage (v_s) and current (i_s) (Figure 1-18) which causes the switching loss. The total switching loss, P_{sw_loss} is the sum of turn on loss, P_{on} and turn off loss, P_{off} (Eq. 1-5). P_{sw_loss} depends on the switching frequency, f_s other than overlapping time, and voltage and current associated with the loss as shown in Eq. 1-6. This type of switching is termed as hard switching.

$$P_{sw\_loss} = P_{on} + P_{off} \qquad \text{Eq. 1-5}$$

$$P_{sw\_loss} = 0.5 v_s i_s f_s (t_{ri} + t_{fv} + t_{rv} + t_{fi}) \qquad \text{Eq. 1-6}$$

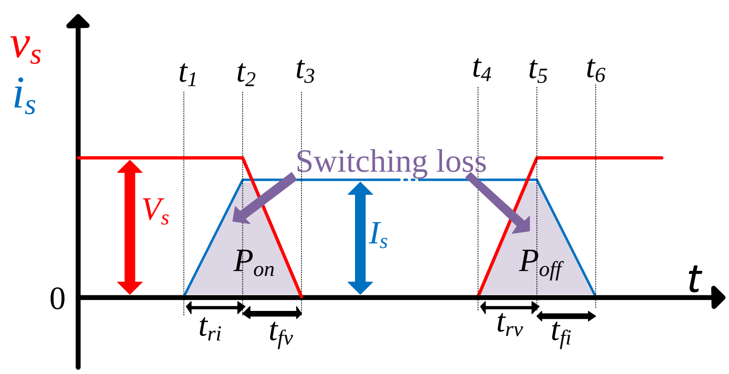

t_{ri}- current rising time
t_{fv}- voltage falling time
t_{rv}- voltage rising time
t_{fi}- current falling time

Figure 1-18 Switching power loss (hard switching)

1.4.2 Soft Switching and Hard Switching

The switching transition (turn on or turn off) where switching losses occur, is termed as hard switching (Figure 1-18). The reason for hard switching is the overlap between the switch voltage and current. Hard switching is explained in the previous section. However, there are several techniques with which the switch voltage and current overlap can be reduced or completely eliminated. Switching transition where switching losses are eliminated or reduced is termed as soft switching.

There are two types of soft-switching: zero-voltage switching (ZVS) and zero-current switching (ZCS) as shown in Figure 1-19. Although there are many different techniques to achieve ZVS and ZCS, they follow the general principles. Both ZVS and ZCS operations can reduce the switching losses of either a MOSFET or an IGBT. However, ZVS is preferred over ZCS for MOSFETs [20]. In the case of MOSFETs, ZVS can substantially reduce the losses caused by the discharging of parasitic capacitance, C_{ds} into the device when it is turned on whereas ZCS cannot.

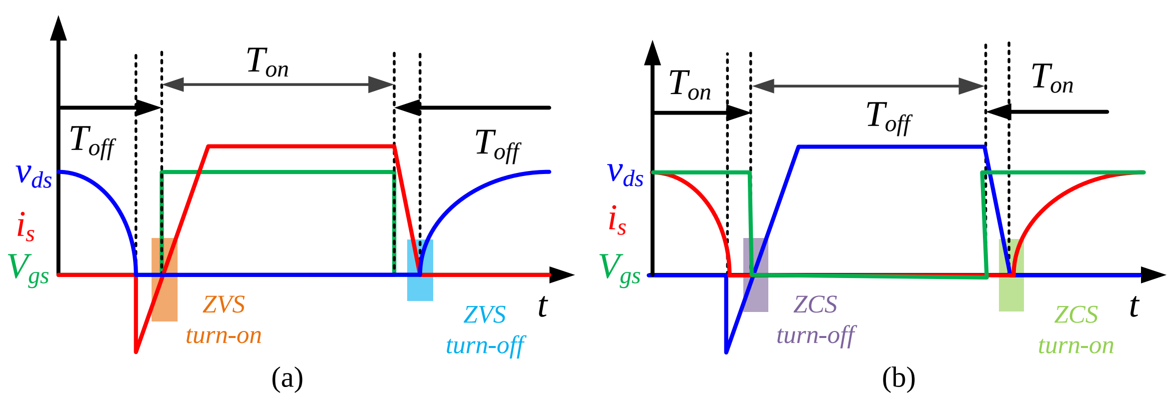

Figure 1-19 Soft switching (a) ZVS buck converter (half wave) and (b) ZCS buck converter (half wave)

1.4.3 Power Quality

The power quality of AC source (such as grid, generator) depends on the harmonic content of line currents drawn by the converter. Power factor is the most important factor to measure power quality. Power factor is the ratio of the real power, P to the apparent power, S drawn by a load from an AC source as shown in Eq. 1-7 [21]. The power factor can also be expressed as the product of the distortion power factor, K_θ and the displacement power factor, K_d. The distortion power factor, K_d is the ratio of the fundamental root-mean-square (rms) current $(I_{rms,1})$ to the total rms current (I_{rms}). The displacement power factor K_θ is the cosine of the displacement angle, and θ is the phase difference between the fundamental input current and the input line voltage.

$$PF = \frac{P}{S} = \frac{v_{rms} i_{rms,1} \cos(\theta_1)}{v_{rms} i_{rms}} = \frac{i_{rms,1}}{i_{rms}} \cos(\theta_1) = K_d K_\theta \qquad \text{Eq. 1-7}$$

When a converter has less than unity power factor, it means that the converter absorbs apparent power that is higher than the active power it consumes. This implies that the power source should be rated to a higher volt-ampere (VA) rating than what the load needs. In addition, the current harmonics generated by the converter deteriorates the power quality of the source, which eventually affects other equipment such as the generator of the wind turbine.

Total harmonic distortion (THD) is another factor that measures the harmonic distortion present in the line current and eventually the power quality. THD is defined as a function of PF (Eq. 1-8) [21]. As the power factor approaches unity, THD will approach zero. However, as THD approaches zero, the power factor becomes a function of θ. A perfectly sinusoidal current can also result in poor power factor if it is out of phase with the line voltage.

$$THD = \sqrt{\frac{1}{PF^2} - 1} \qquad \text{Eq. 1-8}$$

1.5 MPPT Techniques for PV System

Tracking MPP is essential for PV energy system. Otherwise, the captured power could be significantly lower than the available power. The output power from PV is affected by factors such as temperature, light intensity, the angle of the light on the panel, cloud cover, and clarity of the atmosphere. The nonlinear characteristic of V-I and V-P curve of PV module with the change of light intensity is shown in Figure 1-5. Each curve has only one point where the maximum power occurs. The location of the MPP is not known. However, the MPP can be tracked. Figure 1-20 shows the MPPT controller of the PV system.

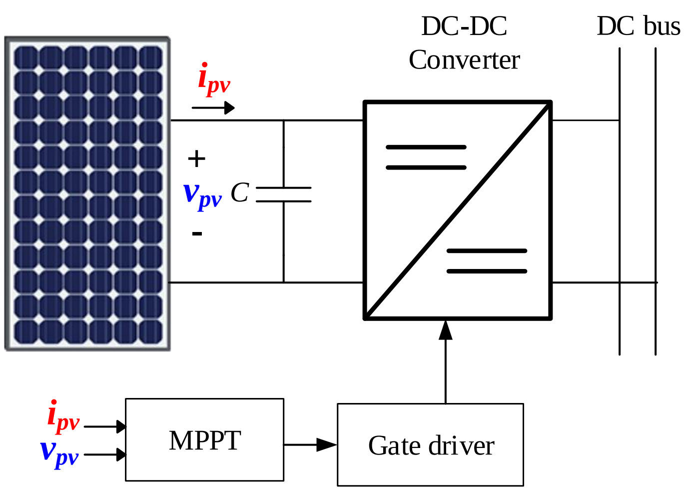

Figure 1-20 MPPT for PV system

Many MPPT technique have been developed and implemented [21]-[29]. Each technique has its own advantages and disadvantages. These techniques vary in different aspect such as complexity, sensor required, convergence speed, cost, range of effectiveness and so on [22] [23]. Among these techniques, most popular techniques can be categorized as –

1. Heuristic search (Perturb & Observe method)
2. Extreme value searching (Incremental conductance)
3. Intelligent control (Fuzzy logic, and neural network)

Among these techniques, the Perturb & Observe (P&O) method [24] [25] is one of the most straightforward and popular algorithms because of its simplicity. The goal of tracking MPP is achieved by varying the control parameter such as frequency and duty ratio. By changing the control parameter, the operating point (operating voltage and current) of the PV panel can be changed. In case of P&O, the change of control parameter continues until the MPP is tracked.

Figure 1-21 shows the V-I (red) and V-P (blue) curves of a panel for two different light intensity 700W/m^2 (dotted lines) and 1000W/m^2 (solid lines). At 700W/m^2, the voltage and current at MPP are 25V and 5.3A, and maximum power is 160W. However, the voltage and current at MPP are 33V and 9A for 1000 W/m^2 and maximum power is 255W. Assume, the panel is operating at MPP for 700 W/m^2. At this point, light intensity changed from 700W/m^2 to 1000W/m^2. Therefore, the characteristics curve of the panel shifted from 700W/m^2 to 1000W/m^2. If the control parameter of the converter remains same, the converter will extract the same power from PV (green dotted arrow from dotted blue curve to solid blue curve). Therefore, the converter is extracting less power compared to available power from PV. In P&O method, a step change in control parameter (duty ratio or frequency) is made and the process is repeated periodically until MPP is reached as shown with the yellow dotted arrow in Figure 1-21.

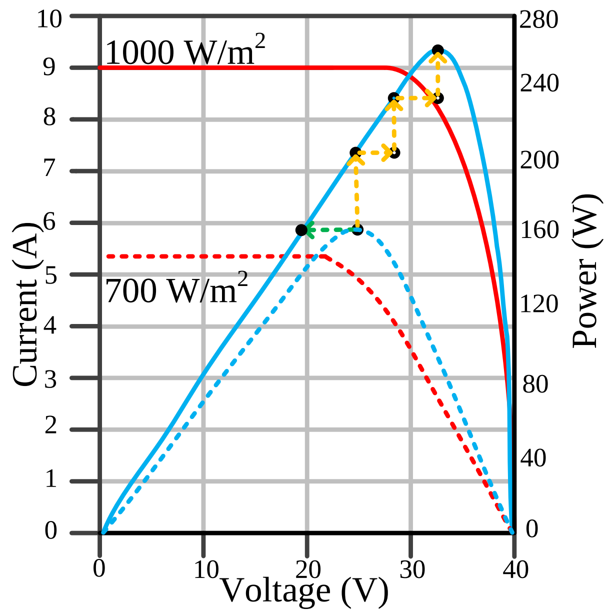

Figure 1-21 Maximum power point tracking using P&O

Continuous oscillation around the MPP is an intrinsic problem of the P&O method. The oscillation can be minimized by reducing the perturbation step size. However, small perturbation size increases the convergence time. One of the solutions of this conflicting problem is to use a variable perturbation step size [24].

Another popular algorithm for tracking MPP is the Incremental Conductance method (IncCond) [26] [27]. The IncCond method is based on the fact that the slope of the V-P curve at MPP is zero (Eq. 1-9), positive on the left side of the MPP (Eq. 1-10) and negative on the right side of MPP (Eq. 1-11). It is developed to eliminate the oscillations around the maximum power point (MPP). However, it requires complex mathematical calculation and results longer time to reach MPP.

$$\frac{dI}{dV} = -\frac{I}{V} \Leftrightarrow \frac{dp}{dV} = 0 \text{ at MPP} \qquad \text{Eq. 1-9}$$

$$\frac{dI}{dV} > -\frac{I}{V} \Leftrightarrow \frac{dp}{dV} > 0 \text{ left of MPP} \qquad \text{Eq. 1-10}$$

$$\frac{dI}{dV} < -\frac{I}{V} \Leftrightarrow \frac{dp}{dV} < 0 \text{ right of MPP} \qquad \text{Eq. 1-11}$$

Microcontrollers have made the intelligent control for tracking MPP popular over the last decade. Intelligent controllers do not require precise input. Fuzzy logic control [28] [29] generally consists of three stages: fuzzification, rule base table lookup, and defuzzification. During fuzzification, numerical input variables are converted into linguistic variables. [28] utilizes five linguistic variables: NB (negative big), NS (negative small), ZE (zero), PS (positive small), and PB (positive big). The more fuzzy levels used by the logic controller, the more accurate its performance is. However, additional levels increase the difficulty of implementation. In the defuzzification stage, the fuzzy logic controller output is converted from a linguistic variable to a numerical variable which provides an analog signal to the power converter to track the MPP.

Neural networks [30] generally have three basic layers: input, hidden, and output layers. The hidden layer could be of with several layers. The number of nodes in each layer vary and are user-dependent. The input variables can be PV array parameters like open circuit voltage (V_{OC}) and short circuit current (I_{SC}), atmospheric data like light intensity and temperature, or any combination of these. The output is usually one or several control signals of the converter.

The intelligent control methods perform well under varying atmospheric conditions. The oscillation at MPP is minimum. However, the effectiveness of these methods varies with PV to PV and different atmospheric conditions. Therefore, these methods require high knowledge and experience to get the best of it.

1.6 Existing Power Electronics Interface for Renewable Energy Systems and Battery Storage Systems

The power electronics interface for renewable energy systems and battery storage systems requires several features including power conditioning such as (1) provide proper input to load power conversion, (2) regulate output voltage, (3) maximum power point tracking (MPPT) of PV and wind energy system, (4) power factor correction (PFC) of wind energy system, (4) bidirectional power path to charge and discharge the battery, and (5) following the battery charging profile (CC- constant current mode and CV-constant voltage mode) as explained in previous section. There are existing standard power converters used in conventional power conversion process of renewable energy systems and battery storage systems. These converters are used for individual power processing by each source.

1.6.1 Standard DC-DC Converter

The basic non-isolated (such as buck, boost, and buck-boost) and isolated (such as flyback, forward, and half-bridge) converters are commercially utilized to convert the generated electrical energy by the renewable energy systems to usable electrical power. Among the non-isolated converters boost converter is popular for the PV system. Figure 1-22 shows the DC-DC boost converter. The boost converter is capable of stepping up the voltage. That means the output voltage is higher than the input voltage. When the switch S_1 is on, the diode D is reverse biased and the inductor L is connected across the input. The inductor stores energy at this time period. When the switch S_1 is off, the diode D is forward biased and allows inductor and the input source to supply power to the load. The other two kinds of basic non-isolated converter (buck and buck-boost converter) also consist of switch, diode, inductor, and capacitor. These converters are single switch converter. With the switch turn on and off, input is connected and disconnected with the output. The inductor is utilized to store energy and diode allows the path to release inductor charge.

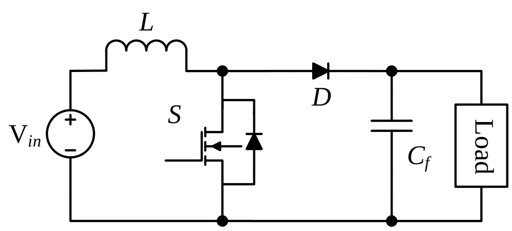

Figure 1-22 DC-DC boost converter

Figure 1-23 shows a buck-boost type isolated converter named flyback converter. The input transformer T_{in} isolates the output from the input. When the switch in on, energy is stored in the transformer and the diode is reverse biased. Therefore, no power flows from input to output. When the switch is off, diode becomes forward biased. The stored energy is now transferred to the output.

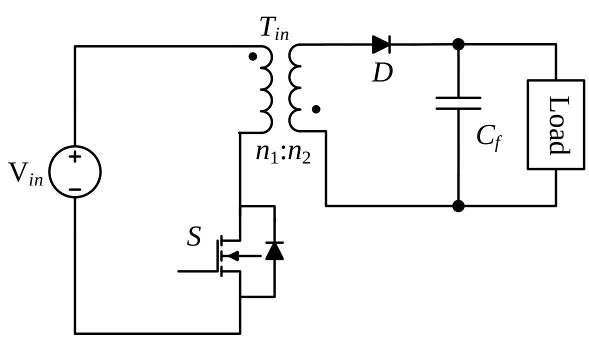

Figure 1-23 Isolated buck-boost type DC-DC converter/flyback converter

The voltage gain expressions of the basic DC-DC converters are presented by Eq. 1-12, Eq. 1-13, and Eq. 1-14. From the gain expressions, the only control parameter of these converters is the duty ratio [21]. All these converters are of single switch converters and hard switching type. These converters are unidirectional converter. That means power only flows from input to the output side.

$$M_{v-buck} = d \qquad \text{Eq. 1-12}$$

$$M_{v-boost} = \frac{1}{1-d} \qquad \text{Eq. 1-13}$$

$$M_{v-buck-boost} = \frac{d}{1-d} \qquad \text{Eq. 1-14}$$

1.6.2 Bidirectional Converter

Bidirectional converters are capable of transferring power in both directions. Bidirectional power flow is necessary for battery storage systems. Different types of non-isolated bidirectional converter are presented in [31] [32]. The basic non-isolated buck-boost type bidirectional converter is shown in Figure 1-24. When power is transferred from V_L to V_H, switch S_1 is on and switch S_2 is off. Similarly, when power is transferred to the opposite direction, S_2 is on and S_1 is off. The converter performs as a boost converter for the power flow from V_L to V_H and as a buck converter for the power flow to the opposite direction. Zhang *et al* [33] introduced resonant tank and Do [34] applied coupled inductor to achieve soft switching in the non-isolated buck-boost converter. Other commonly used bidirectional converters are dual active bridge (DAB) [35] (Figure 1-25.a) and dual half-bridge converter (DHB) [36] [37] (Figure 1-25.b). In DAB, full-bridge voltage fed converters are used for both sides of the isolation transformer. The sign of φ (Eq. 1-15) determines the direction of power flow, where φ is the phase difference between the voltage across the primary and secondary side of the isolation transformer. Both DAB and DHB are capable of ZVS turn on and turn off.

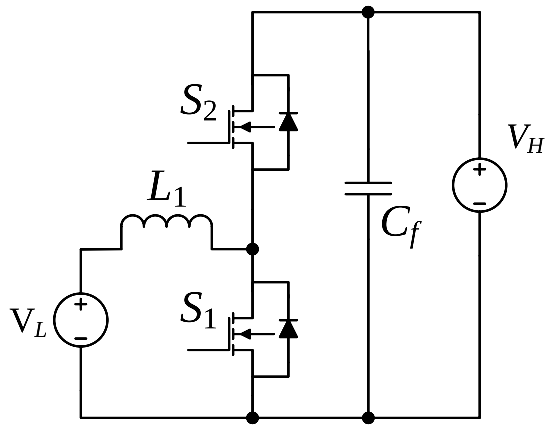

Figure 1-24 Non-isolated buck-boost type bidirectional converter

$$P_0 = \frac{V_1^2}{\omega L_s} \times \frac{d\varphi(\pi - \varphi)}{\pi} \qquad \text{Eq. 1-15}$$

$$d = \frac{V_0}{NV_1} \qquad \text{Eq. 1-16}$$

Bidirectional converters require minimum two active switches to provide bidirectional power path as shown in Figure 1-24. Other standard bidirectional converters require more switches: eight and four switches in case of dual active bridge and dual half bridge converter respectively. Therefore, conduction and switching loss are higher in bidirectional converters in comparison to unidirectional converter.

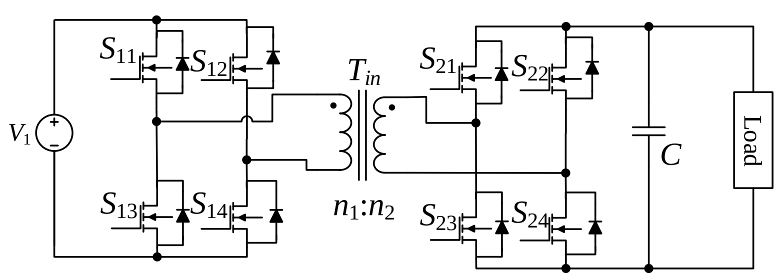

(a)

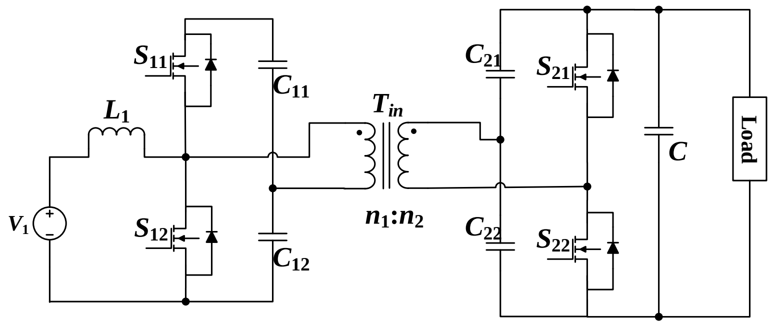

(b)

Figure 1-25 Isolated bidirectional converter (a) dual active bridge (DAB) and (b) dual half bridge (DHB)

1.6.3 Power Factor Correction

The requirement of power factor correction (PFC) is apparent for AC-powered input module, such as wind turbine system. Generally, an AC-DC active full bridge rectifier is used at the front-end of the AC system as a PFC circuit to ensure the unity input power factor. PFC is performed by sensing the three-phase input voltages and currents. This is achieved by controlling the converter switches (on and off) in an appropriate manner. At higher PF, the current in each phase is nearly sinusoidal and in phase with the corresponding phase voltage. The three-phase six-switch front-end boost type rectifier [38] is conventionally used for high power application.

For three-phase low power applications, it is possible to perform PFC by using only a single switch topology [39]- [40] to reduce cost as the current and voltage stress across the switching device is not excessive. An example of such a converter is the three-phase single-switch AC-DC boost converter as shown in Figure 1-26(a) [39]. Other three-phase single-switch converters are based on basic DC-DC converters (buck, boost, buck-boost, Cuk, Zeta, and SEPIC) where the input DC source is replaced with a three-phase AC source and a three-phase diode bridge. The converters consist of three input inductors (L_a, L_b, L_c), three-phase diode-bridge, a switch (S), a diode (D) and a filter capacitor (C); an input filter is used to filter out higher frequency harmonics that are created by the converter's switching operation. The converters are simple as they require only one switch operating at the high switching frequency and they can achieve PFC by operating in discontinuous conduction mode (DCM). These fundamental converters can be divided into two main groups:

- Converters with an inductive input filter (Boost, Cuk and SEPIC)
- Converters with a capacitive input filter (Buck, Buck-boost, and Zeta)

The converters with an inductive input filter ensure the input inductor currents (e.g. i_{La}) rise and fall in every switching cycle, whereas the converters with an input capacitive filter ensure the capacitor voltages (e.g. v_{Ca}) rise and fall. In discontinuous conduction mode PFC circuit, the switching frequency is much higher than the line frequency. Therefore, the input inductors (L_a, L_b, and L_c) are charged and discharged several times within half cycle of the line period and the peak envelope of the input current is sinusoidal.

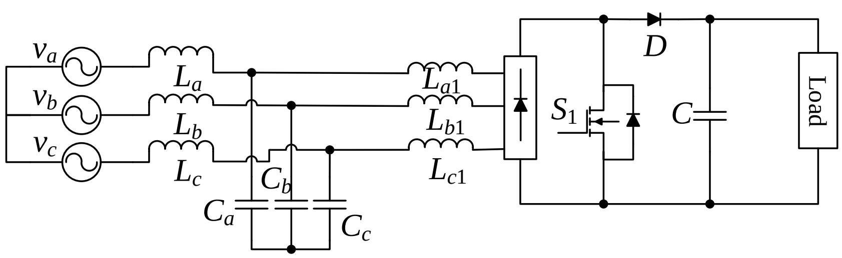

(a)

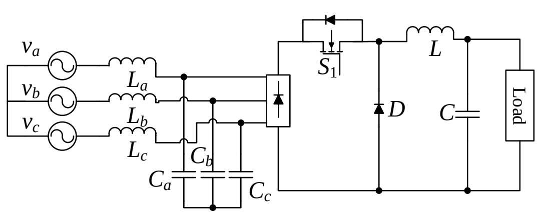

(b)

Figure 1-26 Front-end single-switch PFC converter (a) boost (b) buck [40]

1.6.4 Multi-input Converters

In conventional renewable energy system, individual power converter is used for each of the sources as shown in Figure 1-13. The individual converters can be integrated when several sources are utilized together. The idea is to integrate multiple independent converter into a single converter by sharing the common components of the original converters. This type of converter is termed as multi-input converter (MIC). The MIC is efficient, compact, and cost-effective when multiple resources are utilized.

Numerous MICs have been presented in the literature [41]-[54]. In general, MICs are divided into two broad categories: non-isolated topologies and isolated topologies. Non-isolated topologies are simple in structure with fewer components and therefore, possess advantages of compact structure, low cost, high power density and straightforward power flow control [41]. However, attaining high voltage gain is difficult with non-isolated topologies. Moreover, these topologies cannot be used where galvanic isolation is a requirement. In an isolated converter, a transformer is used to provide the electrical isolation between the input and output. The converter uses the principle of magnetic coupling of the transformers to combine multiple sources.

Non-isolated MICs can be derived from the basic non-isolated DC-DC converters such as buck, boost, buck-boost, Cuk, SEPIC and Zeta. The non-isolated MIC can be synthesised from any single type DC-DC converter such as buck-buck [42] (Figure 1-27.a) and boost/boost [43] (Figure 1-27.b) or from different types of DC-DC converter buck-buck/boost [44] (Figure 1-28.a) and buck-SEPIC [45] (Figure 1-28.b) MIC. Depending on the input source, different types of DC-DC converters are chosen to derive the MIC. These

MICs are capable of individual and simultaneous operations. During individual operation, the MIC performs as a single DC-DC converter.

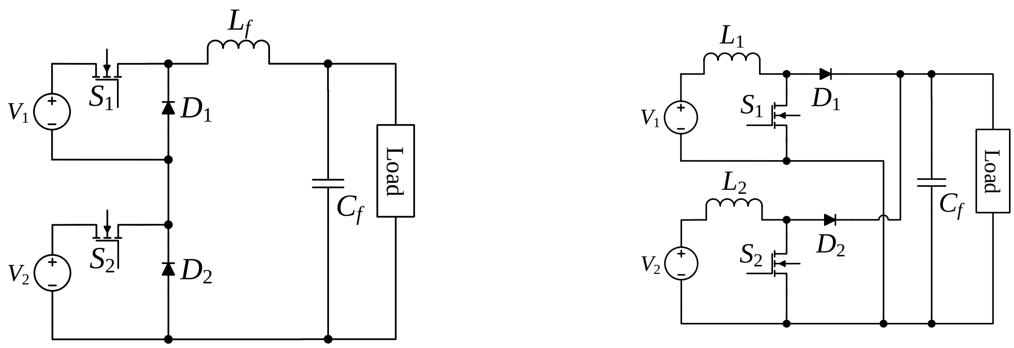

(a) (b)

Figure 1-27 Non-isolated MIC from same PWM converter (a) buck-buck (b) boost-boost

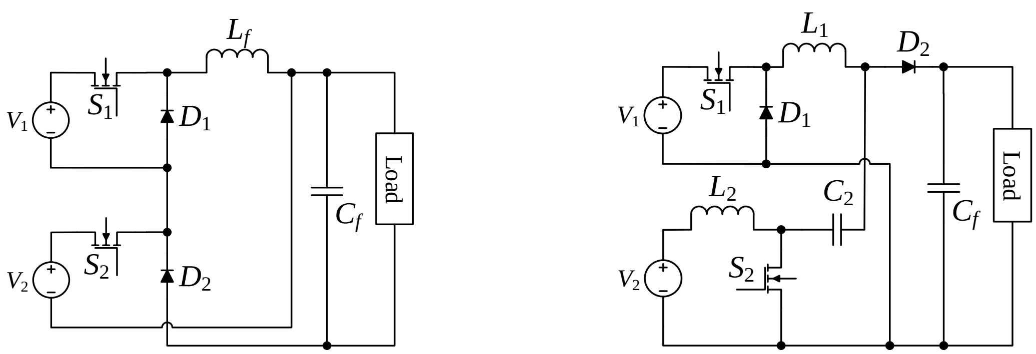

(a) (b)

Figure 1-28 Non-isolated MIC from different PWM converter (a) buck-buck/boost (b) buck-SEPIC

A double input buck-buck MIC is shown in Figure 1-27.a. The switch S_1 and D_1 form the input side of the source#1 and the switch S_2 and D_2 form the input side of the souce#2. The output filter L_f and C_f are shared by both sources. S_1, D_1, D_2, L_f, and C_f are active during the individual operation of source#1 to transfer power from souce#1 to the load. Similarly, S_2, D_1, D_2, L_f, and C_f are active during the individual operation of source#2. During the simultaneous operation, if switch S_1 is off, D_1 provides the continuing path for source#2. On the contrary, if D_1 is off, S_1 creates the continuing path for source#2. Similarly, S_2 and D_2

turn on and turn off complementary to provide the continuing path for source#1. When both switches S_1 and S_2 are off, D_1 and D_2 create the freewheeling path. Other MICs showed in Figure 1-27 and Figure 1-28 work in a similar manner. The output voltage of the MIC is shown in Eq. 1-17 where M_{v1} and M_{v2} is the gain of the converter#1 and converter#2. M_{v1} and M_{v2} depend on the type of the converter. These converters are hard switching type. Wai et al. [46] utilize an auxiliary circuit to achieve ZVS operation of the boost-boost MIC.

$$V_0 = V_1 \times M_{v1} + V_2 \times M_{v2} \qquad \text{Eq. 1-17}$$

The isolated MICs can be derived from the basic topologies of isolated DC-DC converters such fly-back, forward, push-pull, full-bridge, and half-bridge converters same as the non-isolated MICs. Fly-back and forward converters are used for low voltage and low power applications [47], whereas bridge converters (such as half-bridge and full-bridge) are suitable for medium to high voltage and power applications [48]. Figure 1-29 (a) shows the isolated buck-boost type MIC. The coupling inductor plays two roles- input inductor of the buck-boost converter and the flux additivity of the sources. Figure 1-29.b shows the full-bridge MIC [49]. It requires 4 switches for each input source, whereas the half-bridge converter requires fewer switches and the voltage gain is half in case of half-bridge converter in comparison to full-bridge converter.

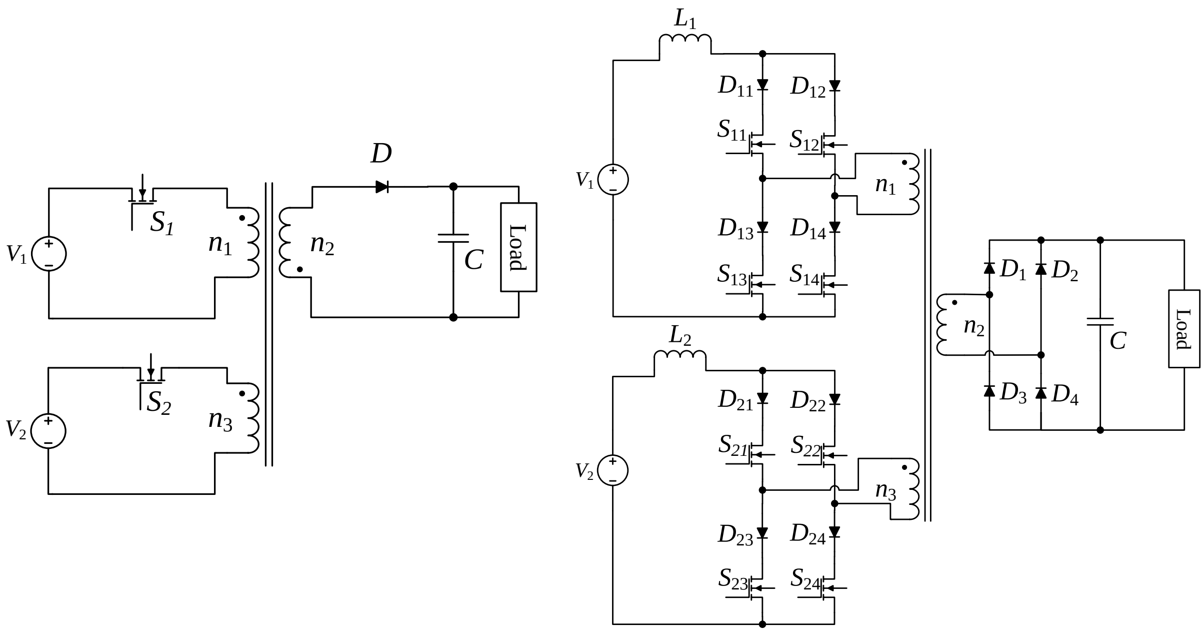

(a) (b)

Figure 1-29 Isolated MIC (a) buck/boost (b) full-bridge

Based on the power flow direction, MICs can be of two types: unidirectional and bidirectional. In case of unidirectional converters, the power flow direction is only from source to load. In contrast, power flow in the bidirectional converter happens in both directions: from input to output and output to input of the converter. Bidirectional converters are required if any storage device (such as battery) is incorporated with the system.

Liu *et al.* [50] presented a systematic synthesizing method for deriving non-isolated converters from the six basic non-isolated converters like buck, boost, buck/boost, Cuk, Zeta, and SEPIC converters. Kwasinsk *et al.* [51] have made some assumptions, restrictions, and conditions to find out the feasible and unfeasible converter. A systematic method for generating multi-input converters has also been described in [52]. A set of connection rules along with the set of basic and hybrid cells, and output filters have been proposed as the building cells of multiple-input converters. A method for reducing the components of isolated multi-input converters (both hard switching and soft switching) is presented in [53]. A systematic approach for synthesizing isolated MICs is explained in [54].

MICs for renewable energy systems and battery storage systems require several features other than combining sources and convert the power. The capability of tracking MPP is necessary for each input source connected to PV or wind. PFC is apparent if wind energy is one of the resources of the renewable energy systems. Charging and discharging paths are required for the battery storage systems. Numerous MICs have been presented in the literature for renewable energy systems and battery storage systems [55]-[81]. Researchers have chosen different renewable resources to build renewable energy systems: such as PV-wind, PV-battery, and PV-FC-battery systems. Based on the resources used in renewable energy systems, the features of the MICs are decided. MICs for the wind-PV system are required to be comprised of AC-DC (with PFC) and DC-DC converters. These converters are usually unidirectional [55] [56]. However, bidirectional converter is required for the energy storage system. MICs composed of bidirectional converters are suitable for battery strings [19]. Converters integrated with unidirectional and bidirectional converters are mostly suitable for renewable energy systems with energy storage [57]- [58]. Research works presented in the literature typically combine wind and PV or PV and battery to form renewable energy systems.

Mangu *et al.* [59] presented renewable energy system with the combination of wind, PV, and battery (Figure 1-30). A bidirectional buck-boost converter is used to charge and discharge the battery. However, the charging profile of the battery is not addressed. The voltage boosting for PV and battery is accomplished by connecting these two sources in series. Further voltage gain is achieved by the transformer turns ratio. The presented MIC utilizes 6 switches to achieve MPPT for PV and wind, and bidirectional power flow for the battery. The output voltage V_0 is not tightly regulated. V_0 varies with the variation of V_{PV} and V_{bat} as shown in Eq. 1-18. Moreover, soft switching is not realized for the switches of this topology, causes higher switching loss.

$$V_0 = V_{C3} + V_{C4} = n(V_{C1} + V_{C2}) = n(V_{bat} + V_{PV}) = \frac{nV_{wind}}{1 - d_{wind}} \quad \text{Eq. 1-18}$$

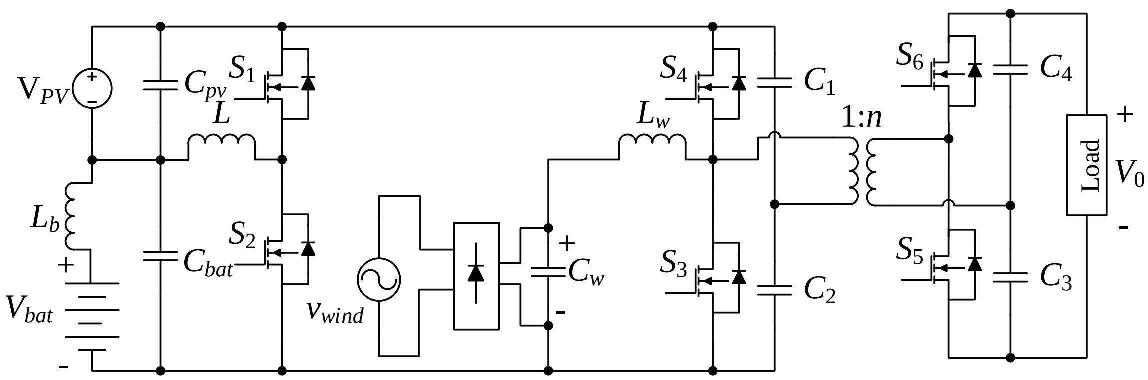

Figure 1-30 Isolated MIC for renewable energy systems (wind-PV-battery) [59]

Chen *et al*. [60] has presented a MIC for wind-PV system comprises of single switch buck converters. MPPT is achieved by the buck converter switch and the DC link voltage regulation is achieved by the load side inverter. Chen *et al*. [61] presented an isolated MIC for wind-PV system for battery charging with single switch for each module with a higher number of diodes and transformer (Figure 1-31). The switches are utilized to achieve MPPT of wind and PV. However, it suffers from higher conduction losses due to series diode and the three-winding transformer. Soft switching is also not realized for this topology.

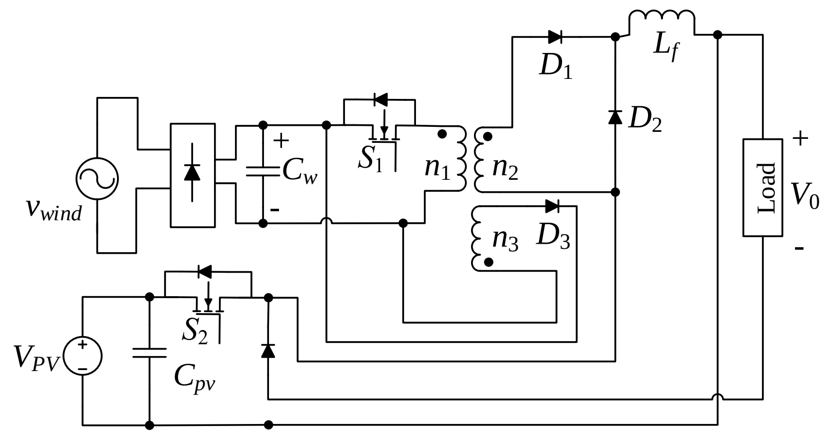

Figure 1-31 Isolated MIC for wind-PV renewable energy systems [61]

Reddi *et al*. [62] presented ZCS MIC for wind-PV system to connect with the inverter. This also utilizes single switch for each input and achieves soft switching. The MPPT for the PV and the wind system is not considered in this work. The switches are controlled to regulate the output voltage rather tracking MPP.

The literatures on wind-PV generation mainly focus on system sizing and optimization rather power electronics interface [59]. MICs presented in the literature for the wind-PV system mostly comprises of DC-DC converter and a bridge rectifier is used at the front end for the wind application [59]- [62] [63] . None of the mentioned topologies consider the PFC for the wind module. [64] presented MIC capable of achieving high PF and tracking MPP. However, the presented MIC requires 4 switches for each input modules. A comparison between MICs which utilizes single switches for each input module, presented in literature for wind-PV system is shown in Table 1-1.

Table 1-1 Comparison of MICs for wind-PV renewable energy systems

		[60]	[61]	[62]
Isolation		Non-isolated	Isolated	Isolated
No. of components	**Switch**	2	2	2
	Diode	2	2	4
	Inductor	1	1	2
	Capacitor	-	-	1
	Transformer	-	1(3 Winding)	1(2 Winding)
Soft-switching		No	No	No
PFC		No	No	No
MPPT		Yes	Yes	No
Output voltage regulation		No	No	Yes
* No filter (input and output) components are counted ** MIC comprises of 1 wind module and 1 PV module				

In the conventional PV-battery system, typically a centralized bidirectional converter connected at the DC link is required to charge and discharge the battery [65] - [68]. Another approach of integrating the battery and the solar PV system is to employ a three port converter [69] - [70]. Different studies have been dedicated to developing efficient and reliable non-isolated [69] [71]- [72]and isolated [73] - [75] power converters for PV-battery systems with high gain capability. Soft switching converter solutions have also been presented for this application to achieve high circuit efficiency [73] [74] [76] . Researches which took the approach of micro-converter as shown in Figure 1-15(c), utilize coupled inductor, switched capacitor and active clamp technique to achieve high gain [74] [75] [77]. Therefore, the circuit becomes complex and faces more components count. Researches which took the approach of utilizing power optimizer (Figure 1-15 (d)) for the PV-battery system, utilize simple topologies [57] [78]-[81]. However, these topologies are capable of tracking MPP along with charging and discharging the battery. [57] and [78] employ bidirectional converter for charging and discharging the battery. The battery module is connected at the front end in [57], whereas the battery module in [78] is connected at the DC link. Therefore, the discharging power in the case of [57] or the charging power in the case of [78] is processed twice as explained in section 1.3 and efficiency suffers. Moreover, these works do not consider soft switching.

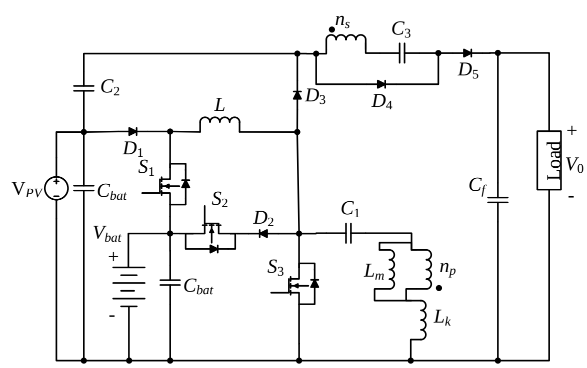

Figure 1-32 Non-isolated three switch MIC for PV-battery system [79]

[79] and [80] integrated the charging module at the front end of the PV module. Therefore, the charging or discharging power is processed once. Chien et al. [79] employ three switches to achieve MPPT, battery management and output voltage regulation (Figure 1-32). The switches of [79] do not have soft switching operation. The MIC presented in [80] requires higher number of switches (Figure 1-33). Two active switches are required even for the individual operations. [81] integrated the bidirectional battery module at the front end of the PV module through a high frequency AC link. Chen et al. [81] utilizes 5 active switches, two coupled inductors and two active-clamp circuits. All the switching transition happen under soft-switching condition. The converters presented in [57] [78]- [81] are not able to track

MPP of the PV system for all operating conditions. A comparison between MICs presented in the literature for PV-battery system is presented in Table 1-2.

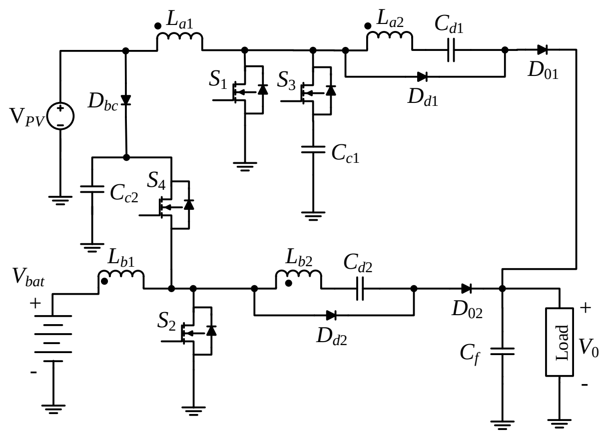

Figure 1-33 Non-isolated four switch MIC for PV-battery system [80]

Table 1-2 Comparison of non-isolated MICs for PV-battery system

		[57]	[79]	[80]	[81]
No. of components	**Switch**	6 (HF)	3 (HF)	4 (HF)	5 (HF)
	Diode	4	5	5	-
	Inductor	3	1	-	2
	Capacitor	7	3	9	2
	Transformer	-	1 (2W)	2 (2W)	1 (4W)
Soft-switching		No	No	Yes	Yes
MPPT for all operating modes		No	No	Control mechanism not reported	No
Rated power		150W	300W	150W	200W
Switching frequency		100kHz	50kHz	50kHz	50kHz
Double power process issue of the battery circuit		Yes	Yes	Yes	Yes
Efficiency		87%	94.3%	95.8%	90.1%

* W- no. of winding, HF- high frequency

** No filter (input and output) components are counted

*** MICs comprise of 1 PV module and 1 battery module

1.7 Research Motivation

In general, different types of MIC topologies and their features and drawbacks have been discussed. Existing MICs reported in the literature for renewable energy systems suffer from one or more of the following challenges:

- Hard switching in at least one of the switches in the MIC circuit topology;
- More than one switch is utilized in at least one of the input modules in the MIC circuit topology;
- Limited soft-switching operating condition or additional auxiliary circuit is required;
- PFC circuit is not considered for AC input source such as wind
- MPP is not tracked for all operating modes
- Double power conversion process in the power interface for the energy storage device;
- Output voltage regulation is not considered in some cases.

The research goal of this thesis is to develop a new class of highly power efficient and compact MIC for renewable energy systems by overcoming the drawbacks. The objectives of this research are:

1. To develop several soft-switched extendable DC-DC MIC topologies, where each input module utilizes only one switch, and a common output filter is shared among different input modules.
2. To integrate an AC-DC three-phase PFC circuit with one of the input modules of the devised DC-DC MIC topologies for interfacing with AC source such as wind turbines, where the new devised module still uses only one switch.
3. To implement a MPPT control technique to the DC-DC unidirectional module of the devised MIC to use it as a PV power optimizer.

4. To integrate DC-DC unidirectional charging and discharging modules of the decentralized battery system with the devised DC-DC PV power optimizer where the new devised charging module is capable of following the battery charging profile.
5. To develop a MIC for PV-battery systems to use in the unregulated grid where the devised MIC is capable of regulating output voltage besides tracking the MPP and following the battery charging profile.
6. To develop the control mechanism of the devised MICs for renewable energy systems.

The developed MICs are modular in nature such that they will provide design flexibility to achieve a higher voltage and power requirement.

1.8 Thesis Organization

In Chapter 1, the importance of renewable energy, especially PV and wind energy, and the necessity of storage systems (Li-ion battery) for the renewable power generation are described. The limitations of conventional power electronics interface for renewable energy systems and energy storage systems are discussed. Important features are identified to make the system more efficient, compact and reliable.

In Chapter 2, different new soft-switched DC-DC MIC circuits are proposed. In particular, each input module of these MICs uses only one switch. The operating principles and analysis of the proposed MICs are discussed. Different types of three-phase PFC circuits are then investigated, where each of them is used to integrate with one of the input modules in the devised DC-DC MIC circuits. The analysis of the derived AC-DC module with PFC is presented. Simulation and experimental results are then presented on selected topologies to highlight their features.

In Chapter 3, a module integrated power optimizer is proposed for the PV-battery systems. The proposed converter is for the regulated DC grid. The battery charging circuit is integrated at the front end of the PV system and the discharge circuit forms the MIC configuration with the PV power optimizer at the output side. The operating principles and analysis of the proposed converter are discussed. Simulation and experimental results are presented to verify the functionality of the proposed converter.

In Chapter 4, another module integrated power optimizer for the PV-battery system is proposed which is applicable for regulating the output voltage of the unregulated DC grid. The operating principles and analysis of the proposed converter are explained. The control principle for the proposed system is discussed. Simulation and experimental results are presented to highlight the performance of the proposed converter as well as the controller of the proposed converter.

In Chapter 5, the conclusion of the dissertation is given. A summary of all the contributions of this research is then presented. Future works associated to this research are also addressed.

Chapter 2 Proposed Soft-switched MICs

Since renewable resources are intermittent in nature, utilizing multiple renewable resources in renewable energy conversion systems can provide a reliable power solution. Multi-input converter (MIC), as described in Chapter 1, is able to provide efficient, compact and cost-effective power converter solution when multiple resources are utilized. In this chapter, a new class of DC-DC MIC is proposed to attain the first objective of this research. Each input module of the proposed MICs utilizes only a single switch. Each switch is able to achieve either ZVS or ZCS during the turn on and turn off transition. A further step is taken to integrate the PFC circuit with one of the modules of the proposed MICs for the AC input source to attain the second objective of this research. Therefore, the proposed MICs is applicable for AC and DC input sources. The descriptions of each proposed MIC topology, and its operating principles are explained in detail in this chapter.

2.1 Single Switch Soft-switched DC-DC MIC

Different single-switch soft-switched DC-DC converters are presented in the literature such as the Class-E converter [82], and zero voltage switching (ZVS) and zero current switching (ZCS) quasi-resonant (QR) converters [83]. Based on these converters presented in the literature, four different soft-switched MICs are first derived and proposed as shown in Figure 2-1. The derived MICs are non-isolated. All of these MICs are capable of supporting individual as well as simultaneous operations. Each module of the MIC requires a single switch. The MICs are synthesized from the same type converters such as ZCS-QR buck-buck MIC, ZVS-QR buck-buck MIC and ZVS-QR Cuk-Cuk MIC as shown in Figure 2-1(a), Figure 2-1(b), and Figure 2-1(c) or from different types of converters such as

ZCS-QR buck- class-E shown in Figure 2-1(d). These converters utilize the resonant tank circuit to achieve soft switching.

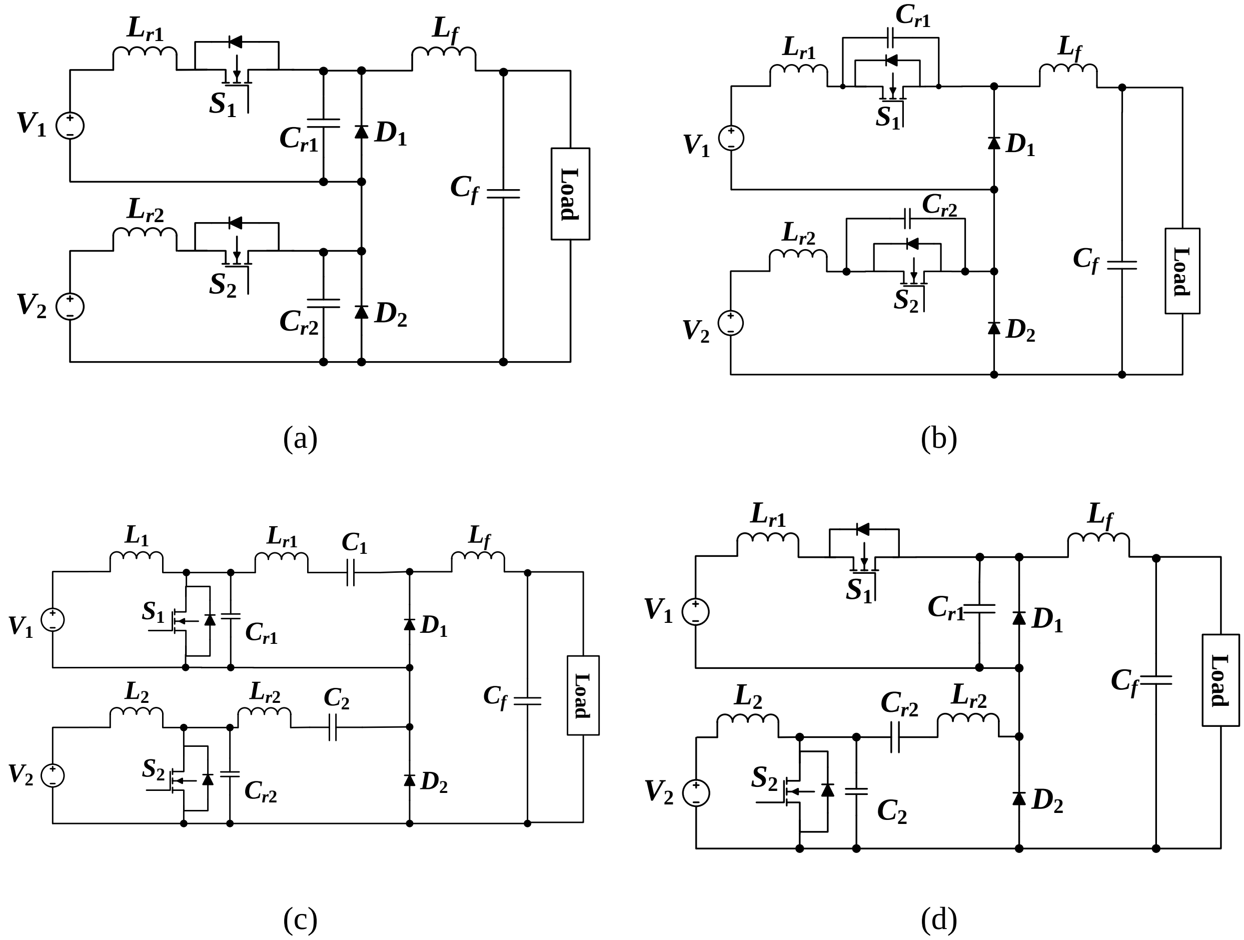

Figure 2-1 A family of soft-switched MICs: (a) ZCS-QR buck-buck MIC (b) ZVS-QR buck-buck MIC (c) ZVS-QR Cuk-Cuk MIC (d) ZCS-QR buck-class-E

The output voltage of the MICs is governed by Eq. 2-1, where M_{vi} is the voltage gain and V_i is the input voltage of the i^{th} module. It should be emphasized that depending on the availability of renewable resources, the derived MICs in Figure 2-1 can be extended to *i* input modules to meet the power and voltage requirement. The modular version of ZVS-QR buck-buck MIC and ZVS-QR Cuk-Cuk MIC are shown in Figure 2-2.

$$V_0 = \sum_{i=1}^{n} V_i \times M_{Vi} \quad \text{Eq. 2-1}$$

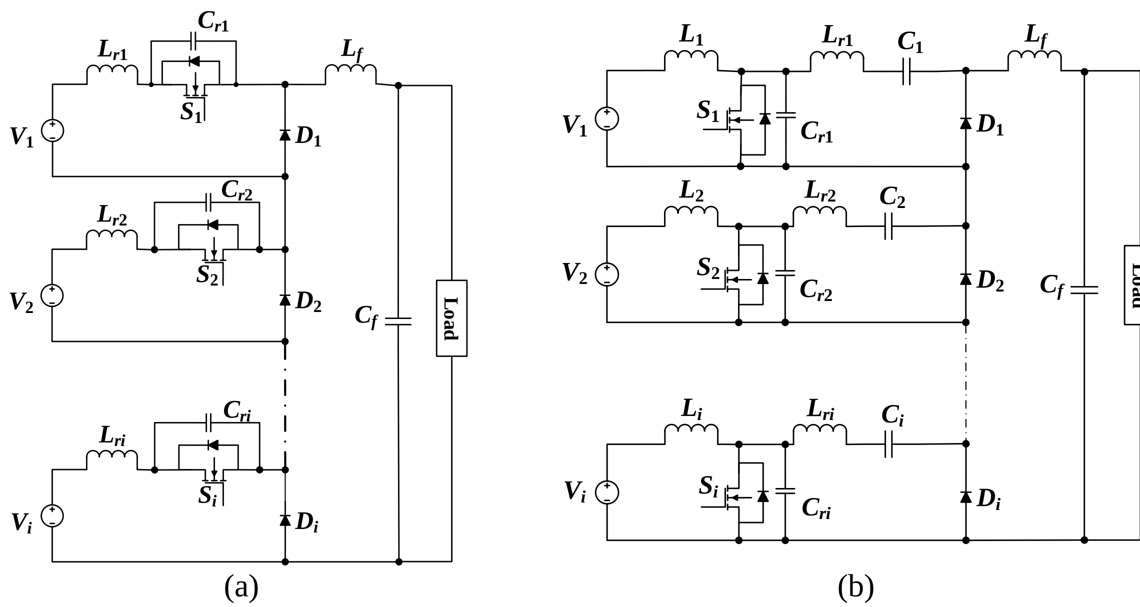

Figure 2-2 Modular version of presented MICs with *i* modules (a) ZVS-QR buck-buck MIC (b) ZVS-QR Cuk-Cuk MIC

Although both ZVS and ZCS operations can reduce the switching losses of either a MOSFET or an IGBT, ZVS is preferred over ZCS for MOSFETs and ZCS is preferred over ZVS for IGBTs [49]. In the case of MOSFETs, ZVS can substantially reduce the losses caused by the discharging of C_{ds} (internal capacitance across drain and source) into the device when it is turned on whereas ZCS cannot.

Among the derived MICs, ZVS-QR buck-buck MIC and ZVS-QR Cuk-Cuk MIC are ZVS type. Therefore, the turn on loss of these MICs are lower compared to other configurations proposed if MOSFET is used as a switching device. The ZVS-QR buck-buck MIC is step down type and the ZVS-QR Cuk-Cuk MIC is the step up/down type. The operation and analysis of these two MICs are described in the following sections.

2.2 Step down MIC (ZVS-QR buck-buck MIC)

The derived step down MIC consists of two ZVS QR buck modules as shown in Figure 2-1 (b). The switch S_1 with tank circuit L_{r1} and C_{r1} and the switch S_2 with tank circuit L_{r2} and C_{r2} form the resonant switches for the ZVS QR buck converter. When the power switches (S_1 and S_2) conduct, the resonant capacitors (C_{r1} and C_{r2}) are shorted and no resonance occurs for that time period. Resonance occurs when the power switches (S_1 and S_2) are off. Both ZVS QR buck modules share the output filter circuit (L_f and C_f) including output diodes (D_1 and D_2).

The ZVS-QR buck-buck MIC is capable of performing individual as well as simultaneous operations. The individual operations are shown in Figure 2-3. During the individual operation of the top module, the components of the top module, output filter components, and the diode D_2 of the bottom module are active. The diode D_2 allows the continuous power flow path for the top module. Similarly, the diode D_1 allows the continuous power flow path during the individual operation of the bottom module. During the individual mode of operations, D_1 and D_2 turn on and turn off at the same time.

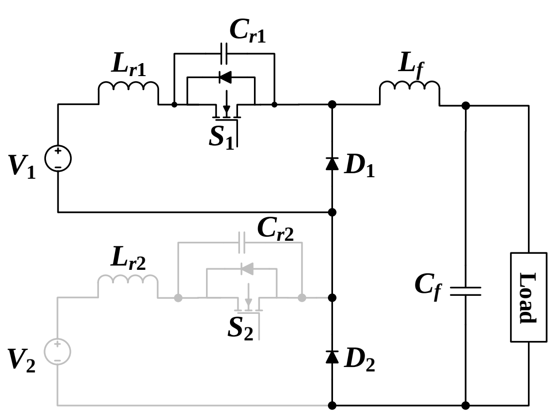

(a) Top module active

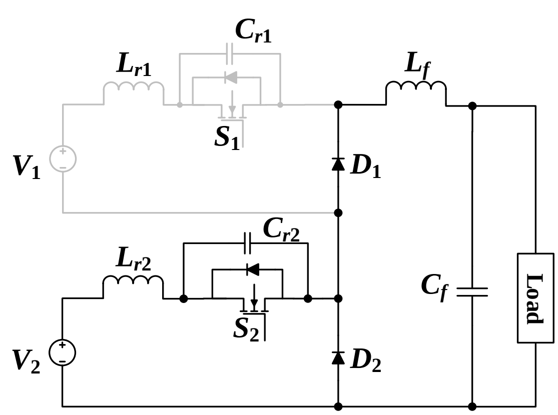

(b) Bottom module active

Figure 2-3 Individual operation of ZVS-QR buck-buck MIC

In case of the QRC, the state of the circuit changes when any of the switches (active and passive) turns on or turns off. For the proposed circuit, each module has one active switch (S_1 and S_2) and a passive switch (D_1 and D_2) with two states: on (equivalent to 1) and off (equivalent to 0). Therefore, there are four different states of each module based on switch turn on and turn off - 00, 01, 11, and 10 where 0 and 1 represent on and off states of S_i and D_i. These four stages of the ZVS QRC are named as:

1. Resonant capacitor charging stage (00)
2. Resonant stage (01)
3. Resonant inductor charging stage (11)
4. Freewheeling stage (10)

During individual mode operations, the power conversion happens in the above mentioned four different stages which will be described in steady state analysis. However, in simultaneous operation, the power flow stages of two modules happen in different operational time steps. The simultaneous mode of operation is discussed in the next section.

2.2.1 Operating Principle of Simultaneous Mode

There are seven operating stages during the simultaneous mode of the ZVS-QR buck-buck MIC. The key operating waveforms are shown in Figure 2-4, where d_1 and d_2 represent the duty cycle of the input modules that work with source#1 and source#2 respectively, with d_1 assumed to be greater than d_2 and T_s is the switching period. Note that the switching frequencies for both input modules are assumed to be the same in this analysis to simplify the operating stages illustration. Each module of the MIC follows the four power flow stages within the seven operating stages of MIC. Figure 2-5 shows the operational stages of the ZVS-QR buck-buck MIC.

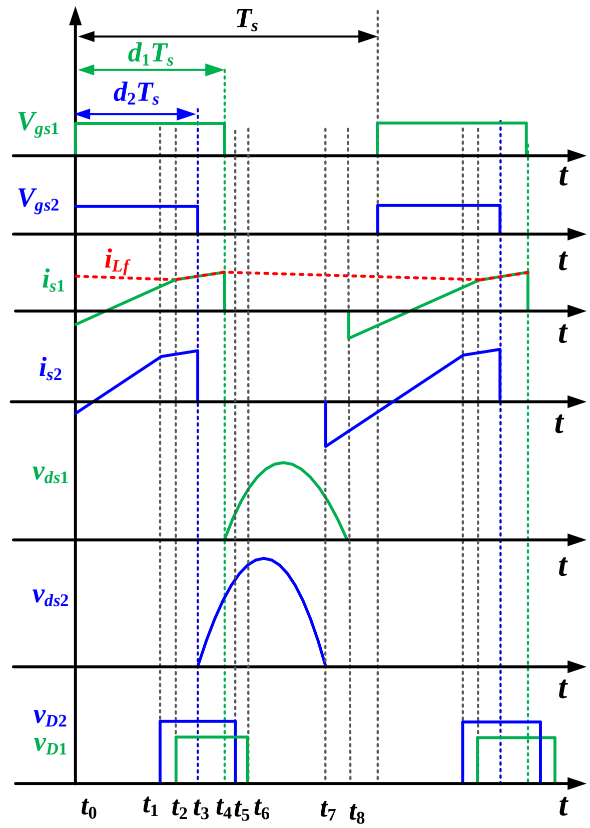

Figure 2-4 Waveforms in simultaneous operation (assuming $d_1 > d_2$)

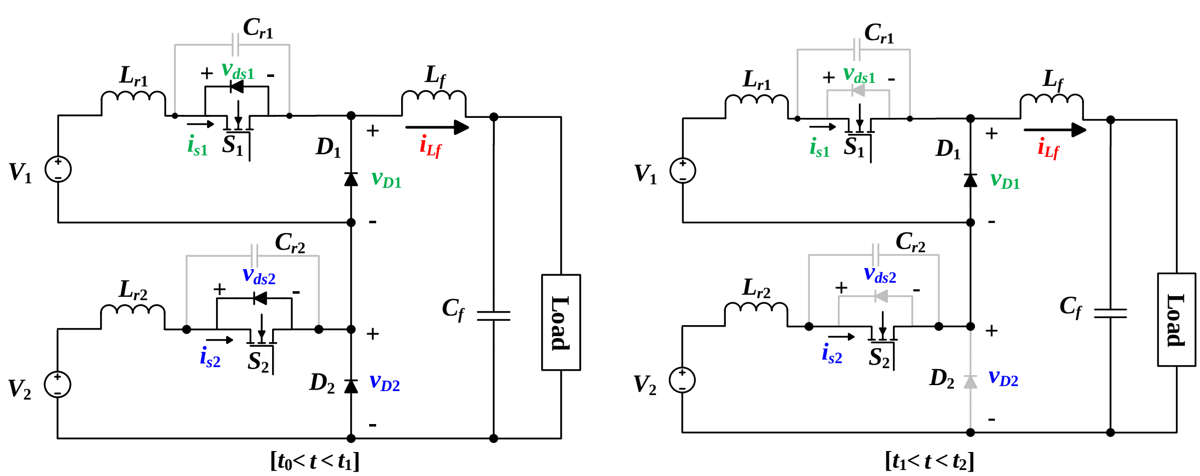

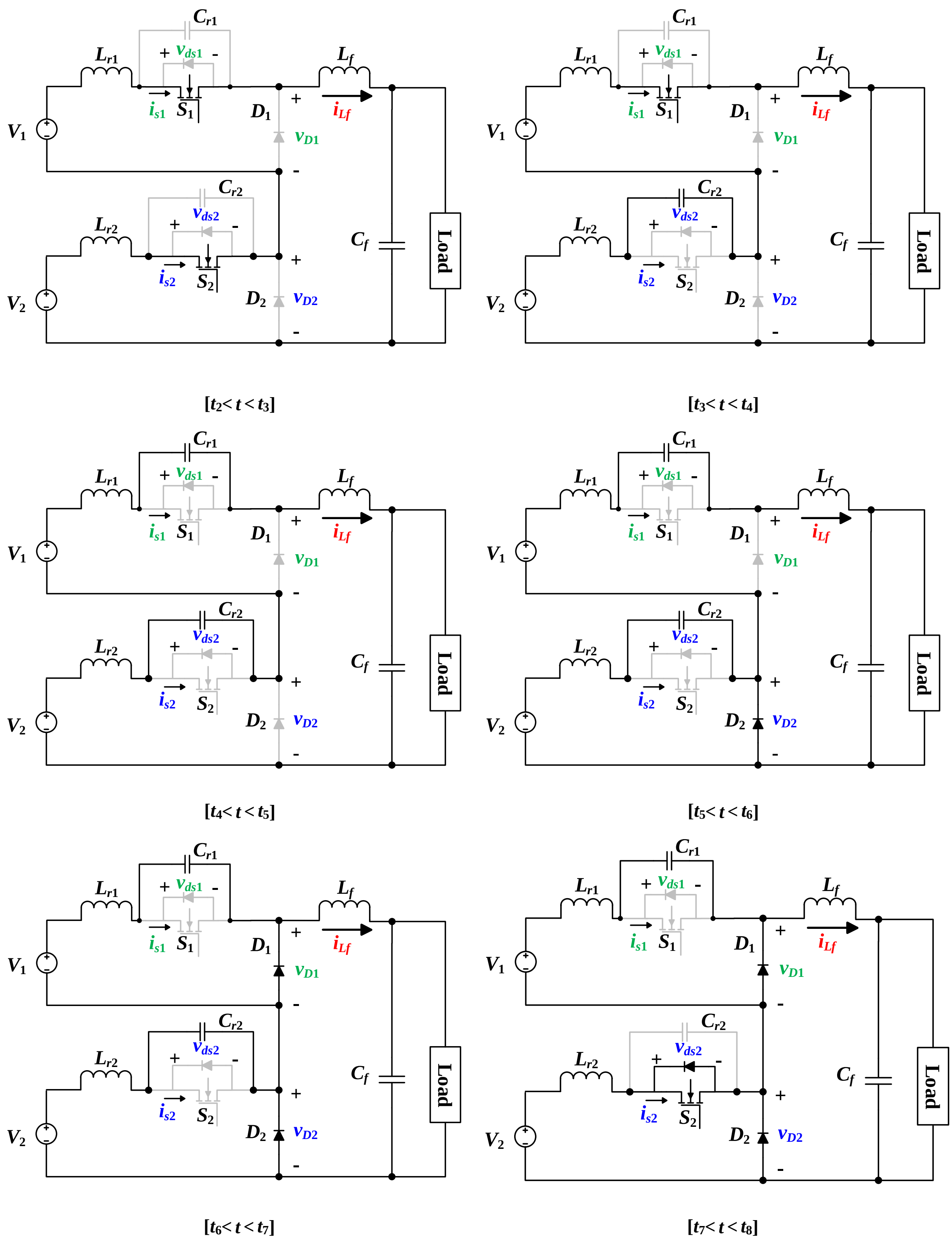

Figure 2-5: Operating stages of the proposed converter in simultaneous operation

[$t_0 < t < t_1$]: Prior to this stage, S_1 and S_2 are off. At t_0, the gate signal is applied to S_1 and S_2. The switch current flows through the anti-parallel diode of S_1 and S_2. The output diode D_1 and D_2 are on. Both modules are in the inductor charging stage. Since i_{s1} and i_{s2} are negative previously, S_1 and S_2 turn on under ZVS condition. Since D_1 and D_2 are on, i_{Lf} continues to discharge linearly through D_1 and D_2.

[$t_1 < t < t_2$]: The top module continues the inductor charging mode. D_2 turns off and the bottom module either moves to the freewheeling stage or continues inductor charging stage with a different current slope. Energy starts transferring from L_{r2} to L_f. So, i_{Lf} starts increasing.

[$t_2 < t < t_3$]: D_1 turns off and the top module either moves to the freewheeling stage or continues inductor charging stage with a different current slope. At this state, L_{r1} and L_{r2} are now transferring energy to L_f. i_{ds1} increases to be equal to i_{Lf} and i_{Lf} continues rising linearly.

[$t_3 < t < t_4$]: At the beginning of this time period, the gate signal is removed from S_2, v_{ds2} starts rising slowly from zero. At the turn off condition, the voltage across the switch is zero. Therefore, ZVS turn-off is achieved. The bottom module is in the capacitor charging module and C_{r2} starts charging. The top module continues the previous state.

[$t_4 < t < t_5$]: At the beginning of this time period, the gate signal of S_1 is removed, v_{ds1} starts rising slowly from zero and S_1 turns off under ZVS. The top module is in the capacitor charging mode.

[$t_5 < t < t_6$]: D_2 turns on and the bottom module enters to resonant state.

[$t_6 < t < t_7$]: D_1 turns on and both modules are at the resonant state in this time period. End of this period, v_{ds2} drops to zero and completes the resonant state.

[$t_6 < t < t_7$]: With the completion of the resonant state of the top module, one cycle of the MIC completes.

2.2.2 Steady State Analysis

In case of QRC, the power conversion happens in four different operating stages: resonant capacitor charging stage, resonant stage, resonant inductor charging stage, and freewheeling stage. The freewheeling state only happens if the resonant inductor current reaches its maximum at the end of the inductor charging state. Otherwise, only the first three states happen.

To analyze the steady state characteristics, the following assumptions are made:

- The output filter inductor L_f is large compared to resonant inductor L_{ri}.
- Output filter L_f-C_f and the load are treated as a constant current sink.
- Semiconductor switches are ideal. That is no forward voltage drop in the on state, no leakage current in the off state, and no time delay at turn on and turn off time.

The resonant components, L_{ri} and C_{ri} of the QRC circuit determine the characteristics of the converter, which can be defined by Eq. 2-2 and Eq. 2-3, where f_{ri} is the resonant frequency of the i^{th} module, Z_i is the characteristic impedance of the i^{th} module, and R_L represents the load resistance.

$$f_{ri} = \frac{1}{2\pi\sqrt{L_{ri}C_{ri}}} = \frac{\omega_i}{2\pi} \qquad \text{Eq. 2-2}$$

$$Z_i = \sqrt{\frac{L_{ri}}{C_{ri}}} = \frac{R_L}{M_{Vi}} \qquad \text{Eq. 2-3}$$

1) *Capacitor charging stage:* The resonant capacitor, C_{ri} is charged linearly through the resonant inductor maximum current i_{Lr_Max} at this stage (Eq. 2-4) which is equal to the output current, I_0. The voltage across the resonant capacitor is shown in Eq. 2-4. The time duration for this period, T_{d1} depends on the resonant inductor maximum current I_0, the input voltage V_{in_i}, the characteristics impedance Z_i, and the angular resonant frequency ω_{ri}.

$$v_{cr\_i} = \frac{1}{C_{ri}} I_0 t \qquad \text{Eq. 2-4}$$

$$T_{d1} = \frac{V_{in\_i}}{Z_i \omega_{ri} I_0} \qquad \text{Eq. 2-5}$$

2) *Resonant stage*: The resonant inductor and capacitor resonate in this stage and is governed by Eq. 2-6 and Eq. 2-7. The resonant capacitor voltage reached its maximum, $V_{in\_i} + Z_i I_0$ and discharge through the resonant inductor. At the end of this stage, the resonant inductor current reached to $I_0 \cos \alpha_i$. α is defined by Eq. 2-8. The duration of this state is T_{d2} (Eq. 2-9).

$$v_{cr\_i}(t) = V_{in\_i} + Z_i I_0 \sin \omega_{ri} t \qquad \text{Eq. 2-6}$$

$$i_{Lr\_i}(t) = I_0 \cos \omega_{ri} t \qquad \text{Eq. 2-7}$$

$$\alpha_i = \sin^{-1} - \varphi = \sin^{-1} \frac{V_{in\_i}}{Z_i I_0} \qquad \text{Eq. 2-8}$$

$$T_{d2} = \frac{\alpha_i}{\omega_{ri}} \qquad \text{Eq. 2-9}$$

3) *Inductor charging stage:* The resonant inductor linearly gets charged (Eq. 2-10) during the time period T_{d3} (Eq. 2-11) by the input voltage, V_{in_i}.

$$i_{Lr\_i}(t) = I_0 \cos \alpha_i + \frac{\omega_{ri}}{Z_i} V_{in\_i} t \qquad \text{Eq. 2-10}$$

$$T_{d3} = \frac{Z_i I_0}{\omega_i V_{in\_i}} (1 - \cos \alpha_i) \qquad \text{Eq. 2-11}$$

4) *Freewheeling stage:* The maximum resonant inductor current freewheels through L_{ri} and switch S_i. This stage finishes when the transistor turns off again. The time duration of this state, T_{d4} is expressed Eq. 2-12.

$$T_{d4} = T_s - T_{d1} - T_{d2} - T_{d3} \quad \text{Eq. 2-12}$$

The voltage gain of ZVS buck QRC can be expressed as Eq. 2-13. The m_i derived from the four states described above where f_{si} is the switching frequency of the i^{th} module.

$$M_{Vi-buck} = 1 - m_i = 1 - \frac{f_{si}}{2\pi f_{ri}}\left[\alpha_i + \frac{\phi_i}{2} + \frac{1}{\phi_i}(1-\cos\alpha_i)\right] \quad \text{Eq. 2-13}$$

The voltage gain of ZVS buck QRC M_{vi} depends on both the duty cycle D_i and the switching frequency, f_{si} [84]. The change of M_{vi} with the change of D_i, F_i, and I_{Ni} is shown in Figure 2-6 where F_i is the normalized switching frequency and I_{Ni} is the normalized initial switching current. Normalized initial switching current I_{Ni} can vary from -1 to 0 to achieve ZVS. The switch of the ZVS QRC converter can be controlled by switching frequency or the duty ratio. However, the switch off time required to be within a certain range to ensure soft switching.

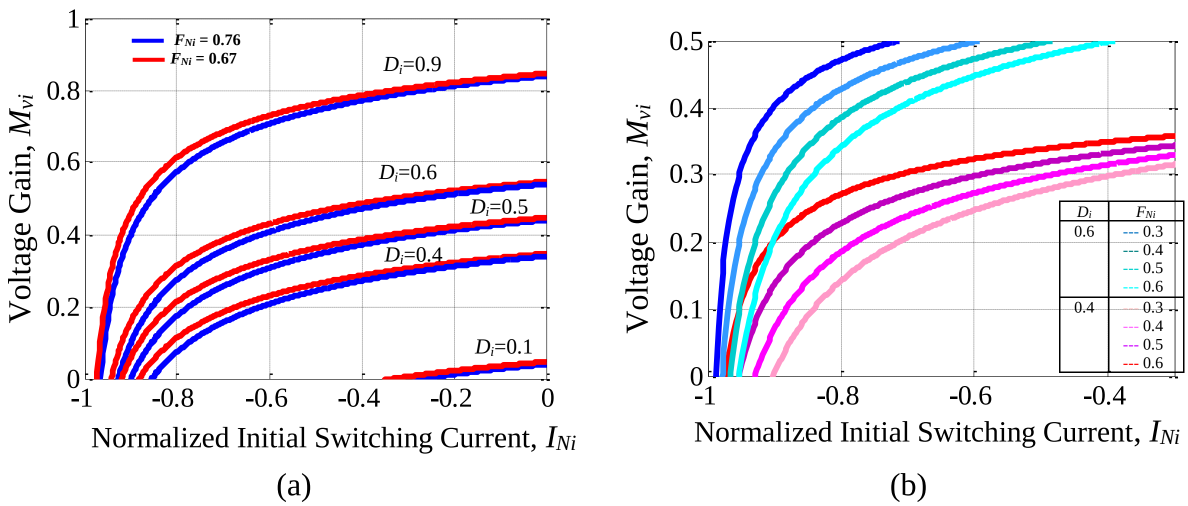

Figure 2-6 Voltage gain of ZVS buck QRC with the change of normalized switching current, normalized switching frequency and the duty ratio

2.3 Step up/down MIC (ZVS-QR Cuk-Cuk MIC)

The derived step up/down MIC consists of two ZVS-QR Cuk modules as shown in Figure 2-1 (c). Because of the location of the active switch (S_i), there are two possible configurations of this proposed MIC as shown in Figure 2-7.

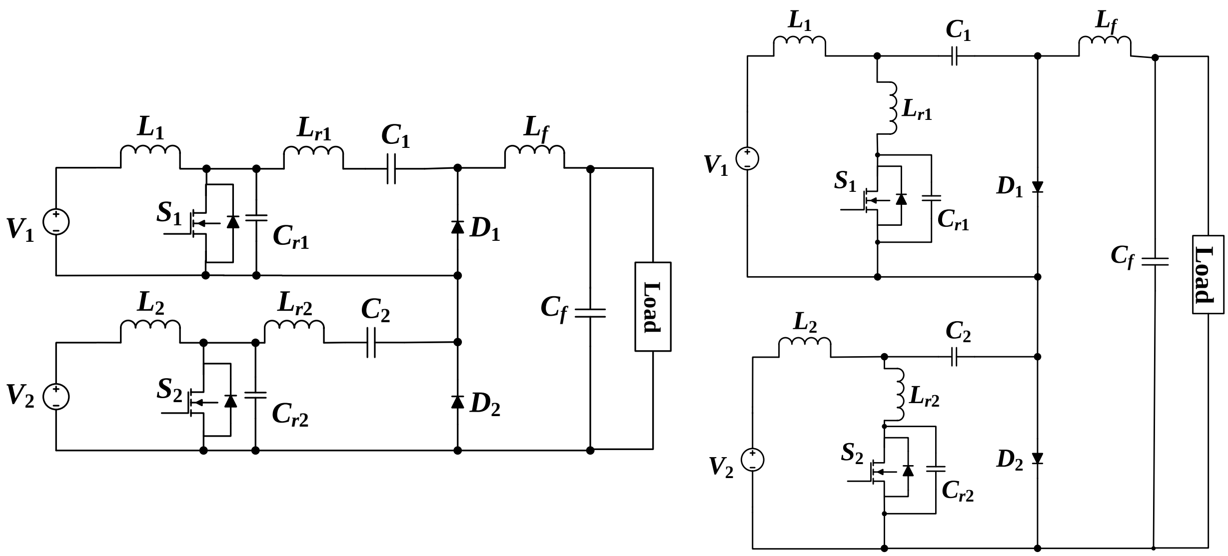

(a) Configuration#1 (b) Configuration#2

Figure 2-7 Two different configurations of ZVS-QR Cuk-Cuk MIC

Among the basic step up/down converters (buck-boost, SEPIC, and Cuk), the Cuk converter has a unique advantage, as both input and output currents of the Cuk converter are ripple free, whereas the other step up/down converters (buck-boost and SEPIC) have pulsating current that occurs on either or both sides (input and output) of the circuit. As a result, those converters require more filter components. Moreover, this ripple causes the pulsation in the circuit which ultimately reduces the efficiency of the circuit [85].

Each of the modules consists of a resonant switch formed with a switch (S_1 or S_2) and resonant components (L_{r1} and C_{r1} or L_{r2} and C_{r2}), input inductor (L_1 or L_2), and one storage capacitor (C_1 or C_2). The output filter components (L_f and C_f) including output diodes (D_1 and D_2) are shared by both modules. The resonant inductor and resonant capacitor happen to be in the same loop during the resonance irrespective of the position of the resonant inductor in two different configurations.

The ZVS-QR Cuk-Cuk MIC is capable of performing individual and simultaneous operations same as the ZVS-QR buck-buck MIC as presented in section 2.2. The individual operation is shown in Figure 2-8. During the individual operation of the top module, other than the components of the top module and output filter, the diode D_2 is also active to allow the continuous power flow path. Similarly, the diode D_1 allows the continuous power flow path for the individual operation of the bottom module.

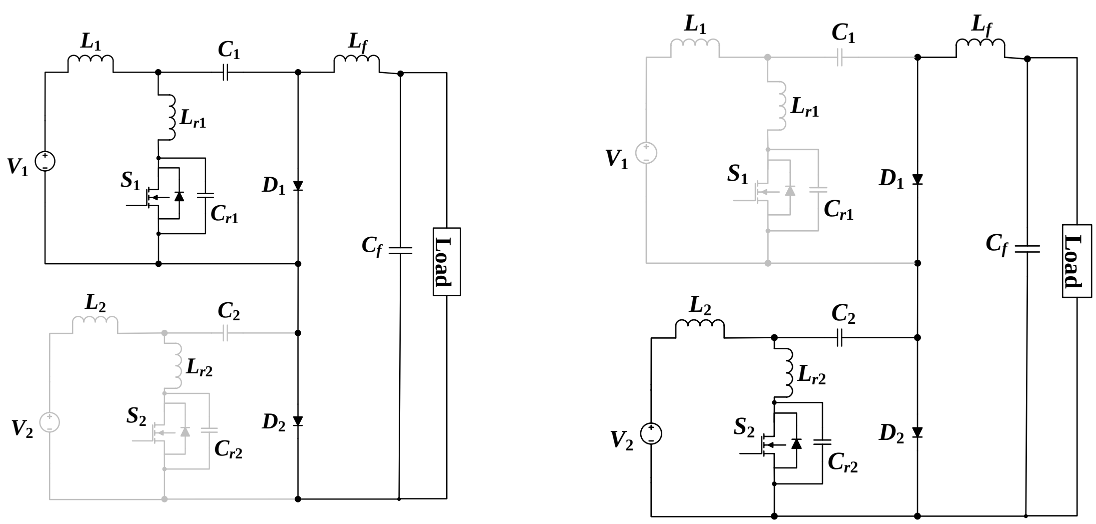

(a) Top module active (b) Bottom module active

Figure 2-8 Individual operation of ZVS-QR Cuk-Cuk MIC

Each of the modules of ZVS-QR Cuk-Cuk has one active switch (S_1 and S_2) and a passive switch (D_1 and D_2) with two states: on (equivalent to 1) and off (equivalent to 0) same as

ZVS-QR buck-buck MIC. Therefore, there are four different operational states of each module based on switch turn on and off - 00, 01, 11, and 10 where 0 and 1 represent on-off states of S_i and D_i. As explained in section 2.2.1, the power conversion happens in four different operating stages named resonant capacitor charging stage, resonant stage, resonant inductor charging stage, and freewheeling stage in case of the QRC. During the individual mode of operations, the power flow stages are the same as the operating stages. The power flow stages are explained in steady state analysis. However, the operating stages are different for the simultaneous operation as the power flow stages happen in different operating stages for the two modules. The simultaneous mode of operation is discussed in the next section. Other than the magnitude of voltage across the resonant capacitor and current through the resonant inductor in different operating stages, the operating principle is similar for both configurations.

2.3.1 Operating Principle of Simultaneous Mode

For simultaneous operation mode, the key operating waveforms are shown in Figure 2-9, where Ts_1 and Ts_2 represent the switching period of the top module and the bottom module respectively, with Ts_2 assumed to be > Ts_1 and d is the duty ratio. Note that the duty ratio for both input modules is assumed to be the same in this analysis to simplify the operating stages illustration. In section 2.2.1, the simultaneous operation of ZVS-QR buck-buck is described with different duty ratios and same switching frequency for top and bottom modules. In this section, the simultaneous operation of ZVS-QR Cuk-Cuk is described with different switching frequency but same duty ratio for top and bottom modules. The reason is to get a better understanding of the operating principle of MICs with ZVS QRC. Figure 2-10 shows the operational stages of the ZVS-QR Cuk-Cuk MIC.

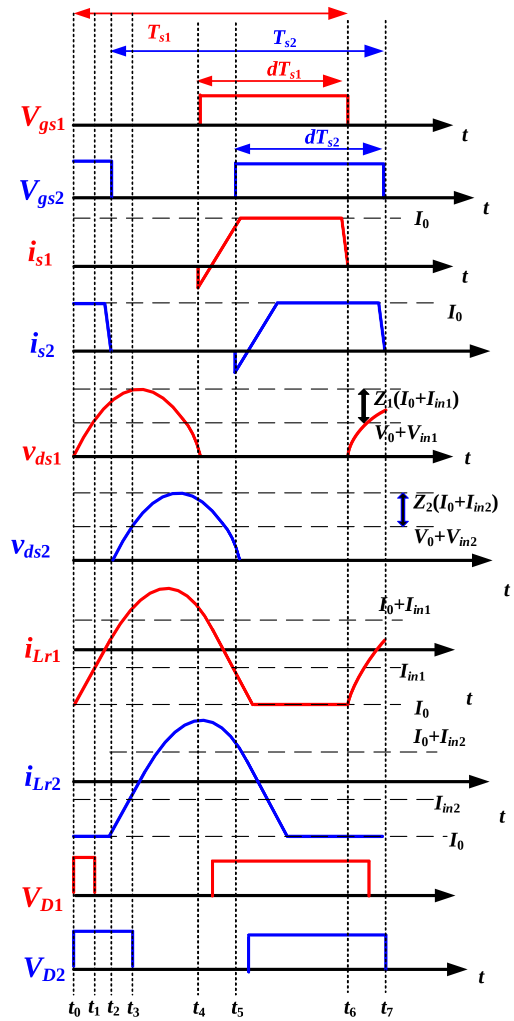

Figure 2-9 Waveforms in simultaneous operation (assuming $T_{s2} > T_{s1}$)

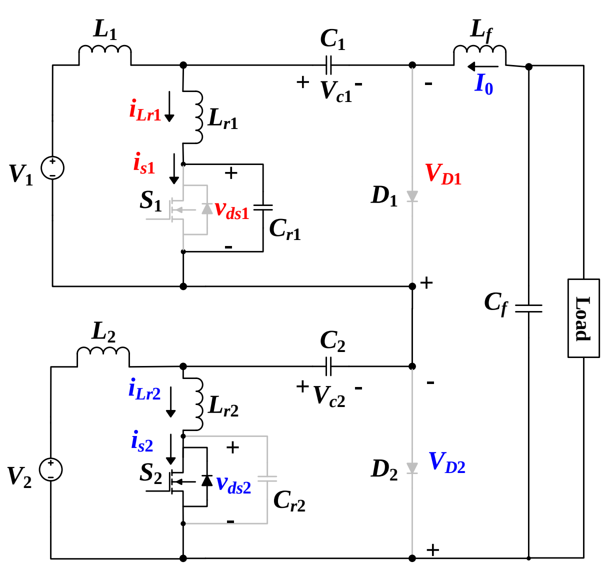

$t_0 < t < t_1$

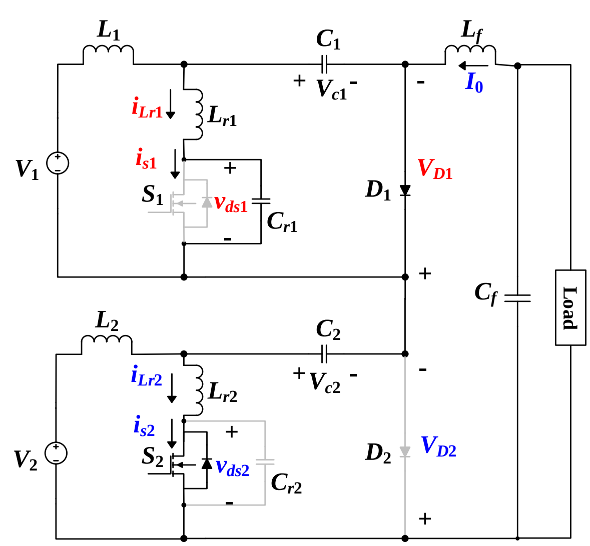

$t_1 < t < t_2$

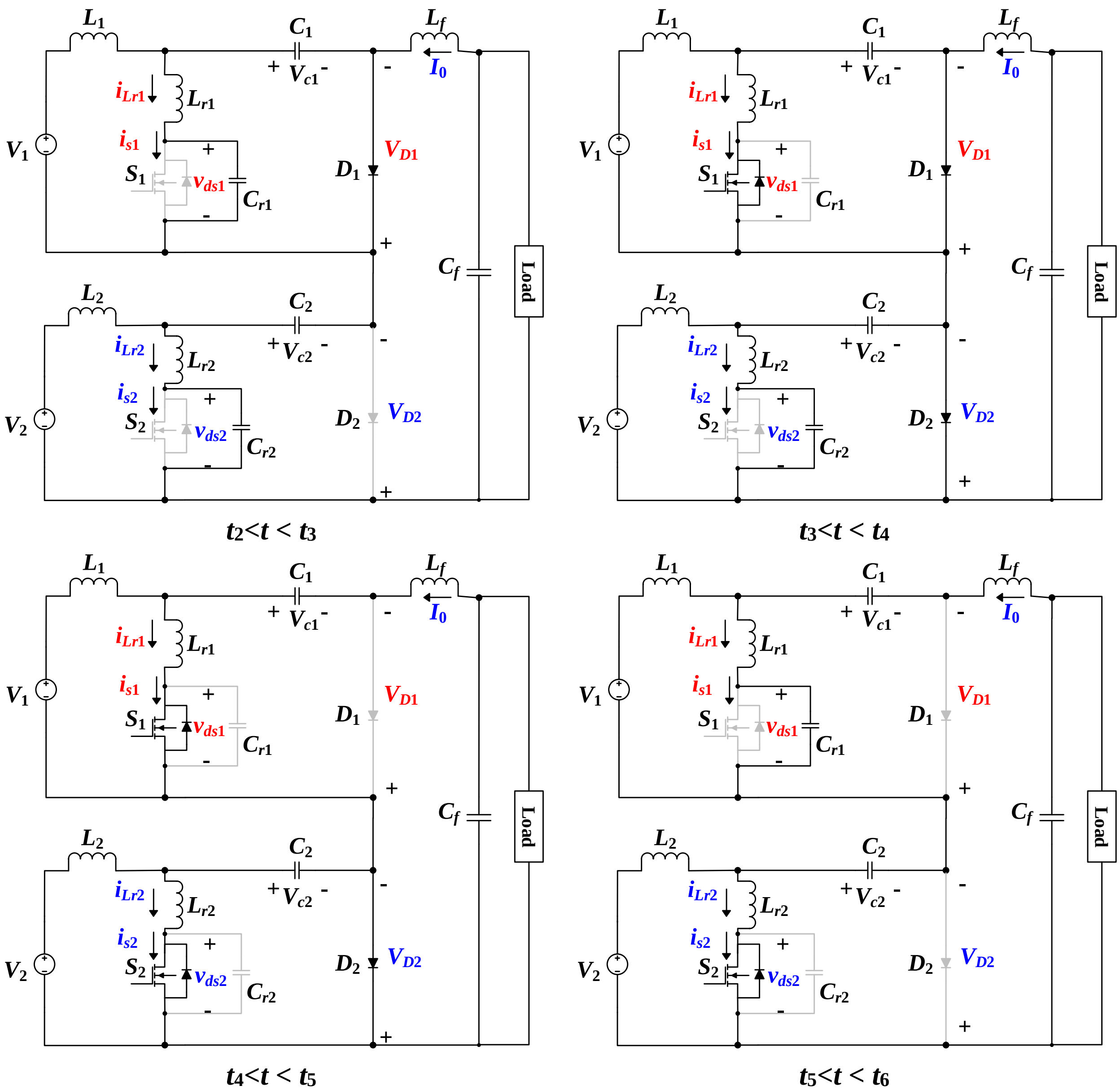

Figure 2-10 Operating stages of the proposed converter in simultaneous operation

[$t_0 < t < t_1$]: At time t_0, the switch S_1 is turned off. Resonant capacitor voltage v_{ds1} rises linearly due to input and output current. The diode D_1 is also off for this time period. This period ends when the capacitor voltage v_{ds1} reaches $V_{in1}+V_0$ and the diode turns on. This is the resonant capacitor charging stage for the top module.

The bottom module is in the freewheeling stage at this time period. Switch S_2 of the bottom module is on. The output current freewheels through the switch and the resonant inductor.

[$t_1 < t < t_2$]: This is the resonant stage for the top module. D_1 is on and L_{r1} and C_{r1} start resonating.

The bottom module is still in the freewheeling stage. The gate signal is removed from S_2 at the end of this stage and the switch S_2 turns off at zero voltage condition.

[$t_2 < t < t_3$]: The top module continues resonant stage.

Before starting this stage, the switch S_2 is turned off. The diode D_2 is also off for this time period. Therefore, the capacitor charging stage starts at the beginning of this period. Resonant capacitor voltage v_{ds2} rises linearly.

[$t_3 < t < t_4$]: The resonant voltage v_{ds1} reaches zero at the end of this period and the anti-parallel diode starts conducting. The resonant voltage v_{ds1} can't be negative because of the anti-parallel diode across the switch.

The bottom module is in the resonant stage. The switch S_2 remains off. The diode D_2 turns on and L_{r2} and C_{r2} start resonating.

[$t_4 < t < t_5$]: The gate signal applied to the switch S_1 and the switch turns on at zero voltage condition. The resonant inductor starts charging by the storage capacitor C_1. Hence, this stage is termed as the resonant inductor charging stage. The diode D_1 turns off when the inductor current reaches $I_{in1}+I_0$ and the top module starts freewheeling through the switch S_1.

The bottom module continues the resonant stage.

[$t_5 < t < t_6$]: The top module continues the inductor charging stage. At the end of this stage, the gate signal of the switch S_1 is removed. The switch turns off at ZVS condition.

The gate signal is applied to the bottom module switch. The S_2 turns on at zero voltage condition and the resonant inductor starts charging by the storage capacitor C_2. The bottom module starts the inductor charging stage. The diode D_2 turns off when the inductor current reaches $I_{in2}+I_0$.

[$t_6 < t < t_7$]: At the start of this time period, the gate signal of the switch S_1 removed and the switch turns off at zero current condition.

The bottom module is freewheeling through the switch S_2. At the end of this period, the switch S_2 turns off.

2.3.2 Steady State Analysis

The basic principle of power conversion in four stages in all types of QRC is similar other than the voltage and current levels in different stages. The four power transferring stages are explained clearly in section 2.2.2 for ZVS-QR buck-buck MIC. Power conversion in ZVS-QR Cuk-Cuk MIC happens in a similar way.

To analyze the steady state characteristics, the following assumptions are made:

- The output filter inductor L_f is large compared to resonant inductor L_{ri}.
- Output filter L_f-C_f and the load are treated as a constant current sink.
- The storage capacitor C_i is large and its voltage is constant.
- Semiconductor switches are ideal. That is, no forward voltage drop in the on state, no leakage current in the off state, and no time delay at turn on and turn off time.

The resonant components, L_{ri} and C_{ri} of the QRC circuit determine the characteristics of the converter, which can be defined by Eq. 2-2 and Eq. 2-3.

1) *Capacitor charging stage:* At this stage, the switch and diode both are off and no current flow through these. The resonant inductor carries I_0 for Figure 2-7 (a) and I_0+I_{in_i} for Figure 2-7(b). At this stage, the resonant capacitor is charging. This stage ends when the capacitor charge reaches to V_0+V_{in_i}.

   State: S_i and D_i off

   Initial condition: $I_{Lr\_i} = I_0$ for Figure 2-7 (a)

   and $i_{Lr\_i} = I_0 + I_{in\_i}$ for Figure 2-7 (b)

   Characteristic equation: $C_r \dfrac{dv_{cr\_i}}{dt} = I_0 + I_{in\_i}$

   Boundary condition: $v_{Cr\_i} = V_0 + V_{in\_i}$

   Solution: $v_{cr\_i} = \dfrac{I_0 + I_{in\_i}}{C_{r\_i}} t$ Eq. 2-14

   Time period: $t_{d1\_i} = \dfrac{V_{in\_i} + V_0}{I_0 + I_{in\_i}} C_{r\_i}$ Eq. 2-15

2) *Resonant stage*: At this stage, the diode is conducting. However, the switch remains off. The analysis is same for both configurations as the resonant inductor and resonant capacitor is in the same loop.

   State: S_i off and D_i on

   Characteristic equation:

$$L_{r\_i} \frac{di_{Lr\_i}}{dt} = V_0 + V_{in\_i} - v_{Cr\_i}$$

$$C_{r\_i} \frac{dv_{cr\_i}}{dt} = i_{Lr\_i}(t)$$

   Boundary condition:

$$v_{Cr\_i} = 0$$

Solution:

$$v_{cr\_i} = (V_{in\_i} + V_0) + Z_i (I_0 + I_{in\_i}) \sin \omega_{r\_i} t$$ Eq. 2-16

$$i_{Lr\_i} = (I_0 + I_{in\_i}) \cos \alpha_i - I_{in\_i}$$ Eq. 2-17

Where $\alpha_i = \sin^{-1} \dfrac{V_{in\_i} + V_0}{Z_i (I_0 + I_{in\_i})} = \sin^{-1} \varphi_i$

for half wave, $\pi \langle \alpha_i \langle 3 \dfrac{\pi}{2}$

Time period: $t_{d2\_i} = \dfrac{\alpha_i}{\omega_{0\_i}}$ Eq. 2-18

3) *Inductor charging stage:* At this stage, the switch and the diode are on. The resonant inductor stores energy at this stage. The analysis of this stage is also same for both configurations as the resonant inductor and the storage capacitor form the loop in this stage.

State: S_i and D_i on

Initial condition: $v_{Cr\_i} = C_{r\_i} \dfrac{dv_{cr\_i}}{dt} = 0$

Characteristic equation:

$$L_{r\_i} \frac{di_{Lr\_i}}{dt} = V_0 + V_{in\_i}$$

Boundary condition: $i_{Lr\_i} = I_0$

Solution:

$$I_0 = \frac{1}{L_{r\_i}} (V_{in\_i} + V_0) t + (I_0 + I_{in\_i}) \cos \alpha_i - I_{in\_i}$$ Eq. 2-19

Time period:

$$t_{d3\_i} = L_{r\_i} \frac{I_0 + I_{in\_i}}{V_{in\_i} + V_0} (1 - \cos \alpha_i) = \frac{(1 - \cos \alpha_i)}{\omega_{r\_i} \phi_i}$$ Eq. 2-20

4) *Freewheeling stage:* Both the switch and the diode are off.

State: S_i on and D_i off

Initial condition: $i_{Lr\_i} = I_o$

Time period: Eq. 2-21

$$t_{d4\_i} = T_{s\_i} - t_{d1\_i} - t_{d2\_i} - t_{d3\_i}$$

The voltage gain of ZVS Cuk QRC can be derived from the time period of the four states described above as Eq. 2-22 where m_i is the same as Eq. 2-13.

$$M_{Vi-Cuk} = \frac{1-m_i}{m_i} \quad \text{Eq. 2-22}$$

The voltage gain M_{Vi} of Cuk QRC with the change of D_i, F_i, and I_{Ni} is shown in Figure 2-11 where F_{Ni} is the normalized switching frequency, D_i is the duty ratio and I_{Ni} is the normalized initial switching current of the i^{th} module. Normalized initial switching current I_{Ni} needs to be within -1 to 0 to achieve ZVS as mentioned in section 2.2.2.

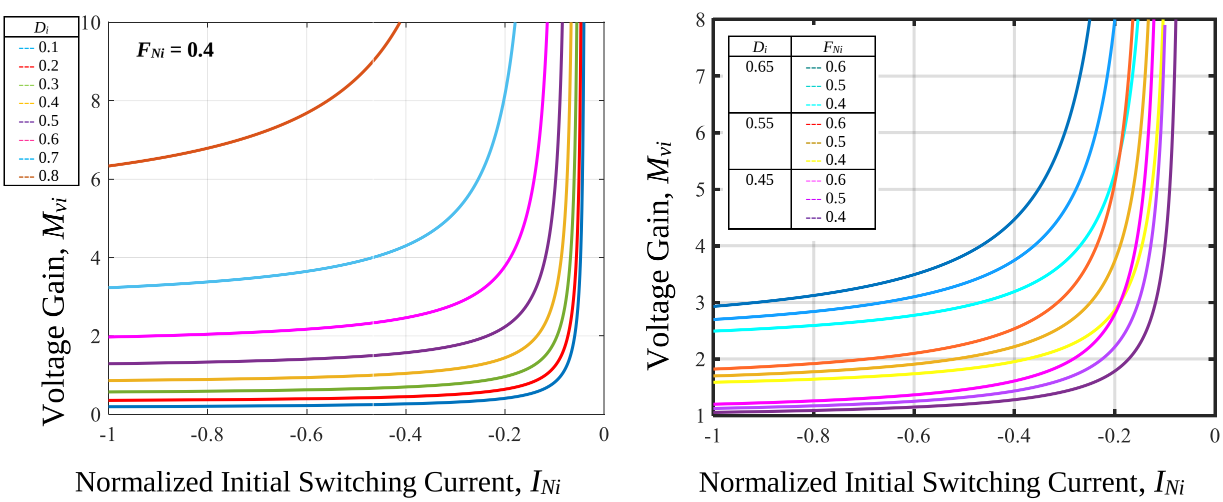

(a) (b)

Figure 2-11 Voltage gain of ZVS Cuk QRC with the change of normalized switching current, normalized switching frequency and the duty ratio

The voltage gain of QRC can be expressed in terms of m_i (Eq. 2-13 and Eq. 2-22) same as the PWM converter. The voltage gain of the PWM converter is expressed in terms of the duty ratio, d_i [86] [87] as shown in Table 2-1. Therefore, (1-m_i) is equivalent to the duty ratio d_i or m_i is equivalent to the off time (1- d_i). The frequency or the duty ratio or both can be utilized as a control parameter. However, the switch off time requires to be within a range to maintain the soft switching.

Table 2-1 Voltage gain comparison of PWM converter and QR converter

Type of Converter	Quasi-resonant converter	PWM converter
Buck	$M_{Vi-buck} = 1 - m_i$	$M_{Vi-buck} = d_i$
Boost	$M_{Vi-boost} = \frac{1}{m_i}$	$M_{Vi-boost} = \frac{1}{1-d_i}$
Buck-boost	$M_{Vi-buck-boost} = \frac{1-m_i}{m_i}$	$M_{Vi-buck-boost} = \frac{d_i}{1-d_i}$
$m_i = \frac{f_{si}}{2\pi f_{ri}}\left[\alpha_i + \frac{\phi_i}{2} + \frac{1}{\phi_i}\left(1-\cos\alpha_i\right)\right]$		

2.4 Front-end PFC Integration

The MICs presented in section 2.2 and section 2.3 are applicable for the DC input sources such as with PV panels. When the MIC is required to work with AC input sources such as wind energy, an AC-DC rectifier is required prior to the DC-DC converter. Moreover, in WECS, a balanced three-phase close to sinusoidal output current of the turbine generator is essential. Therefore, an additional power factor corrector circuit is required as explained in section 1.4.3. A three-phase diode rectifier and a boost PFC are added in front of the bottom module of ZVS-QR buck-buck MIC of Figure 2-1(a). Hence, the new configuration is applicable for PV-wind system as shown in Figure 2-12. However, the overall size of the bottom module becomes bulky. Hence, a step is taken further to combine the 3-phase boost

PFC circuit with the bottom ZVS buck QRC. The final circuit of the proposed soft-switched MIC with integrated boost PFC in the AC input module is shown in Figure 2-13.

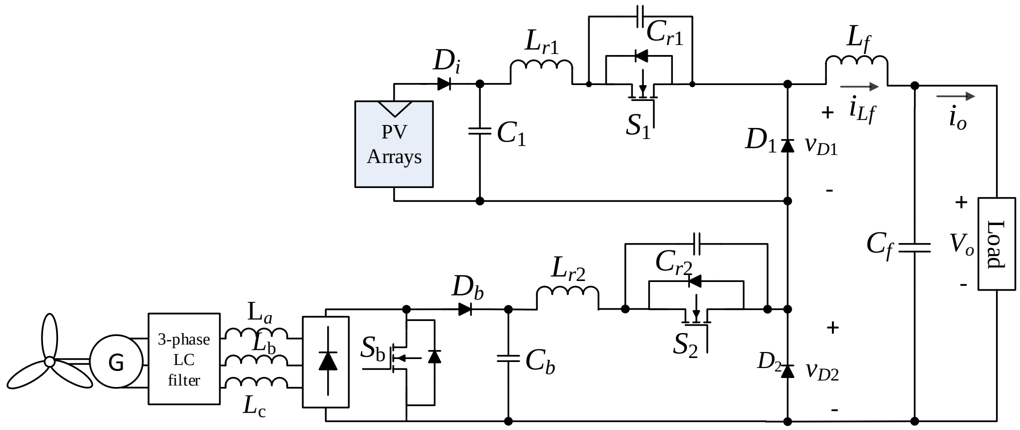

Figure 2-12 MIC configuration for PV-wind system

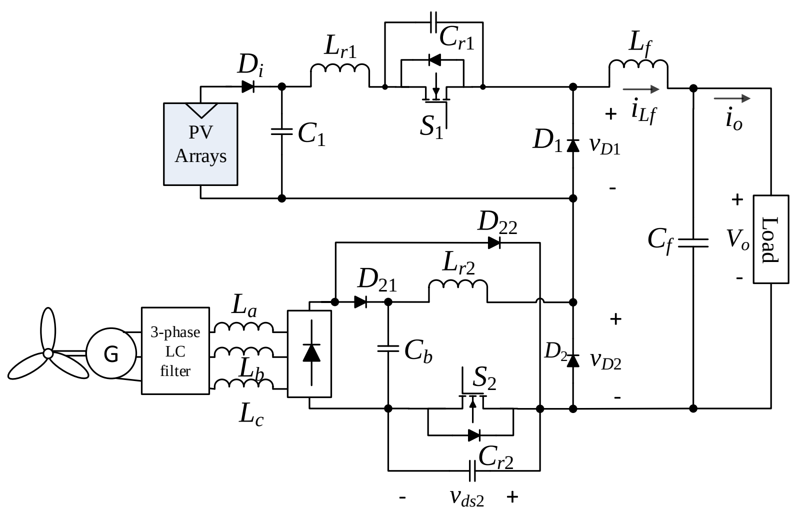

Figure 2-13 Proposed single switch soft-switched step down MIC with integrated PFC function

Four more different soft-switched MICs with one module with PFC function are derived by combining different soft-switched converter for the PV-wind application as shown in Figure 2-14. The top module is for the solar energy and the bottom module is for the wind energy. ZCS buck QRC, ZCS zeta QRC, and ZVS Cuk QRC as shown in Figure 2-14(a), Figure

2-14(b), and Figure 2-14(c) respectively are naturally capable of achieving three-phase PFC [40]. The SEPIC PFC is integrated with the ZVS buck QRC in Figure 2-14(d) for the bottom module in a similar way as did in Figure 2-13. The switch S_2 with resonant capacitor C_{r2} with either resonant inductor L_{r2} or three resonant inductors L_{ra}, L_{rb} and L_{rc} form the resonant switch for the QRCs of wind module. In case of QRCs, resonance occurs only for a part of the period. During the period of resonance, when the four tank elements (C_{r2}, L_{ra}, $L_{rb,}$ and L_{rc}) of ZCS buck QRC and ZCS zeta QRC create the resonance, three line current low frequency components are approximately proportional to the respective line-neutral voltage. Thus, the ZCS QRCs draw a high quality line current. However, for ZVS Cuk QRC, integrated boost PFC, and integrated SEPIC PFC the three line inductors (L_a, L_b and L_c) of the PFC circuit must operate in discontinuous conduction mode to achieve high PF.

The mathematical analysis of ZVS Cuk QRC as a PFC circuit is discussed below. Both ZVS-QR Cuk-Cuk MIC as shown in Figure 2-7 are capable of performing as a 3-phase PFC. The following mathematical analysis is applicable for both configurations. The three-phase discontinuous mode (DCM) PFC of the second configuration of ZVS-QR Cuk-Cuk MIC is shown in Figure 2-15.

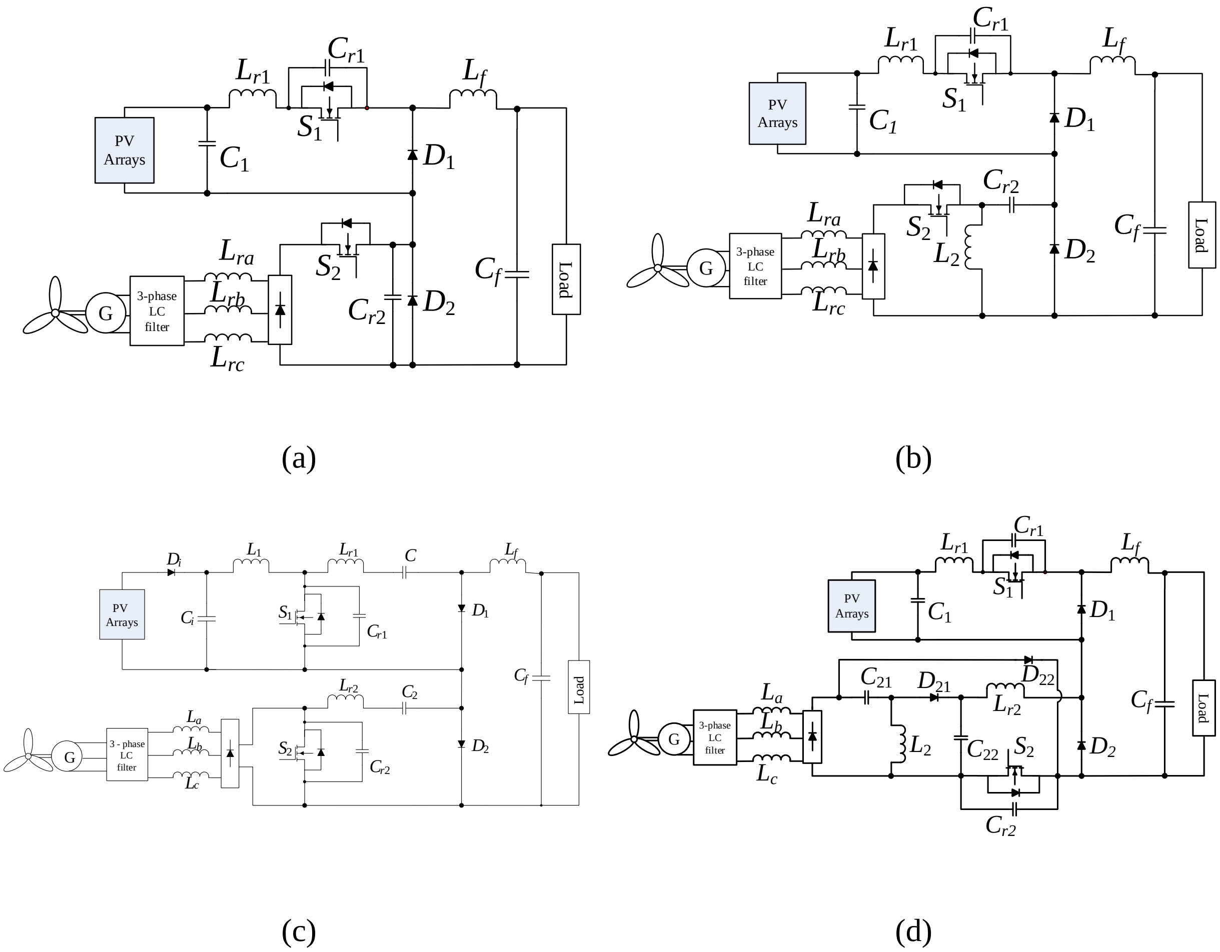

Figure 2-14 Proposed MICs with front end PFC for PV-wind system (a) ZVS-QR buck-buck MIC (b) ZVS-QR buck -ZCS-QR zeta (c) ZVS-QR Cuk-Cuk MIC (d) ZVS-QR buck-buck MIC with SEPIC PFC

Since the switching frequency of ZVS Cuk QRC (switch S_2) is much higher than the line frequency (v_a, v_b, and v_c), the input inductors (L_a, L_b, and L_c) are charged and discharged several times within half cycle of the line period. The envelope of the input current is sinusoidal as shown in Figure 2-16(a) where x represents the phase a, b or c. Figure 2-16(b) shows the input voltage waveform for a line cycle of 2π which is divided into 12 intervals. Figure 2-16(c) shows the inductor current waveform in a switching cycle during [0, $\pi/6$] which is applicable to any of the 12 intervals where d_{s2} is the duty cycle and T_{s2} is the switching cycle of switch S_2. The equivalent switching circuit is shown in Figure 2-17.

Mode#1 happens when the switch S_2 is on irrespective of D_2 (on or off). Mode#2 and mode#3 occur when D_2 is on irrespective of S_2 (on or off). In mode#3, one of the phase currents (i_a in case of 0 to π/6 interval) is zero. The three inductors (L_a=L_b=L_c=L) operate in discontinuous conduction (DCM) mode.

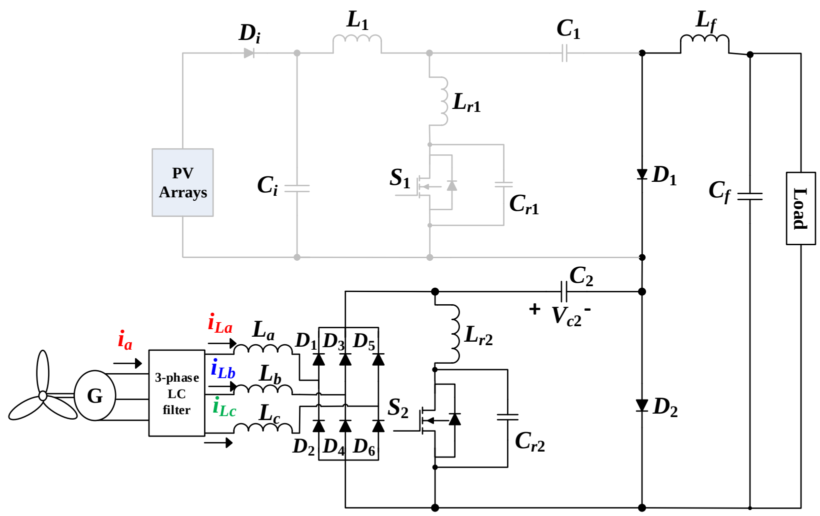

Figure 2-15 DCM ZVS Cuk QRC for wind energy system PFC

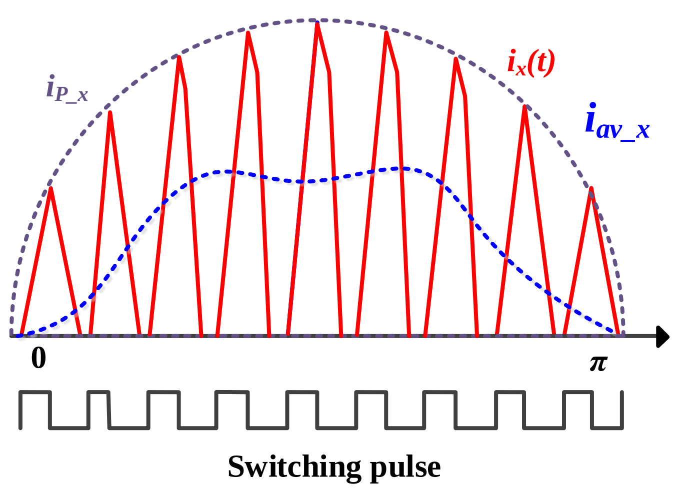

(a)

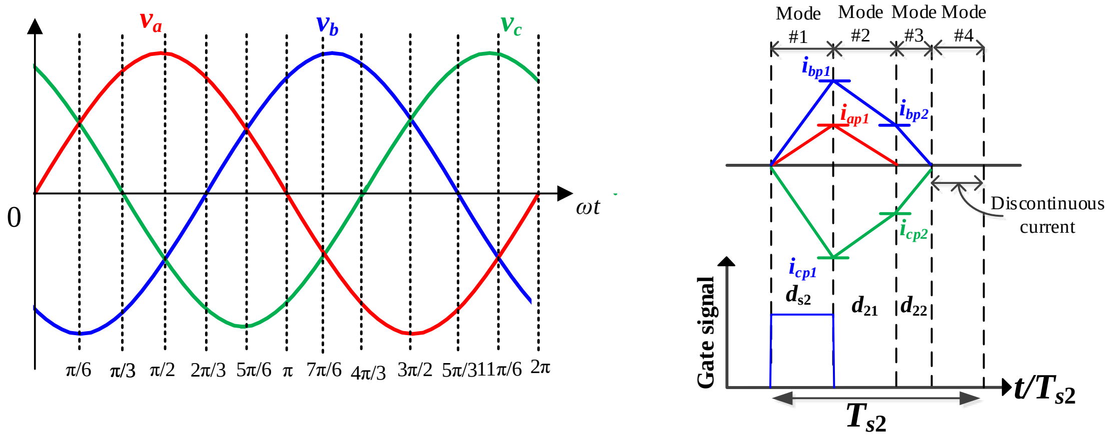

(b) (c)

Figure 2-16 DCM ZVS Cuk QRC with PFC (a) input inductor current waveform in a half cycle (b) input voltage waveforms in a full cycle (c) input inductor current waveform in a switching cycle during [0, π/6]

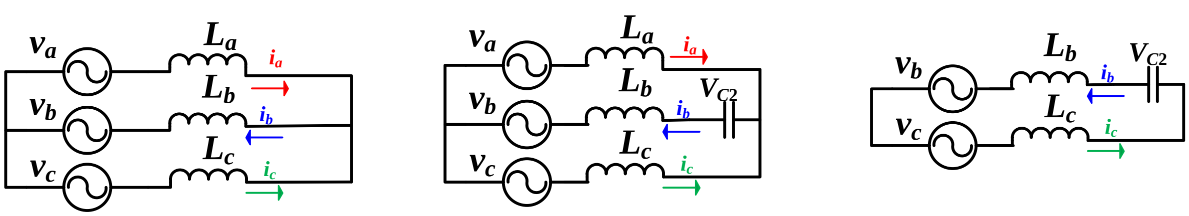

(a) (b) (c)

Figure 2-17 Equivalent circuits of three switching modes of DCM ZVS Cuk QRC with PFC (a) mode 1 (b) mode 2 (c) mode 3

The three-phase input voltages are defined as Eq. 2-23, Eq. 2-24 and Eq. 2-25 where V_m and ω are the amplitude and angular frequency.

$$v_a = v_m \sin \omega t \qquad \text{Eq. 2-23}$$

$$v_b = v_m \sin\left(\omega t - 2\pi / 3\right) \qquad \text{Eq. 2-24}$$

$$v_c = v_m \sin\left(\omega t + 2\pi / 3\right) \qquad \text{Eq. 2-25}$$

1) *Mode 1*:

During this mode, the switch S_2 is on and D_2 is off. D_1, D_4, and D_5 are conducting. The equivalent circuit of this mode is shown in Figure 2-17(a). The maximum inductor current of each phase is shown by Eq. 2-26, Eq. 2-27, and Eq. 2-28.

$$i_{ap1} = \frac{di_a}{dt} d_{s2} T_{s2} = \frac{v_a d_{s2} T_{s2}}{L} \qquad \text{Eq. 2-26}$$

$$i_{bp1} = \frac{di_b}{dt} d_{s2} T_{s2} = \frac{v_b d_{s2} T_{s2}}{L} \qquad \text{Eq. 2-27}$$

$$i_{cp1} = \frac{di_c}{dt} d_{s2} T_{s2} = \frac{v_c d_{s2} T_{s2}}{L} \qquad \text{Eq. 2-28}$$

2) *Mode 2*:

During this mode, the switch S_2 is on and D_2 is off. The equivalent circuit of this mode is shown in Figure 2-17(b). At the end of this interval, i_a reaches zero. Therefore, the current through phase *a* and *b* becomes equal.

$$i_{bp2} = i_{bp1} + \frac{di_b}{dt} d_{21} T_{s2} \qquad \text{Eq. 2-29}$$

$$i_{cp2} = -i_{bp2} \qquad \text{Eq. 2-30}$$

$$d_{21} = \frac{3v_a}{V_{C2} - 3v_a} d_{s2} \qquad \text{Eq. 2-31}$$

3) *Mode 3*:

The state of the switch S_2 and D_2 remain the same as the previous mode. In this mode of operation, i_a is zero. Therefore, the current through phase *a* and *b* is equal throughout the interval. The equivalent circuit of this mode is shown in Figure 2-17(c).

$$d_{22} = \frac{2V_{C2}\left(v_b + 2v_a\right)}{\left(V_{C2} + v_b - v_c\right)\left(3v_a - V_{C2}\right)} d_{s2} \qquad \text{Eq. 2-32}$$

4) *Mode 4*:

Inductor current of all three-phases are zero during this interval.

The average inductor current during the interval can be expressed by Eq. 2-33, Eq. 2-34, and Eq. 2-35 where $\mu = \frac{3V_m}{2V_{C2}}$ and $R_{eff} = \frac{2L}{d_{s2}^2 T_{s2}}$.

$$i_{av}(t) = \frac{V_m}{R_{eff}} \frac{\sin \omega t}{1 - 2\mu \sin \omega t} \qquad \text{Eq. 2-33}$$

$$i_{bv}\left(t\right) = \frac{V_m}{R_{eff}} \frac{\sin 2\omega t - \frac{\sqrt{3}}{2\mu}\sin(\omega t + \pi/3)}{1 - \mu \sin \omega t} \qquad \text{Eq. 2-34}$$

$$i_{cv}\left(t\right) = \frac{V_m}{R_{eff}} \frac{\frac{\sqrt{3}}{2\mu}\cos(\omega t + \pi/6) - \frac{1}{2}\sin \omega t}{1 - \mu \sin \omega t} \qquad \text{Eq. 2-35}$$

2.5 Performance Analysis

To evaluate the performance of the proposed MICs, a 650W double-input ZVS-QR buck-buck MIC with integrated boost PFC is designed (Figure 2-13) for an output voltage of 48V. Two 500 W double-input ZVS-QR Cuk-Cuk MIC (Figure 2-14.c) with inherent PFC characteristics are designed for step down and step up to 48V and 380V respectively. The DC input source (V_1) is 140V DC that emulates 4 series-connected PV panels and the AC input source (V_2) represents a micro wind turbine generator with the 3-phase voltage of $70V_{rms}$, 60Hz.

2.5.1 Design Procedure of the QR MIC

The voltage gain of the multi-input converter is expressed by Eq. 2-1 where M_{vi} is the voltage gain of the i^{th} module. The voltage gain M_{Vi} of i^{th} module is the ratio of the output voltage and the input voltage of the i^{th} module. The voltage gain of different QR converter is tabulated in Table 2-1 where m_i is equivalent to the off time (1-d) of PWM converter. m_i can be expressed in terms of switching frequency f_{si}, resonant frequency f_{ri}, φ_i, and α_i. The resonant frequency f_{ri}, and the characteristic impedance Z_i of the i^{th} module are defined by Eq. 2-2 and Eq. 2-3 respectively. The normalized load resistance R_{n_i} can be expressed by Eq. 2-36 where R_L represents the load resistance. φ_i, and α_i can be represented in terms of M_{vi} and R_{ni} as of Eq. 2-37 and Eq. 2-38.

$$R_{n\_i} = \frac{R_L}{Z_i} \qquad \text{Eq. 2-36}$$

$$\phi = \frac{R_{n\_i}}{M_{Vi}} \qquad \text{Eq. 2-37}$$

$$\alpha_i = \sin^{-1} - \phi = \sin^{-1} \frac{R_{n\_i}}{M_{Vi}} \qquad \text{Eq. 2-38}$$

Table 2-2 Maximum switch voltage stress in ZVS QRC

Type of ZVS QRC	Maximum voltage stress of switch
Buck	$v_{ds\_\max\_i} = V_{in\_i} + Z_i I_0$
Boost	$v_{ds\_\max\_i} = V_0 + Z_i I_{in\_i}$
Buck/boost or Cuk	$v_{ds\_\max\_i} = (V_{in\_i} + V_0) + Z_i (I_0 + I_{in\_i})$

In case of ZVS QRC, the resonant capacitor is connected in parallel to the main switch, Therefore, the voltage across the switch (S_1 and S_2) and the resonant capacitor (C_{r1} and C_{r2}) is same irrespective of the type of ZVS QRC. The maximum switch voltage can be derived from the characteristic equation of resonant state (Eq. 2-6 and Eq. 2-16). The maximum voltage across the switch is tabulated in Table 2-2 for different types of ZVS QRC. Therefore, Z_i should be minimized to reduce v_{ds_max}. However, Z_i should be maximized to increase the load range at zero voltage switching (Eq. 2-36). Hence, the key design parameter is the characteristic impedance, Z_i. The optimum characteristic impedance for Cuk or buck/boost is expressed by Eq. 2-40.

$$Z_i\left(I_0 + I_{in\_i}\right) \geq \left(V_{in\_i} + V_0\right) \text{ or } R_{n\_i} \leq M_{v\_i} \qquad \text{Eq. 2-39}$$

$$Z_{optimum\_i} = \frac{R_{L\_Max\_i}}{M_{v\_Min\_i}} \qquad \text{Eq. 2-40}$$

The design equations derived from Table 2-1 are presented in Table 2-3. The voltage gain M_{Vi}, optimum characteristic impedance $Z_{optimum\_i}$ and normalized load resistance R_{ni} are found from the input voltage, output voltage, and power requirements. The switching frequency f_{si} is assumed. Therefore, the resonant frequency f_{ri} can be calculated from the tabulated equations (Table 2-3). The resonant inductor L_{r_i} and resonant capacitor C_{r_i} value can be found from the resonant frequency and the characteristic impedance.

Table 2-3 Design equations of ZVS QRC

Type of converter	Design equation
Buck	$\frac{f_{s\_i}}{f_{r\_i}}=\frac{2\pi\left(1-M_{V\_i}\right)}{\left[\alpha_i+\frac{R_{n\_i}}{2M_{V\_i}}+\frac{M_{V\_i}}{R_{n\_i}}\left(1-\cos\alpha_i\right)\right]}$
Boost	$\frac{f_{s\_i}}{f_{r\_i}}=\frac{2\pi}{\left[\alpha_i+\frac{R_{n\_i}}{2M_{V\_i}}+\frac{M_{V\_i}}{R_{n\_i}}\left(1-\cos\alpha_i\right)\right]M_{V\_i}}$
Buck-boost/Cuk	$\frac{f_{s\_i}}{f_{r\_i}}=\frac{2\pi}{\left[\alpha_i+\frac{R_{n\_i}}{2M_{V\_i}}+\frac{M_{v\_i}}{R_{n\_i}}\left(1-\cos\alpha_i\right)\right]\left(1+M_{V\_i}\right)}$
Resonant Inductor	$L_{r\_i}=\frac{Z_i}{2\pi f_{r\_i}}$
Resonant capacitor	$C_{r\_i}=\frac{1}{2\pi f_{r\_i}Z_i}$

2.5.1 Simulation Results

Step down MIC with Integrated PFC: A 650W 2-input proposed MIC (ZVS-QR buck-buck MIC with integrated boost PFC) is designed to give an output voltage of 48V. In this design, input source 1 is connected to 140V DC which emulates 4 series connected 35V PV panels. Input source 2 is connected to the output of a 70V_{rms} 60Hz wind turbine generator. The range of the operating switching frequency is 250-340 kHz. The components parameters are calculated as explained in section 2.5.1. L_b and C_b are calculated as presented [88]. The designed components are listed in Table 2-4.

Table 2-4 Circuit parameters of the designed converter for simulation work (ZVS-QR buck-buck MIC with integrated boost PFC)

Circuit designator	***Component values***
L_{r1}	6.2 µH
C_{r1}	20 nF
L_{r2}	16 µH
C_{r2}	11 nF
L_b	10 µH
C_b	47 µF
L_f	650 µH
C_f	1.2 µF
L_a, L_b, L_c	16 µH

Figure 2-18 and Figure 2-19 show the simulation results of the individual operation of PV and wind modules at full load condition respectively when both of the input voltages operate at their rated values. The top module (PV) switching frequency is 255kHz and the bottom module (wind) switching frequency is 275kHz. Figure 2-20 shows the simulation results of the simultaneous operation. The switching frequency of the top module (PV) and bottom module (wind) are 310kHz and 320kHz. The output voltage is regulated by varying the switching frequency of the top and bottom modules. In all three cases (individual operation of PV and wind, and simultaneous operation), d_1 and d_2 remain the same (d_1= 0.5 and d_2= 0.4). It can be observed that ZVS turn on (blue shaded) and ZVS turn off (red shaded) are achieved for all cases. The output voltage and current are also shown.

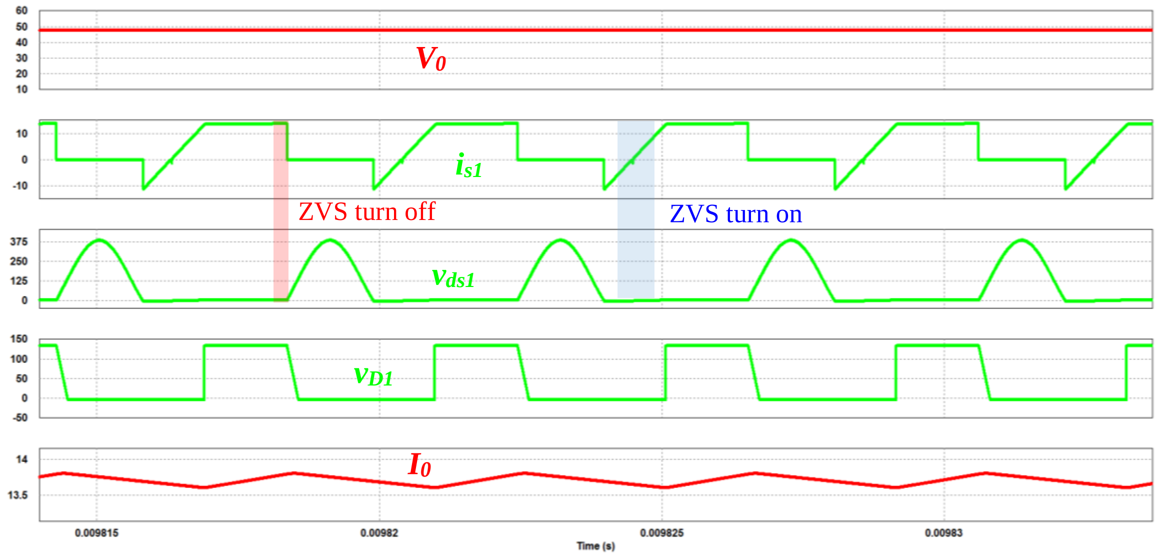

Figure 2-18 Individual operation for top module (f_{s1} = 255kHz)

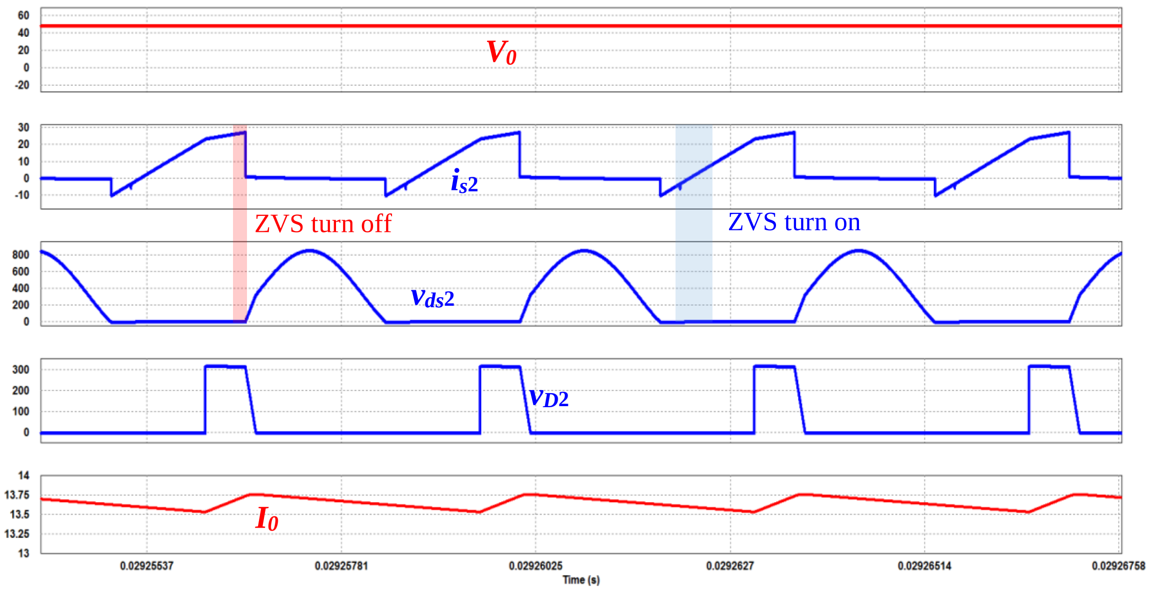

Figure 2-19 Individual operation for bottom module (f_{s2} = 275kHz)

Figure 2-21 shows the input current waveform before and after the filter for individual and simultaneous wind module operations. The PF achieved for individual and simultaneous operation is close to 0.99 for both cases.

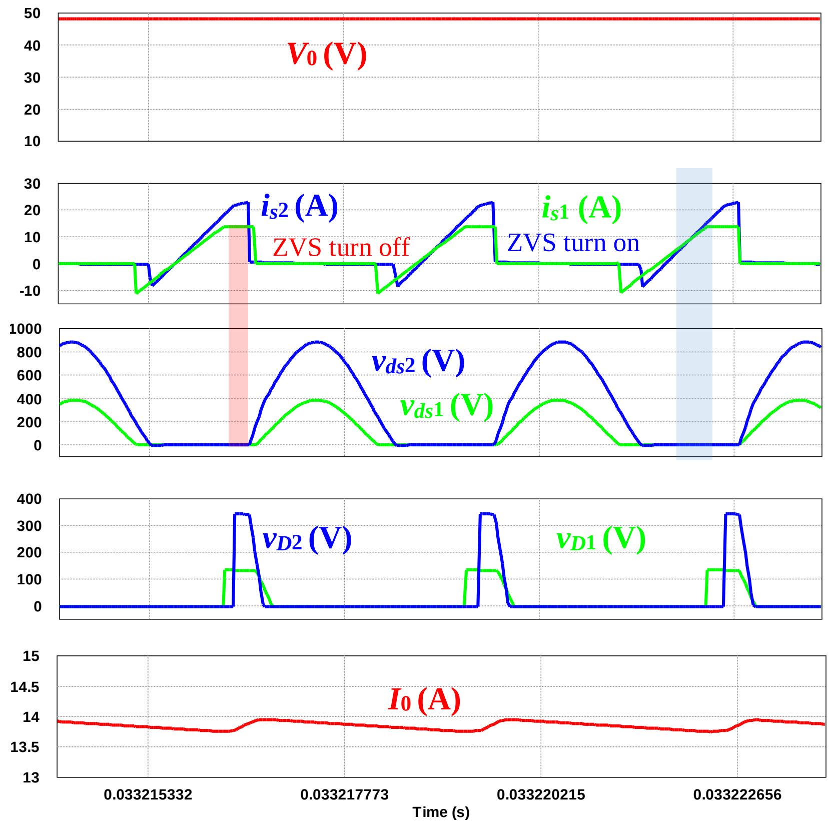

Figure 2-20 Simultaneous operation of top and bottom energy (f_{s1} = 310kHz, f_{s2} = 320kHz)

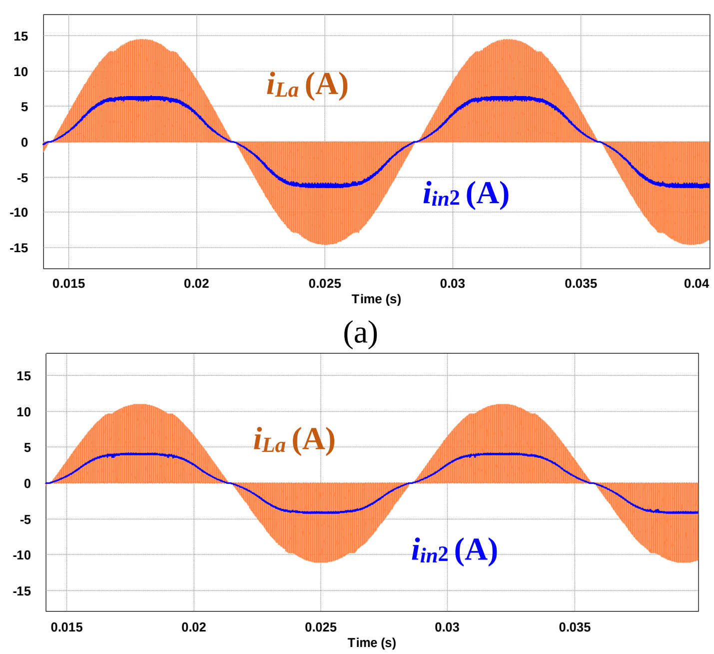

Figure 2-21 Per-phase input current of the input module that works with AC input (a) individual operation (b) simultaneous operation

<u>Step up/down MIC with Inherent PFC</u>: One step down (48V) and one step up (380V) 500W double-input proposed MIC (ZVS-QR Cuk-Cuk MIC with inherent PFC) are designed for the following input parameters: input source 1 (V_1): 140V DC that emulates 4 series-connected PV panels, input source 2 (V_2): a 3-phase variable voltage source with $70V_{rms}$, 60Hz wind turbine generator. The converter is designed based on the procedure explained in section 2.5.1. The designed components are listed in Table 2-5.

Table 2-5 Circuit parameters of the designed converter for simulation work
(ZVS-QR Cuk-Cuk MIC with inherent PFC)

Component designation	***Component values* (48V)**	***Component values* (380V)**
L_{r1}	6 µH	17 µH
C_{r1}	34 nF	1.9 nF
L_{r2}	9 µH	13 µH
C_{r2}	22 nF	3.3 nF
L_1	33 µH	33 µH
L_{2a}, L_{2b}, L_{2c}	9 µH	9 µH
C_1, C_2	250 nF	250 nF
L_f	25 µH	25 µH
C_f	13 µF	13 µF

Figure 2-22 shows simulation results of the step down individual operations of the designed converter. Figure 2-22(a) and (b) show the operation of solar (top) and wind (bottom) module respectively. In step down individual mode, the switching frequencies are 285 kHz and 280 kHz for the solar and the wind module respectively.

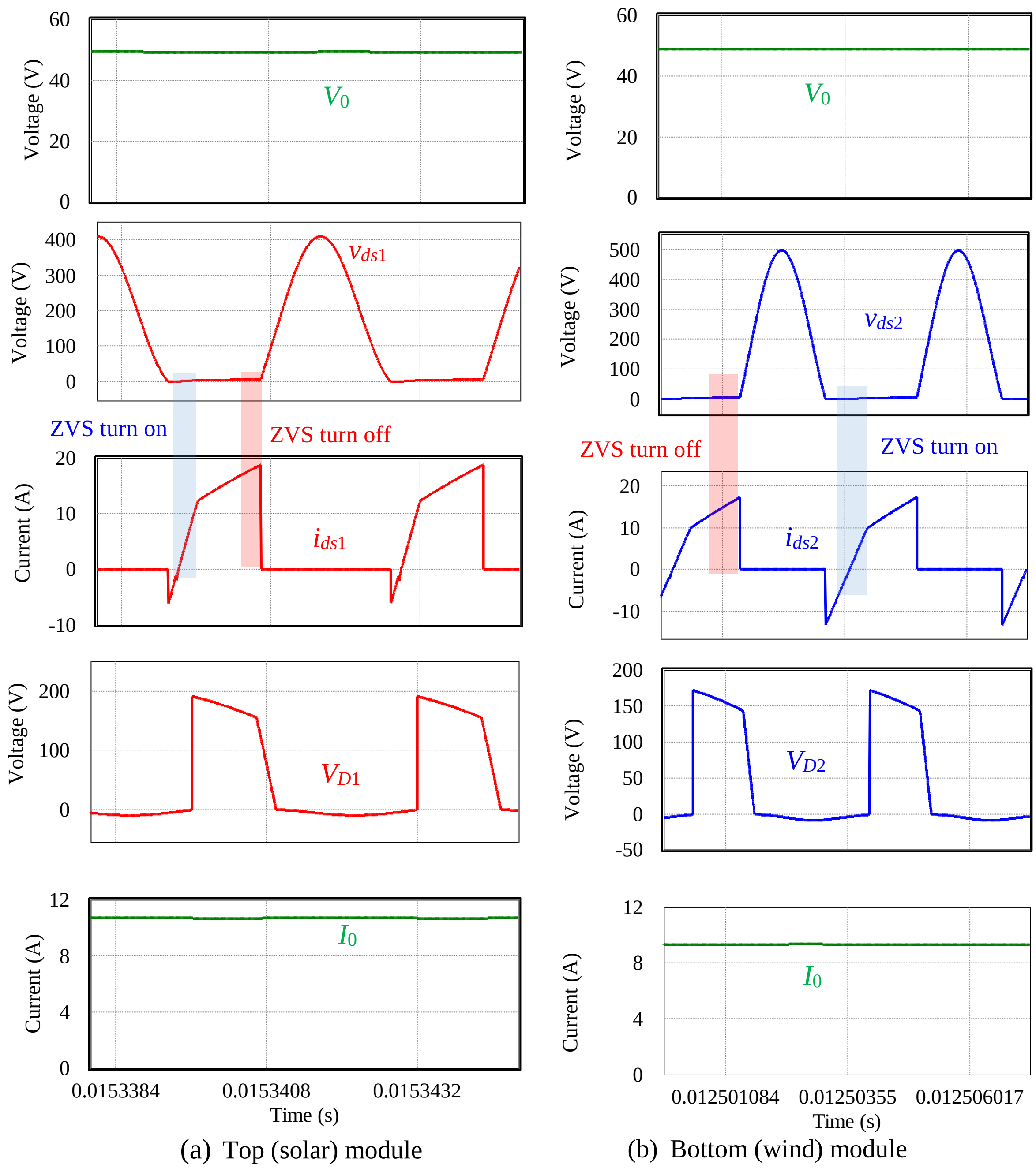

Figure 2-22 Simulation results for step down individual operation (a) top module (f_{s1} = 285kHz and d_1=0.38) (b) bottom module (f_{s2} = 280kHz and d_2 = 0.4)

Figure 2-23 shows the step up individual operation of PV (top) and wind (bottom) modules. For the step up operation, the switching frequencies are 240 kHz and 300 kHz for the PV and wind module respectively. For all individual operations, soft switching is achieved. Figure

2-24 shows the per phase input current during individual operation: filtered input current and the discontinuous input current envelope. The PF achieved is 0.99 for both cases.

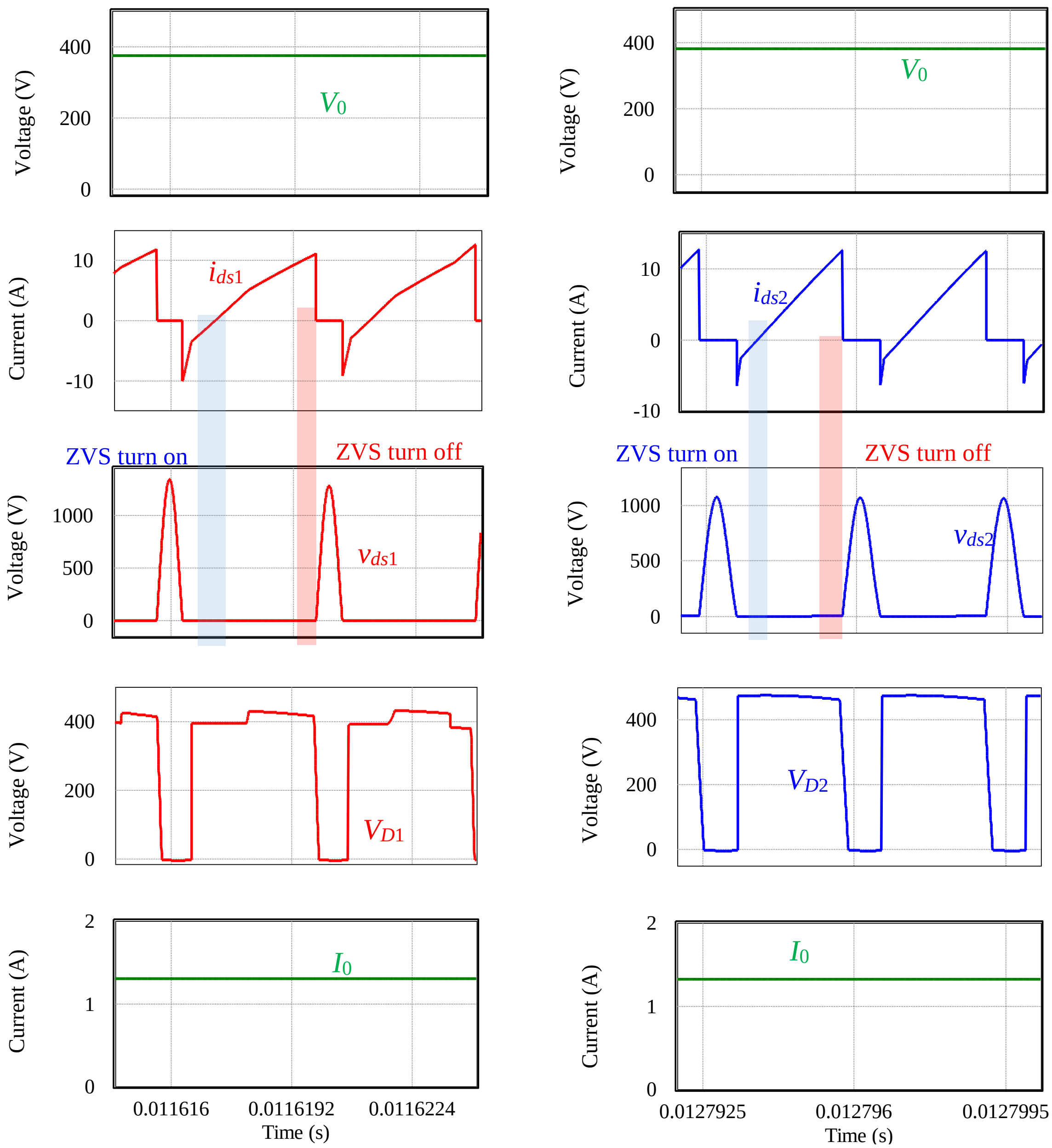

(a) Top (PV) module (b) Bottom (wind) module

Figure 2-23 Simulation results for step up individual operation (a) top (PV) module (f_{s1} = 240kHz and d_1=0.75) (b) bottom (wind) module (f_{s2} = 300kHz and d_2=0.7)

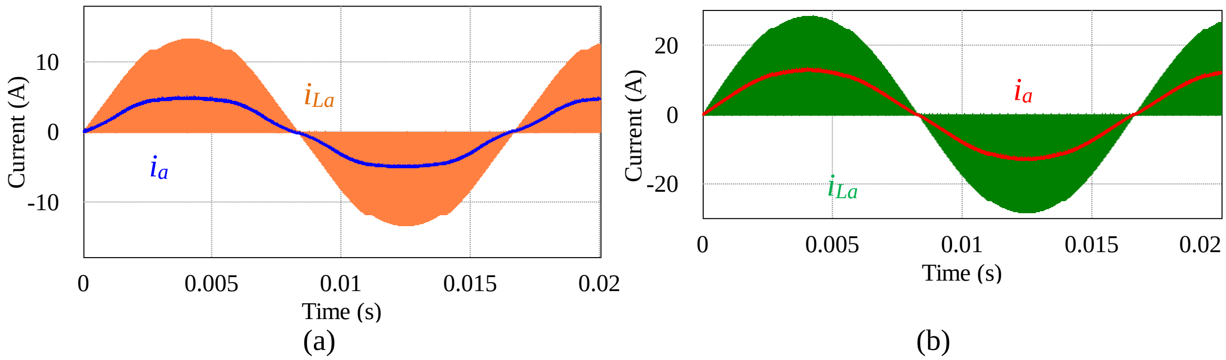

Figure 2-24 Per-phase input current of the bottom (wind) module for individual operation (a) step down operation, 48V (orange- discontinuous input current envelop and blue- filtered input current) and (b) step up operation, 380V (green- discontinuous input current envelop and red- filtered input current)

Step down (48V) and step up (380V) simultaneous operations are shown in Figure 2-25. For all cases, the switch voltage and current, the voltage across the output diodes, and output voltage and current waveforms are shown. The switch voltage and current waveforms confirm the soft switching operations of the converter in simultaneous mode. In simultaneous mode, the switching frequencies are 318 kHz and 322 kHz for the step down operation for the PV and wind modules respectively. For the step up operation in simultaneous mode, the switching frequencies are 405 kHz and 425 kHz for the PV and wind modules respectively. Figure 2-26 shows the input current waveforms for the bottom module in simultaneous operation and confirms high PF (0.99) for both cases. The efficiency measured for individual and simultaneous operation is over 95% and 97% respectively. This efficiency is achieved for both step up and step down operations.

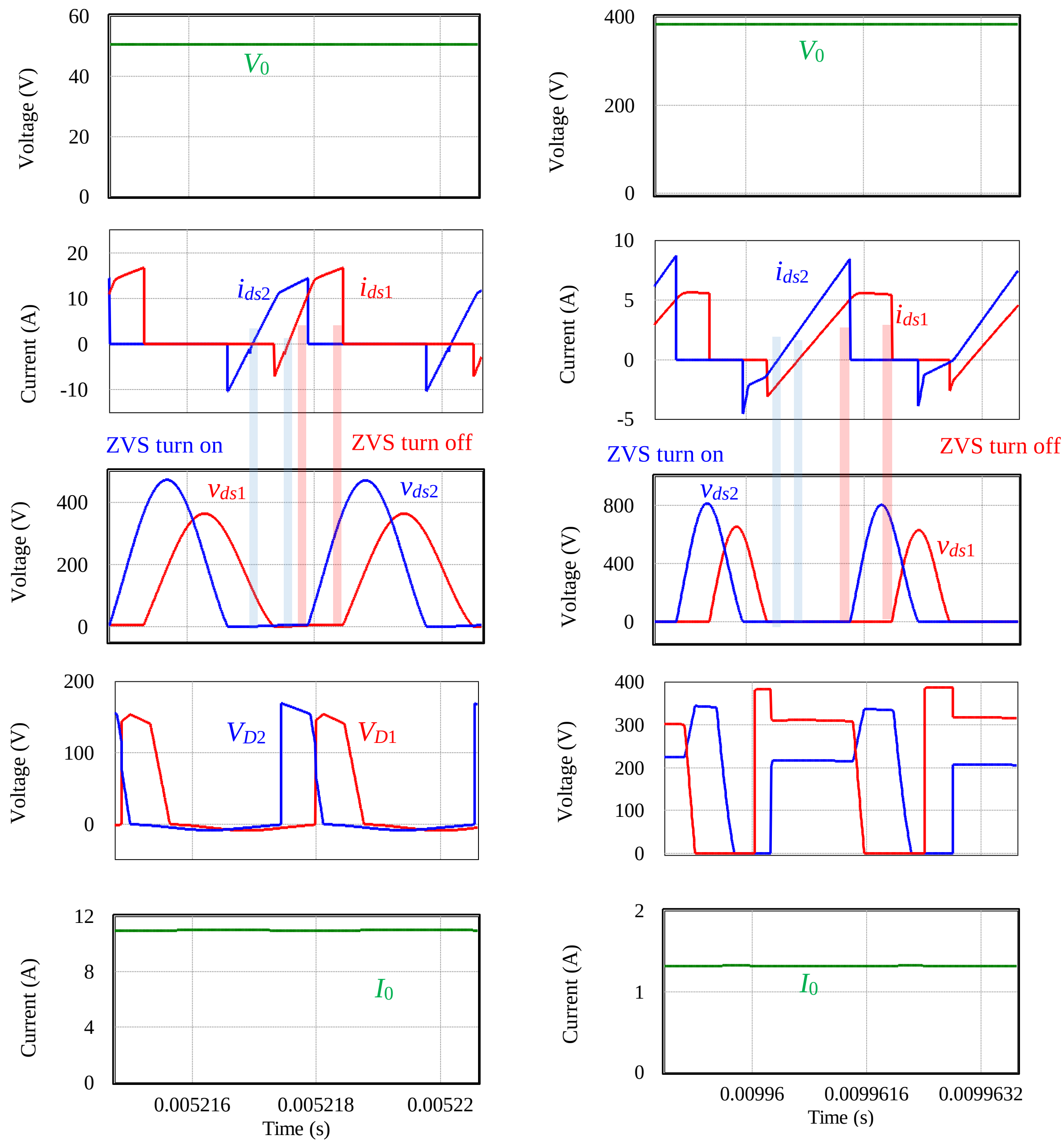

(a) Step down operation (48V)   (b) Step up operation (380V)

Figure 2-25 Simultaneous operation (a) step down operation (fs_1 = 318 kHz, fs_2 = 322 kHz, d_1=0.31 and d_2=0.29) (b) step up operation (fs_1 = 405 kHz, fs_2 = 425 kHz, d_1=0.6 and d_2=0.6)

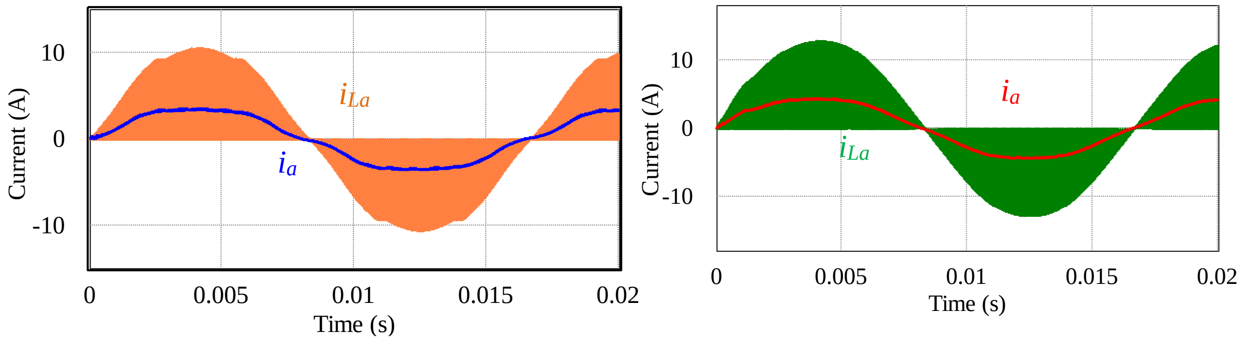

(a) (b)

Figure 2-26 Simultaneous operation: per-phase input current of the bottom (wind) module (a) step down operation, 48V (orange- discontinuous input current envelop and blue- filtered input current) and (b) step up operation, 380V (green- discontinuous input current envelop and red- filtered input current)

2.5.2 Experimental Results

A 500W double-input proposed MIC (ZVS-QR Cuk-Cuk MIC with inherent PFC) is designed and built for hardware testing. The prototype is shown in Figure 2-27. The top module input is 70V DC that emulates 2 series-connected PV panels and the bottom module input is a 3-phase voltage source with $80V_{rms}$, 60Hz that emulates the wind turbine generator. The designed components are listed in Table 2-6.

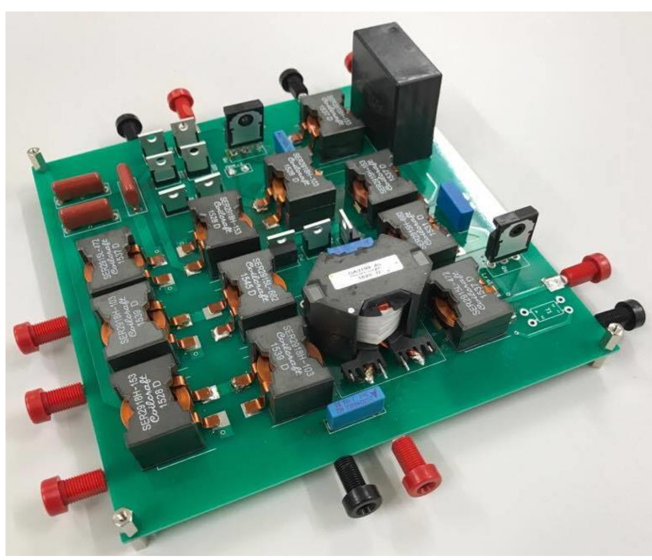

Figure 2-27 Experimental prototype ZVS-QR Cuk-Cuk MIC

Table 2-6 Circuit parameters of the designed converter for experimental work

(ZVS-QR Cuk-Cuk MIC with inherent PFC)

Component designation	***Component values***	***Part number***
L_{r1}	3.9 µH	SER2915H
C_{r1}	7.2 nF	B32672L1722K
L_{r2}	2.7 µH	SER2915H
C_{r2}	10 nF	B32621A6103J
L_1, L_{2a}, L_{2b}, L_{2c}	33 µH	SER2915H
C_1, C_2	240 nF	MKP385324063JCA2B0
L_f	25 µH	GA3199-AL
C_f	13 µF	EZP-E1D256MTA
S_{pv}, S_{bat}	600V, 18A	STP24N60DM2-EP
D_1, D_2, D_{bat}	600V, 15A	MUR1560

Figure 2-28 shows the switching waveforms of the top (PV) module. The input voltage is 70V DC and the switching frequency is 370kHz. The waveform confirms the soft switching turn on and turn off for the top module. Figure 2-29 shows the waveforms for the bottom module with three-phase AC input. The input voltage is 80V and the switching frequency is 350kHz. Figure 2-29(a) confirms the soft switching transitions of the high frequency switch. Figure 2-29(b) shows the three-phase input current of the bottom module. Figure 2-29(b) confirms the balanced three-phase input current. The PF is 0.98 and the THD is 20%.

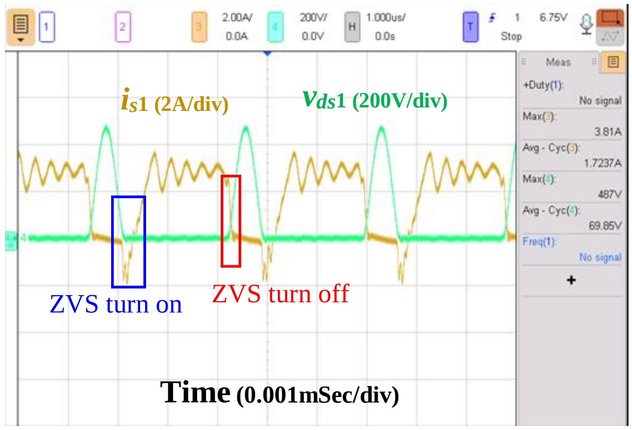

Figure 2-28 Experimental waveforms of the top module (PV) of ZVS-QR Cuk-Cuk MIC for 70V input and switching frequency 370kHz

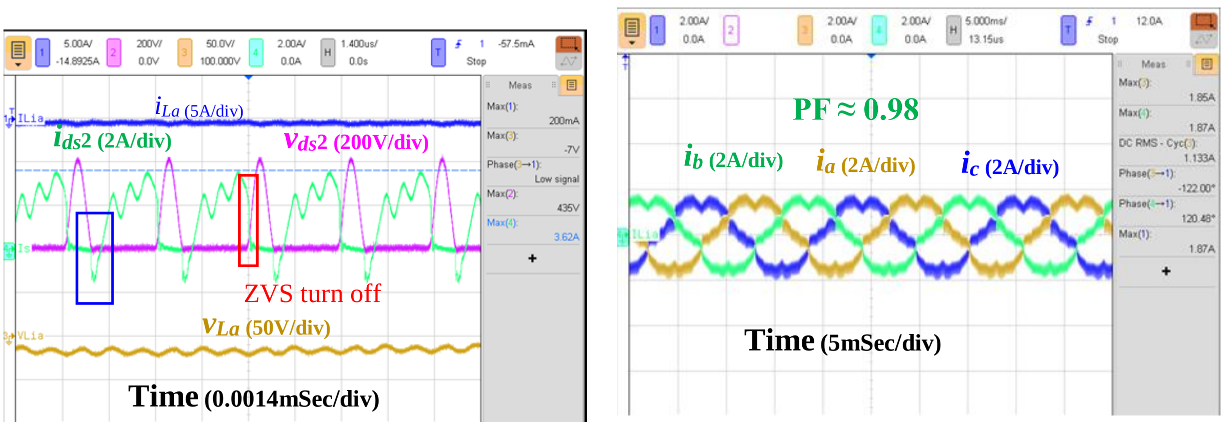

(a) Switching waveform (b) Input currents waveform

Figure 2-29 Experimental waveforms of the bottom module (wind) of ZVS-QR Cuk-Cuk MIC for three-phase AC (80V) input and switching frequency 350kHz

2.6 Chapter Summary

A family of DC-DC MIC for renewable energy systems is presented in this chapter. Each module of the presented MICs requires only one high frequency switch. The switching turn on and turn off happen under soft-switching (ZVS or ZCS) condition. All the MICs are capable of performing individual and simultaneous operations. Among these MICs, two MICs: ZVS-QR buck-buck MIC and ZVS-QR Cuk-Cuk MIC are then chosen to discuss in detail. The operation and analysis of these two MICs are explained. The AC input module (such as wind) requires PFC in addition to AC-DC conversion. The front end PFC circuit integration with the DC-DC module of MIC is also presented. The operation and analysis of the front end PFC circuit are then discussed. The design procedure is explained. In the last section of this chapter, the performance of the presented MICs is verified through the simulation and experimental results.

Chapter 3 Proposed MIC with Energy Storage System

The third objective of this research is to develop a DC-DC module integrated PV power optimizer. The maximum output voltage of a PV module is lower than the minimum standard DC grid voltage level. Therefore, stepping up voltage is a required feature of the power optimizer. In chapter 2, two different MICs (DC-DC): ZVS-QR buck-buck MIC and ZVS-QR Cuk-Cuk MIC are discussed. Between these two MICs, ZVS-QR buck-buck MIC is a step down converter. Hence, ZVS-QR buck-buck MIC is not suitable for the power optimizer application. Therefore, in this chapter, one module of the ZVS-QR Cuk-Cuk MIC is utilized for PV application. A MPPT technique is developed that is suitable for the devised PV power optimizer.

The fourth objective of this research is to integrate the decentralized battery with the PV power optimizer. In this chapter, DC-DC unidirectional step up/down converters are utilized as battery charging and discharging modules. The battery charging circuit is integrated at the front end of the power optimizer to reduce overall active and passive components. While, the battery discharging circuit uses one module of the devised ZVS-QR Cuk-Cuk MIC. The devised integrated PV-battery system is able to follow the battery charging profile. The descriptions of the proposed MIC topology, and its operating principles are explained in detail in this chapter.

3.1 Description of the Proposed Configuration

The proposed ZVS-QR Cuk-Cuk MIC presented in Chapter 2 is taken to integrate the battery circuit. The two-input proposed MIC (Figure 2-7) can serve the PV power optimizer and the battery discharge circuit. Therefore, a battery charging circuit is required. To achieve that, a flyback converter is integrated at the front-end of the power optimizer. Between the two different configurations of ZVS-QR Cuk-Cuk MIC shown in Figure 2-7, the configuration#2 (Figure 2-7 (b)) is taken to integrate the battery charging circuit. Therefore, the resonant inductor is also a part of the charging circuit which is not possible for configuration#. In this way, the charging circuit also becomes a soft switching converter (ZVS flyback QRC). The integrated flyback converter shares the input inductor and the resonant switch (switch, and resonant inductor and capacitor) of the ZVS Cuk QRC (power optimizer). As a result, the number of required switches and passive components are reduced. The final PV-battery configuration is shown in Figure 3-1.

The PV power optimizer with integrated battery charging circuit utilizes ZVS-QR Cuk with integrated ZVS-QR flyback converter as discussed above. The integrated ZVS-QR Cuk-flyback converter shares the input transformer, T_{in} and the resonant switch (resonant inductor, L_{r_pv} and capacitor, C_{r_pv}, and switch, S_{pv}). ZVS-QR Cuk converter is used for the discharge circuit. Power switches S_{pv} and S_{bat} are high frequency switches and realize soft switching (ZVS turn on and turn off). A solid state switch S_{Aux} is used to activate and deactivate the battery charging circuit. The switch remains on during the battery charging; otherwise, it remains off. The discharging circuit is independent of the power optimizer. The output filter (L_f and C_f) is shared by power optimizer and the battery discharge circuit. The power flows unidirectionally through this system. The proposed converter is capable of performing all required individual and simultaneous operations as listed Table 3-1.

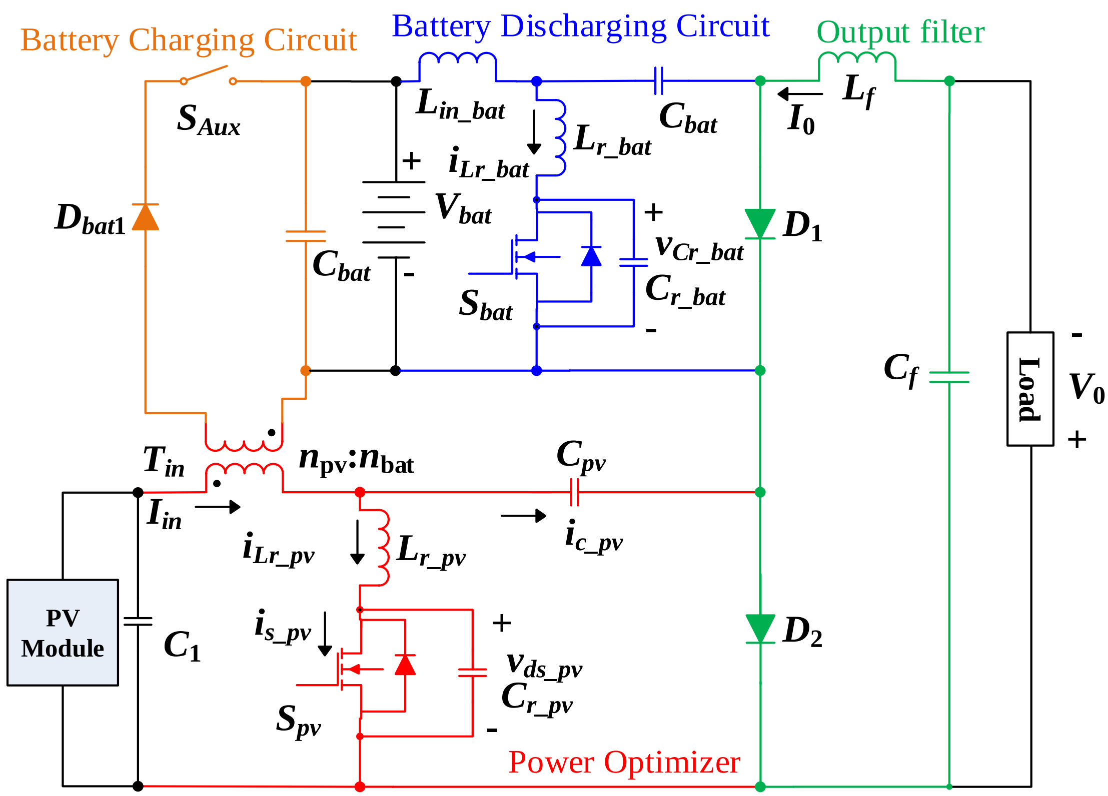

Figure 3-1 Proposed PV-battery integrated converter

Table 3-1 Operating modes of PV-battery system

Individual operations		**Simultaneous operations**	
Mode 1	PV to load (power optimizer)	**Mode 1**	PV to load and battery (power optimizer and charge circuit)
Mode 2	battery to load (discharge circuit)	**Mode 2**	PV and battery to load (power optimizer and discharge circuit)

3.2 Operating Principles of the Proposed Converter

The individual and simultaneous operations of Cuk-Cuk converter (individual operation mode 1 and mode 2, and simultaneous operation mode 2) are presented in the Chapter 2. Therefore, simultaneous mode 2 is presented in this chapter.

The resonant components, $L_{r\text{-}pv}$ and $C_{r\text{-}pv}$ of the QR converter determine the characteristics of the converter. The angular resonant frequency ω_{r_pv}, characteristic impedance Z_{pv} and the normalized load resistance $R_{N\text{-}pv}$ are defined by Eq. 3-1, Eq. 3-2 and Eq. 3-3 respectively where with R_L represents the load resistance.

$$f_{r\_pv} = \frac{1}{2\pi\sqrt{L_{r\_pv}C_{r\_pv}}} \qquad \text{Eq. 3-1}$$

$$R_{N\_pv} = \frac{R_L}{Z_{pv}} \qquad \text{Eq. 3-2}$$

$$Z_{pv} = \sqrt{\frac{L_{r\_pv}}{C_{r\_pv}}} \qquad \text{Eq. 3-3}$$

The key theoretical operating waveforms are shown in Figure 3-2. The proposed ZVS-QR Cuk-flyback converter consists of single active switch S_{pv} and two diodes D_2 and D_{bat}. In case of the QR converter, the state of the circuit changes when any of the switches turns on or turns off. For the proposed circuit, there are three switches (S_{pv}, D_{bat} and D_2) with two states: on (equivalent to 1) and off (equivalent to 0). Among those switches, one switch, S_{pv} is controllable. However, all three switches play the key role for power conversion. Therefore, there are eight different states of the proposed converter based on switch turn on and off - 000, 001, 011, 111, 110 and 100 where 0 and 1 represent on-off states of S_{pv}, $D_{bat,}$ and D_2 respectively. In case of ZVS-QR converters, resonance happens during the off time of the active switch (S_{pv} for the proposed converter). However, total energy transfer from input to the output for a ZVS-QR converter requires four steps named capacitor charging, resonant, inductor charging and freewheeling as mentioned in Chapter 2. The operation of the proposed converter is described below following the eight states of the switch and the four energy transfer steps of the converter.

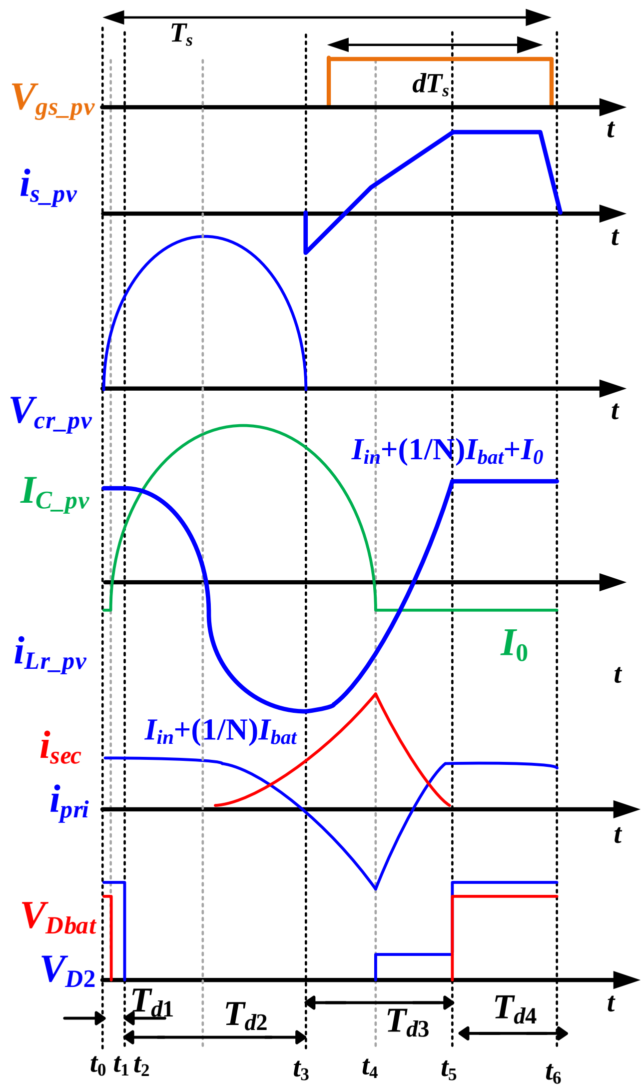

Figure 3-2 Theoretical waveforms of the proposed converter

[$t_0 < t < t_1$]: At time t_0, the gate signal is removed from the switch S_{pv} and the switch S_{pv} is turned off. Resonant capacitor voltage v_{cr_pv} rises linearly due to resonant inductor maximum current, I_M ($I_M = I_{in} + \frac{1}{N} I_{bat\_crg} + I_0$) which is constant throughout this period. Both diodes D_2 and

D_{bat} are off for this time period. This period ends when the diode D_{bat} turns on and the resonant capacitor voltage, v_{cr_pv} reaches to (V_{in}+NV_{bat}), where N is the turns ratio. The battery charging circuit remains off as the current through the transformer remains unchanged. This stage is called the capacitor charging stage. The duration of this stage T_{d1a} is presented by Eq. 3-4 and depends on the resonant inductor maximum current I_M, the input voltage V_{in}, the battery voltage V_{bat}, the characteristics impedance Z_{pv}, the turns ratio N, and the angular resonant frequency ω_{r_pv}.

$$T_{d1a} = \frac{\left(V_{in} + NV_{bat}\right)}{Z_{pv}\omega_{r\_pv}I_M} \qquad \text{Eq. 3-4}$$

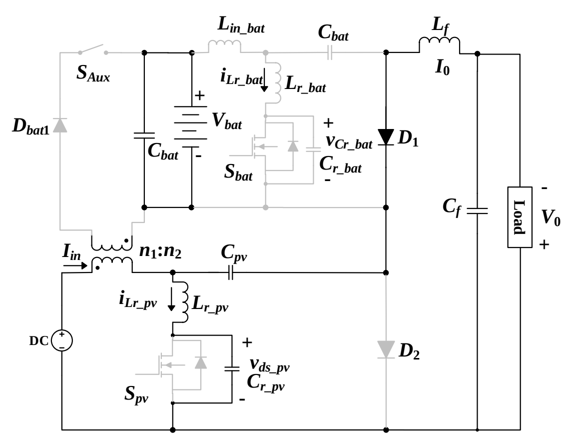

(a) $t_0 < t < t_1$

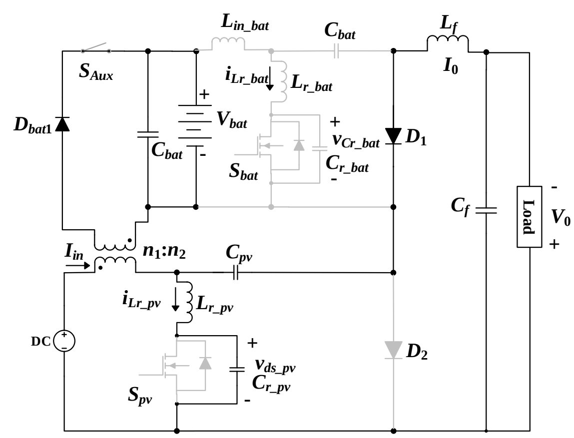

(b) $t_1 < t < t_2$

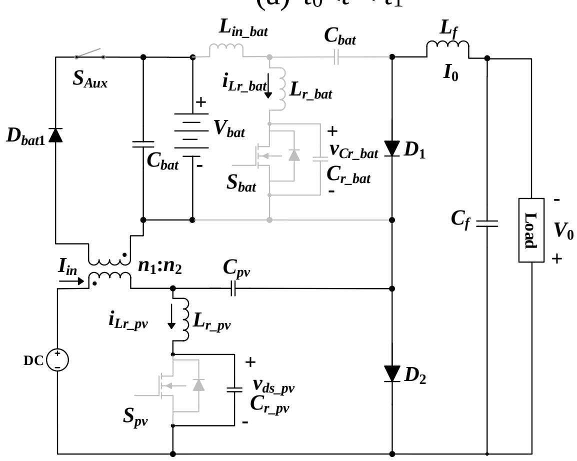

(c) $t_2 < t < t_3$

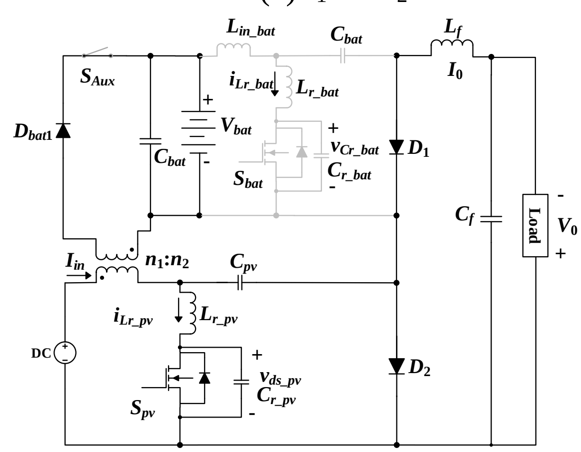

(d) $t_3 < t < t_4$

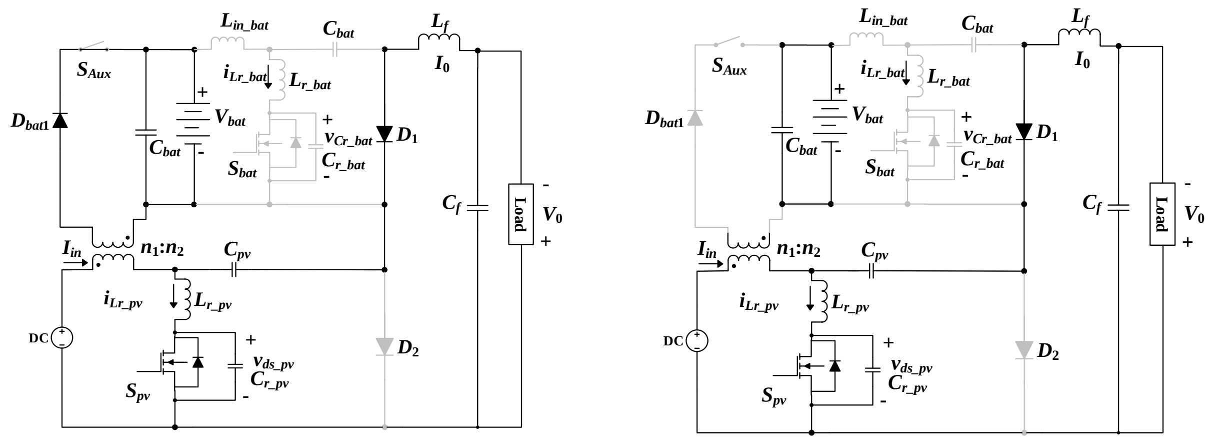

(e) $t_4<t<t_5$ (f) $t_5<t<t_6$

Figure 3-3 Operating stages of the proposed converter

[$t_1 < t < t_2$]: The capacitor charging stage continues through this stage. This period ends when the resonant capacitor voltage, v_{cr_pv} reaches to (V_{in}+V_0), and diode D_2 turns on. The duration of this stage is significantly short compared to other stages. The duration of this stage T_{d1b} is presented by Eq. 3-5 and depends on the resonant inductor maximum current I_M, output voltage V_0, battery voltage V_{bat}, characteristics impedance Z_{pv}, turns ratio N, and angular resonant frequency ω_{r_pv}.

$$T_{d1b} = \frac{(V_0 - NV_{bat})}{Z_{pv}\omega_{r\_pv} I_M} \qquad \text{Eq. 3-5}$$

[$t_2 < t < t_3$]: At the beginning of this stage, L_{r_pv} and C_{r_pv} start resonating. D_2 and D_{bat} are on and, S_{pv} remains off throughout the period. As resonance happens in this period, this period is termed as the resonant stage. The resonant capacitor voltage reaches its maximum and then starts discharging through the resonant inductor. The resonant inductor current, i_{Lr_pv} reaches to its negative maximum during this period. This period ends when resonant capacitor voltage, v_{cr_pv} reaches zero and the anti-parallel diode of switch S_{pv} starts conducting.

The duration of this stage T_{d2} is presented by Eq. 3-6, where T_{d2} depends on the angular resonant frequency ω_{pv} and α_{pv}. α_{pv} is the inverse sine function of φ_{pv} (see Eq. 3-7) and the range of α_{pv} is 2π to 3π/2. φ_{pv} depends on the resonant inductor maximum current I_M, the input voltage V_{in}, the output voltage V_0, and the characteristics impedance Z_{pv} as presented by Eq. 3-8.

$$T_{d2} = \frac{\alpha_{pv}}{\omega_{r\_pv}} \quad \text{Eq. 3-6}$$

$$\alpha_{pv} = \sin^{-1}\left(-\varphi_{pv}\right) \quad \text{Eq. 3-7}$$

$$\varphi_{pv} = \frac{V_{in} + V_0}{Z_{pv} I_M} \quad \text{Eq. 3-8}$$

[$t_3 < t < t_4$]: The gate signal is applied and the switch S_{pv} turns on at this stage. S_{pv} experiences zero voltage turn on as the antiparallel diode was conducting prior. The diode D_{bat} and D_2 remain on throughout the period. At the end of this period, D_2 turns off and the storage capacitor, C_{pv} starts carrying I_0. The secondary current reaches its maximum and primary current reaches its minimum [I_M-(1/N)i_{sec}]. This is the inductor charging stage. The duration of this stage is presented by Eq. 3-9, where d_{bat} and d_2 are the duty ratio of D_{bat} and D_2 diode respectively, and f_s represents the switching frequency of S_{pv}.

$$T_{d3a} = \frac{\frac{Z_{pv}}{\omega_{r\_pv}}\left[I_M\left(1-\cos\alpha_{pv}\right)\right] - \frac{1}{f_s}\left[V_{in}\left(d_{bat} - d_2\right) + V_0\right]}{V_{in} + V_0} \quad \text{Eq. 3-9}$$

[$t_4 < t < t_5$]: The inductor charging stage continues. The resonant inductor current, i_{Lr_pv} keeps rising and reaches to its maximum I_M at the end of this period. Primary transformer current also reaches to its positive maximum. At the end of this period, D_{bat} turns off and the battery charging circuit as well. The duration of this stage is presented by Eq. 3-10, where T_{d3} is the total duration for the inductor charging stage and is represented by Eq. 3-11 and T_{d3a} is given by Eq. 3-9.

$$T_{d3b} = T_{d3} - T_{d3a}$$ Eq. 3-10

$$T_{d3} = L_{r\_pv} \frac{I_M}{V_{in} + V_{01}} \left(1 - \cos\alpha_{pv}\right) = \frac{\left(1 - \cos\alpha_{pv}\right)}{\omega_{r\_pv}\varphi_{pv}}$$ Eq. 3-11

[$t_5 < t < t_6$]: S_{pv} is on and D_2 and D_{bat} remain off throughout the period. The maximum resonant inductor current, I_M freewheels through the switch and the resonant inductor. At the end of this stage, the switch S_{pv} turns off at zero voltage condition. The battery charging circuit remains off though this freewheeling stage. The duration of this stage T_{d4} is represented by Eq. 3-12, where T_s is the time period of the switch S_{pv}.

$$T_{d4} = T_s - T_{d1a} - T_{d1b} - T_{d2} - T_{d3}$$ Eq. 3-12

3.3 Steady State Analysis

To analyze the steady state characteristics, the following assumptions are made:

- The output filter inductor L_f is large compared to resonant inductor L_{ri}.
- Output filter L_f-C_f and the load are treated as a constant current sink.
- The storage capacitor C_{pv} is large and its voltage is constant.
- Semiconductor switches are ideal. That is, no forward voltage drop in the on state, no leakage current in the off state, and no time delay at turn on and turn off time.

1) Capacitor charging stage:

The resonant capacitor, C_{r_pv} is charged linearly through the resonant inductor maximum current I_M at this stage Eq. 3-13. The resonant inductor maximum current I_M is the function of the input current (I_{in}), the battery charging current (I_{bat_crg}), and the output load current I_0 as shown in Eq. 3-14, where $N = \frac{n_{pv}}{n_{bat}}$. The capacitor charging happens during T_{d1a} and T_{d1b} as described in the previous section. Therefore, T_{d1} continues from t_0 to t_2 as given by Eq. 3-15.

T_{d1} depends on the resonant inductor maximum current I_M, the input voltage V_{in}, the output voltage V_0, the characteristics impedance Z_{pv}, and the angular resonant frequency ω_{r_pv}.

$$v_{cr\_pv} = \frac{1}{C_{r\_pv}} I_M t \qquad \text{Eq. 3-13}$$

$$I_M = I_{in} + \frac{1}{N} I_{bat\_crg} + I_0 \qquad \text{Eq. 3-14}$$

$$T_{d1} = \frac{(V_{in} + V_0)}{Z_{pv}\omega_{r\_pv} I_M} \qquad t_0 < T_{d1} < t_2 \qquad \text{Eq. 3-15}$$

2) Resonant stage:

The resonant inductor and capacitor resonate in this stage and is governed by Eq. 3-16 and Eq. 3-17. The resonant capacitor voltage reached its maximum, $(V_{in} + V_{01}) + Z_{pv} I_M$ and discharge through the resonant inductor. At the end of this stage, the resonant inductor current reached to $I_M \cos\alpha$.

$$v_{cr\_pv}(t) = (V_{in} + V_{01}) + Z_{pv} I_M \sin\omega_{r\_pv} t \qquad \text{Eq. 3-16}$$

$$i_{Lr\_pv}(t) = I_M \cos\alpha_{pv} t \qquad \text{Eq. 3-17}$$

3) Inductor charging stage:

The resonant inductor linearly gets charged Eq. 3-18 during two time periods- T_{d3a} and T_{d3b}. For the time period T_{d3a}, the inductor is charged by the input voltage, V_{in} and the output voltage, V_0. The primary current reached its minimum and secondary current reached its maximum Eq. 3-19. The secondary current of the transformer, T_{in} depends on its magnetizing inductance L_m, the output voltage V_0, the α_{pv} (Eq. 3-7), and the angular frequency ω_{r_pv}. During T_{d3b}, resonant inductor charged by the input voltage, V_{in} and reached its maximum I_M.

$$i_{Lr\_pv}(t) = I_M \cos\omega_{r\_pv} + \frac{\omega_{r\_pv}}{Z_{pv}}\left[(V_{in}+V_0)t_{d3a} + V_{in}t_{d3b}\right] \qquad \begin{matrix} t_3 < t_{d3a} < t_4 \\ t_4 < t_{d3b} < t_5 \end{matrix} \qquad \text{Eq. 3-18}$$

$$I_{Sec\_\max} = \frac{1}{L_m} V_0 \frac{\alpha_{pv}}{\omega_{r\_pv}} \qquad \text{Eq. 3-19}$$

4) Freewheeling stage:

At this stage, only diode D_2 is on and allows freewheeling maximum resonant inductor current, I_M through the diode.

The ZVS-Cuk and the ZVS-flyback converters are of buck/boost type converter and their voltage gain is same [89]. The voltage gain of the ZVS-flyback and the ZVS-Cuk converter are given by Eq. 3-20 and Eq. 3-21 respectively and the relation between the output voltage of battery side and the load side is shown by the Eq. 3-22. For both converters, the gain depends on m_i, which is the function of normalized frequency, f_N, and α, and φ as presented in Eq. 3-23. The normalized frequency, f_N is the ratio of the switching frequency f_s and the resonant frequency f_r as presented in Eq. 3-24. α is the arcsine function of φ, $\alpha = \sin^{-1}(-\varphi)$ and the range of α is 2π to $3\pi/2$. φ is defined by Eq. 3-8. The gain of the flyback converter also depends on the turns ratio, N. The voltage gain relation of the Cuk converter with the normalized frequency with the variation of the normalized load is shown in Figure 3-4. The relation of voltage gain with the normalized frequency for two different normalized loads and the variation of turns ratio for flyback converter is shown in Figure 3-5.

$$M_{v\_Flyback} = \frac{V_{bat}}{V_{pv}} = \frac{1}{N} \times \frac{m_i}{1-m_i} \qquad \text{Eq. 3-20}$$

$$M_{v\_Cuk} = \frac{V_0}{V_{pv}} = \frac{m_i}{1-m_i} \qquad \text{Eq. 3-21}$$

$$V_0 = NV_{bat} \qquad \text{Eq. 3-22}$$

$$m_i = \frac{f_N}{2\pi}\left[\alpha + \frac{\phi}{2} + \frac{1}{\phi}(1-\cos\alpha)\right] \qquad \text{Eq. 3-23}$$

$$f_N = \frac{f_s}{f_r} \qquad \text{Eq. 3-24}$$

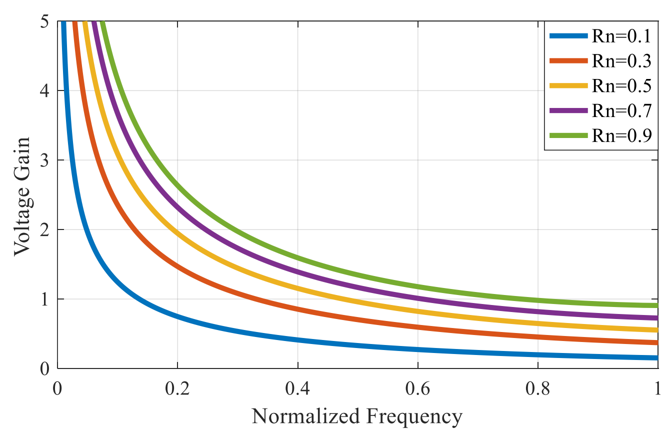

Figure 3-4 Voltage gain and the normalized frequency with the variation of the normalized load of Cuk converter

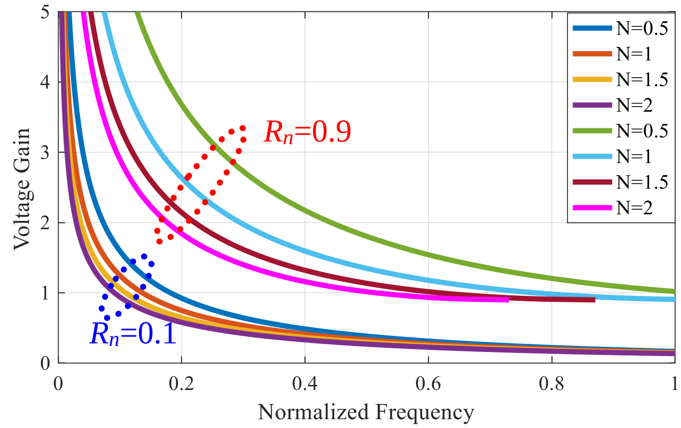

Figure 3-5 Voltage gain and the normalized frequency with the variation of the normalized load and turns ratio of the flyback converter

3.4 Small Signal Analysis

The voltage gain equation presented Eq. 3-20 and Eq. 3-21 are identical when the turns ratio, N is equal to 1. Therefore, same analysis will be applicable for charging (QR-ZVS flyback) and discharging (QR-ZVS Cuk) circuit of the battery and the converter (QR-ZVS Cuk) for PV to load. The gain equation is identical to PWM buck/boost converter if m_i is replaced by the switch off time. Therefore, the small signal analysis of quasi-resonant ZVS converter can be analyzed similar way as PWM converter [90] [91]. The duty ratio of PWM converter is an independent variable. However, m_i of QR-ZVS converter depends on f_s and φ as expressed in Eq. 3-25. The resonant frequency, f_r is constant for a particular designed converter and for half wave QR-ZVS converter (with bidirectional switch), $G(\varphi) \approx 1$. Eq. 3-26 is achieved for small perturbations $\hat{f}_s$, where K_s is represented by Eq. 3-27.

$$m_i = 1 - \frac{f_s}{f_r} G(\phi) \qquad \text{Eq. 3-25}$$

$$\hat{m}_i = m_s \hat{f}_s \qquad \text{Eq. 3-26}$$

$$m_s = \left(\frac{\partial m}{\partial f_s} \right)_{f_s = F_s}$$ Eq. 3-27

The Laplace transform of the small signal model is shown in Eq. 3-26

$$\hat{M}(s) = m_s \hat{F}(s)$$ Eq. 3-28

The conventional method of closed loop control of QR converter is voltage-mode control (Figure 3-6). The change of frequency, $\hat{F}(s)$ is proportional to the change of the error voltage, $\hat{V}_E$. The error voltage, v_E is obtained Eq. 3-29 from a sample of the output voltage, βv_0 and a reference voltage V_{ref} by using a differential amplifier and a compensator with gain $A_v(s)$.

$$\hat{V}_E(s) = A_v(s) \beta \hat{V}_o(s)$$ Eq. 3-29

The input-to-output transfer function G_{IO}, control-to-output transfer function, G_{C0} is shown by Eq. 3-30 and Eq. 3-31 respectively [92] [93]. where K_C, Q_1, ω_{p1}, Q_2 and ω_{p2} is presented by Eq. 3-32- Eq. 3-36 respectively where L_e is the effective inductance of the leakage inductance of T_{in} and C_e is the effective capacitance of the storage capacitor.

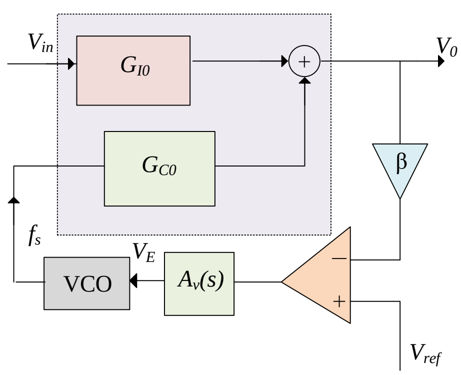

Figure 3-6 Closed loop control of the ZVS-QR converter

$$G_{I0} = M_V \frac{1}{\left[1+\frac{1}{Q_1}\frac{s}{\omega_{p1}}+\left(\frac{s}{\omega_{p1}}\right)^2\right]\left[1+\frac{1}{Q_2}\frac{s}{\omega_{p2}}+\left(\frac{s}{\omega_{p2}}\right)^2\right]} \quad \text{Eq. 3-30}$$

$$G_{C0} = K_C \frac{1-s\left[\frac{L_e}{R_L}-R_eC_e\left(1-m_i\right)\right]+s^2L_eC_e(1-m_i)}{\left[1+\frac{1}{Q_1}\frac{s}{\omega_{p1}}+\left(\frac{s}{\omega_{p1}}\right)^2\right]\left[1+\frac{1}{Q_2}\frac{s}{\omega_{p2}}+\left(\frac{s}{\omega_{p2}}\right)^2\right]} \quad \text{Eq. 3-31}$$

$$K_c = \frac{V_{in}\big|_{t_0} - V_0\big|_{t_o}}{F_s\big|_{t_0}} \quad \text{Eq. 3-32}$$

$$Q_1 = \frac{R_L}{\sqrt{\frac{L_e}{C_e}}} \quad \text{Eq. 3-33}$$

$$\omega_{p1} = \frac{1}{\sqrt{L_eC_e}}\left(1-m_i\right) \quad \text{Eq. 3-34}$$

$$Q_2 = \frac{R_L}{\sqrt{\frac{L_F}{C_F}}} \quad \text{Eq. 3-35}$$

$$\omega_{p2} = \frac{1}{\sqrt{L_FC_F}}\left(1-m_i\right) \quad \text{Eq. 3-36}$$

3.5 Control Mechanism of the Proposed System

The proposed converter integrates the PV module and battery cell. The modular version of the proposed system can be utilized for high power and high voltage application. The proposed system can be connected to the DC grid as a part of the distributed generation system or to the AC grid with an intermediate inverter. Therefore, the voltage of the DC bus would be regulated by either the other power electronics interfaces of distributed generation system or the intermediate inverter. The controller for the switch S_{pv} is responsible for achieving MPPT and battery charging profile.

3.5.1 MPPT Technique for PV Module

Different MPPT techniques are discussed in section 1.5. Among those techniques, P&O method is chosen for this work as P&O is straightforward and simple. However, P&O has the issue of oscillation near the MPP rather staying at MPP. Small step size reduces the oscillation near MPP. However, it increases the convergence time. Therefore, a different technique is applied to reduce the oscillation without compromising the convergence time.

The control variables of the proposed MICs are switching frequency and duty ratio. However, the response of the converter with the variation of switching frequency is significant in comparison of duty ratio. Therefore, the variable frequency control is chosen to track MPP of the proposed converter.

The controller inputs are the operating current (i_k) and voltage (v_k) of the respective PV panel where k is the current operating state. The controller calculates the captured power (P_k), the change of power (ΔP) and voltage (Δv) from previous state of the panel. It also stores the voltage (v_{k-1}) and power (P_{k-1}) value of the previous operating state (k-1). The sign of the perturbation of the switching frequency (Δf) of Eq. 3-40 depends on ΔP and Δv.

$$P_k = v_k \times i_k \qquad \text{Eq. 3-37}$$

$$\Delta P = P_k - P_{k-1} \qquad \text{Eq. 3-38}$$

$$\Delta v = v_k - v_{k-1} \qquad \text{Eq. 3-39}$$

$$f_k = f_{k-1} \pm \Delta f \qquad \text{Eq. 3-40}$$

The modified P&O method consists of five scenarios based on the sign of ΔP and Δv as shown in Table 3-2. When Δv and ΔP both are positive or negative, the operating point is at the left side of the MPP on V-P curve. On the other hand, when Δv and ΔP are opposite (one positive and the other is negative), the operating point is at the right side of the MPP on V-P curve. When the operating point is on left side of MPP, the frequency requires to be decreased to reach MPP. Therefore, Δf is negative. Δf is positive when the operating point is on the right side of the MPP to increase the switching frequency. In case of the fifth scenario, the controller would compare the change of power (ΔP) with a constant value (γ). If ΔP is less than γ, the operating point is very close to MPP irrespective of sign of Δv. Therefore, no need to change the control variable, that is switching frequency. That is why, Δf is zero. Δf remains zero until ΔP becomes larger than γ. Therefore, the oscillation of operating point around MPP is reduced. The flow chart of MPPT algorithm is shown in Figure 3-7.

Table 3-2 Possible scenarios of MPP tracking

	Change of Power (ΔP)	**Change of Voltage (Δv)**	**Change of Frequency (Δf)**	**Operating point location on V-P curve from MPP**
1	**Positive**	**Positive**	**Negative**	**Left side**
2	**Negative**	**Positive**	**Positive**	**Right side**
3	**Positive**	**Negative**	**Positive**	**Right side**
4	**Negative**	**Negative**	**Negative**	**Left side**
5	**Less than γ**	**-**	**zero**	**At MPP**

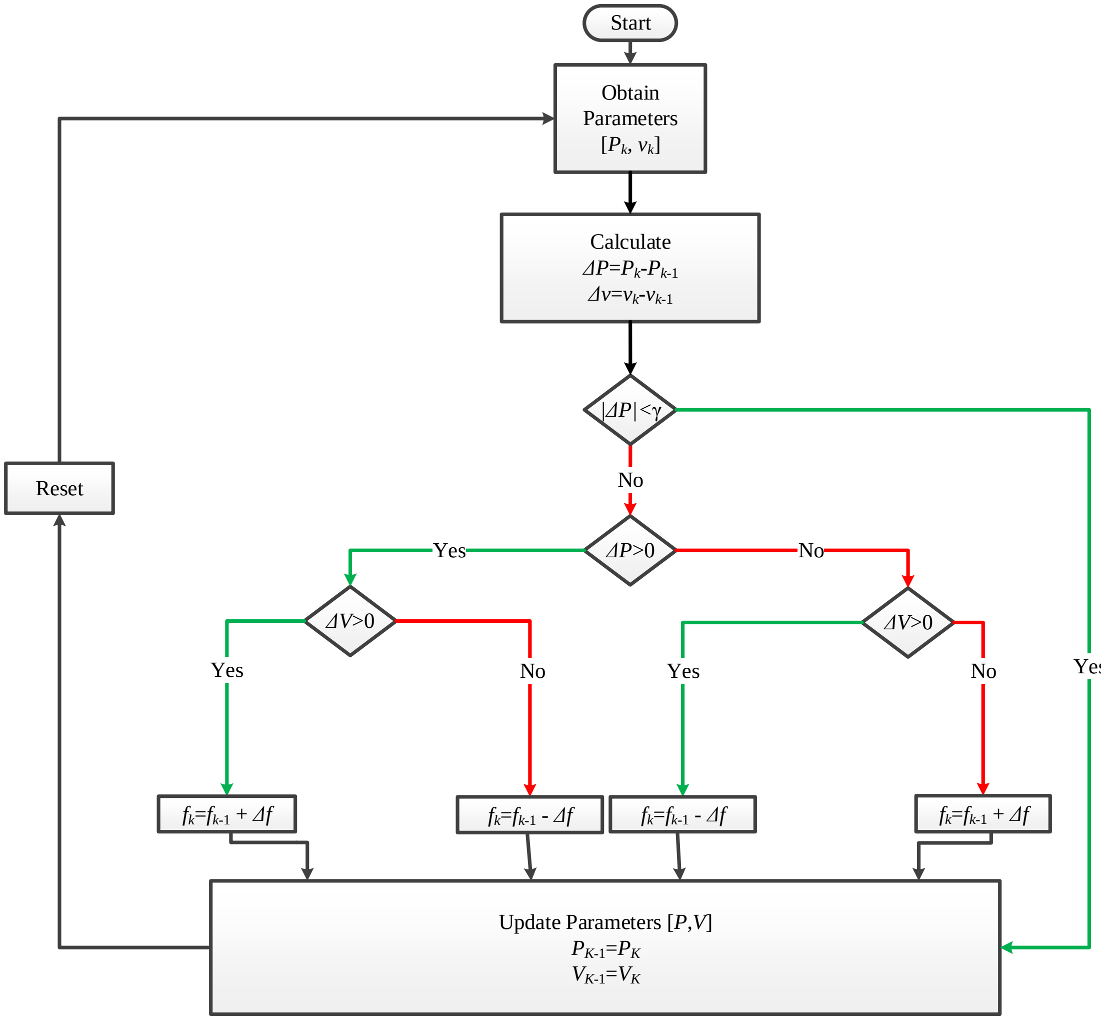

Figure 3-7 Flow chart of the modified P&O method for MPPT

European standard EN 50530 [94] defines the static and dynamic efficiency of the MPPT controller. MPPT efficiency is the ratio of the energy drawn by the converter (p_{cap}) within a defined measuring period (T_T) to the energy provided theoretically by the PV at MPP (p_{MPP}) as shown in Eq. 3-41.

$$\eta_{MPPT} = \frac{\int_0^{T_T} p_{cap}(t)dt}{\int_0^{T_T} p_{MPP}(t)dt} \qquad \text{Eq. 3-42}$$

3.5.2 Control Mechanism of the System

The logic flow chart of the control system of the proposed converter is shown in Figure 3-8. The PV source and the DC bus load are considered as the primary source and the primary load respectively. That means the power available from the PV source is first delivered to the DC bus. If the power obtained from the PV panel is more than the DC bus load demand, then the remaining power from the PV source will be used for charging the battery. If the power captured from the PV source is not sufficient to meet the DC bus demand, the battery will be in the discharging mode (if P_{bat}>0). If the PV and the battery cannot meet the DC bus demand, other sources will meet the demand. In the flow chart, the grey block shows the scenarios when power from the PV is not available, the blue block shows when power from the PV is available and the battery is in the discharging mode, and the yellow block shows when the PV is available and the battery is in the charging mode. Other than available power from the PV, the state of charge, SoC of the battery is used to decide the battery charging and discharging mode. If SoC reaches its minimum value, SoC^{min} battery should be in the charging mode. On the other hand, if SoC reaches its maximum value, SoC^{max} battery should be in the discharging mode. In case of battery SoC is in between the SoC^{max} and the SoC^{min}, the battery charging and discharging mode will be decided based on the available power from the battery and the load demand. By comparing the battery voltage with the battery float voltage, CV and CC mode can be decided. In general, the rated power of a single PV panel is limited to several hundred watts which mean the maximum current from a single panel is less than the allowable current of the battery pack in CC mode. Hence, the converter operates at MPP mode to supply available maximum current to the battery pack. As a result, the current limiter is not required in the battery charge controller. In CV mode, however, maintaining the float voltage to charge the battery is essential, and hence, in CV mode, the converter will operate in V_{bat_ref} mode to maintain the battery charging voltage. The DC bus voltage is maintained by the DC-bus voltage control unit. The DC-bus voltage control unit consists of other renewable energy sources and/or grid. For this work, the battery discharge circuit is also controlled by the DC-bus voltage control unit.

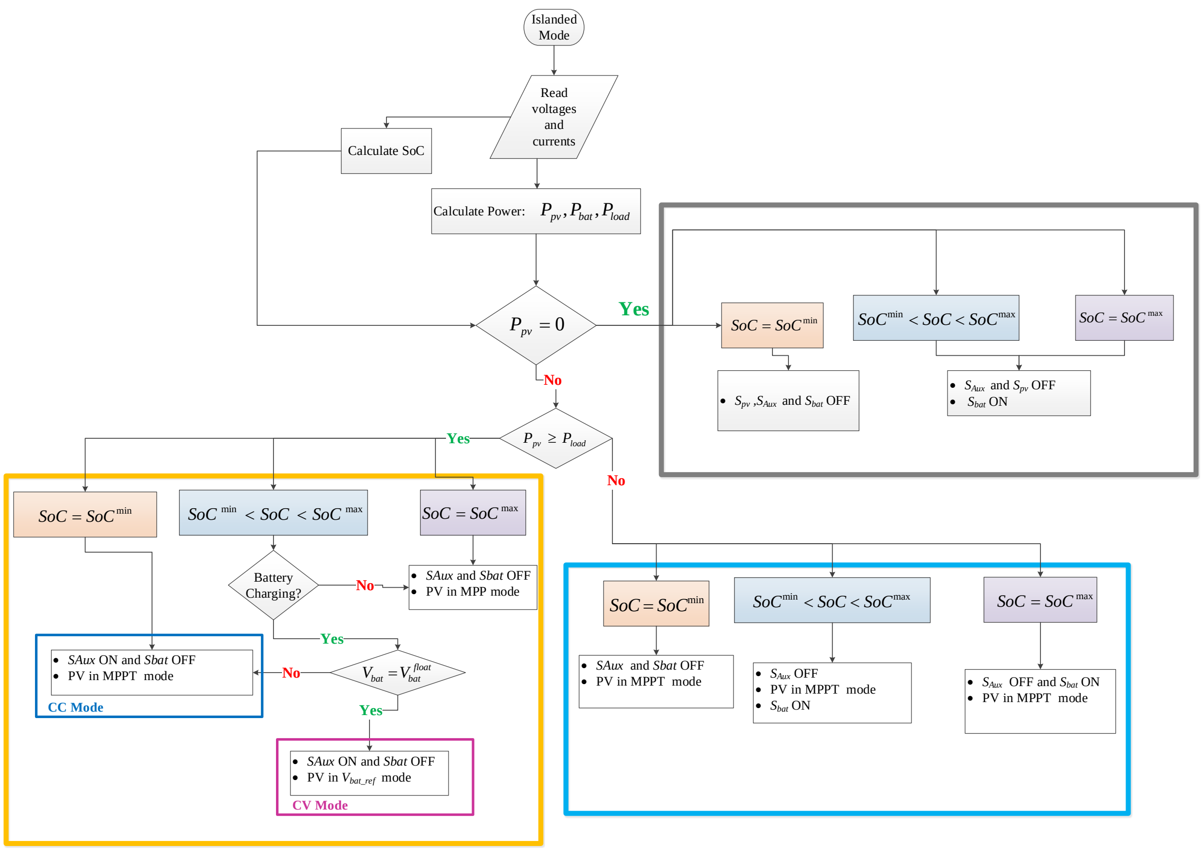

Figure 3-8 Control flow chart of the proposed converter control

The controllers for S_{pv}, S_{Aux} and S_{bat} are shown in Figure 3-9, with the following parameters: V_{pv}, I_{pv}, the SoC and the voltage, V_{bat} of the battery, and the voltage V_{DC}^{bus} of the DC bus. The MPPT uses the voltage, V_{pv} and current, I_{pv} of the PV to search the MPP. Other than tracking MPP, S_{pv} is controlled for regulating the battery voltage (in CV mode). $V_{ref\_ctrl}^{bat}$ is 1 when S_{pv} is in battery voltage control mode. S_{Aux} is on when power from PV is higher than the load demand and battery is in charging mode. S_{bat_ctrl} is 1 to activate the discharging mode. S_{bat} is controlled by the DC bus voltage controller. S_1, S_2…S_n are the switches of the discharge circuit of the other module of the MIC and the switches of the converter of the other renewable resources connected with the system for the voltage regulation.

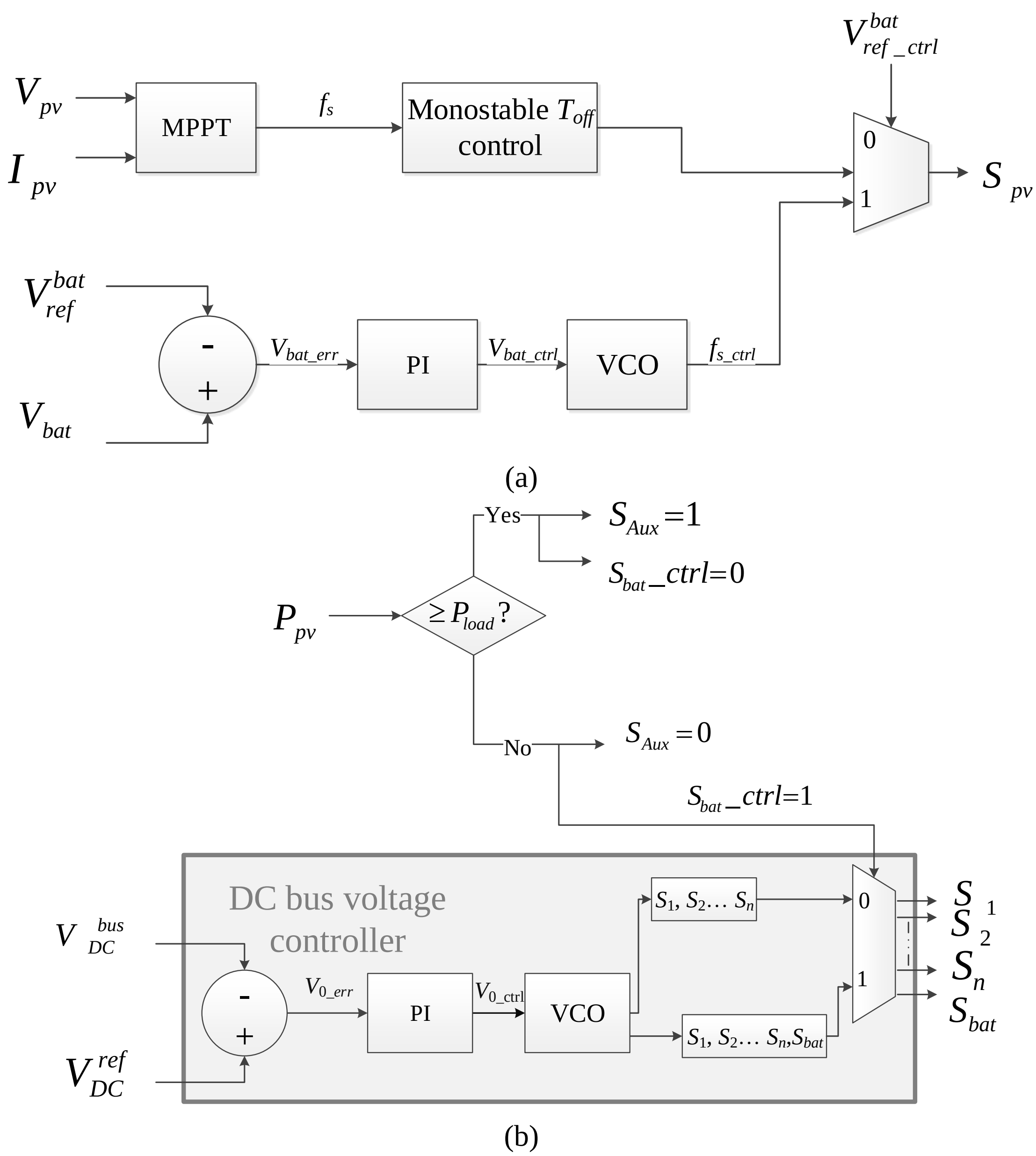

Figure 3-9 Control diagram of the proposed converter

3.6 Performance Analysis of the Proposed Converter

To evaluate the performance of the proposed converter, the converter is designed and then first verified with the simulation work in PSIM. A proof-of-concept prototype is designed and built for hardware testing. The design procedure, the list of designed and chosen components, simulation results and the experimental results are presented in the following section.

3.6.1 Design Procedure of the Proposed Converter

The converter is designed for 48V load voltage and 48V battery voltage. The battery charging is a slow process with respect to converter switching frequency. Therefore, the battery can be modeled as a resistor, R_{bat} from its DC equivalent resistor. It should be mentioned that R_{bat} has no relation to the battery internal resistance.

Assume a battery pack consists of p parallel connected batteries and s series connected cells in each battery. The battery voltage varies from 3sV to 4.2sV and the current varies from pCA to 0.05pCA where C is the discharge capacity of the battery (C is the maximum current the battery can supply for 1hr). Therefore, R_{bat} varies from $\frac{3s}{pC}$ to $\frac{4.2s}{0.05pC}$ throughout the charging profile. The charging profile is shown in section 1.2 (Figure 1-11) for p=1, s=1 and C=1. The nominal battery resistance, $R_{n\text{-}bat}$ is the ratio of the maximum charging current ($I_{M\text{-}chrg}$=pC) and the maximum charging voltage ($V_{M\text{-}chrg}$=4.2s). R_{bat} varies from 0.714 $R_{n\text{-}bat}$ to $R_{n\text{-}bat}$ for CC mode and from $R_{n\text{-}bat}$ to 20 $R_{n\text{-}bat}$ for CV mode. Therefore, variation happens mostly in CV mode.

The turns ratio of the transformer, N is selected to be 1, as the output voltage of the Cuk converter (load side) and flyback converter (battery side) of the proposed converter is equal

Eq. 3-22. Therefore, Eq. 3-20 and Eq. 3-21 become identical for this design. The battery voltage different from the load voltage can be achieved by varying *N* value. Based on Eq. 3-21, Eq. 3-23 and Eq. 3-24, the design equation Eq. 3-43 is derived. Other two design equations Eq. 3-44 and Eq. 3-45 are also derived from Eq. 3-1 and Eq. 3-2. The experimental circuit is designed for 175W and input voltage is 35V.

The characteristics impedance, Z is another important factor for designing the quasi-resonant converter. The peak resonant capacitor voltage which also represents the maximum voltage stress of the switch depends on characteristics impedance (as shown in Eq. 3-46. Therefore, Z should be minimized to reduce v_{ds_max}. On the other hand, Z should be maximized to increase load range at zero voltage switching. Hence, the key design parameter is the characteristic impedance, Z [95]. The optimum characteristic impedance is expressed in Eq. 3-47.

As $Z_{optimum}$ (as given by Eq. 3-47 depends on the minimum voltage gain and maximum load, therefore for the design the load is taken as 75W and the design switching frequency is chosen 350 kHz. α is taken as $3\pi/2$. Using Eq. 3-43 and Eq. 3-47, the resonant frequency, f_r and $Z_{optimum}$ is calculated. The resonant tank components L_r and C_r are found to be 4.3µH and 8.6nF respectively according to Eq. 3-44 and Eq. 3-45.

$$\frac{f_s}{f_r} = \frac{2\pi}{\left[\alpha + \frac{\varphi}{2} + \frac{1}{\varphi}(1-\cos\alpha)\right](1+M_v)} \qquad \text{Eq. 3-43}$$

$$L_r = \frac{Z_{optimum}}{2\pi f_r} \qquad \text{Eq. 3-44}$$

$$C_r = \frac{1}{2\pi f_r Z_{optimum}} \qquad \text{Eq. 3-45}$$

$$V_{cr\_\max} = V_{ds\_\max} = (V_{in} + V_0) + Z\ I_M \qquad \text{Eq. 3-46}$$

$$Z_{optimum} = \frac{R_{0\_Max}}{M_{v\_Min}} \quad \text{Eq. 3-47}$$

The magnetizing inductance, L_m of the transformer T_{in} is calculated by Eq. 3-48, where d is the duty ratio of the switch S_{pv} and β is the ripple factor in full load and minimum input voltage condition. For continuous conduction mode operation (CCM), β varies 0.25-0.5 [96]. β and d are chosen 0.4 and 0.7 respectively for this design. The leakage inductance adds up with the resonant inductor and takes a part in resonance. Therefore, while choosing transformer and resonant inductor, leakage inductance needs to be in consideration. The storage capacitor C_{pv} is designed from Eq. 3-49, where λ represents the percentage of voltage ripple of the voltage across C_{pv} with respect to output voltage V_0. As the storage capacitor is at the intermediate stage of the power conversion, the ripple factor is taken as 20%. The output load, R_0 is 30 Ω. The output filter inductor L_f is calculated for 10% ripple factor. The output current ripple factor is γ as presented in Eq. 3-50. From Eq. 3-48, Eq. 3-49, and Eq. 3-50, L_m, C and L_f are found 23uH, 333.4nF and 23uH respectively.

$$L_m = \frac{\left(V_{bat} \times d\right)^2}{2P_{in} f_s \beta} \quad \text{Eq. 3-48}$$

$$C_{pv} = \frac{d}{f_s R_0 \lambda} \quad \text{Eq. 3-49}$$

$$L_f = \frac{\left(1-d\right) R_L}{f_s d \gamma} \quad \text{Eq. 3-50}$$

3.6.2 Simulation Results

In order to investigate the performance of the proposed converter, the proposed converter is first simulated in PSIM. The simulation prototype is designed for 35V, 315W commercial PV panel (OPT315-72-4-100) and 48V, 13Ah commercial battery pack (HE-4813) and 48V

DC load. The components used for the simulation work are presented in Table 3-3. The battery equivalent resistance for CC mode varies from 11Ω to 15Ω and in CV mode varies from 15Ω to 300Ω. The equivalent resistance is calculated using the procedure presented in section 3.5.

Table 3-3 Circuit parameters of the designed converter for simulation work

Circuit Designator	***Component Value***
PV	OPT315-72-4-100 (36.5V, 315W)
Battery	HE-4813 (48V, 13 Ah)
f_s	150kHz-300kHz
C_{r_pv}	5.6 nF
L_{r_bat}	1.8 µH
C_{bat1}	47 µF
C	250 nF
L_{mag}	47 µH
L_f	650 µH
C_f	82 µF

The SUNIVA 315W PV panel (OPT315-72-4-100) is chosen for the simulation work. The selected PV panel is first modeled in PSIM using the parameters of the PV panel shown in Table 3-4. The listed parameters are obtained from the panel data sheet. Some parameters such as the band gap energy, ideality factor, and shunt resistance depend on cell type. The selected PV panel is modeled in PSIM as shown in Figure 3-10. The physical model of PV panel in PSIM is capable of functioning as a real PV panel. That means this model can recreate the V-I and V-P curve of the PV panel with the change of light intensity. The simulation work is performed at different light intensity (500W/m^2, 200W/m^2 and 1000W/m^2) for both CC and CV mode.

Table 3-4 Characteristics of the PV panel from SUNIVA (OPT315-72-4-100)

PV Panel Characteristic	*Component Value*
Power Classification (P_{max})	315 W
Voltage at Max. Power Point (V_{mp})	36.50 V
Current at Max. Power Point (I_{mp})	8.62 A
Open Circuit Voltage (V_{oc})	45.90 V
Short Circuit Current (I_{sc})	9.10 A
The electrical data apply to standard test conditions (STC): Irradiance of 1000 W/m2 with AM 1.5 spectra at 25°C.	

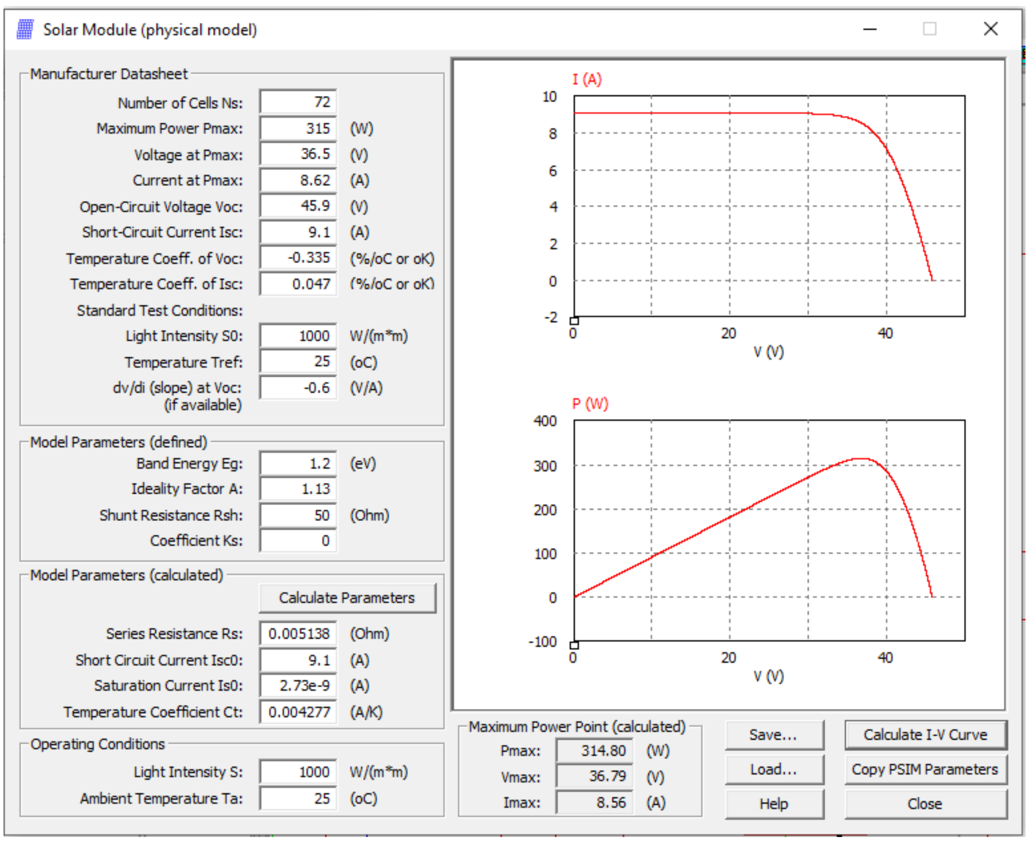

Figure 3-10 PSIM physical model of the PV panel

Figure 3-11 shows the MPP tracking of the proposed converter in different battery charging mode. Figure 3-11(a) shows the variation of three different light intensity: 500W/m^2, 200W/m^2 and 1000W/m^2. At different light intensity, the available power (blue) and the actual captured power (red) by the converter is shown in Figure 3-11(b) and Figure 3-11(c) for CV and CC mode respectively. For all cases, the MPPT efficiency is over 99%.

Figure 3-12 and Figure 3-13 show the current through and the voltage across the switch S_{pv} at different light intensity for CV and CC mode respectively. For all the six conditions, ZVS turn on and turn off are achieved. To track MPP, frequency varies from 150 kHz to 300 kHz. The switching off time should be kept within a range to maintain soft-switching of ZVS QRC. Therefore, duty ratio requires to be changed from 65% to 75% to maintain constant switching off time with the variation of the switching frequency.

Figure 3-14 shows the battery charging current in CV and CC mode. The battery charging current range varies 0.4A to 0.65A for the variation of the light intensity from 200W/m^2 to 1000W/m^2. However, the battery charging current varies from 3.5A to 5A in CC mode with the same light intensity variation. Therefore, the current limiter is not required for the battery charging as the CC mode charging current doesn't exit the safe charging current limit of the battery while achieving MPP.

The efficiency of the converter is shown in Figure 3-15 for CV and CC mode at different light intensity. The red waveform represents the actual captured power from PV panel which is the same as the red waveform of the Figure 3-11. The orange waveform shows the total output power of the converter which is the sum of the load power and the battery charging power. The efficiency of the converter is over 95% for all cases.

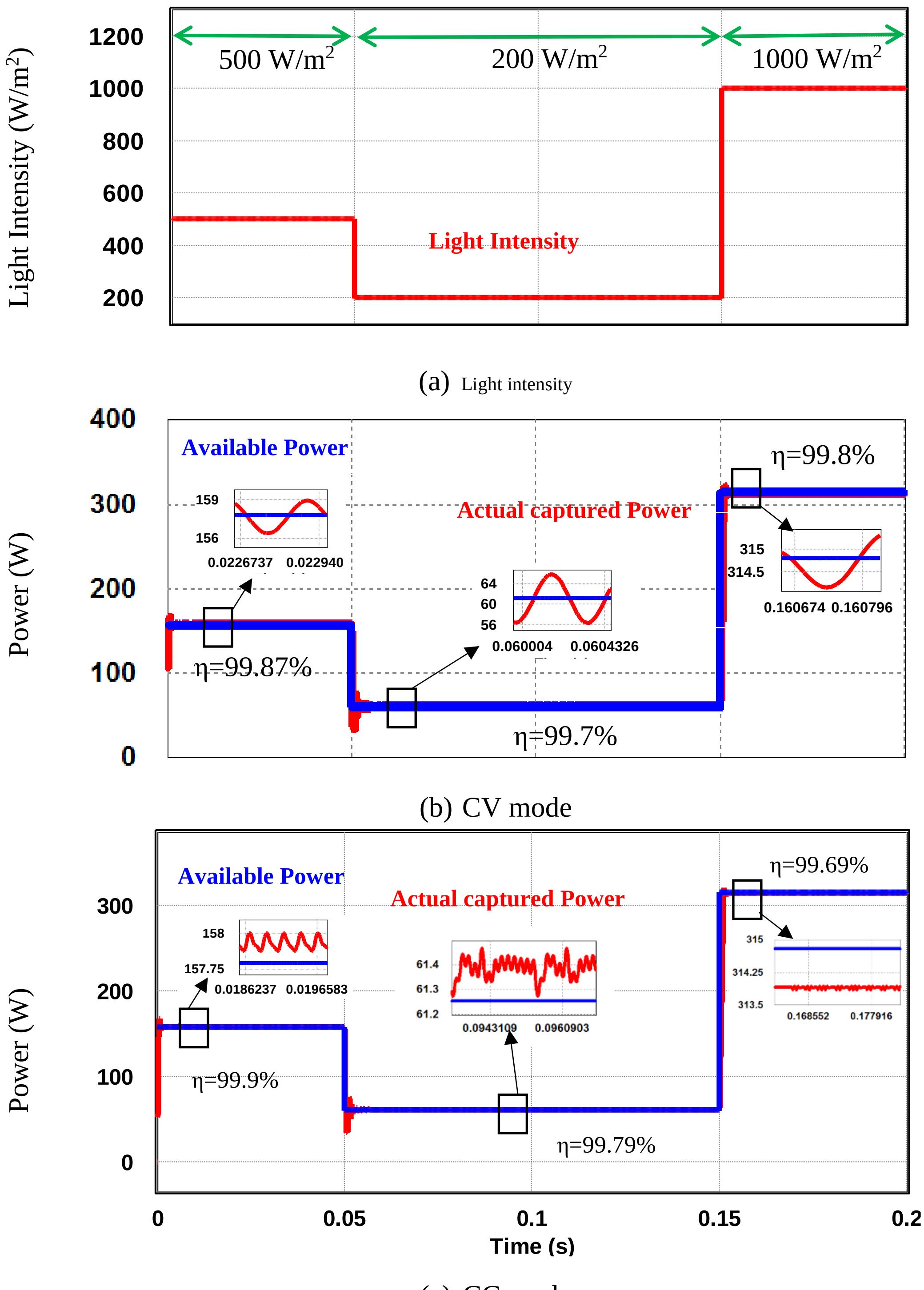

(c) CC mode

Figure 3-11 MPP tracking of the proposed converter in CV and CC mode at different light intensity

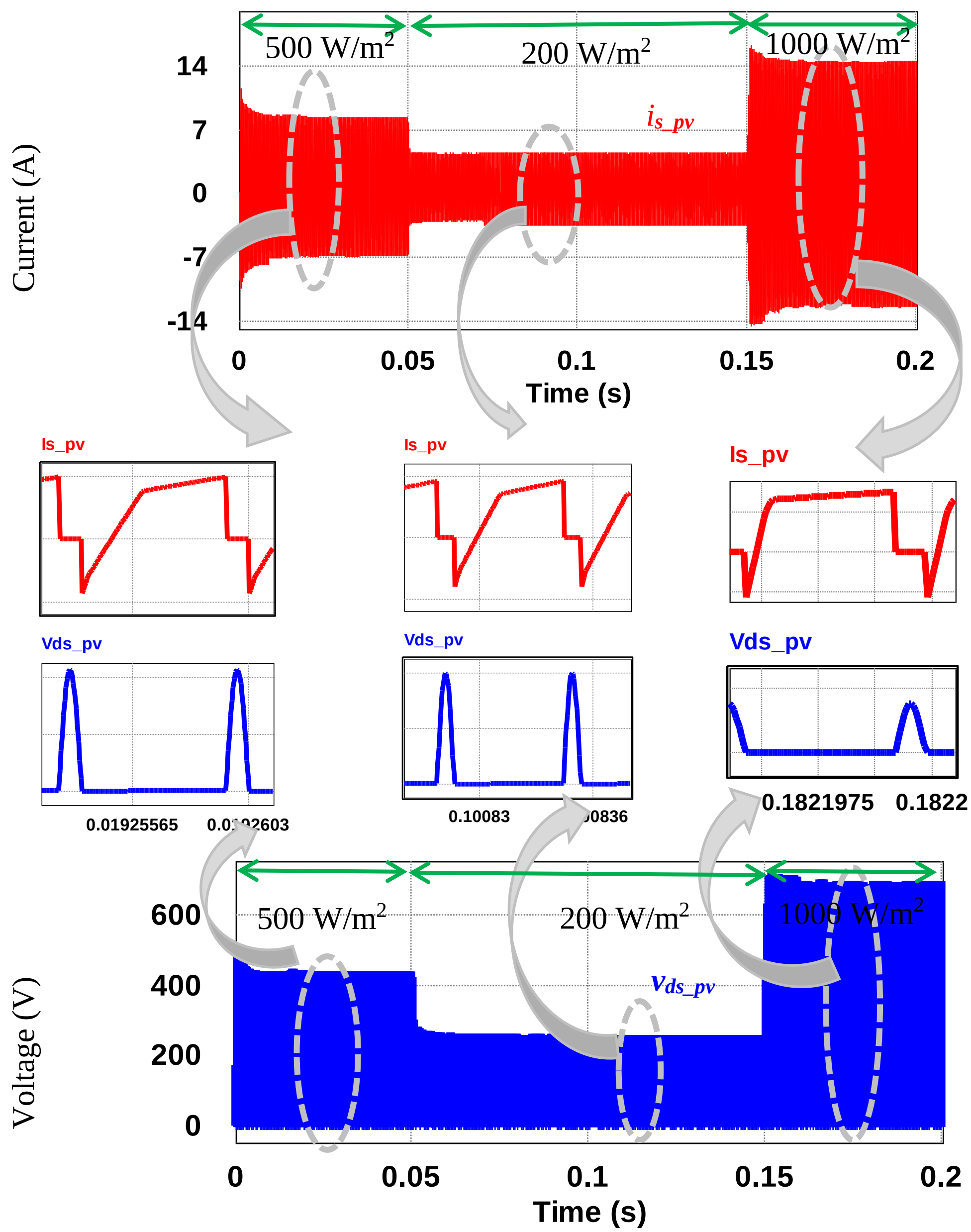

Figure 3-12 Soft-switching performance of the proposed converter in CV mode at different light intensity

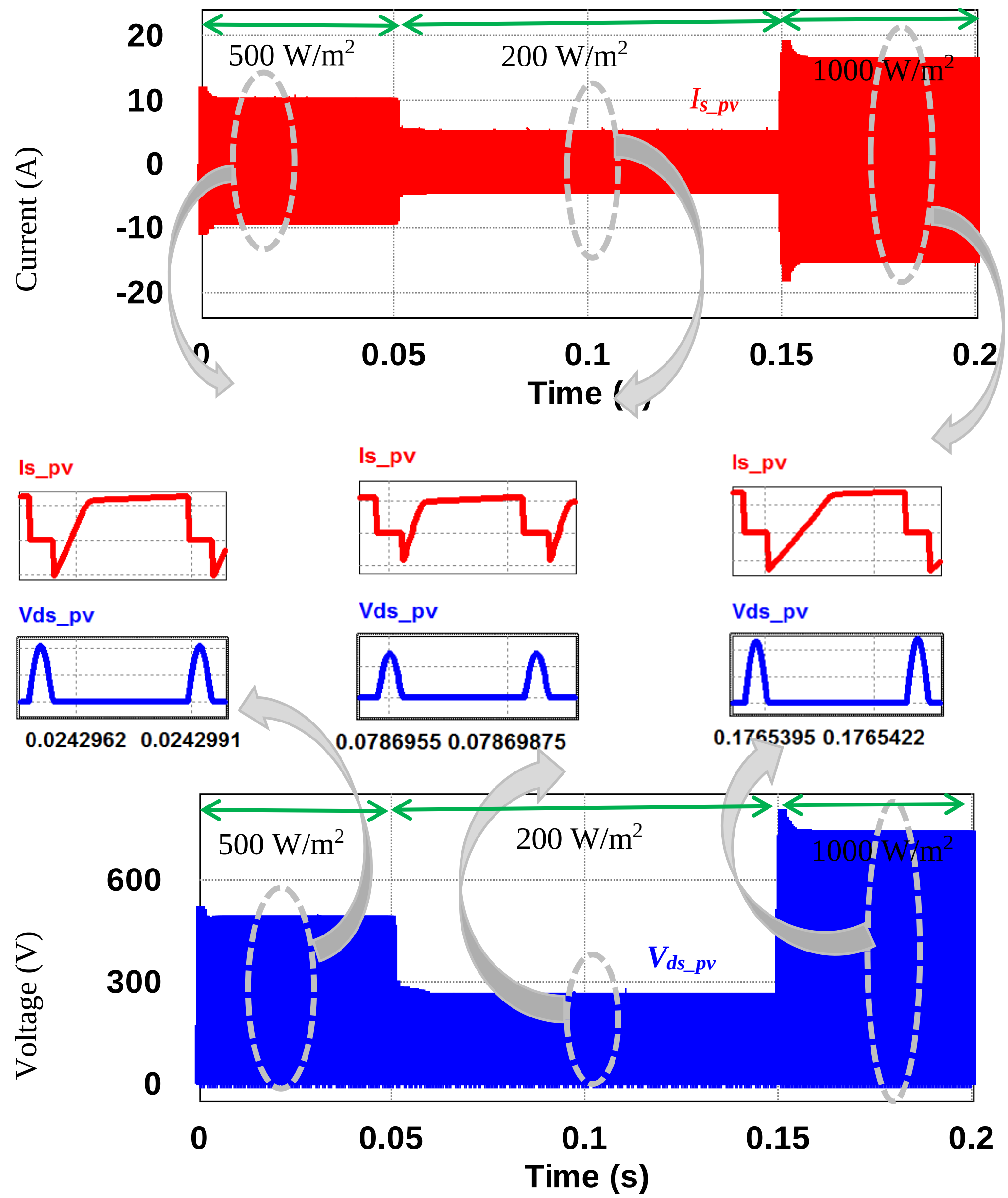

Figure 3-13 Soft-switching performance of the proposed converter in CC mode at different light intensity

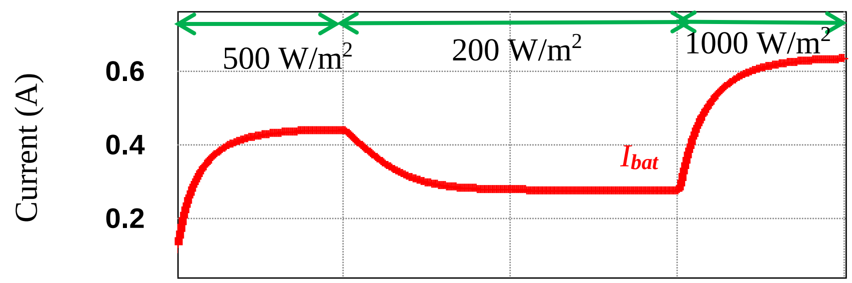

(a) CV mode

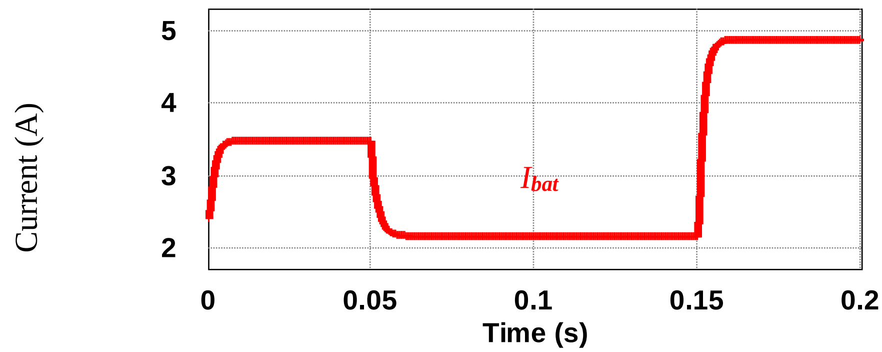

(b) CC mode

Figure 3-14 Battery charging current in CV and CV mode at different light intensity

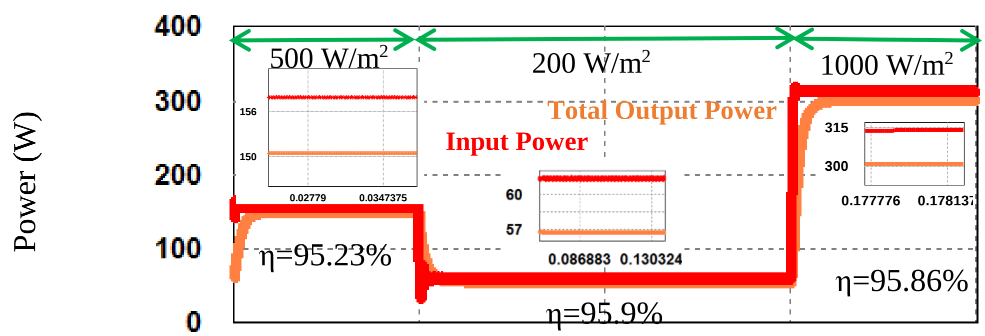

(a) CV mode

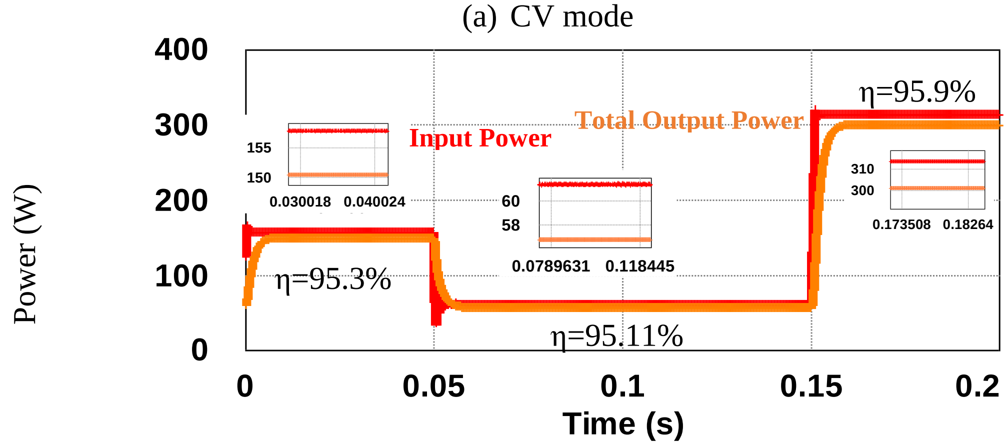

(b) CC mode

Figure 3-15 Efficiency of the converter in CV and CC mode at different light intensity

3.6.3 Experimental Results

The Experimental prototype is designed for 35V, 175W PV panel and 48V, 13Ah battery pack and 48V DC load. The components used for the simulation and the experimental work are presented in Table 3-5. The experimental prototype is shown in Figure 3-16.

The SHARP 175W PV panel (NT-175U1) is chosen for the experimental work. The parameters of the selected PV panel are shown in Table 3-6. Experimental exercise is performed for 1000W/m^2 and 800W/m^2 light intensity. For experimental work, E4360A (1200W) PV emulator from *Keysight* is used. Two units of E4360A are paralleled to replicate the NT-175U1 single PV panel as each unit (300V and 2.5A) of the two units is capable to supply maximum 2.5A. STP24N60DM2-EP (600V) is selected as switching device. The maximum voltage across the switch is around 300V from the theorical calculation and simulation. As the prototype is to prove the concept, the components are selected with higher rating rather optimized one.

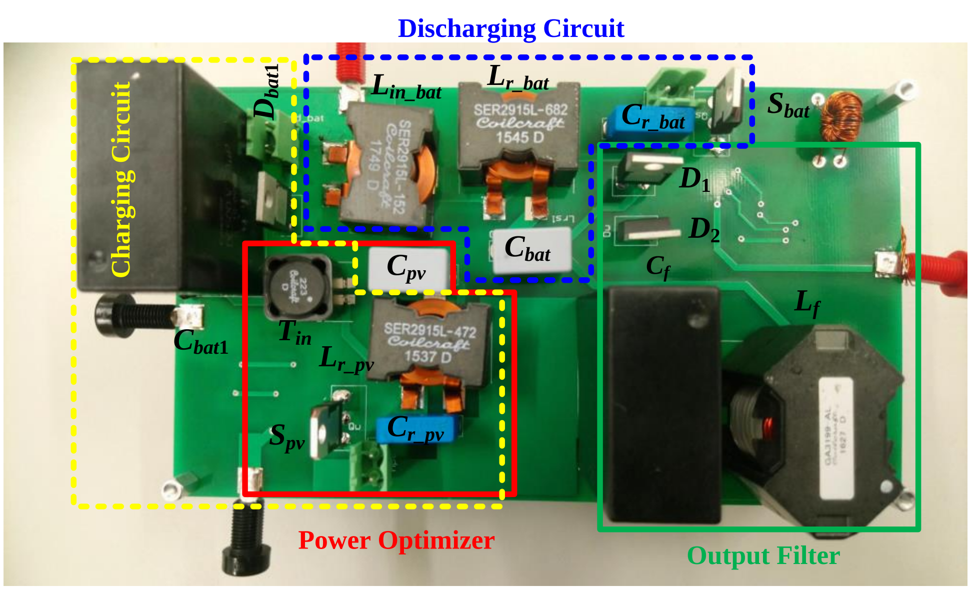

Figure 3-16 Experimental prototype of the proposed converter

Table 3-5Circuit parameters of the designed converter for experimental work

Components	***Part number***	***Component Value***
PV	NT-175U1 (SHARP)	35.4V, 175W
Battery	HE-4813	48V, 13 Ah
f_s		200-350kHz
L_{r_pv}, L_{r_bat}	SER2915H	4.7µH, 6.8µH
C_{r_pv}, C_{r_bat}	R75TI1560AA30J	9.4nF, 8nF
L_{mag}	MSD1048-223D	22µH
C_{pv}, C_{bat}	MKP383430200JPI2T0-ND	150nF
S_{pv}, S_{bat}	STP24N60DM2-EP	600V, 18A
D_1, D_2, D_{bat}	MUR1560	600V, 15A
L_f	GA3199-AL	650µH
C_f	EZP-E1D256MTA	25µF
C_{bat1}	EZP-E1D256MTA	25µF

Table 3-6 Characteristics of the PV panel from SHARP (NT-175U1)

PV Panel Characteristic	***Component Value***
Power Classification (P_{max})	175 W
Voltage at Max. Power Point (V_{mp})	35.40 V
Current at Max. Power Point (I_{mp})	4.95 A
Open Circuit Voltage (V_{oc})	44.4 V
Short Circuit Current (I_{sc})	5.4 A
The electrical data apply to standard test conditions (STC): Irradiance of 1000 W/m2 with AM 1.5 spectra at 25°C.	

Figure 3-17(a) shows the PV emulator output for both channels in CV mode at 1000W/m^2. The output voltage is 36V and output current is 2.4A for both channels. Therefore, each channel is supplying 86.3W. As a result, a total of 173W power is extracted by the proposed converter from the PV emulator. Figure 3-17(b) shows the operating point (blue squares) on the panel characteristic curve. The operating point is at the MPP. The MPP tracking efficiency of the proposed converter is 99.93% (blue circled).

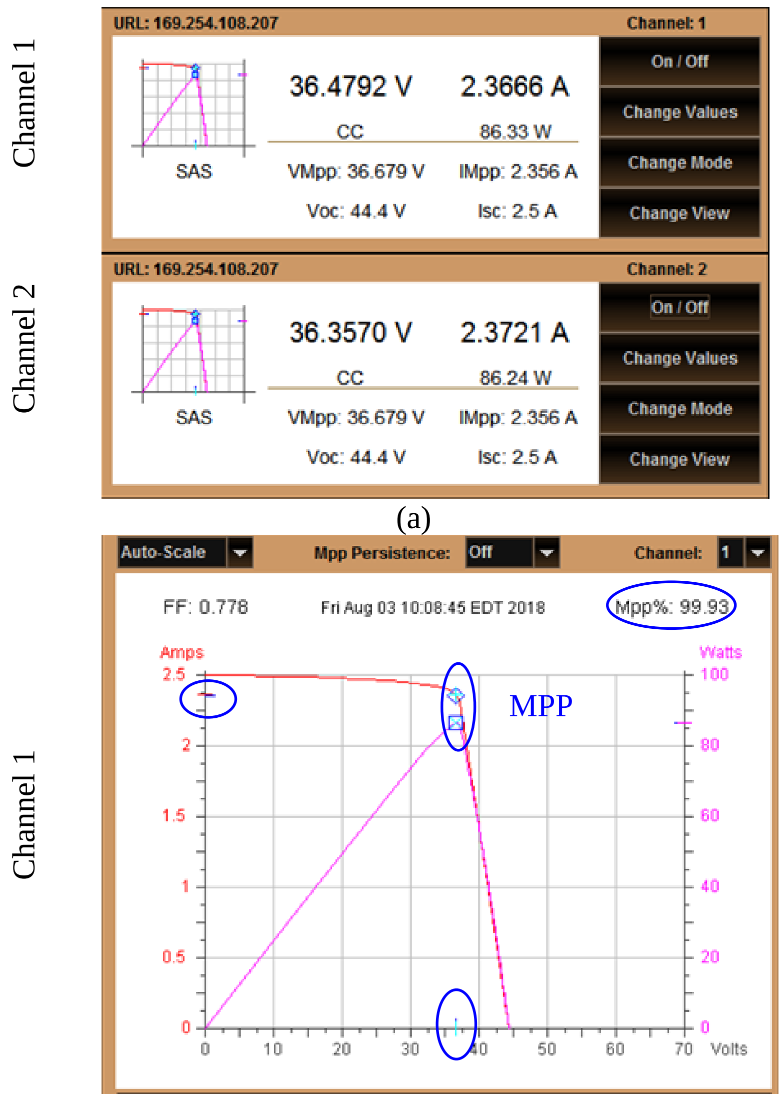

(b)

Figure 3-17 PV emulator output at 1000W/m^2 in CV mode (a) output voltage, current and power of both channels (b)MPP tracking and MPP efficiency of channel 1

Figure 3-18 shows the PV emulator output for both channels in CV mode at 800W/m^2. With the decrease of light intensity from 1000W/m^2 to 800W/m^2, the output current of each channel changes from 2.4A to 1.9A. Therefore, the power from each channel decreases from

86.3W to 71.8W and the total power decreases from 173W to 143.6W. The proposed converter is tracked the MPP with an efficiency of 99.9% as shown in Figure 3-18 (b).

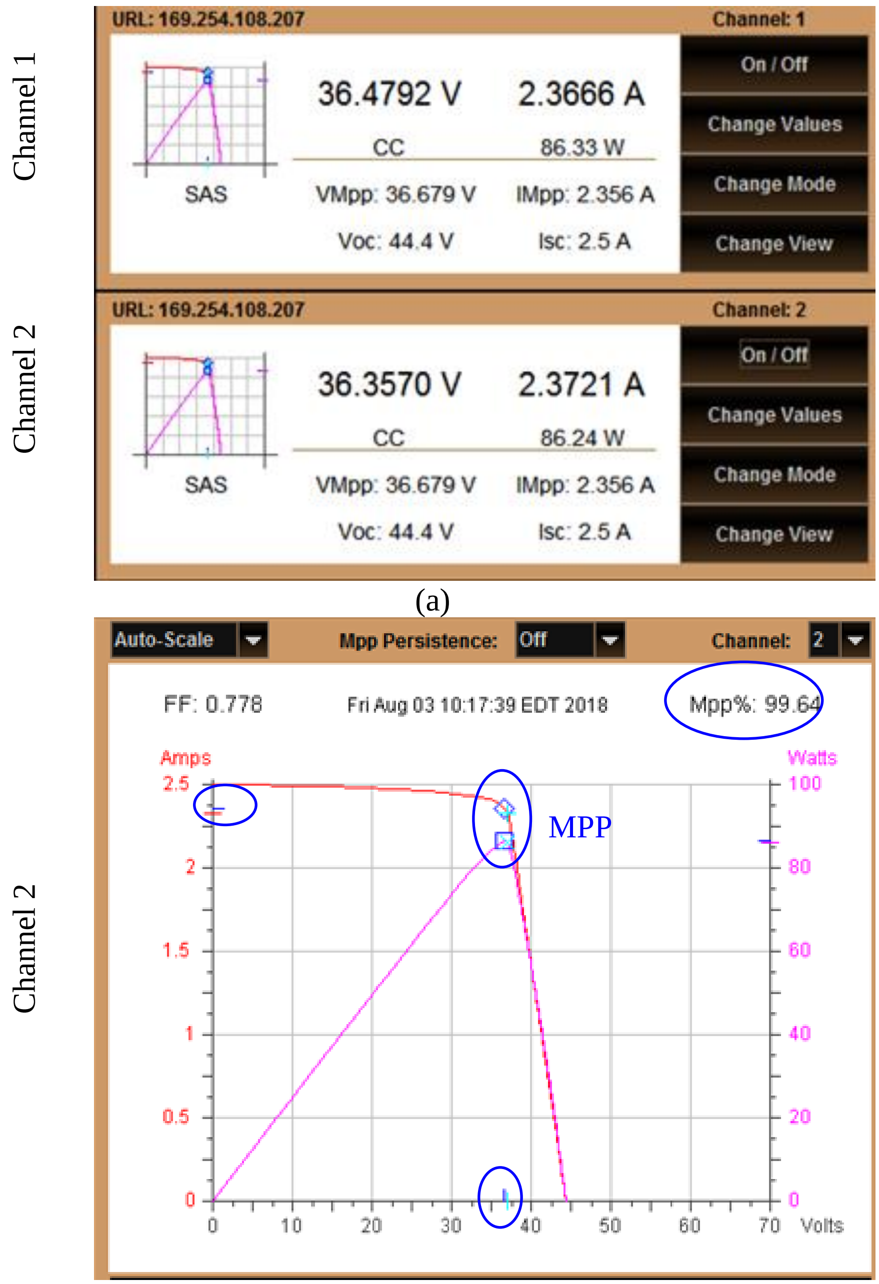

(b)

Figure 3-18 PV emulator output at 800W/m^2 light intensity in CV mode (a) output voltage, current and power of both channels (b) MPP tracking and MPP efficiency of channel 2

Figure 3-19 and Figure 3-20 show the PV emulator output and the converter MPP tracking at 1000W/m^2 and 800W/m^2 light intensity in CC mode respectively. From Figure 3-17 to Figure

3-20 confirm that the proposed converter is capable of tracking MPP irrespective of CV and CC mode at different light intensity with a very high efficiency (over 99.5%).

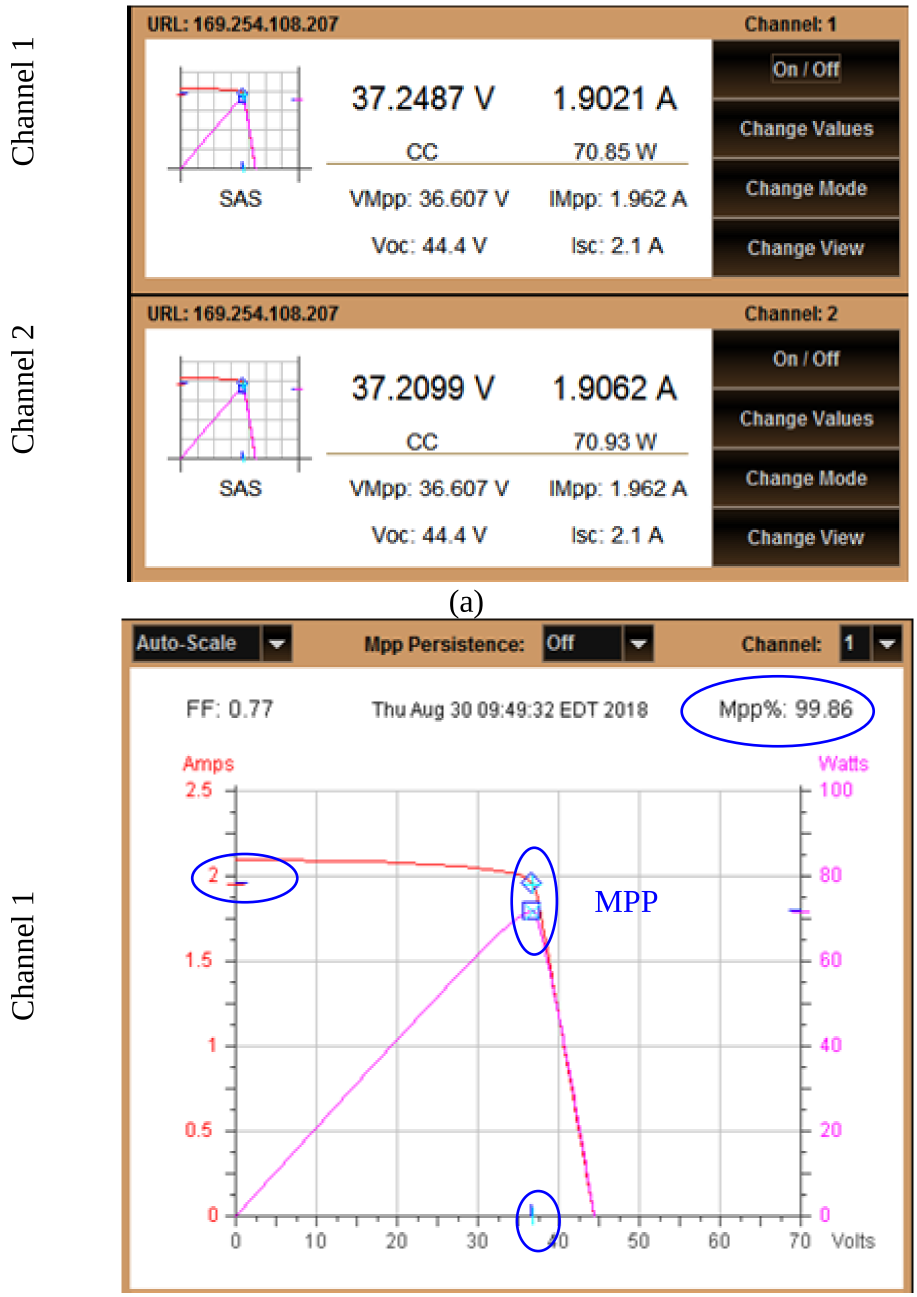

(b)

Figure 3-19 PV emulator output at 1000W/m^2 light intensity in CC mode (a) output voltage, current and power of both channels (b) MPP tracking and MPP efficiency of channel 1

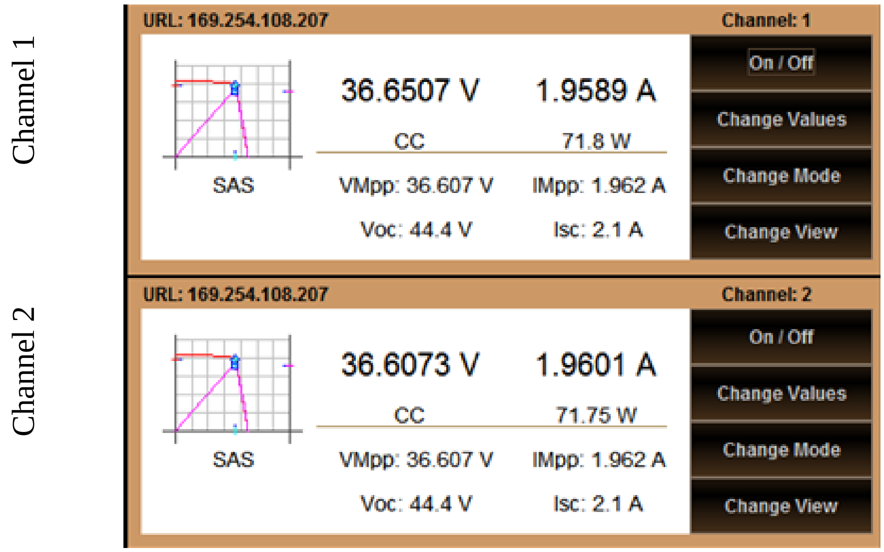

(a)

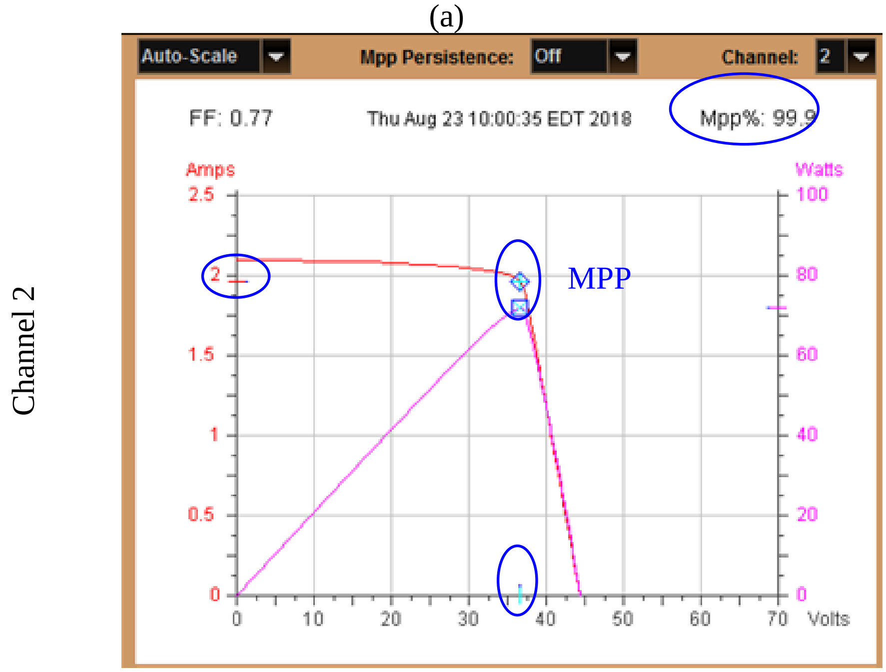

(b)

Figure 3-20 PV emulator output at 800W/m^2 light intensity in CC mode (a) output voltage, current and power of both channels (b) MPP tracking and MPP efficiency of channel 2

Figure 3-21 shows the current through and the voltage across the switch S_{pv} at 1000W/m^2 light intensity in CV and CC mode. The switching frequency and duty ratio are 250 kHz-270 kHz and 65%-70%. For both cases, the switch turns on and off under ZVS condition. During turn off, a overlap between the switch voltage and current is observed. However, the overlap time is too small. Therefore, the turn off loss is negligible. The voltage stress across the switch is around 300V. The CC mode switch current stress (9.5A) is little bit higher than that of CV mode (8.8A).

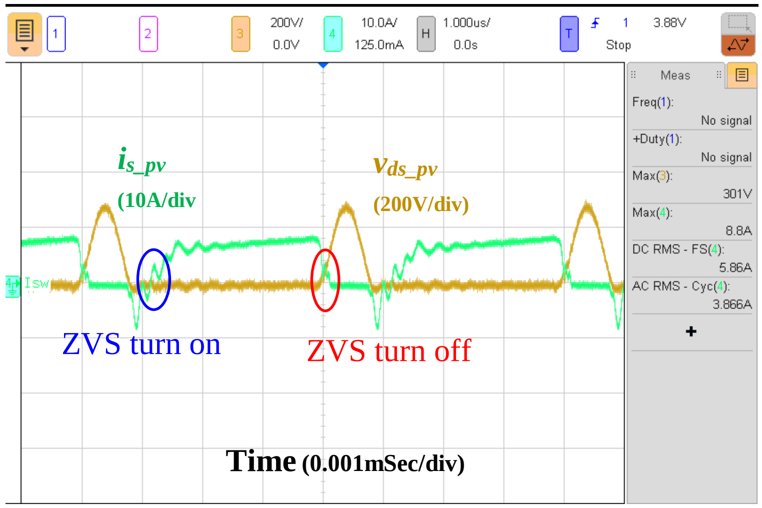

(a) CV mode

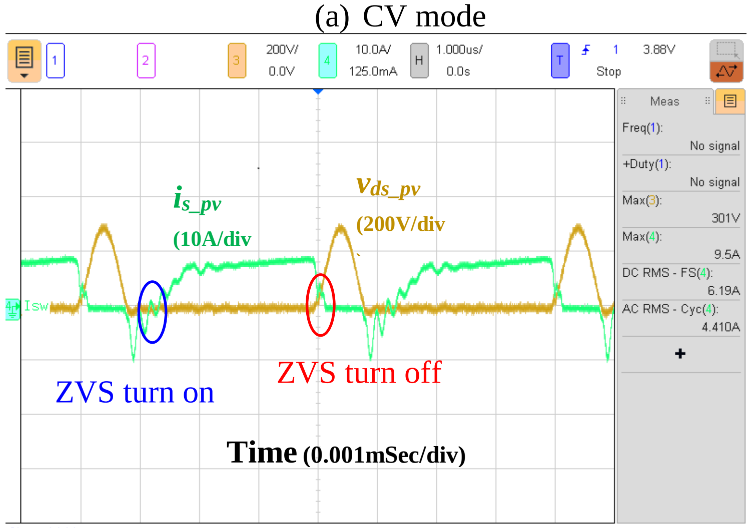

(b) CC mode

Figure 3-21 Soft Switching and voltage stress across the switch at 1000W/m^2 light intensity

Figure 3-22 shows the current through and the voltage across the switch S_{pv} at 800W/m^2 light intensity in CV and CC mode. With the change of light intensity, the voltage stress and current stress are reduced compared to 1000W/m^2 as power is reduced. The voltage stress is around 250V. The current stress is 7.4A in CV mode and 8.4A in CC mode. Same as the 1000W/m^2, the current through the switch is higher in CC mode compared to CV mode. Obvious ZVS turn on and a negligible turn off loss are observed.

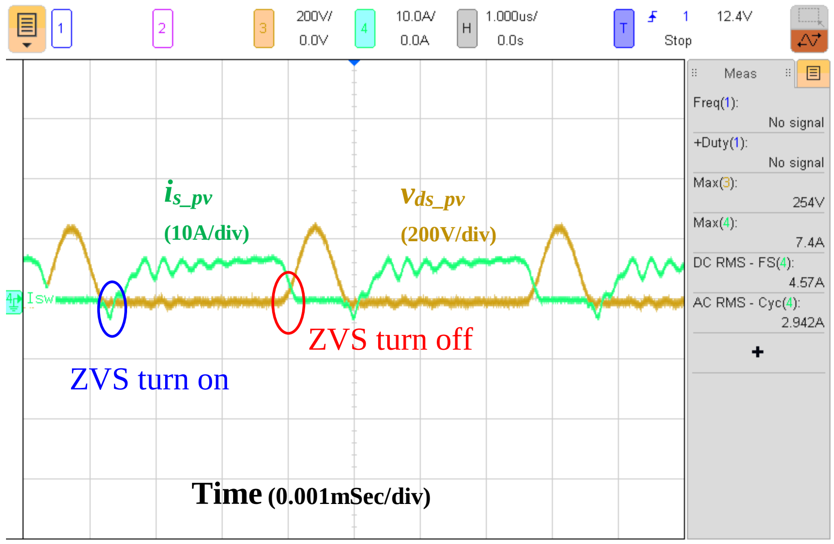

(a) CV mode

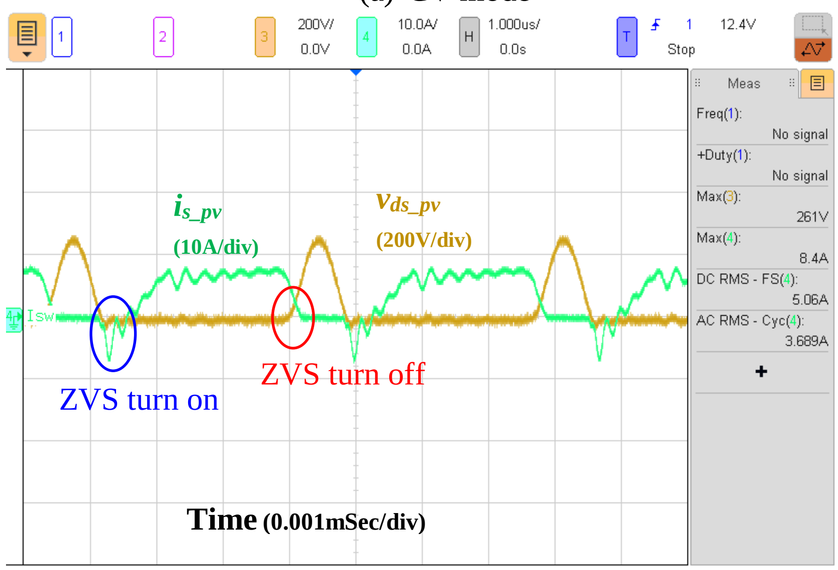

(c) CC mode

Figure 3-22 Soft Switching and voltage stress across the switch at 800W/m^2 light intensity

The output load voltage and current, and the battery charging voltage and current is shown in Figure 3-23 and Figure 3-24 at 1000W/m^2 and 800W/m^2 light intensity respectively in CV and CC mode. The output side voltage, V_0 varies from 47V to 51V. The battery charging current in CV mode varies from 0.7A to 1A and in CC mode varies from 2A to 2.3A. Therefore, the battery charging current is higher in CC mode than that of in CV mode. The battery voltage in CC mode is at 36V which is much lower than the float voltage and in CV mode the battery voltage is equal to the battery float voltage 48V.

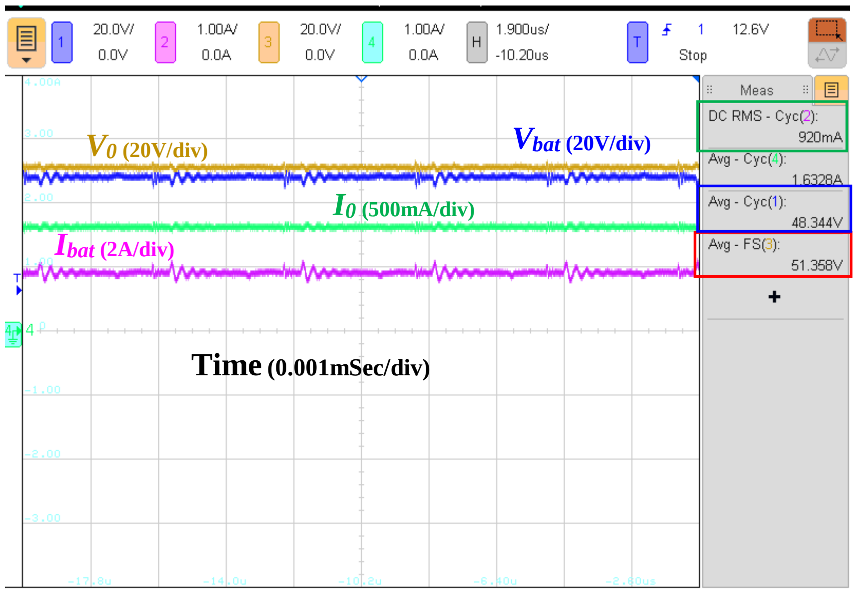

(a) CV mode

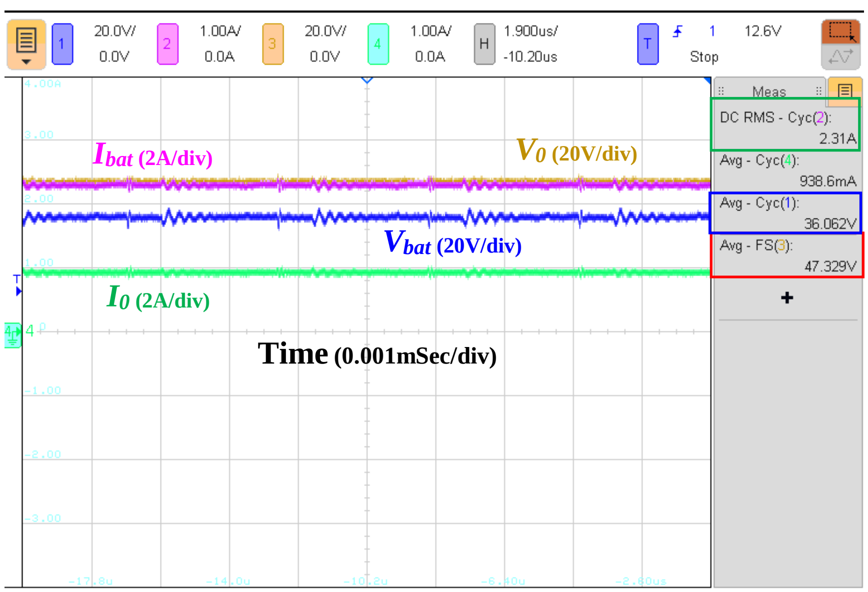

(b) CC mode

Figure 3-23 Voltage and current of output and battery charging at 1000W/m^2 light intensity

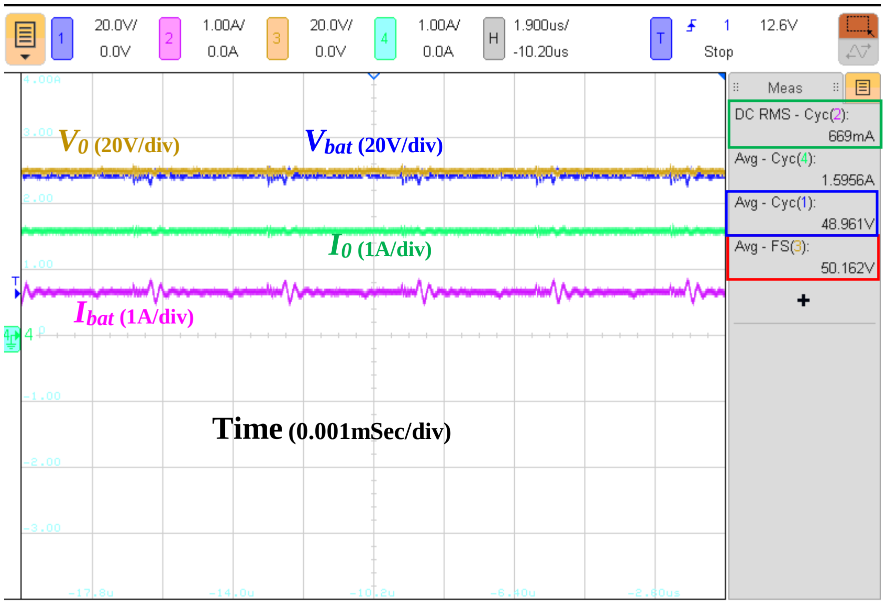

(a) CV mode

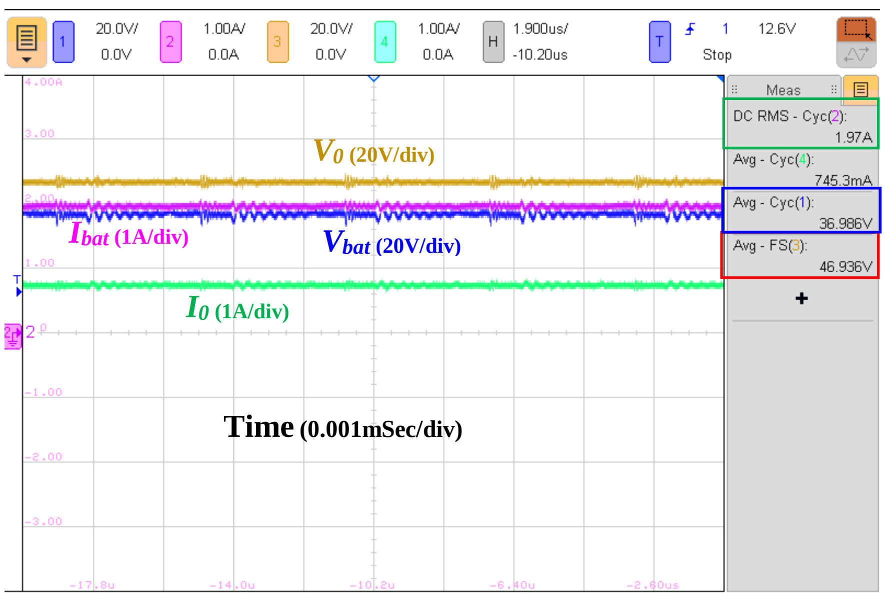

(b) CC mode

Figure 3-24 Voltage and current of output and battery charging at 800W/m^2 light intensity

The switching waveforms of simultaneous operation (from PV and battery to load) are shown in Figure 3-25. Both switches S_{pv} and S_{bat} achieved soft switching. Figure 3-26 shows the primary and secondary side currents (purple) of the input transformer.

The battery voltage varies from 36V to 52V during the discharging mode. Therefore, the battery discharging circuit requires to step up, pass through and step down the voltage. The step up, pass through and step down operation of the battery discharge circuit is shown in Figure 3-27, Figure 3-28 and Figure 3-29 respectively. The converter is controlled by varying the switching frequency (200kHz to 275kHz) in this mode of operation. For all conditions, the switch turns on and turns off under ZVS condition. The switch voltage stress is below 300V and current stress is below 5A.

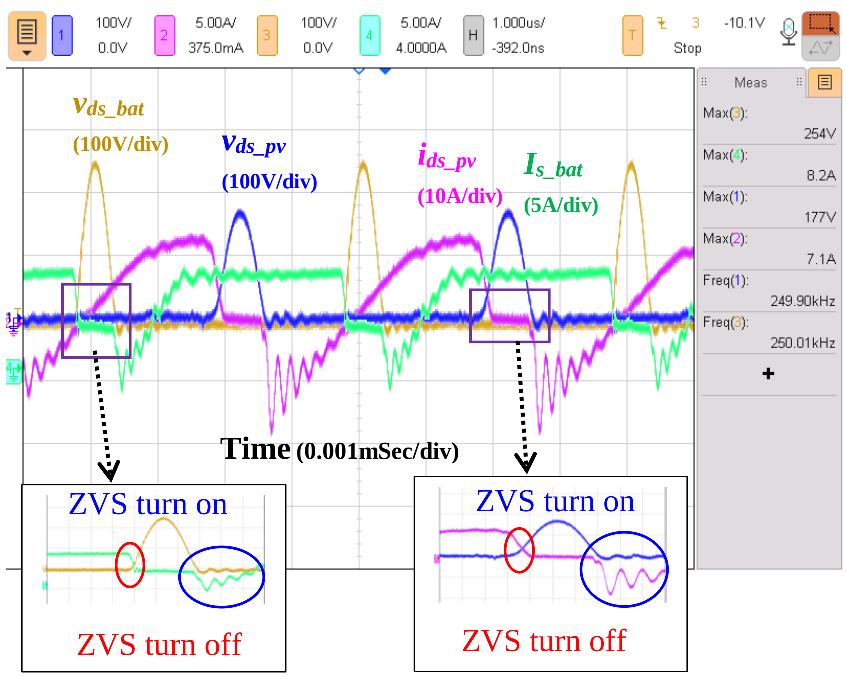

Figure 3-25 simultaneous operation: from PV and battery to load

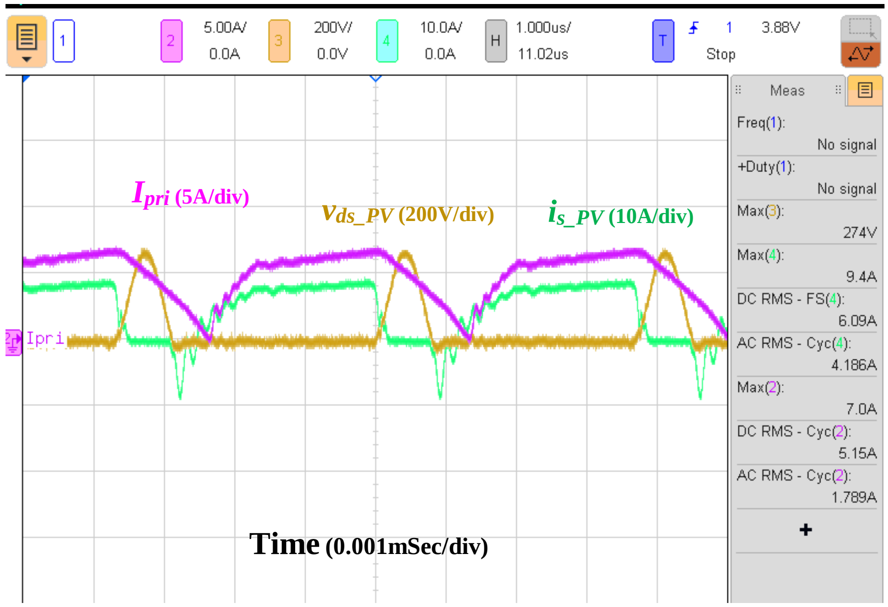

(a)

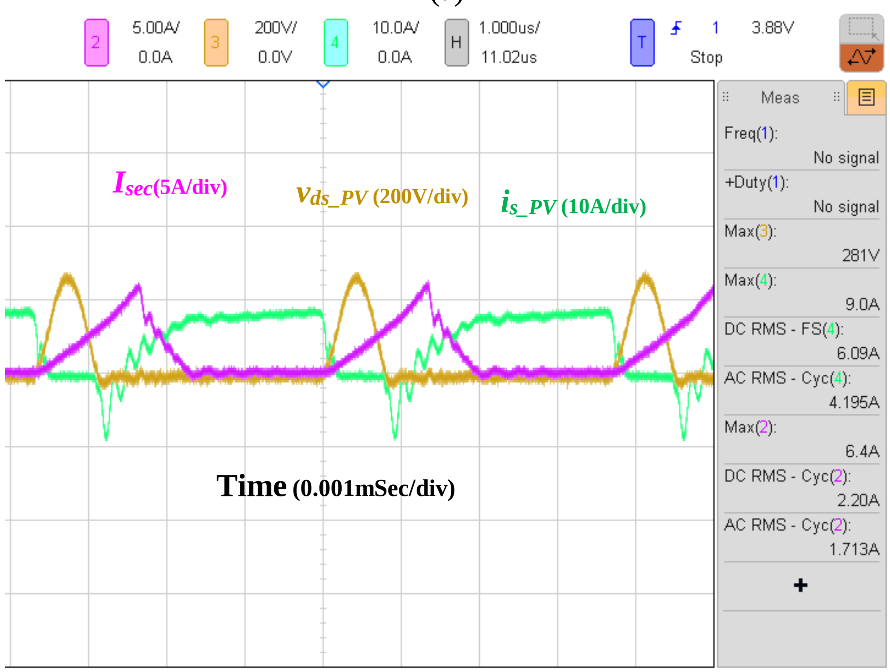

(b)

Figure 3-26 Input (continuous) and secondary side current

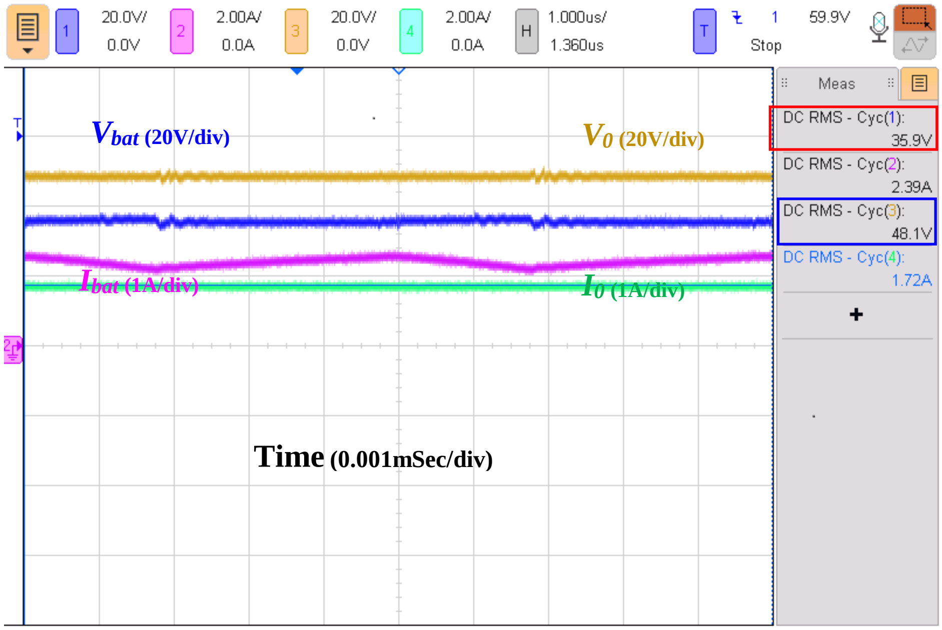

(a) Input and output voltage and current

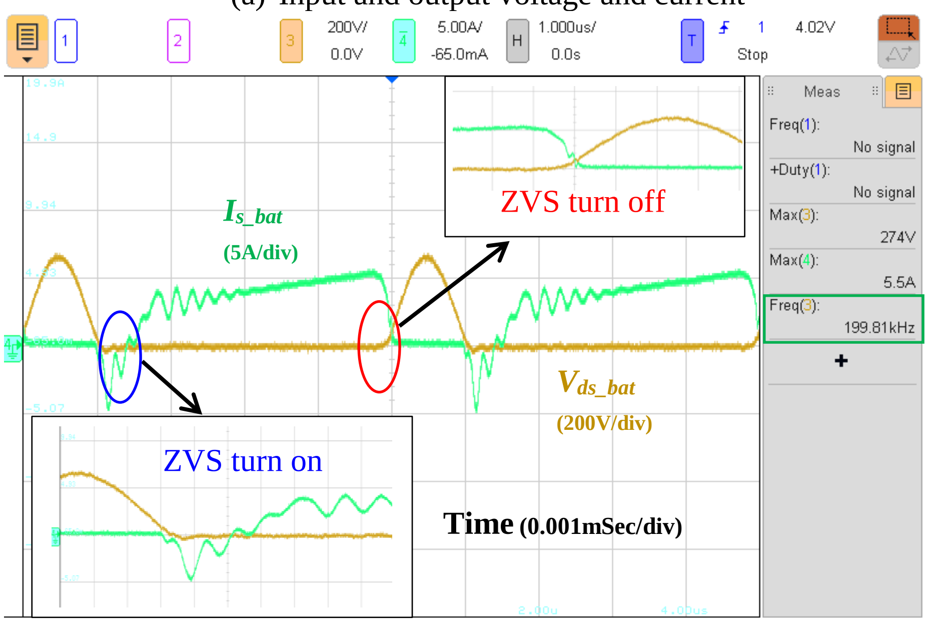

(b) Switch voltage and current

Figure 3-27 Performance of battery discharge circuit in step up mode

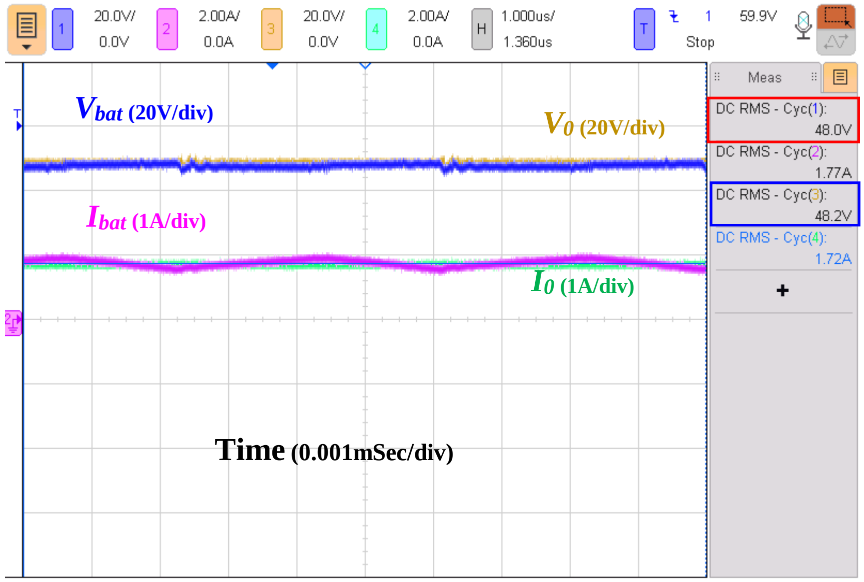

(a) Input and output voltage and current

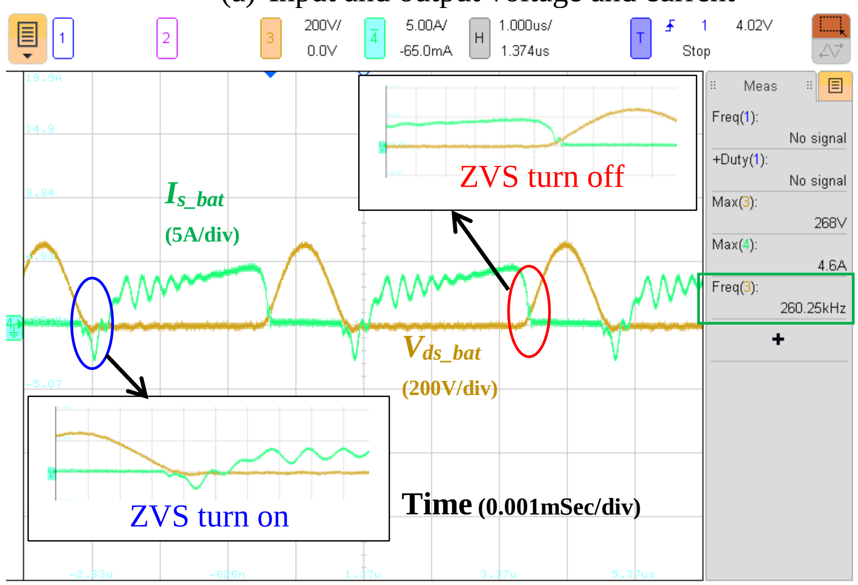

(b) Switch voltage and current

Figure 3-28 Performance of battery discharge circuit in pass through mode

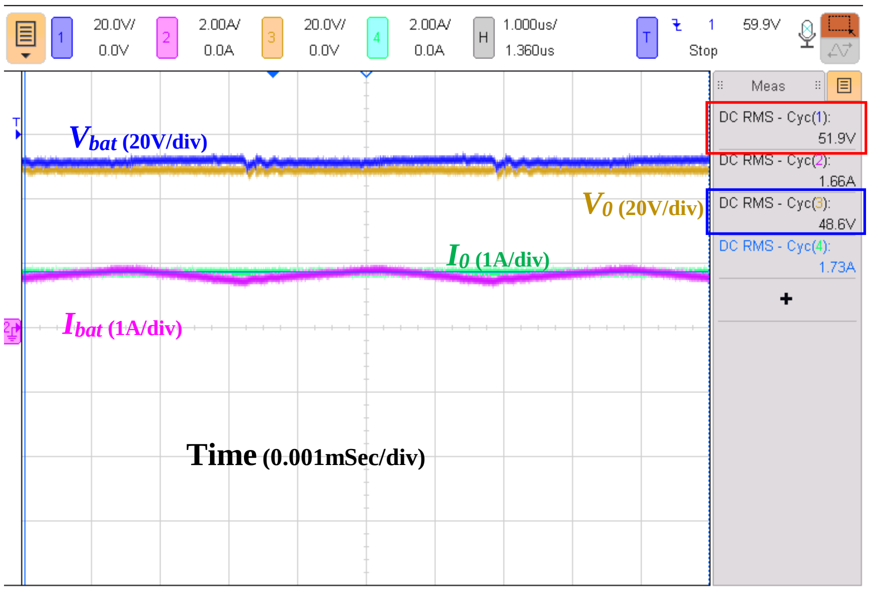

(a) Input and output voltage and current

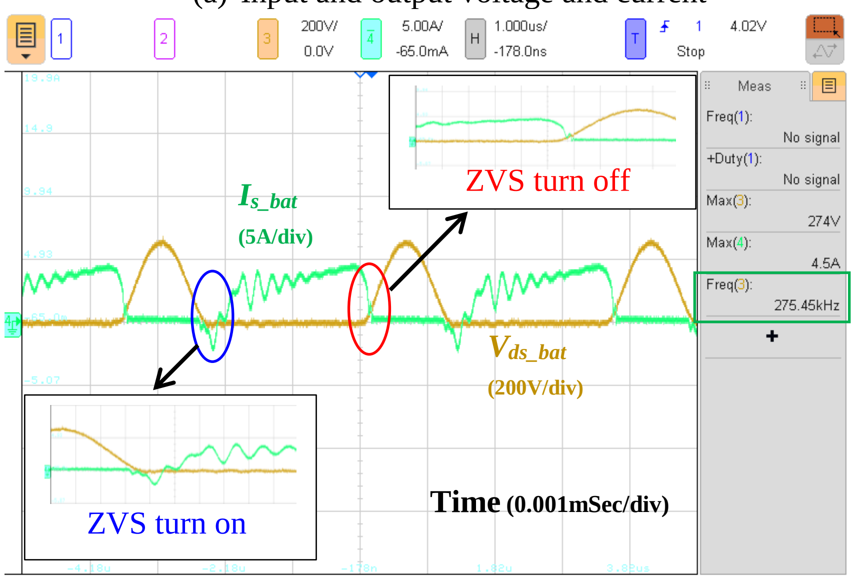

(b) Switch voltage and current

Figure 3-29 Performance of battery discharge circuit in step down mode

The efficiency curve of simultaneous operation (from PV to battery and load) is shown in Figure 3-30(a). The maximum efficiency achieved is 97.1%. Up to 40% of load, the efficiency is over 96%. Below 30% of load, the converter loses soft-switching. At 50% load, the duty ratio is low to maintain the soft switching. Therefore, conduction loss reduced and efficiency increased. The efficiency of individual operation (from the battery to load) is shown in Figure 3-30(b). The maximum efficiency achieved is 96.9%. The efficiency of the battery discharge circuit deteriorates more with the change of the load in comparison of simultaneous operation. The efficiency is measured with the power analyzer (DSOX4PWR) function of the oscilloscope (DSOX4104A).

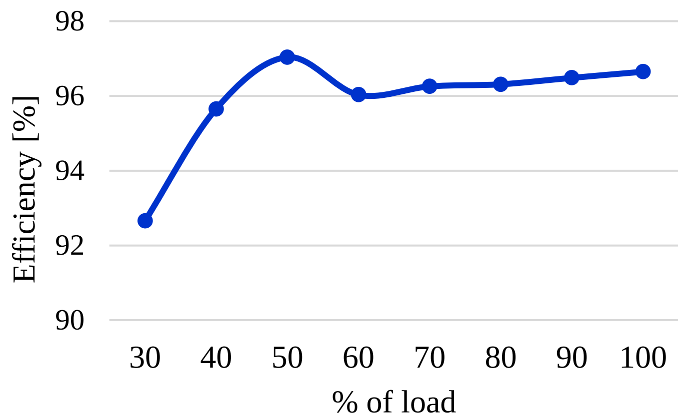

(a) Simultaneous operation from PV to load and battery

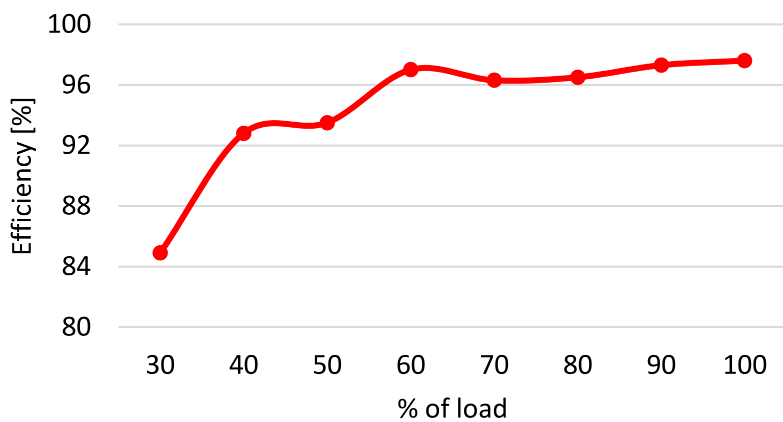

(b) Individual operation from battery to load

Figure 3-30 Efficiency curve of the proposed converter

The component power losses of the proposed converter are estimated at full load. These losses are calculated by measuring required root mean square (rms) values of currents flowing through the switching devices using digital oscilloscope and selecting required parameter from the device datasheet. Total power loss of the converter is 6.5 W. All the switches achieve soft switching during turn on and turn off. As the switching frequency is

250kHz, resonant components are very small and ESR of those components is negligible. The loss breakdown is shown in Figure 3-31. Percentage of switch loss (switching loss and conduction loss) breakdown of total switching loss is shown in Figure 3-32. The S_{pv} switch loss includes the switch and the antiparallel loss. There is no snubber loss. All the switches achieve soft switching during turn on and turn off. Therefore, switching loss is too small.

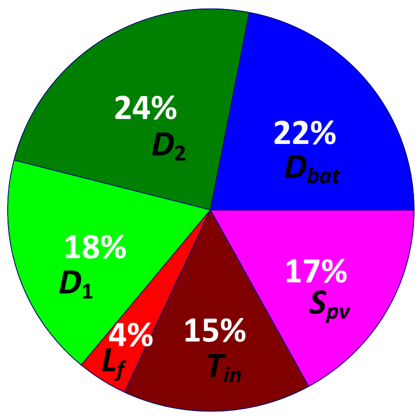

Figure 3-31 Loss breakdown of the key components in percentage of total loss

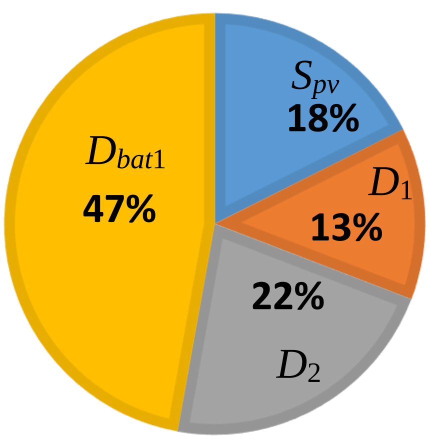

(a) Percentage of conduction loss breakdown

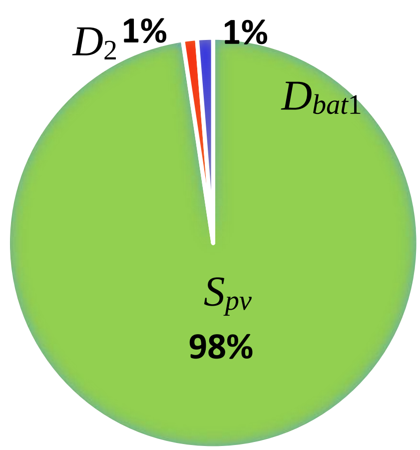

(b) Percentage of switching loss breakdown

Figure 3-32 Loss breakdown of the switching components in percentage of total switch loss

3.7 Chapter Summary

In this chapter, an integrated battery interface with soft-switching capability for module integrated PV systems is presented. In this approach, the battery charging circuit is integrated at the input side of the PV power optimizer while the battery discharging circuit of the proposed system shares the output filter of the PV power optimizer. The proposed converter is capable of addressing different charging profiles of the battery system with PV MPP tracking. The operating principles, steady state and small signal analysis, and controller for the proposed converter system are presented in this chapter. Finally, simulation and experimental results are provided to verify the performance of the proposed converter for a wide range of the light intensity, output load, and battery power. The proposed system can be connected to DC grid as a part of distributed generation system or to the AC grid with an intermediate inverter.

Chapter 4 Proposed MIC with Energy Storage System and Output Voltage Regulation

The converter presented in Chapter 3 is proposed for the regulated DC grid application as the output side is not tightly regulated by the converter. In this chapter, another converter is proposed targeting the unregulated DC grid application to attain the fifth objective of this research. The proposed new converter requires another control parameter for regulating the output voltage besides tracking the MPP and following the battery profile. Hence, an additional switch is utilized in the new topology to achieve output voltage regulation.

The power optimizer presented in Chapter 3 is a ZVS-QR Cuk converter and capable of stepping up and down the input voltage. To achieve step up/down voltage conversion and to reduce the input and output ripple, the Cuk converter utilizes an intermediate capacitor storage, and input and output filter components which ultimately increase the number of passive components compared to the basic buck, boost and buck-boost converter. The output voltage of PV module is always lower than the DC grid. Therefore, for the module integrated PV system, only the step up feature is required, whereas the step up/down feature is required for the battery charging and discharging circuit. Therefore, the proposed new converter utilizes a step up type converter for the PV power optimizer and step up/down type converters for the battery charging and discharging circuit. The description, operating principle, and analysis of the proposed topology are explained in this chapter. The control principle of the proposed system is presented to attain the final objective of this research.

4.1 Description of the Proposed Converter

The proposed converter is composed of the PV power optimizer and the battery charging and discharging circuit. The proposed module integrated converter is shown in Figure 4-1. In the proposed approach, zero-voltage switching (ZVS) multi-resonant (MR) boost converter is integrated with a flyback converter. The output side diode of the boost converter is replaced with a bidirectional switch (S_2) which gives another degree of freedom for the converter control system. The ZVS-MR serves the MPPT, output voltage regulation and stepping up the voltage. The flyback converter is the battery charging circuit. For battery discharging, a ZVS quasi-resonant (QR) buck/boost converter is used.

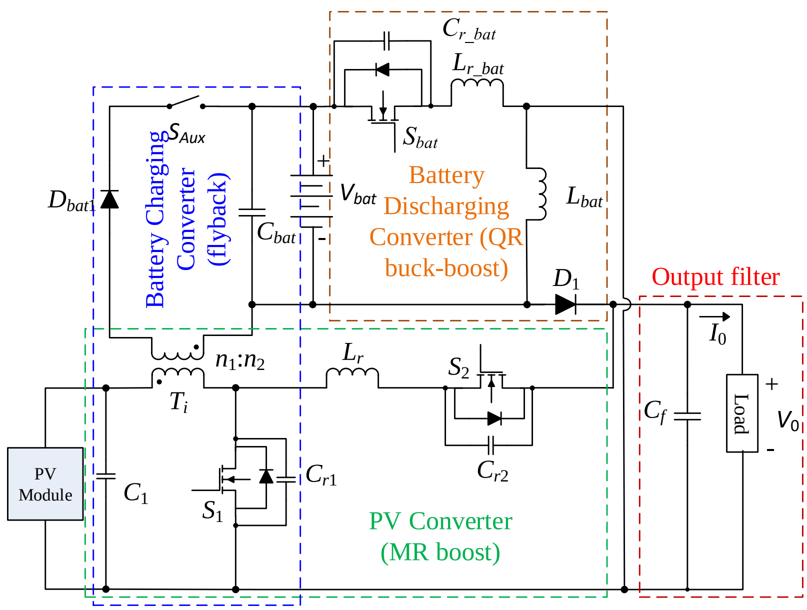

Figure 4-1The proposed PV-battery converter with voltage regulation

The switches S_1, S_2 and the resonant components L_r, C_{r1} and C_{r2} form the MR boost converter. The switches S_1 and the input transformer T_i is shared by the MR boost converter and the flyback converter. The switch S_{bat} and the resonant components L_{r_bat}, and C_{r_bat} form the ZVS-QR buck-boost converter. The PV power optimizer and the battery discharge circuit share the output filter. The switch S_{Aux} is used only to activate and deactivate the battery charging circuit. The proposed converter is capable of performing all required individual and simultaneous operations as listed in Table 3-1. The different modes of operation of the proposed converter are shown in Figure 4-2.

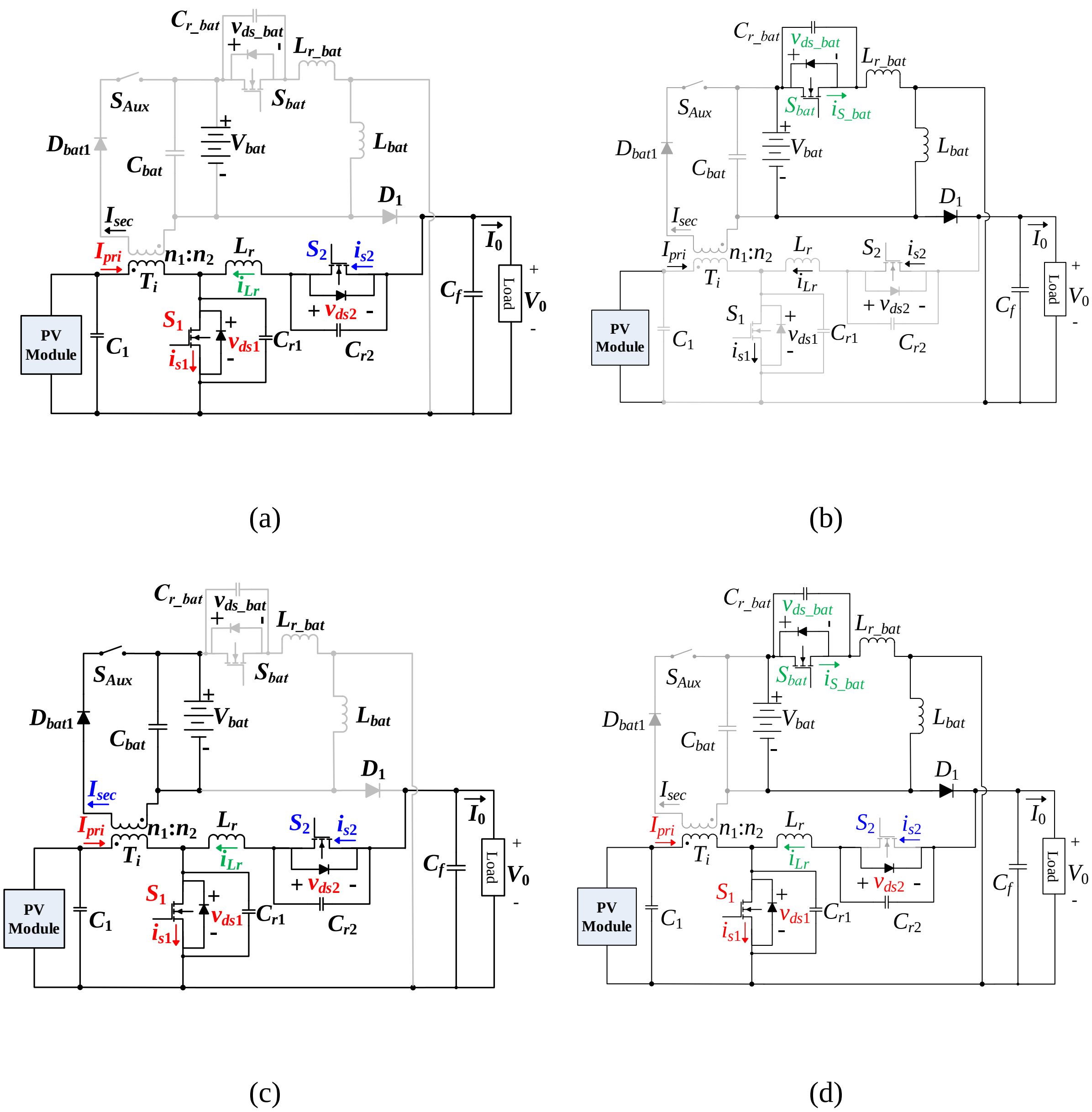

Figure 4-2 Operating modes of the proposed converter (a) individual mode 1 (b) individual mode 2 (c) simultaneous mode 1 and (d) simultaneous mode 2

4.2 Operating Principle

The individual modes of operation are very straight forward. The individual mode 1 is the variable frequency MR boost converter and the individual mode 2 is the ZVS QR buck-boost converter. The operation of ZVS-QR Cuk converter is presented in Chapter 2 and Chapter 3. The simultaneous modes of operation are described below.

***Simultaneous operation mode 1 (PV to load and battery charging)*:**

In this mode of operation, switch S_1 and S_2 are active. Both switches are operating at the same frequency (f_s=f_{s1}=f_{s2}). However, the duty ratio of the switch S_1 and S_2 are different (d_{s2}<d_{s1}). When one of the switches or both switches is off, resonance occurs. The antiparallel diode of switch S_2 carries the output current. The switch S_2 turns on to send back the extra power of the load side to the input side for charging the battery. The antiparallel diodes carry the current prior to the switches turn on. Therefore, the transition of the switches happens under zero-voltage conditions. When the switch S_1 is off, current flows through the secondary winding of the input transformer. Hence, power transferred to the battery side to charge the battery. Figure 4-3 shows the theoretical waveforms of this mode of operation.

[$t_0 < t < t_1$]: At time t_0, the resonant capacitor voltage v_{ds1} reaches zero and the gate signal is applied to switch S_1. Resonant inductor L_r and resonant capacitor C_{r2} keep resonating. The anti-parallel diode of switch S_1 carries the resonant current. The primary current of the transformer T_{in} keeps rising. At the end of this stage, resonance ends. The battery charging circuit turns off at the beginning of this stage and remains off during this stage. The battery is getting charged by C_{bat}.

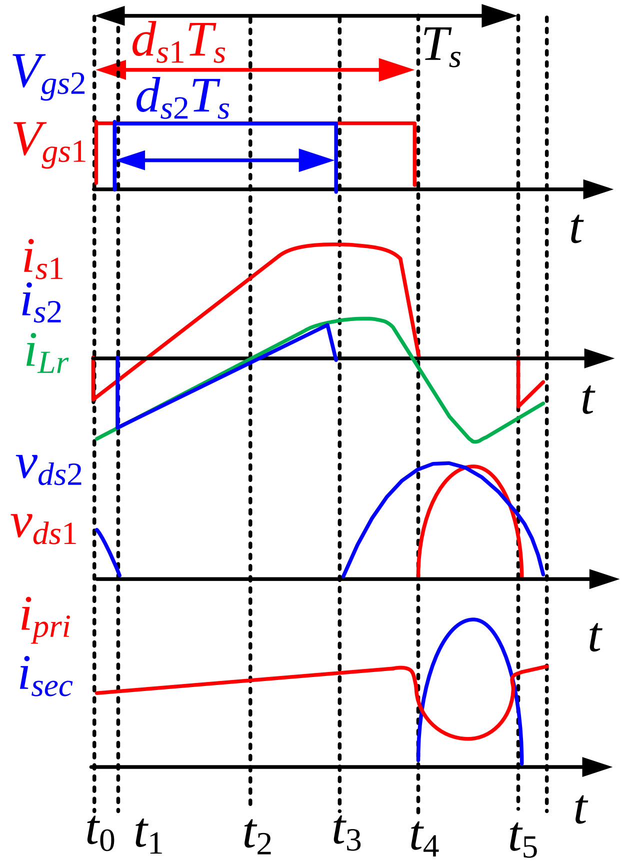

Figure 4-3 Theoretical waveforms of the proposed converter in simultaneous mode 1 operation

[$t_1 < t < t_2$]: At the beginning of this stage, the resonant capacitor voltage v_{ds2} reaches zero and the gate signal is applied to switch S_2. The anti-parallel diode of switch S_2 starts conducting to carry resonant inductor current. The switch S_1 turns on under ZVS condition as the antiparallel diode conducted prior. At this stage, the switch S_2 also turns on under ZVS condition. The battery charging circuit remains the same as the previous stage.

[$t_2 < t < t_3$]: Both S_1 and S_2 are on throughout this stage. The primary current keeps increasing and reached to its maxima. This stage ends when switch S_2 turns off.

[$t_3 < t < t_4$]: The resonant inductor L_r and resonant capacitor C_{r2} start resonating. The resonant voltage v_{ds2} across the resonant capacitor C_{r2} starts rising. At the end of this stage switch S_1 turns off.

[$t_4 < t < t_5$]: At this stage, resonance happens between resonant inductor L_r, resonant capacitor C_{r1} and C_{r2}. The resonant voltage v_{ds1} across the resonant capacitor C_{r1} starts rising. The battery circuit turns on and the secondary current starts flowing. The primary current drops in proportional to the secondary current. At the end of this stage, the battery circuit turns off.

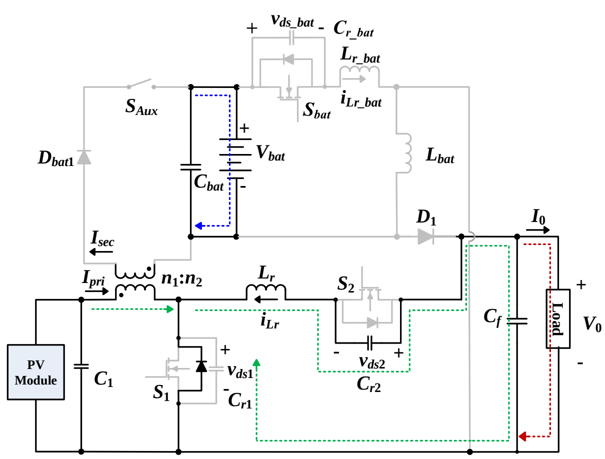

(a) $t_0 < t < t_1$

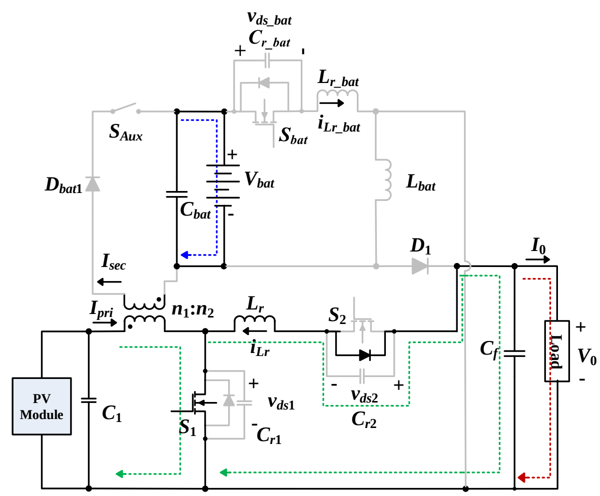

(b) $t_1 < t < t_2$

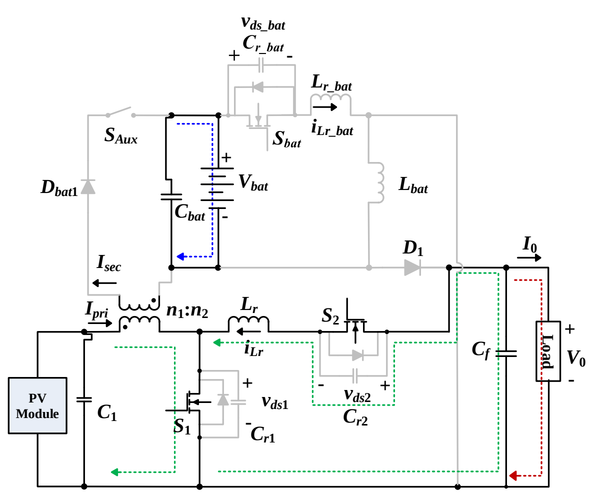

(c) $t_2 < t < t_3$

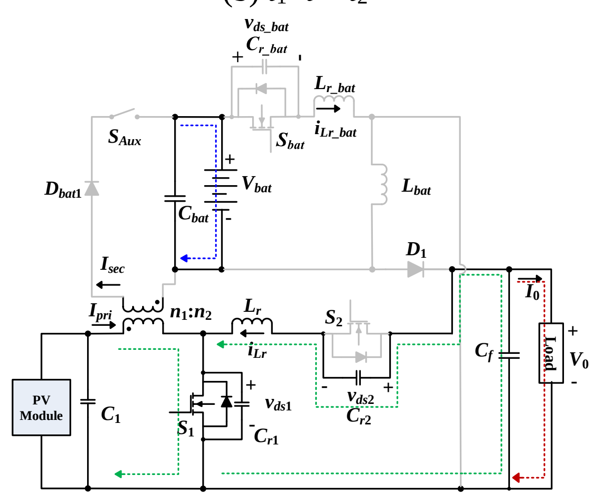

(d) $t_3 < t < t_4$

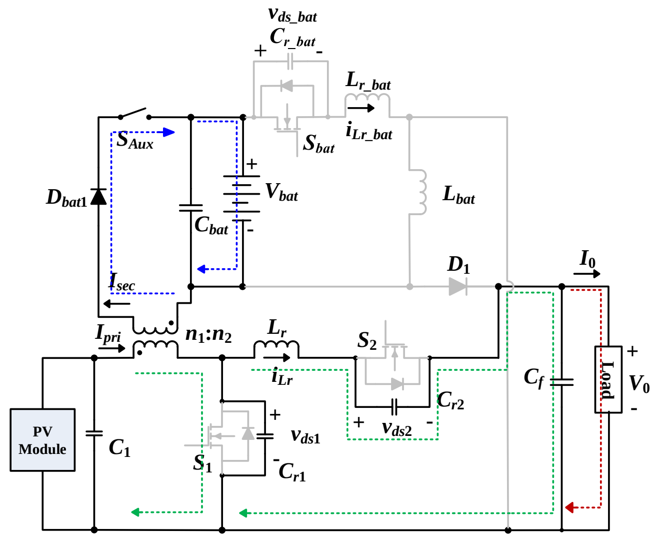

(e) $t_4 < t < t_5$

Figure 4-4 Operating stages of the proposed converter individual operation mode 1

***Simultaneous operation mode* 2 *(PV to load and battery discharging)*:**

In this mode of operation, the power optimizer and the battery discharge circuit are active. The power optimizer is in MPP mode and the discharge circuit performs the output voltage regulation. The switch S_1 and S_{bat} are active but independent. That means the frequency and duty ratio of both switches are not related to each other. Figure 4-5 shows the theoretical waveforms of this mode of operation.

[$t_0 < t < t_1$]: At time t_0, the gate signal is applied to switches S_1 and S_{bat}. Prior to this stage, the antiparallel diode of the switches S_1 and S_{bat} were conducting. Therefore, both switches turn on under ZVS condition. The antiparallel diode of switch S_2 and the diode D_1 is on and contributing to the output current.

[$t_1 < t < t_2$]: At the beginning of this stage, the diode D_1 turns off. The current though L_{bat} and S_{bat} are increasing. The PV power optimizer circuit remains the same throughout this stage.

[$t_2 < t < t_3$]: The antiparallel diode of switch S_2 stops carrying the load current at the beginning of this state. The resonant inductor L_r and resonant capacitor C_{r2} start resonating. At the end of this stage, the switch S_{bat} turns off.

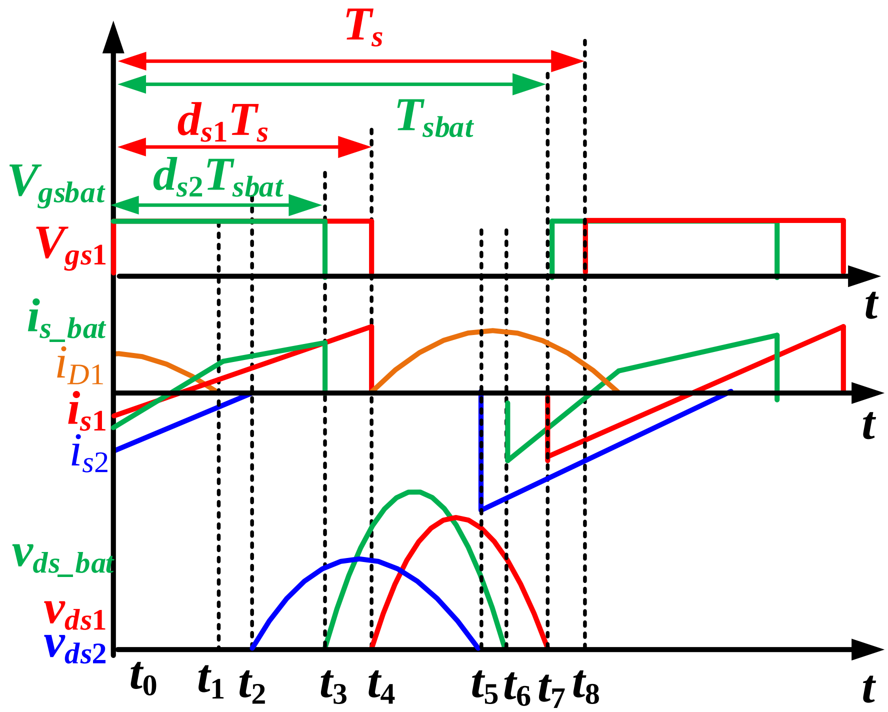

Figure 4-5 Theoretical waveforms of the proposed converter simultaneous mode 2

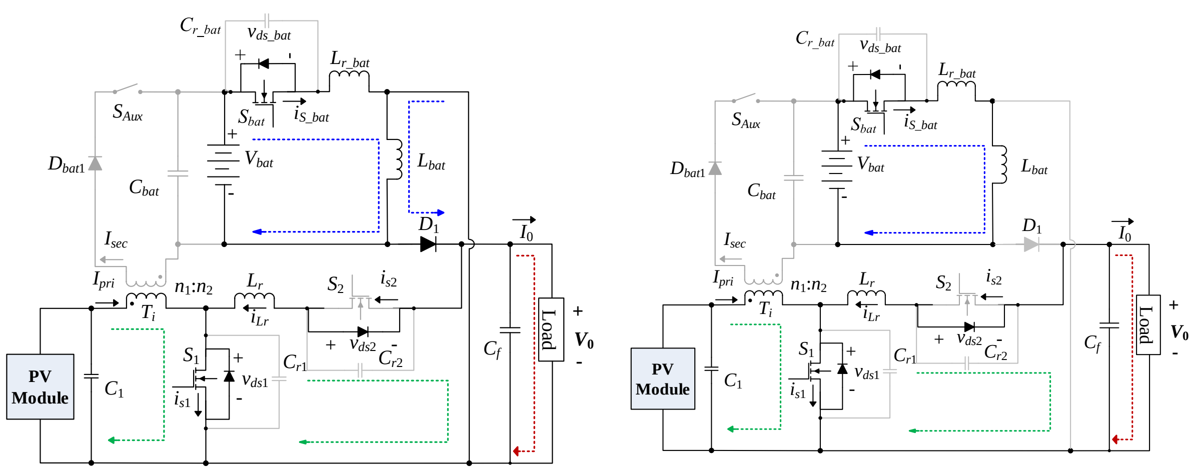

(a) $t_0 < t < t_1$

(b) $t_1 < t < t_2$

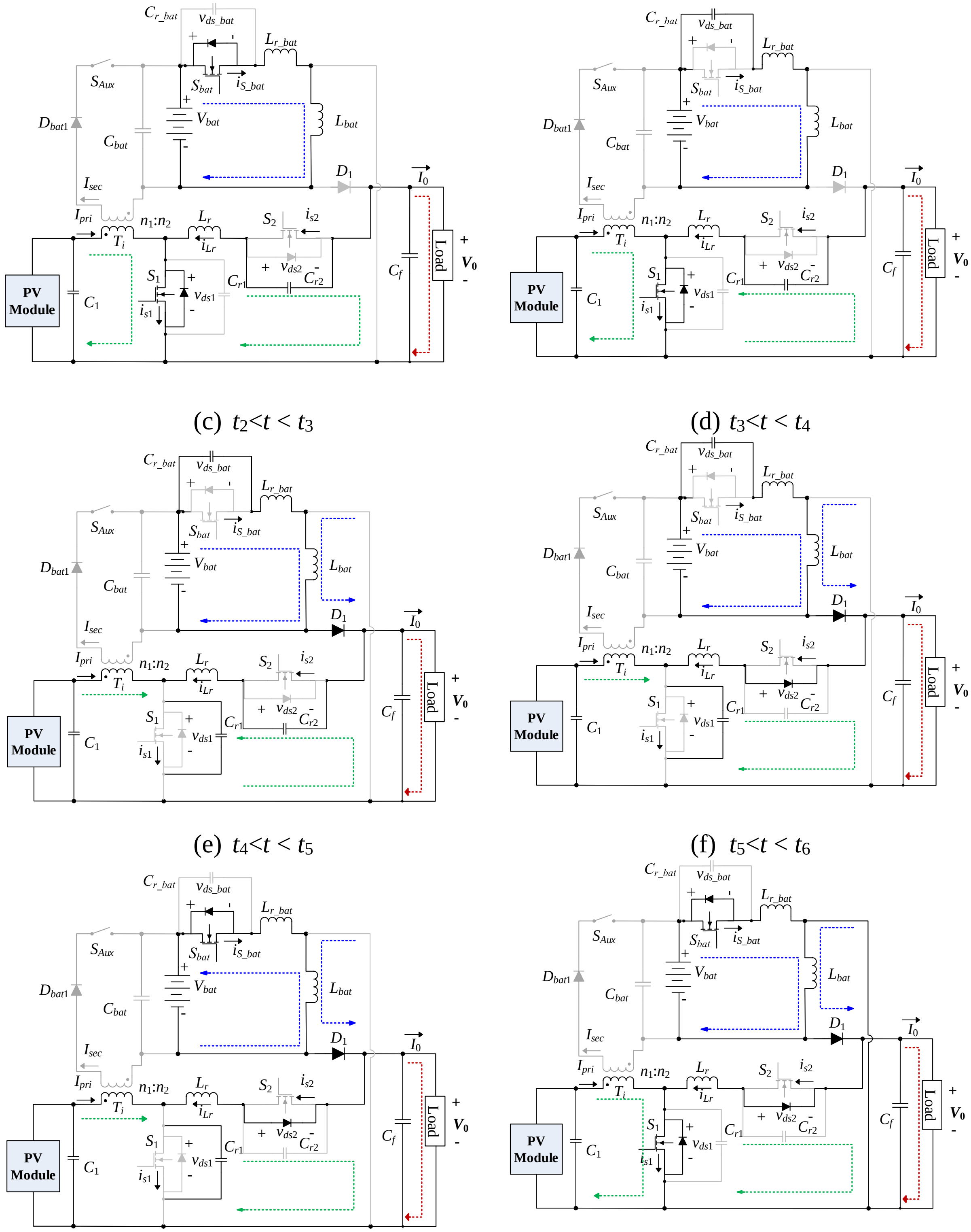

(c) $t_2 < t < t_3$

(d) $t_3 < t < t_4$

(e) $t_4 < t < t_5$

(f) $t_5 < t < t_6$

(g) $t_6 < t < t_7$

(h) $t_7 < t < t_8$

Figure 4-6 Operating stages of the proposed converter individual operation mode 2

[$t_3 < t < t_4$]: The resonant inductor L_{r_bat} and resonant capacitor C_{r_bat} starts resonating. The resonance in PV power optimizer (L_r and C_{r2}) continues until the switch S_1 turns off at the end of this stage.

[$t_4 < t < t_5$]: At the beginning of this stage, the diode D_1 starts conducting. The resonant inductor L_r, and resonant capacitor C_{r1} and C_{r2} resonates at this stage. At the end of this stage, the antiparallel diode of switch S_2 starts conducting.

[$t_5 < t < t_6$]: The resonant inductor L_r and resonant capacitor C_{r1} resonates at this stage. At the end of this stage, the resonant inductor L_{r_bat} and resonant capacitor C_{r_bat} stops resonating.

[$t_6 < t < t_7$]: The antiparallel diode of switch S_{bat} starts conducting and diode D_1 keeps conducting. At the end of this stage, the resonant inductor L_r and resonant capacitor C_{r1} stops resonating. The switching cycle of the battery circuit completed at the end of this stage.

[$t_7 < t < t_8$]: The antiparallel diode of switch S_{bat} starts conducting. With the completion of this period, the switching cycle of the power optimizer completes.

4.3 Steady State Analysis

In MR converters, resonance happens between L_r, C_{r1}, and C_{r2}. In the proposed converter, the MR converter is formed with two controllable switches S_1 and S_2. In simultaneous mode 1, the passive switch D_{bat1} is also active. All the switches possess two states- on (equivalent to 1) and off (equivalent to 0). However, the state change of the passive switch D_{bat1} is not taking part in power conversion as the state of the switch D_{bat1} is the inverse of the state of the switch S_1. There are four possible different states of the proposed converter based on and off state of switch S_1 and S_2: 00, 01, 11 and 10, where 0 and 1 represent the on and off states of S_1 and S_2 respectively. Based on the sequence of the switch states, there are four modes of operations of ZVS-MR converter. However, the proposed converter is kept to operate only in one mode for this application. The operating sequences are: 11, 10, 00 and 10. Therefore, state 01 will not occur in this operating mode. The resonance happens during either or both switches S_1 and S_2 are off.

The resonant components L_r, C_{r1}, and C_{r2} of the MR converter determine the characteristics of the converter. The characteristics equations are shown by Eq. 4-1 - Eq. 4-6.

$$\omega_{r1} = \frac{1}{\sqrt{L_r C_{r1}}} \qquad \text{Eq. 4-1}$$

$$Z_{01} = \frac{L_r}{C_{r1}} \qquad \text{Eq. 4-2}$$

$$\omega_r = \frac{1}{\sqrt{L_r C_r}} \qquad \text{Eq. 4-3}$$

$$Z_0 = \frac{L_r}{C_r} \qquad \text{Eq. 4-4}$$

$$C_r = \frac{C_{r1} C_{r2}}{C_{r1} + C_{r2}} \qquad \text{Eq. 4-5}$$

$$C_N = \frac{C_{r2}}{C_{r1}} \qquad \text{Eq. 4-6}$$

For the DC analysis, a generalized approach proposed by [97] [98] is taken. In this approach, the analysis is irrespective of the position of switch or type of converter. The analysis is done with the normalized values and in the following equations, the superscript 'N' stands for the normalized value. The base quantities for normalization are voltage V_0, current V_0/Z_0, time $1/\omega_r$, and the frequency f_r. The normalized values used in the following section are: i_{Lr}^N - the normalized resonant inductor current, I_0^N - the normalized output current, v_{s1}^N - the normalized drain to source voltage across switch S_1, and v_{s2}^N - the normalized drain to source voltage across switch S_2.

1) *Stage* 11:

At this stage, both switches (S_1 and S_2) are on and the resonant inductor stores energy. Therefore, the voltage across the switches is zero (v_{s1}=0 and v_{s2}=0). The state equation of this period is shown by Eq. 4-7. The resonant inductor current of this period is derived from Eq. 4-7 as shown by Eq. 4-8, where $I_{Lr\_nn}^N$ is the initial normalized resonant inductor current of stage 11.

<u>State</u>: $v_{s1} = 0$ and $v_{s2} = 0$

<u>Equation</u>: $$\frac{di_{Lr}^N}{dt} = 1 \qquad \text{Eq. 4-7}$$

<u>Solution</u>: $$i_{Lr}^N(t) = \omega_r t + I_{Lr\_nn} \qquad \text{Eq. 4-8}$$

2) *Stage* 10:

At this stage, switch S_1 is on and the switch S_2 is off. Therefore, the voltage across switch S_1 and the current through the switch S_2 are zero. The resonance happens in between the resonant inductor L_r and the resonant capacitor C_{r2}. The state equations are shown by Eq. 4-9. The resonant inductor current and the resonant capacitor voltage are shown by Eq. 4-10 and Eq. 4-11 respectively where $I_{Lr\_nf}^N$ is the initial normalized resonant inductor current of stage 10 and $V_{s1\_nf}^N$ is the initial normalized drain to source voltage across switch S_1 of stage 10

<u>State</u>: $v_{s1} = 0$ and $i_{s2} = 0$

Equation: $\frac{di_{Lr}^N}{dt} = 1 - v_{s2}^N$ and $\frac{dv_{s2}^N}{dt} = i_{Lr}^N$ Eq. 4-9

Solution:

$$i_{Lr}^N(t) = I_{Lr\_nf}^N \cos\omega_r t + \left(1 - V_{s2\_nf}^N\right)\sin\omega_r t$$ Eq. 4-10

$$v_{s2}^N(t) = 1 + I_{Lr\_nf}^N \sin\omega_r t + \left(V_{s2\_nf}^N - 1\right)\cos\omega_r t$$ Eq. 4-11

3) *Stage* 00:

At this stage, both switches (S_1 and S_2) are off. Therefore, the current through the switches S_1 and S_2 are zero. The resonance happens in between the resonant inductor L_r and the resonant capacitors C_{r1} and C_{r2}. The state equations are shown by Eq. 4-12. The resonant inductor current and the voltages across the resonant capacitors are shown by Eq. 4-13, Eq. 4-14, and Eq. 4-15 respectively where I_{Lr-ff}^N is the initial normalized resonant inductor current of stage 00, V_{s1-ff}^N is the initial normalized drain to source voltage across switch S_1 of stage 00, and V_{s2-ff}^N is the initial normalized drain to source voltage across switch S_2 of stage 00.

State: $i_{s1} = 0$ and $i_{s2} = 0$

Equation: $\frac{di_{Lr}^N}{dt} = 1 - v_{s1}^N - v_{s2}^N$, $\frac{dv_{s1}^N}{dt} = \frac{1}{C_N}\left(i_{Lr}^N - I_0^N\right)$ and $\frac{dv_{s2}^N}{dt} = i_{Lr}^N$ Eq. 4-12

Solution:

$$i_{Lr}^{N}(t)=\frac{I_{0}^{N}}{1+C_N}\left(1-\cos\sqrt{\frac{1+C_N}{C_N}}\omega_r t\right)$$
$$+I_{Lr\_ff}^{N}\cos\sqrt{\frac{1+C_N}{C_N}}\omega_r t$$
$$+\sqrt{\frac{C_N}{1+C_N}}\left(1-v_{s1\_ff}^{N}-v_{s2\_ff}^{N}\right)\sin\sqrt{\frac{1+C_N}{C_N}}\omega_r t \qquad \text{Eq. 4-13}$$

$$v_{s1}^{N}(t)=\frac{1}{1+C_N}\left(1+C_N V_{s1\_ff}^{N}-V_{s2\_ff}^{N}\right)-\frac{I_0^N}{1+C_N}\omega_r t$$
$$+\frac{1}{\sqrt{C_N\left(1+C_N\right)}}\left(I_{Lr\_ff}^{N}-\frac{I_0^N}{1+C_N}\right)\sin\sqrt{\frac{1+C_N}{C_N}}\omega_r t \qquad \text{Eq. 4-14}$$
$$+\frac{1}{1+C_N}\left(V_{s1\_ff}^{N}+V_{s2\_ff}^{N}-1\right)\cos\sqrt{\frac{1+C_N}{C_N}}\omega_r t$$

$$v_{s2}^{N}(t)=\frac{C_N}{1+C_N}\left(1-V_{s1\_ff}^{N}-\frac{V_{s2\_ff}^{N}}{C_N}\right)+\frac{I_0^N}{1+C_N}\omega_r t$$
$$+\sqrt{\frac{C_N}{1+C_N}}\left(I_{Lr\_ff}^{N}-\frac{I_0^N}{1+C_N}\right)\sin\sqrt{\frac{1+C_N}{C_N}}\omega_r t \qquad \text{Eq. 4-15}$$
$$+\frac{C_N}{1+C_N}\left(V_{s1\_ff}^{N}+V_{s2\_ff}^{N}-1\right)\cos\sqrt{\frac{1+C_N}{C_N}}\omega_r t$$

The voltage gain of the PV to load converter is shown by Eq. 4-16 where T_{11} is the time period for state 11, f_N is the normalized switching frequency, I_0 is the output load current and i_{Lr1} and i_{Lr4} is the resonant inductor current during t_1 to t_3 and t_0 to t_1 of the simultaneous operation mode 1 (Figure 4-3) respectively. The normalized frequency f_N is the ratio of switching frequency f_s and resonant frequency f_r of the ZVS-MR circuit.

$$m=\frac{V_0}{V_{in}}=\frac{2I_{in}^{N}\omega_0 T_s}{\left(I_{Lr\_fn}^{N}+I_{Lr\_4}\right)\omega_0 T_{11}} \qquad \text{Eq. 4-16}$$

The current i_{Lr4} (Eq. 4-17) depends on factor C_N, i_{Lr3} and v_{s2_3} where i_{Lr3} and v_{s2_3} are the resonant inductor current and voltage across switch S_2 during t_3 to t_4.

$$I_{Lr\_4} = \sqrt{\left(I_{Lr\_fn}^{N}\right)^2 + \left(1 - V_{s1\_fn}^{N}\right)^2 - 1} \qquad \text{Eq. 4-17}$$

A closed-form solution cannot be found analytically for ZVS-MRC. Therefore, numerical analysis is used to determine the characteristics of ZVS-MR boost converter. The load to voltage gain curves with respect to the factor C_N are shown in Figure 4-7(a). With the increase of C_N, the voltage gain range increases. The load to voltage gain curve with respect to the switching frequency for C_N=3 is shown in Figure 4-7(b). The soft switching range of the MR converter depends on C_N, I_N, and f_N. With the increase of C_N, the I_N range increases under soft switching condition.

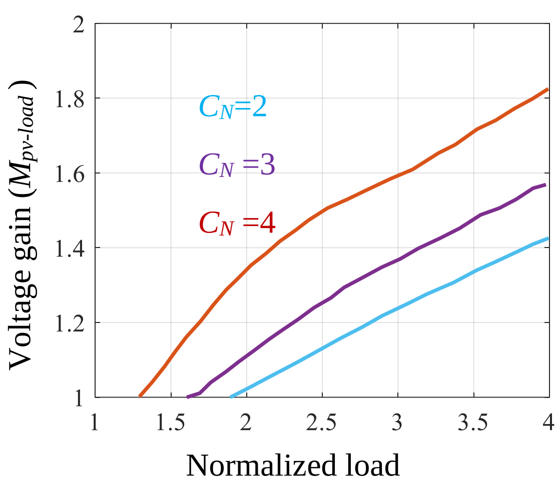

(a)

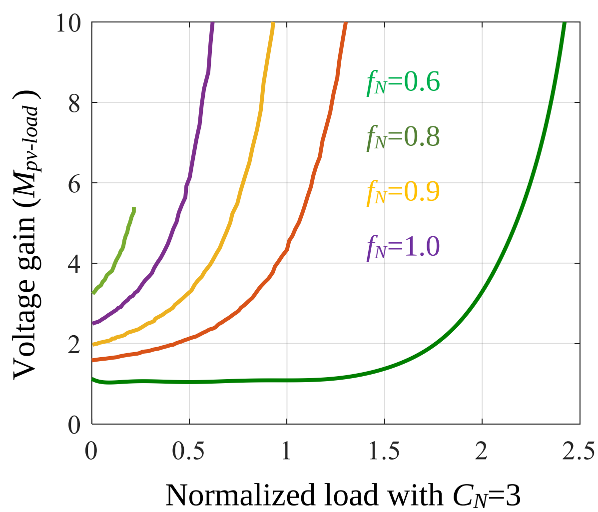

(b)

Figure 4-7 Normalized load to output characteristics (a) with the change of C_N (b) with the change of normalized switching frequency

4.4 Small Signal Model

The dynamic behavior of the proposed converter can be obtained by replacing the resonant switches with the voltage sources. The circuit order of the QRC and MRC is the same as the PWM version of the converter as the resonant capacitors are in parallel with the voltage sources [90] [99]. The small signal model of the proposed converter is shown in Figure 4-8.

This model is valid only for the frequencies well below the switching frequency. Among these three sources, two (V_N and I_N) are dependent on internal electrical magnitude. The V_N, and I_N represent the normalized value of the loop voltage of the switch and node current of the resonant inductor. The perturbation of voltages across the switches are shown by Eq. 4-18, Eq. 4-19, and Eq. 4-20. t_{c1} and t_{c2} are the on time of the switch S_1 and S_2 respectively.

$$\hat{v}_1 = k_{v1}\hat{V}_N + k_{i1}\hat{I}_N + k_1(\hat{t}_{c1}) \qquad \text{Eq. 4-18}$$

$$\hat{v}_2 = k_{v2}\hat{V}_N + k_{i2}\hat{I}_N + k_2(\hat{t}_{c2}) \qquad \text{Eq. 4-19}$$

$$\hat{v}_{bat} = k_{vb}\hat{V}_{Nb} + k_{ib}\hat{I}_{Nb} + k_{fb}(\hat{f}_{sbat}) \qquad \text{Eq. 4-20}$$

$$G_{vp} = G_{0p}\frac{1-\dfrac{s}{\omega_{zp}}}{1+\dfrac{1}{Q_p}\dfrac{s}{\omega_p}+\left(\dfrac{s}{\omega_p}\right)^2} \qquad \text{Eq. 4-21}$$

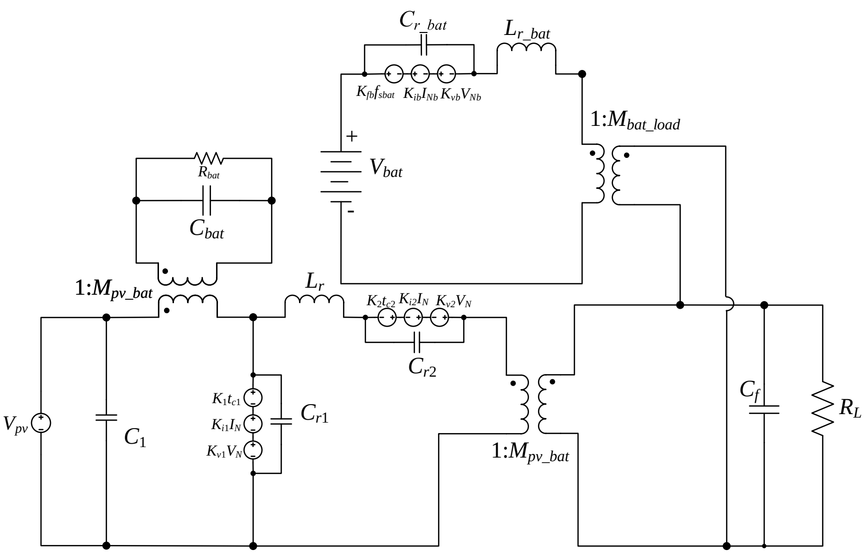

Figure 4-8 Small signal model of the proposed converter

The control to output transfer function is shown by Eq. 4-21 where p can be 1, 2 and b to represent controller for CV mode, load regulation by power optimizer circuit and load regulation by battery discharge circuit respectively [90]. The salient features of the small signal transfer function are shown in Table 4-1.

Table 4-1 Coefficients of control to output transfer function of battery discharge circuit

<table>
<tr><td rowspan="8">$p = x$</td><td colspan="4">$G_{0x} = \left(\frac{\omega_x}{\omega_{Fx}}\right)^2 m'_x V_x k_x$</td></tr>
<tr><td colspan="4">$\omega_x = \omega_{Fx}\sqrt{m'^2_x - V_x K_{vx} m'_x + V_x K_{ix}\frac{1+m_x}{R_0}}$</td></tr>
<tr><td colspan="4">$Q_x = \left(\frac{\omega_x}{\omega_{Fx}}\right)^2 \frac{1}{\frac{R_{Fx}}{R_0}\left[1 - V_i K_{vx}\frac{m_x}{m'_x} + V_i\frac{K_{ix}}{R_{Fix}}\right]}$</td></tr>
<tr><td colspan="2">$k_{ix} = -\frac{\partial m_x}{\partial I_{Nx}}\frac{R_0}{V_i}$</td><td colspan="2">$k_{vx} = -\frac{\partial m_x}{\partial I_{Nx}}\frac{R_0 I_{Nx}}{(V_i)^2}$</td></tr>
<tr><td>$\omega_{zx} = \frac{m'^2_x R_0}{L_x m_x}$</td><td colspan="2">$\omega_{Fx} = \frac{1}{\sqrt{L_x C_f}}$</td><td>$R_{Fx} = \sqrt{\frac{L_x}{C_f}}$</td></tr>
<tr><td>$x = b$</td><td>$k_b = -\frac{m_b}{F_{sbat}}$</td><td>$V_b = V_{bat} - V_0$</td><td>$L_b = L_{bat}$</td></tr>
<tr><td rowspan="2">$x = 2$</td><td>$k_2 = \frac{m_2(d_1 - d_2)}{F_s}$</td><td>$V_2 = V_0$</td><td>$L_2 = L_m$</td></tr>
<tr><td colspan="3">$m_2 = m(C_N, I_N, T_c)$</td></tr>
<tr><td rowspan="2">$p = 1$</td><td colspan="2">$G_{01} = \frac{V_{pv} - \frac{1}{n}V_{bat}}{d_1(1-d_1)}$</td><td colspan="2">$Q_1 = \frac{(1-d_1)R_{bat}}{R_{F1}}$</td></tr>
<tr><td colspan="2">$\omega_{z1} = \frac{(1-d_1)^2}{d_1}\frac{R_{bat}}{L_m}$</td><td>$\omega_{F1} = \frac{1}{\sqrt{L_m C_{bat}/n}}$</td><td>$R_{F1} = \sqrt{\frac{nL_m}{C_{bat}}}$</td></tr>
</table>

4.5 Control Technique

The proposed converter requires performing all the required individual and simultaneous operations. The control parameter of the quasi-resonant converter is the switching frequency and the control parameters of the multi-resonant converter are the switching frequency and the duty ratio of the switches. In case of constant frequency multi-resonant converter, equal switching frequency for S_1 and S_2 is required to achieve ZVS operation. Therefore, the control parameters of the proposed converter are the switching frequency and the duty ratio of the switch S_1, duty ratio of the switch S_2 and the switching frequency of the switch S_{bat}. Figure 4-9 shows the control flow chart of the proposed converter.

When the load demand is lower than the available PV power or the battery SoC (state of charge) is at its allowable minimum level, the converter operates in individual mode 1. In this mode of operation, only the power optimizer (PV to load converter) is active. Switch S_1 and S_2 are operating at the same frequency (f_s=f_{s1}=f_{s2}). However, the duty ratio of the switch S_1 and S_2 are different (d_{s2}<d_{s1}). The converter operates as a variable frequency multi-resonant converter with two controllable switches. When the PV power is not available, the converter operates in individual mode 2. In this mode of operation, only the battery discharging circuit is active.

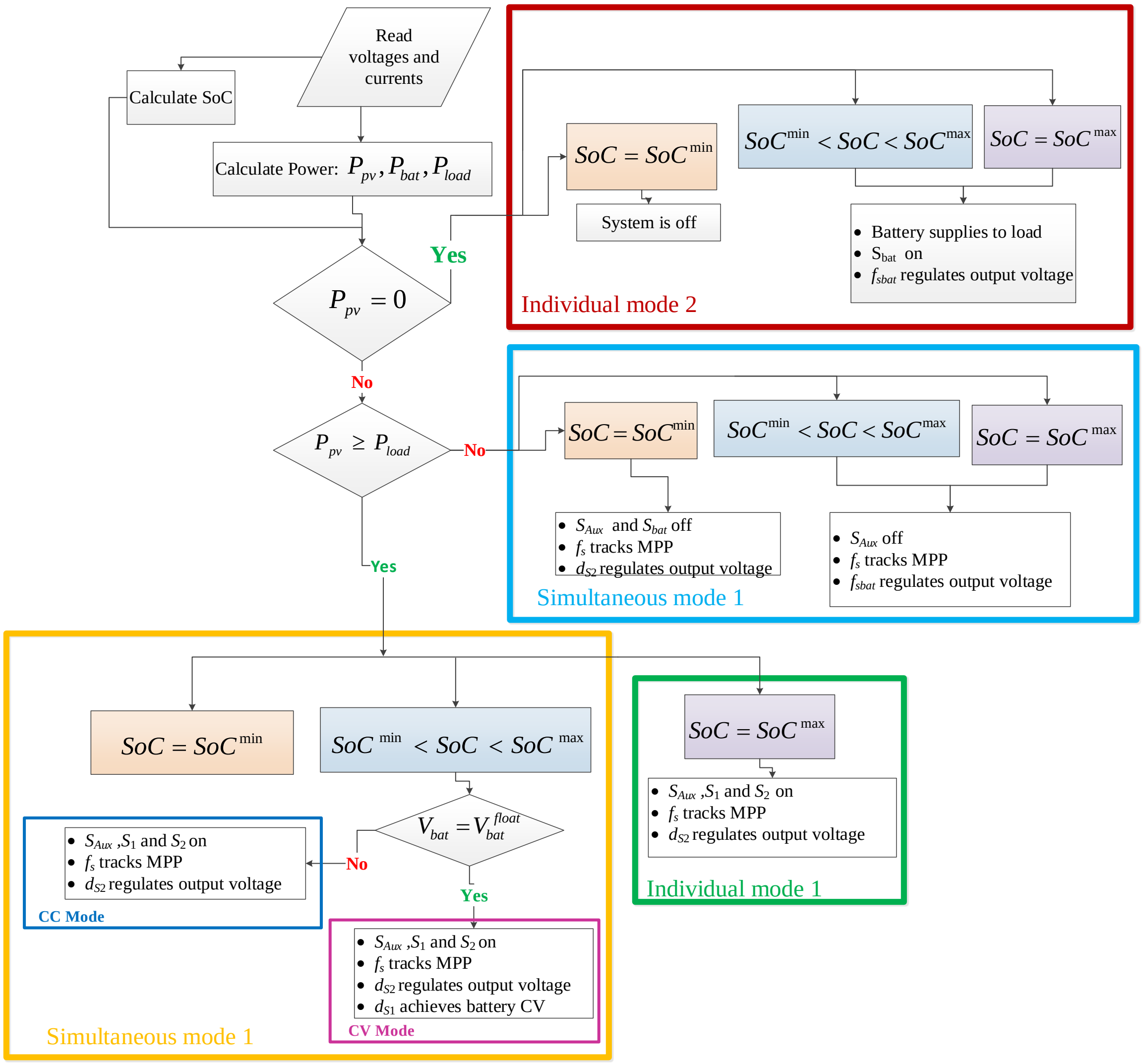

Figure 4-9 Control flow chart of the proposed converter

When the PV power is higher than the load demand and battery is not at its allowable maximum SoC, the simultaneous mode 1 occurs. There are two sub-modes under this mode of operation based on the battery voltage. If the battery voltage is the same as the battery float voltage, the converter is in CV mode. If the battery is lower than the battery float voltage, the converter is in CC mode. In the proposed system, the output side load is treated as the primary load and battery charging as the secondary load for the PV. Therefore, battery charging happens only with the power that is not used by the load (battery charging power= PV power-load power). If the light intensity and output side load remain same, the charging current will be the same. However, with the variation of light intensity or output side load, the charging current may vary. The varying charging current does not result in losing the capacity of the battery as long as it is not higher than the allowable limit. Rather, it varies the CV mode charging time. When the PV power is less than the load demand and battery SoC is higher than the allowable minimum level, the converter operates in simultaneous mode 2. The PV to load converter (power optimizer) extracts the maximum power from PV and supplies to the load. The remaining load demand (load demand- PV power) is supplied by the battery.

The control block diagram of the proposed converter is shown in Figure 4-10. The MPP is achieved by varying the switching frequency of the switch S_1 and the switching frequency of S_2 is the same as the switching frequency of S_1. The voltage regulation of the load side is achieved by the duty ratio of S_2 and the CV operation of the battery is achieved by the duty ratio of S_1 during PV battery charging simultaneous operation. The maximum current from a single panel is less than the allowable current of the battery pack in the CC mode, as the rated power of a single panel is limited to a few hundred watts. Therefore, the current limiter is not required. During PV battery discharge simultaneous operation, load side voltage regulation is achieved by the frequency control of the switch S_{bat}.

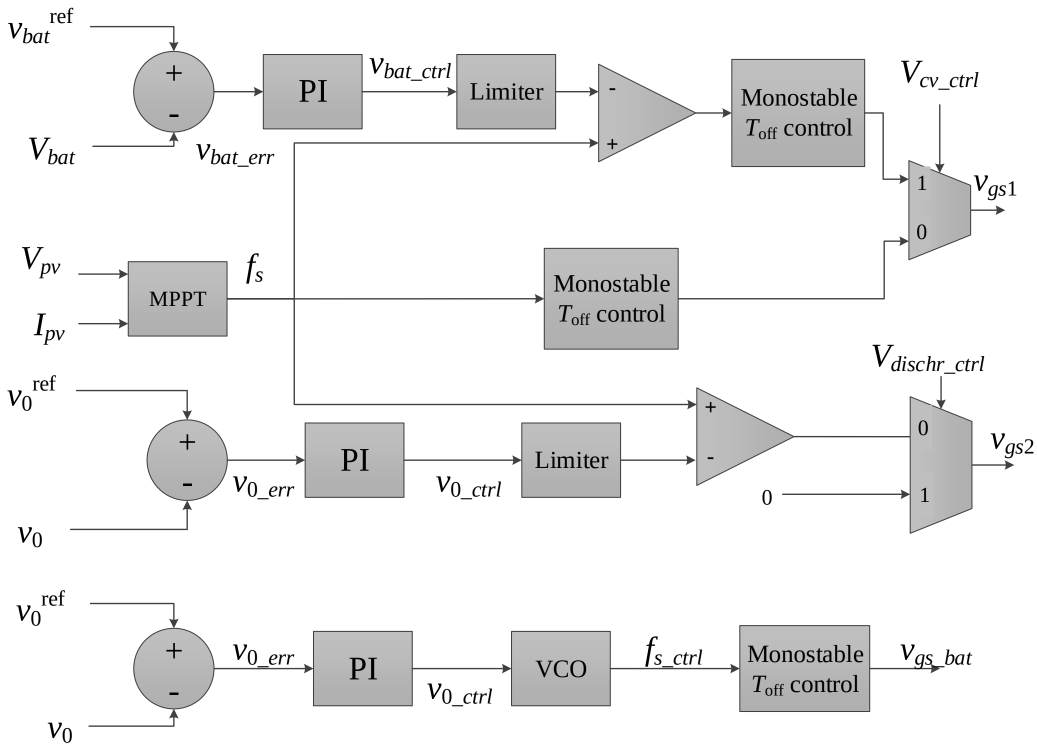

Figure 4-10 Control diagram of the proposed converter

The perturb and observe method presented in section 3.5.1 is used to achieve MPPT. The MPP block decides the switching frequency, f_s for the switch S_1 and S_2. $V_{cv\_ctrl}^{bat}$ is 1 during CV battery charging mode and $V_{dischr\_ctrl}^{bat}$ is 1 during battery discharge mode. During PV battery discharge simultaneous operation, the switch S_2 remains off. A voltage-controlled oscillator (VCO) is used for the variable frequency control of the switch S_{bat}. Monostable multivibrator is used for constant T_{off} control of switches S_1 and S_{bat}.

The mathematical representation of the output voltage regulation and the battery side CV charging is shown by Eq. 4-22 and Eq. 4-23 where the control perturbations are $\hat{T}_c(s)$, and $\hat{f}_{sbat}(s)$ (the switching frequency of S_{bat}). $T_c(s)$ is defined in Eq. 4-24 where d_1 and d_2 are the duty ratio of switch S_1 and S_2 and T_s is the time period of switch S_1 and S_2.

$$\hat{v}_0(s) = G_{v2}\,\hat{T}_c(s) + G_{vb}\,\hat{f}_{sbat}(s) \qquad \text{Eq. 4-22}$$

$$\hat{v}_{bat}(s) = G_{v1}\,\hat{T}_c(s) \qquad \text{Eq. 4-23}$$

$$T_c(s) = \frac{1}{s}\left(\frac{d_1 - d_2}{T_s}\right) = \frac{1}{s}\left(t_{c1} - t_{c2}\right) \qquad \text{Eq. 4-24}$$

$$\hat{\omega}_{sbat} = \omega_{VCO} - K_{VCO}.V_{ctrl} \qquad \text{Eq. 4-25}$$

The VCO is used for the frequency control of the battery discharging circuit. The relation between the control voltage and the output switching frequency is shown in Eq. 4-25(15) where K_{VCO} is the VCO gain and ω_{VCO} is the quiescent frequency of the oscillator. Ziegler–Nichols tuning method is used to tune the PI parameters. The objective of PI is to boost the low-frequency loop gain to minimize the steady-state error while maintaining a sufficient phase margin.

The stability of three controllers of the converter is verified by closed loop bode plot as shown in Figure 4-11. The bode plot is performed in PSIM. Figure 4-11 (a) shows the stability of the control loop for output voltage regulation by the switch S_2. The bode plot shows two different load conditions: full load and 10% load. Phase margin (PM) at full load is 58deg, whereas phase margin at 10% load is 88deg. Figure 4-11 (b) and (c) show the bode plot of the control loops for output voltage regulation by S_{bat} and battery side voltage regulation in CV mode by switch S_1 respectively. The phase margin for the control loop of S_{bat} is 37 deg and the phase margin for the control loop of S_1 is 112 deg.

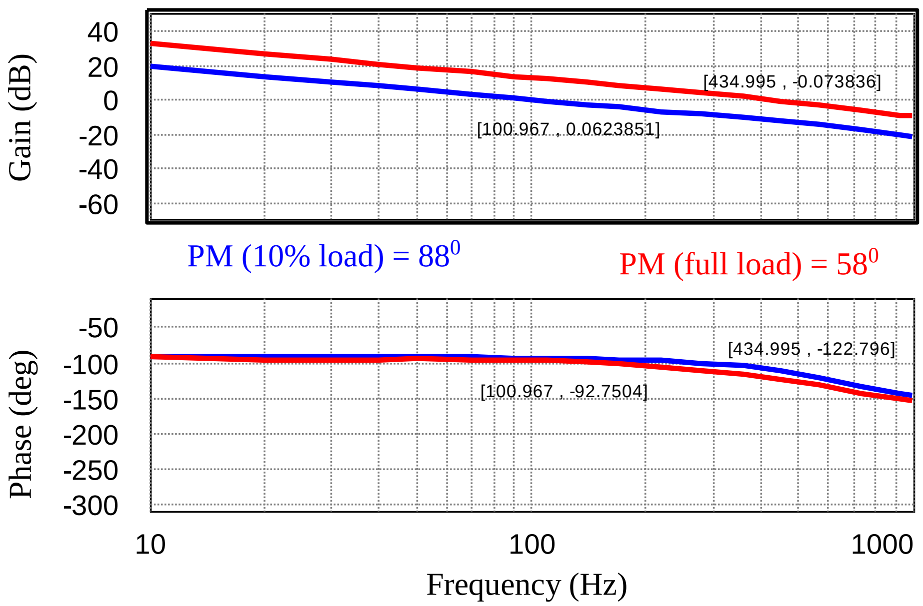
Gain (dB)
40
20
0
-20
-40
-60
[434.995 , -0.073836]
[100.967 , 0.0623851]
PM (10% load) = 88⁰
PM (full load) = 58⁰
Phase (deg)
-50
-100
-150
-200
-250
-300
[434.995 , -122.796]
[100.967 , -92.7504]
10
100
1000
Frequency (Hz)

(a)

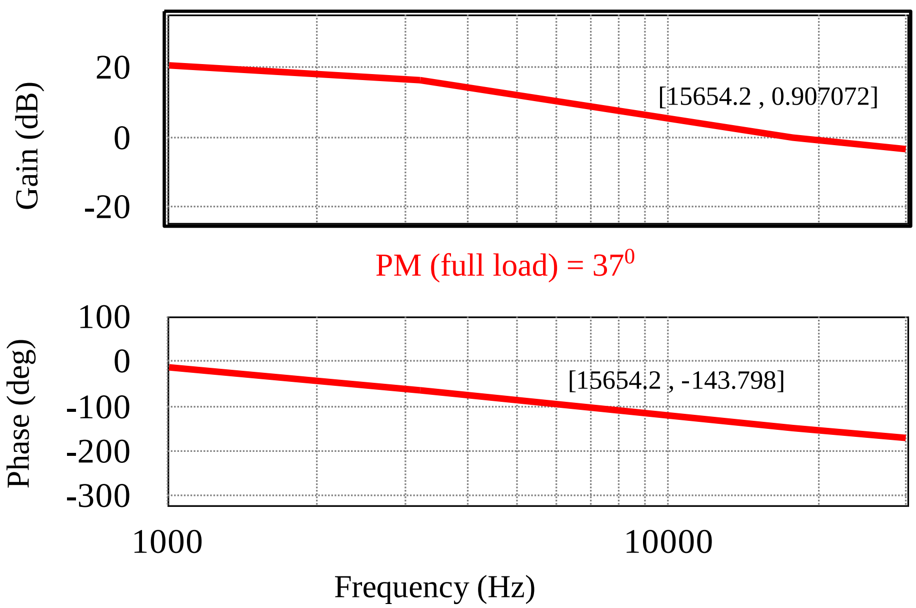
Gain (dB)
20
0
-20
[15654.2 , 0.907072]
PM (full load) = 37⁰
Phase (deg)
100
0
-100
-200
-300
[15654.2 , -143.798]
1000
10000
Frequency (Hz)

(b)

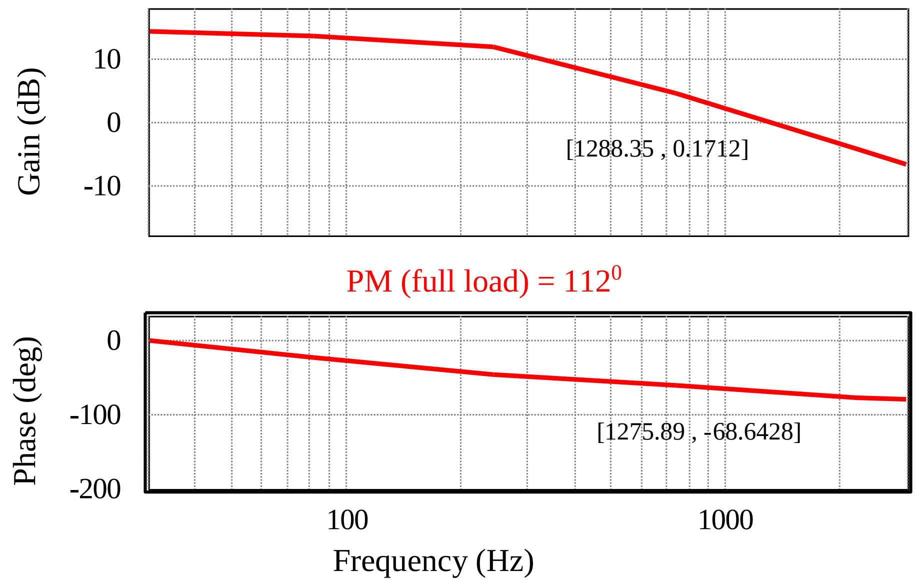

(c)

Figure 4-11 Closed loop bode plot (a) output voltage regulation with different load condition (full load and 10% load) for output voltage regulation by switch S_2 (b) Output voltage regulation by switch S_{bat} (c) battery voltage regulation (CV mode) by switch S_1

4.6 Performance Analysis of the Proposed Converter

To evaluate the performance of the proposed converter, the converter is designed, simulated in PSIM and performed experimental testing on proof-of-concept prototype. The commercial PV panel OPT315-72-4-100 and NT-175U1-SHARP used for this work are the same as the PV panel used in previous work presented in Chapter 3. The equivalent resistance of the commercial battery (HE-4813) is also presented in Chapter 3.

4.6.1 Design Procedure of the Proposed Converter

A 48V, 175W prototype is designed for the simulation and experimental work. The closed-form gain equation cannot be found analytically for ZVS-MRC as mentioned in section 3.3. Therefore, numerical analysis is used to present the characteristics of ZVS-MRC. The voltage gain range increases with the increase of C_N as shown in Figure 4-7 (a). However, the switch stresses (voltage and current) increase with the increase of C_N. Therefore, the tradeoff between the switch stresses and the voltage gain range is required. The minimum C_N for the required voltage gain is 3 for this design. The load to voltage gain curve with respect to the switching frequency for C_N=3 is shown in Figure 4-7 (b). For this design normalized switching frequency f_N is selected as 0.6. The switching frequency is chosen 300kHz. The resonant inductor L_r and C_{r1} are selected from Eq. 4-26 and then the resonant capacitor C_{r2} is calculated from Eq. 4-6.

$$f_N = {f_s}/{f_{r1}} = 2\pi f_s \sqrt{L_r C_{r1}} \qquad \text{Eq. 4-26}$$

The voltage gain of the battery charging converter is governed by Eq. 4-27, where d_{s1} is the duty ratio of switch S_1 and d_{s1} is found from the off time required for the switch S_1 to maintain soft-switching. The duty ratio is taken 0.65 for the design. Therefore, the value of n is 0.5 for the minimum input voltage 25V. The transformer leakage inductance and switch parasitic components add up with the resonant components. Therefore, transformer design and components selection become simple. The magnetizing inductance, L_m of the input transformer is calculated by Eq. 3-48 as described in section 3.6.1.

$$m_{pv\_bat} = \frac{V_{bat}}{V_{pv}} = \frac{1}{n}\frac{d_{s1}}{1-d_{s1}} \qquad \text{Eq. 4-27}$$

The battery discharging circuit is designed in a similar way as explained in section 2.5.1 and 3.6.1. The components list of the designed converter is shown in Table 4-2.

Table 4-2 Circuit parameters of the designed converter

Components	***Part number***	***Component Value***
PV	NT-175U1	35.4V, 175W
Battery	HE-4813	48V, 13 Ah
f_s		250kHz-350kHz
L_r, L_{r_bat}, L_{bat}	SER2915H	10μH, 22μH, 22μH
C_{r1}, C_{r2}, C_{r_bat}	MKP383	18nF, 47nF, 6.8nF
L_{mag}		47μH
S_1, S_2, S_{bat}	STP24N60DM2-EP	600V, 18A
D_1, D_{bat1}	MUR1560	600V, 15A
C_f, C_1, C_{bat1}	ECQ-E1106JF	10 μF

4.6.2 Simulation Results

A 48V, 175W prototype is simulated in PSIM to demonstrate the functionality and the performance of the proposed converter. The commercial PV panel (OPT315-72-4-100) is used for the simulation work at the light intensity 600W/m^2 and 400W/m^2.

Figure 4-12 shows the available power from the PV and the actual power extracted from the PV for the light intensity 600W/m^2 to 400W/m^2. The tracking time is less than 2ms and MPP efficiency is over 99.9%. The allowable switching frequency for the designed converter is 150kHz to 350kHz to ensure soft-switching.

The battery charging voltage and the output side voltage are regulated by the duty ratio of the switch S_1 and S_2 respectively. Figure 4-13 and Figure 4-14 show the voltage regulation of the output side with the change of light intensity in CV and CC mode respectively. In CV mode, the battery charging voltage is also tightly regulated at the float voltage as shown Figure 4-13. In CC mode, when the light intensity increases, the battery charging current increases as the output load is fixed (Figure 4-14). Moreover, the battery charging current is much lower than the maximum allowable battery charging current. This confirms that the current limiter circuit is not necessary. The settling time is less than 7ms.

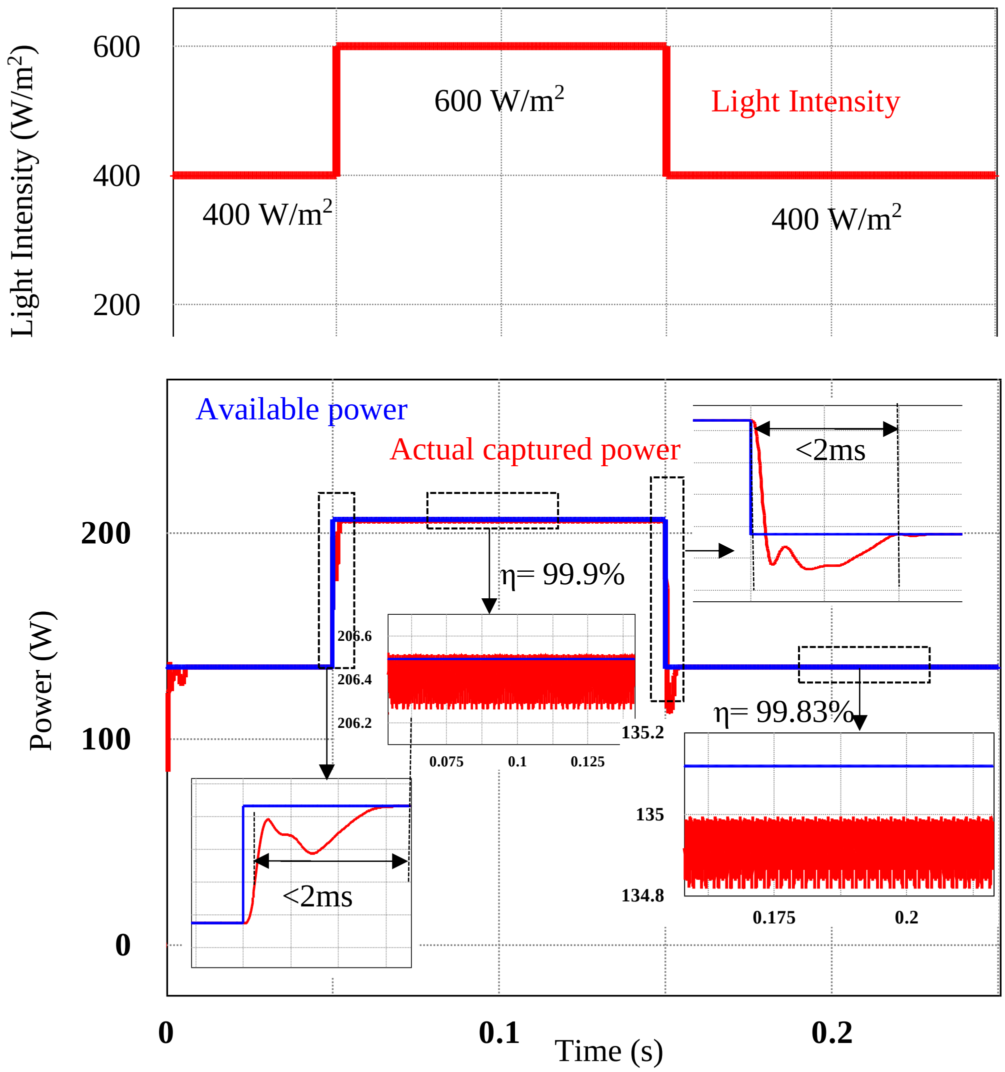

Figure 4-12 MPPT with the change of light intensity from 600W/m^2 to 400W/m^2 in simultaneous mode 1

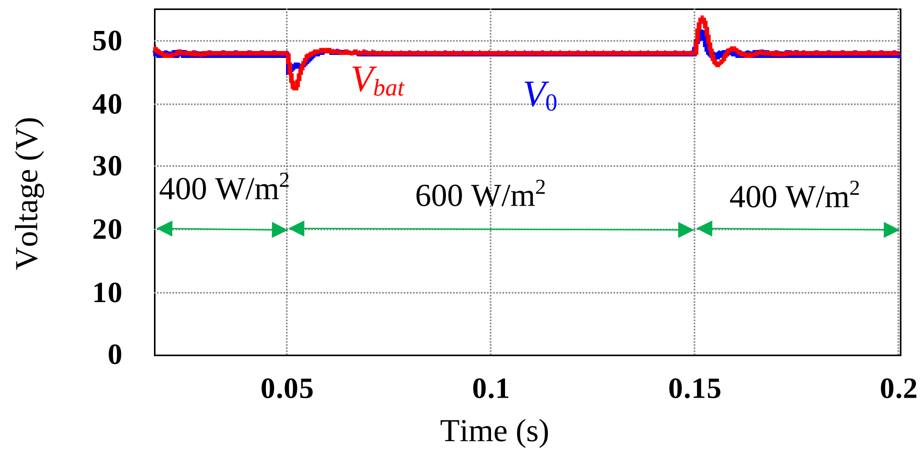

Figure 4-13 output voltage regulation and CV battery charging voltage with the change of light intensity from 600W/m^2 to 400W/m^2 in simultaneous mode 1

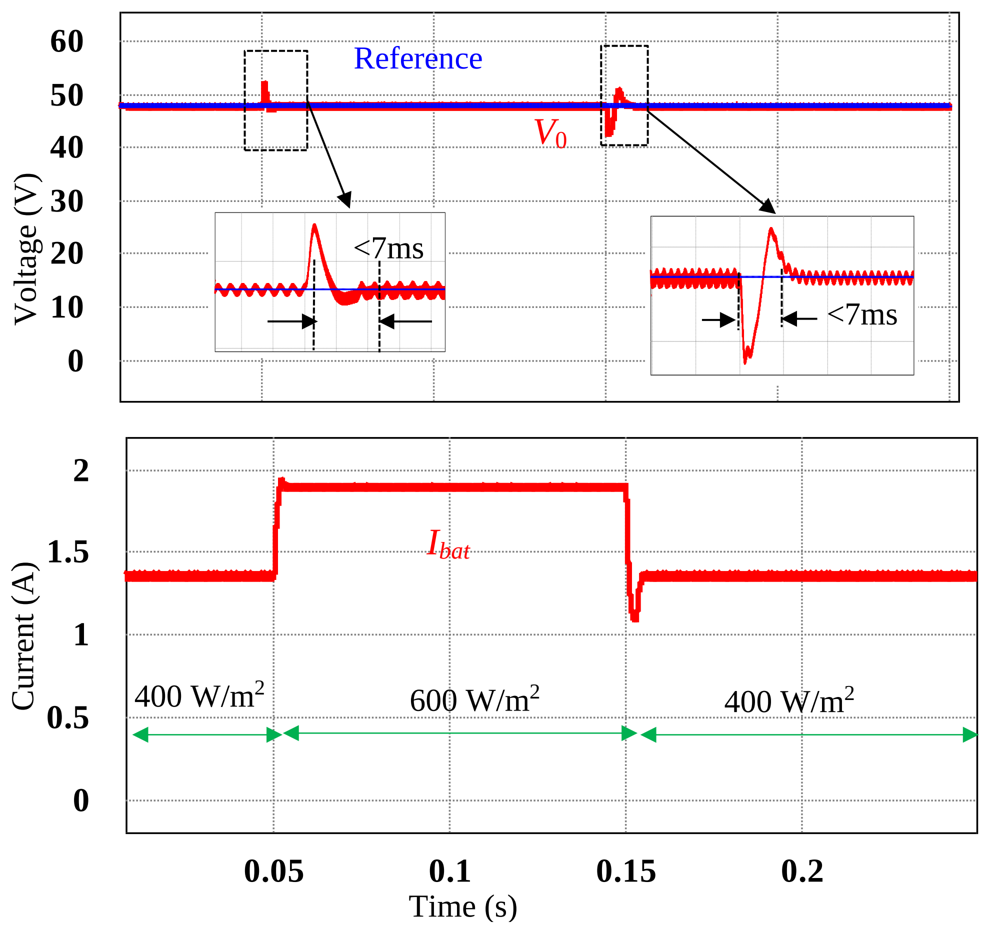

Figure 4-14 Output voltage regulation and CC battery charging with the change of light intensity from 600W/m^2 to 400W/m^2 in simultaneous mode 1

The voltage regulation with 40% of load change is shown in Figure 4-15. The light intensity remains the same throughout the time period. In the beginning, the load is 60% of full load and at 0.15ms, the output load increased to full load. To supply the additional 40% new load, the battery charging current becomes low. The controller settling time for load change is less than 9ms and the voltage ripple is less than 0.5V.

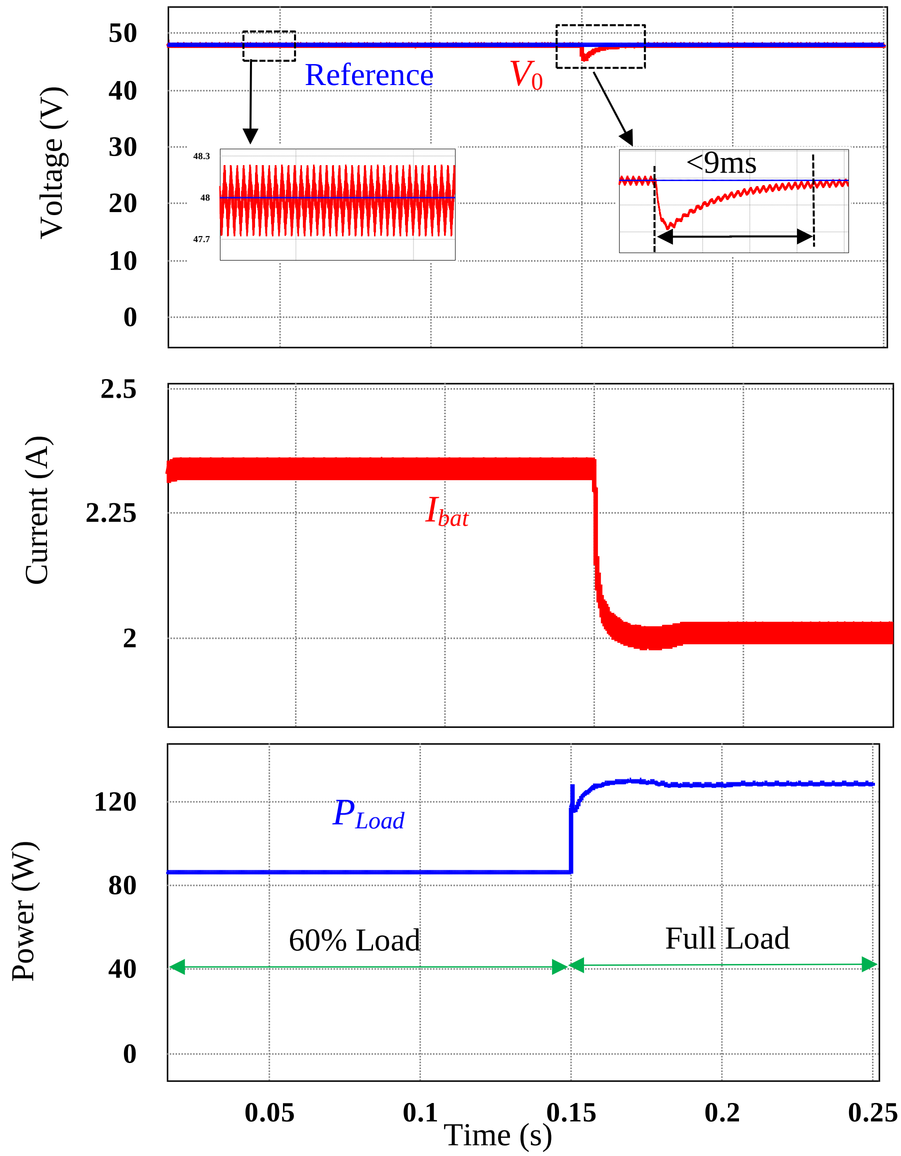

Figure 4-15 Output voltage regulation, output voltage ripple, settling time, battery charging current and load power with the change of load

The voltage regulation for the simultaneous operation mode 2 (PV to load and battery discharge) is shown in Figure 4-16. As the light intensity increases, the power from PV increases and supply from the battery decreases to ensure the maximum use of PV power. On the contrary, with the decrease of light intensity, supply from battery increases to support the load. The power to the load remains the same throughout the time period.

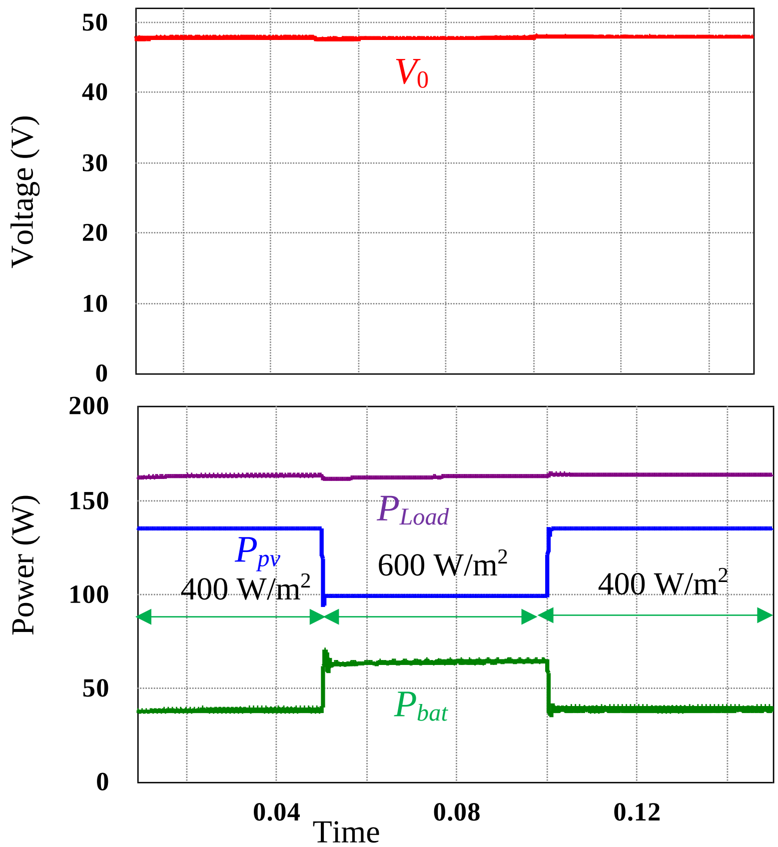

Figure 4-16 Output voltage regulation and PV, battery, and load power with the change of light intensity from 400W/m^2 to 200W/m^2 in simultaneous mode 2

For all cases, soft switching of all switches is ensured. The switching waveforms for switch S_1 and S_2 for the simultaneous operation mode 1 (PV load and battery charging) mode are shown in Figure 4-17. The switching frequency f_s is the same for switch S_1 and S_2. However, the duty ratio d_1 and d_2 are different. The red shaded area shows the turn on situation of the switch S_1 and S_2 and confirms the ZVS turn on for both switches. The blue shaded area shows the turn off situation of the switch S_1 and also confirms the ZVS turn off for the switch S_1.

The switching waveforms for simultaneous operation mode 2 (PV to load and battery discharge) are shown in Figure 4-18. The switch S_2 is off during this operation. However, the antiparallel diode of switch S_2 conducts and current is discontinuous through the antiparallel diode of switch S_2. The switching frequency of S_1 and S_{bat} is different. The red and blue shaded area show the turn on and turn off situation respectively for the switch S_1 and S_{bat}. Figure 4-18 confirms the soft switching of S_1 and S_{bat}.

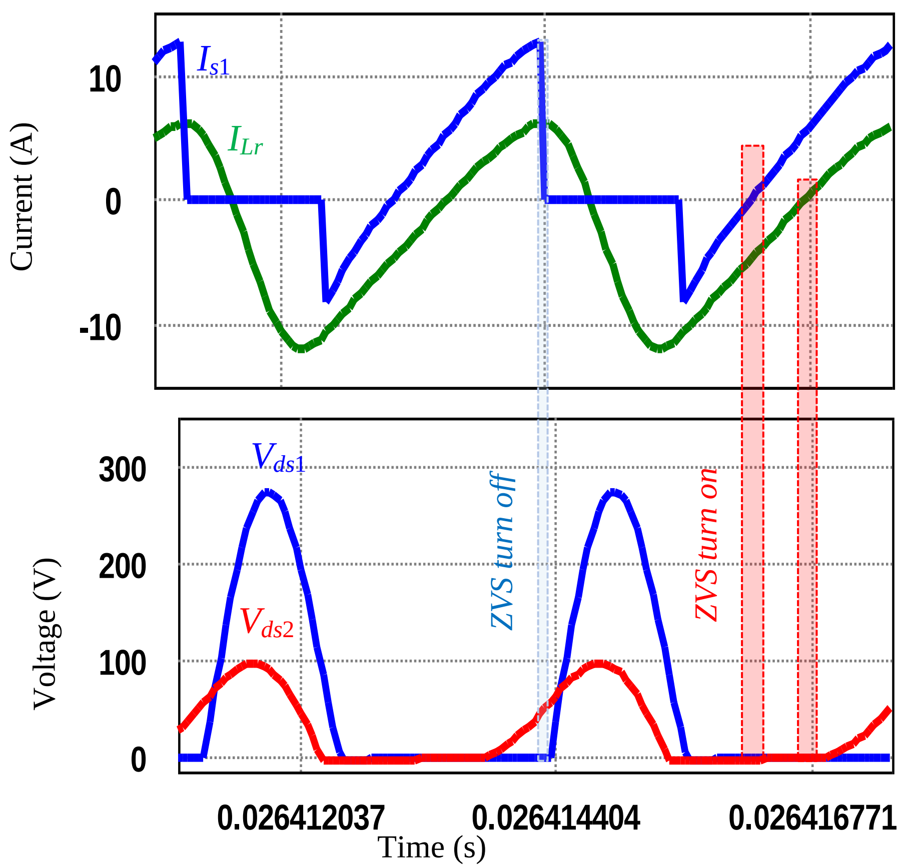

Figure 4-17 Soft switching operation of S_1 and S_2 in simultaneous mode 1

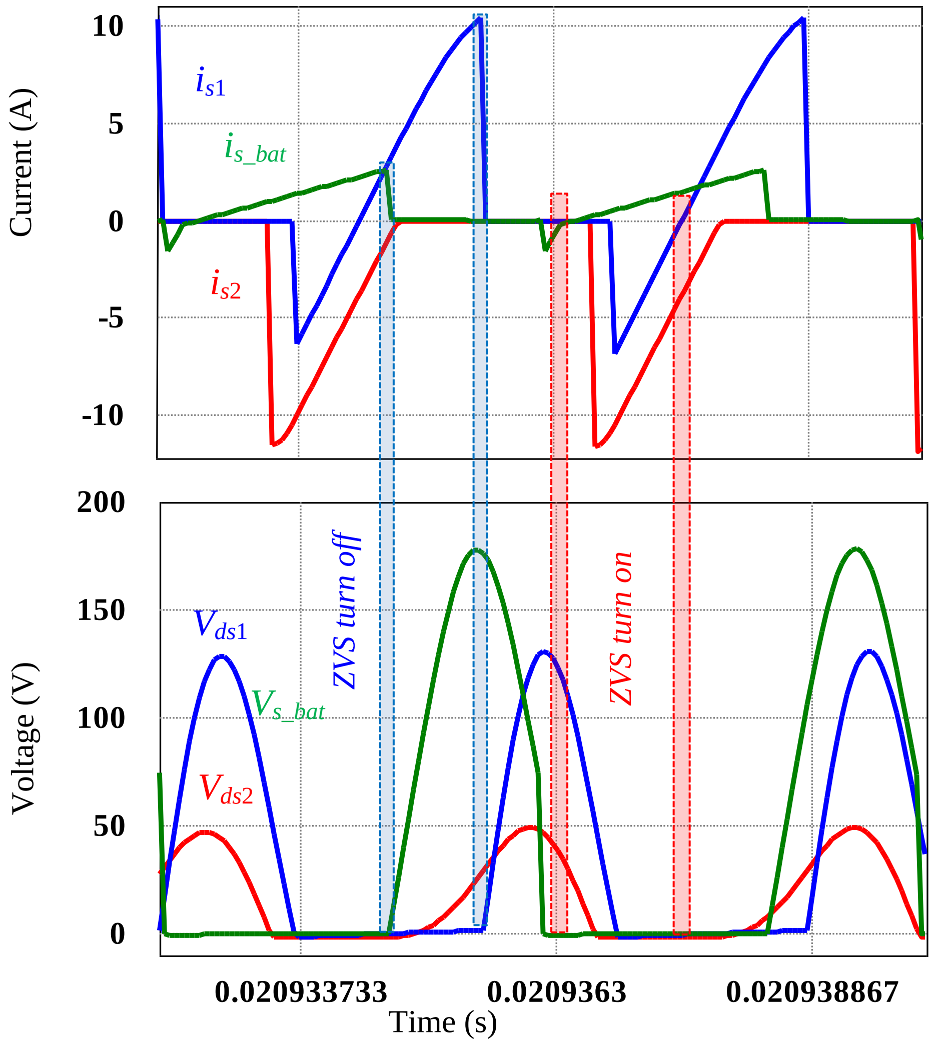

Figure 4-18 Soft switching operation of S_1, S_2, and S_{bat} in simultaneous mode 2

4.6.3 Experimental Results

A 48V-output, 175W prototype is built and tested in the laboratory. For experimental work, E4360A (1200W) PV emulator from *Keysight* is used. Two units of E4360A are paralleled to replicate the NT-175U1 single PV panel as each unit (300V and 2.5A) of the two units is capable to supply maximum 2.5A. The experimental prototype is shown in Figure 4-19.

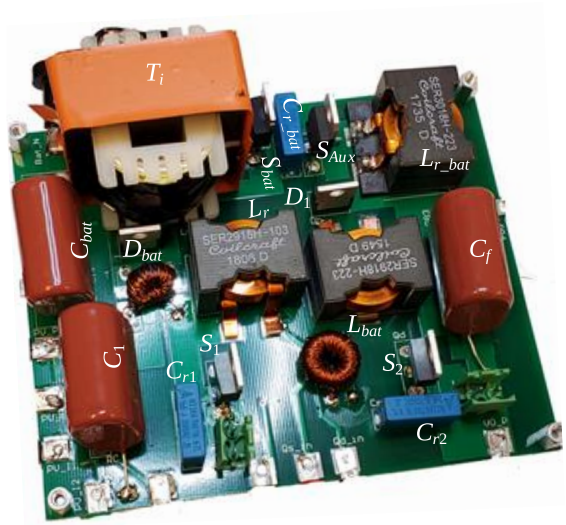

Figure 4-19 Experimental prototype of the proposed converter

The web interface of the PV emulator is shown in Figure 4-20. Figure 4-20 shows the channel 2 of the two channels. The V-I and V-P curves are shown. The MPP, voltage, and current at MPP, operating point and MPP efficiency are also shown in Figure 4-20. In all cases, the MPP and the operating point is observed using this web interface and ensures MPP efficiency over 99.5%.

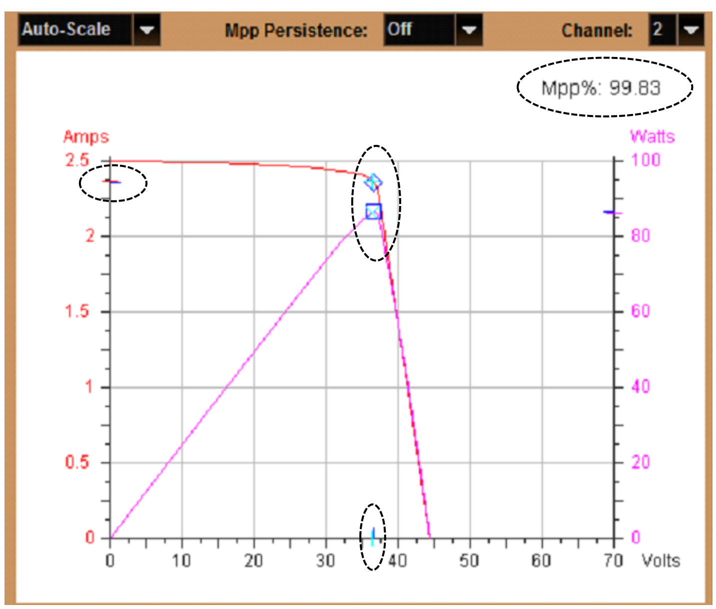

Figure 4-20 MPP tracking and MPP efficiency of the proposed converter in simultaneous mode 1

Figure 4-21 shows the individual operation mode 1 (PV to load). The input voltage is 36V and the output voltage is 48V with an efficiency of 96.3%. Figure 4-22 shows the sub-modes (CV) of simultaneous operation mode 1. Both the output voltage and battery voltage are at 48V. The battery charging current is only 0.9 A.

Figure 4-23 shows the CC mode of operation while the output load and light intensity remains same. The equivalent resistor of the battery in CC mode varies from 15ohm to 20ohm. Experimental work is done for two extremes of CC mode and shown in Figure 4-23. The battery charging current remains same whereas the battery voltage is increased.

The voltage regulation with a step change in the input voltage is shown in Figure 4-24. As the light intensity changes from 1000 W/m^2 to 800 W/m^2. The switching frequency and the duty ratio changes accordingly to achieve MPP and regulate the output voltage. The converter settling time is 80ms and the voltage ripple is less than 1V.

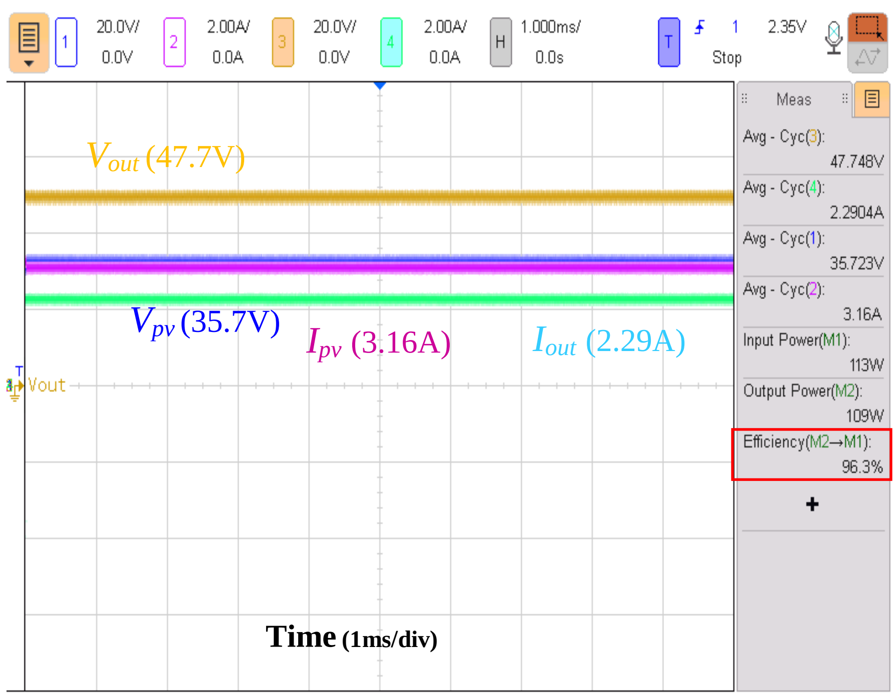

Figure 4-21 Input and output voltage and current of individual operation mode 1

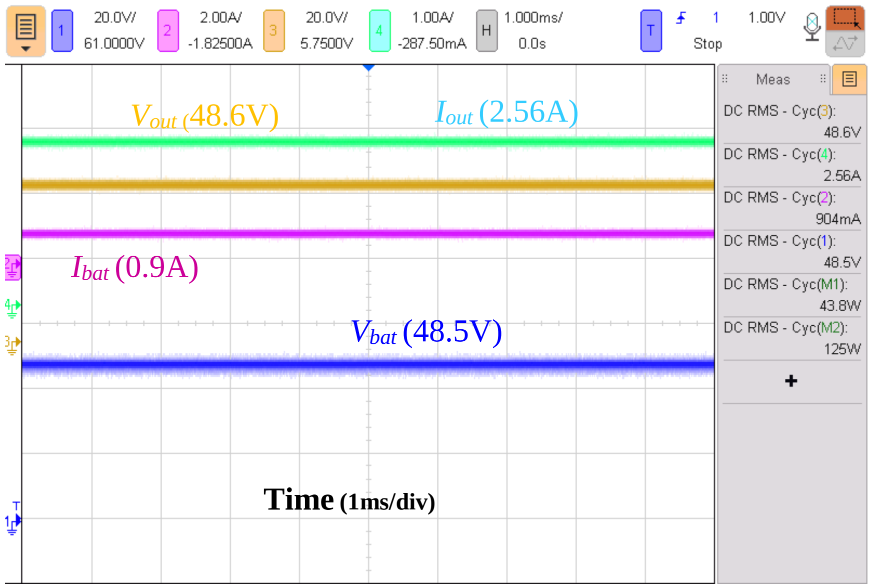

Figure 4-22 CV sub-mode of simultaneous operation mode 1

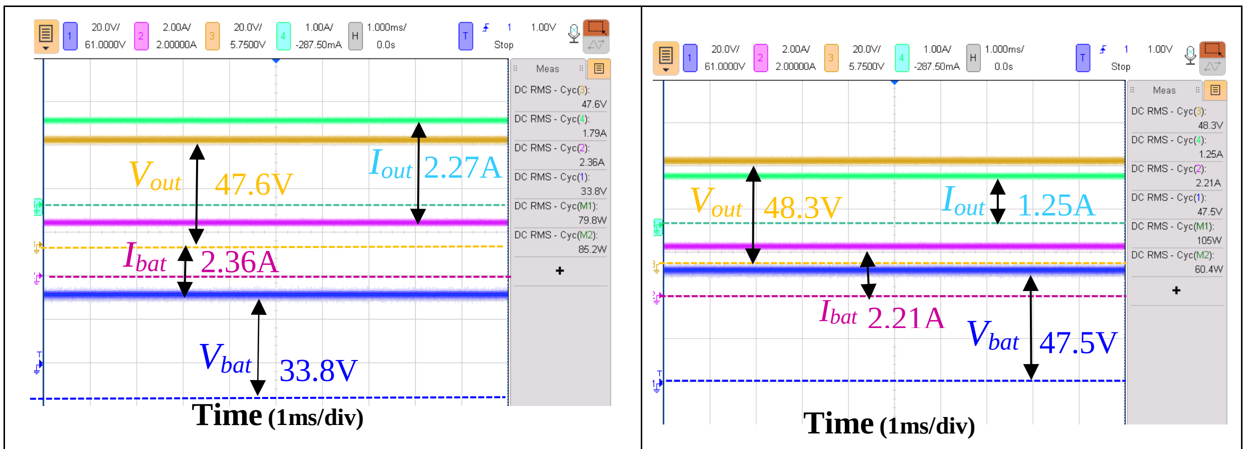

(a) (a)

Figure 4-23 CC sub-mode of simultaneous operation mode 1 (a) at the beginning of CC mode (b) at the end of CC mode

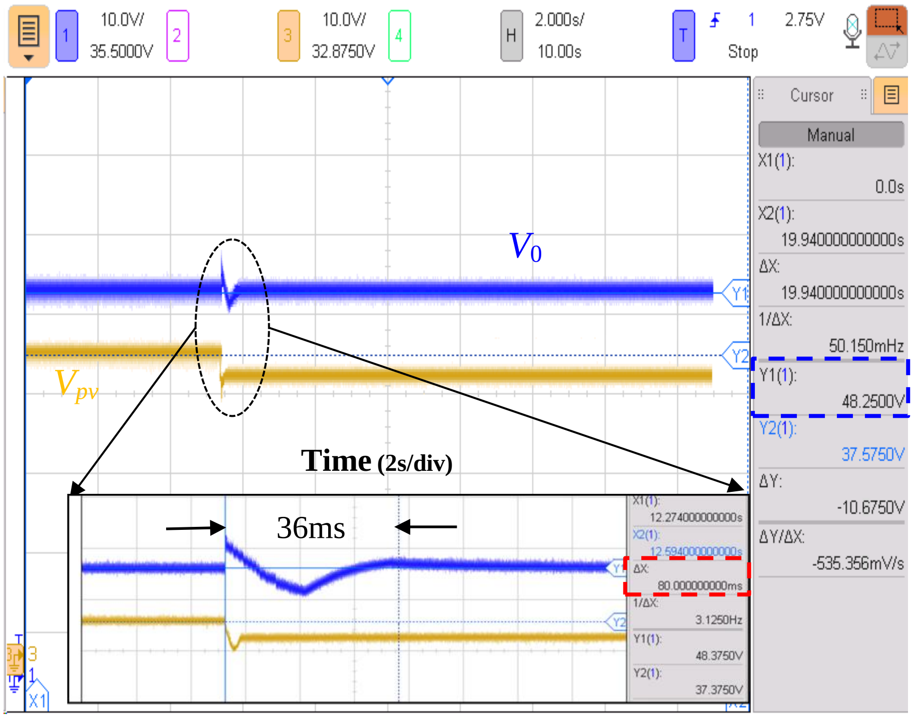

Figure 4-24 Output voltage regulation with the change of input voltage (with the change of light intensity) in simultaneous mode 1

The voltage regulation when the output changes from full load to 60% load is shown in Figure 4-25. For 60% load, the duty ratio of the switch S_2 is 51.6% and for full load, the duty ratio of the switch S_2 is 38%. The converter settling time is 36ms and the voltage ripple is less than 1V. Figure 4-26 shows the primary and secondary side current of the input transformer T_i for simultaneous mode 1.

Figure 4-27 presents the performance of the converter for the transition from simultaneous operation mode 1 to the individual operation mode 1. The battery voltage and current become zero in individual mode 1. As the output voltage remains the same in simultaneous and individual mode, the output current increases in individual mode to balance the power. The settling time is 80ms. Figure 4-28 demonstrate the switching waveforms of the switch S_1 and S_2 for different duty ratio d_2 while regulating the output voltage. The switching frequency is

250kHz. The switching voltage and current waveforms for simultaneous operations mode 1 and 2 are shown in Figure 4-29. The maximum voltage stress 201V for the switch S_1 happens during the simulation operation PV to load and battery discharge. The maximum voltage for the switch S_2 and S_{bat} is much lower: 89V for S_2 and 72V for S_{bat}. The current stress of the switches S_1, S_2 and S_{bat} are 10A, 8.5A, and 3.8A respectively.

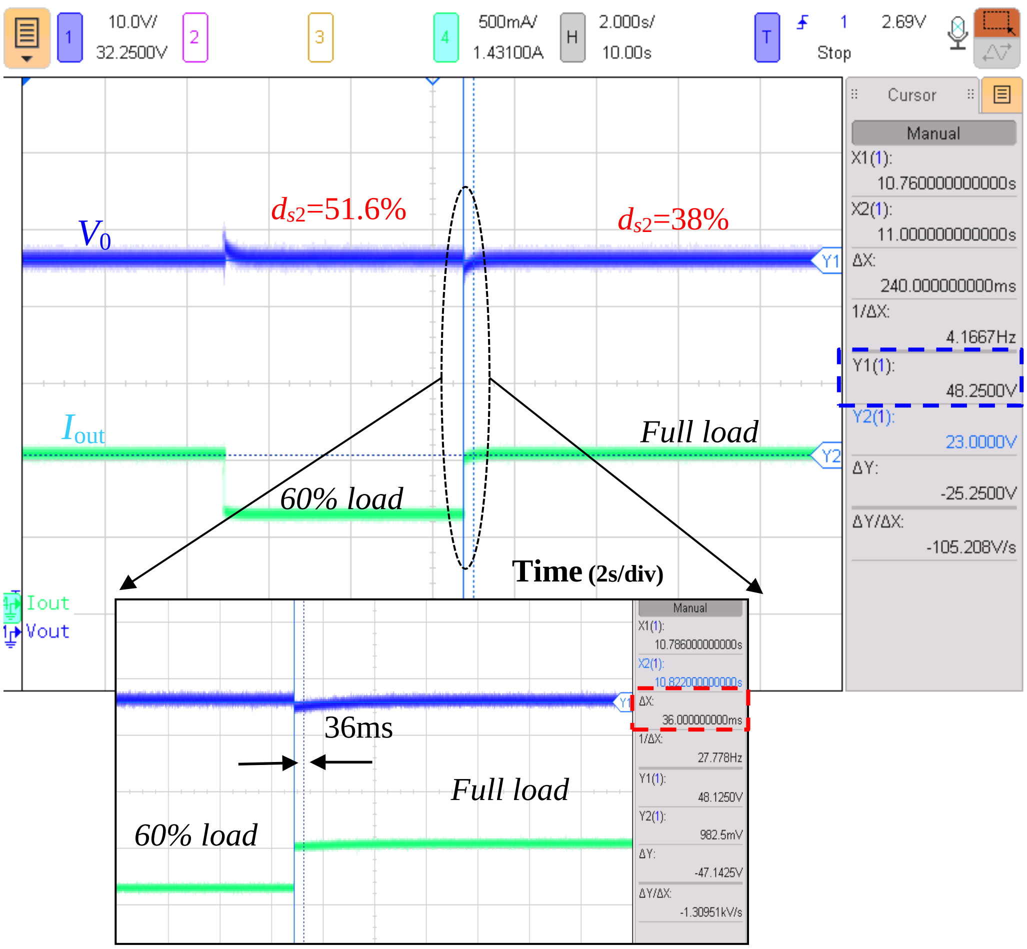

Figure 4-25 output voltage regulation with the change of load in simultaneous mode 1

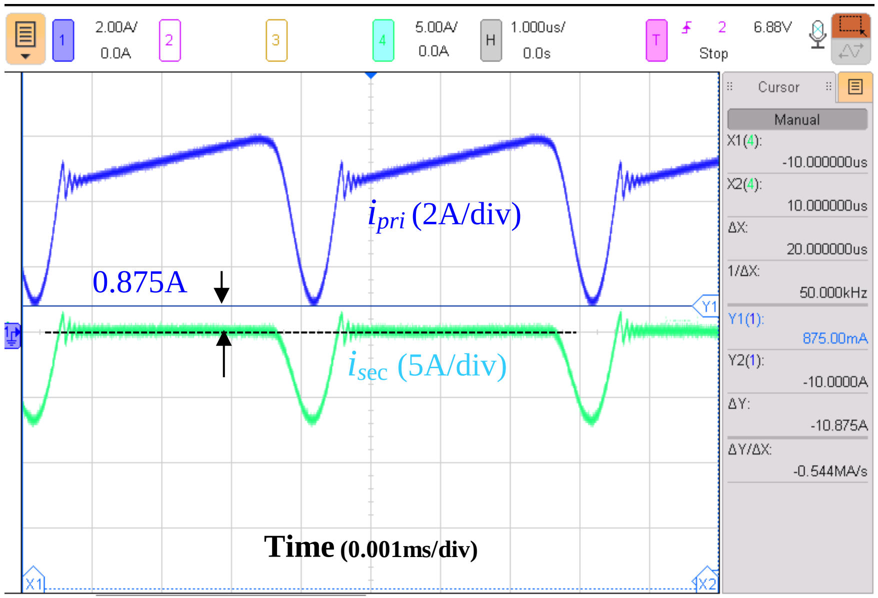

Figure 4-26 Continuous input current in simultaneous mode 1

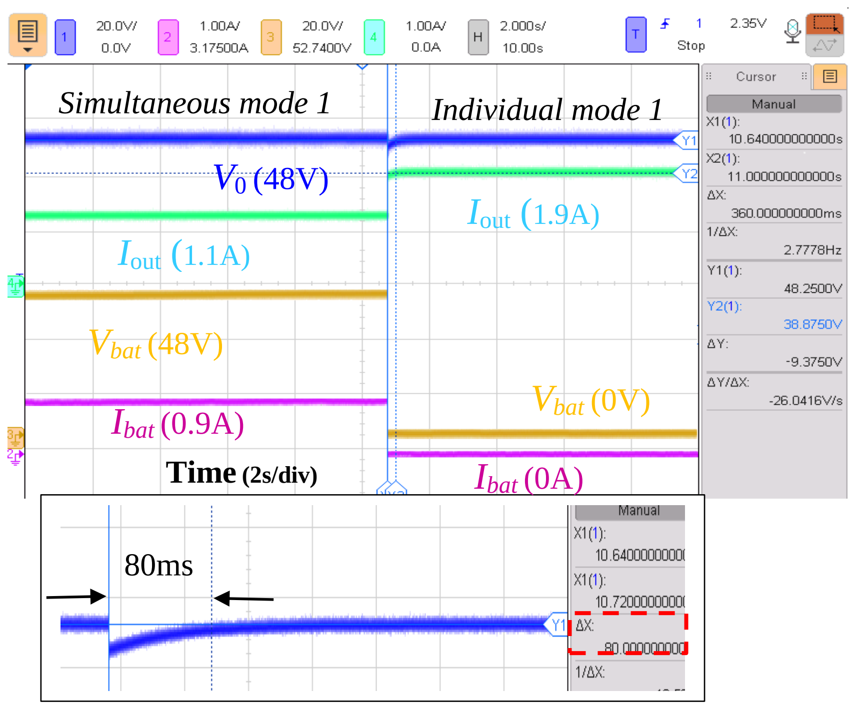

Figure 4-27 Transition from simultaneous mode 1 to individual mode1

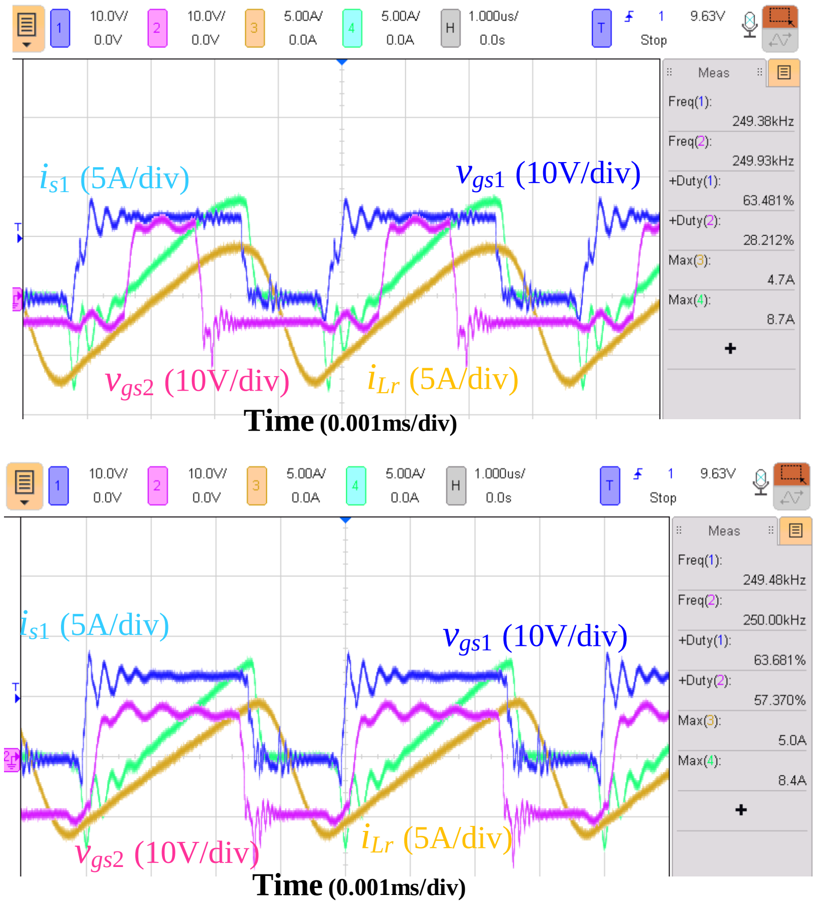

Figure 4-28 Simultaneous mode 1: switching waveforms at different duty ratio: d_2 =28.21% (top) and d_2 =57.4% (bottom)

The efficiency of the simultaneous operations of the proposed converter is shown in Figure 4-30. The efficiency is over 95% for the full load range. The efficiency curve drops at 60% load for simultaneous mode 2 where PV and the battery are supplying to the load. The change is observed because of percentage of the load sharing between the battery and load. Up to 60% load, the change of the load is equally shared by the PV and battery. That means at 90% of load, the PV is generating 90% of the power generated by the PV at 100% load (90% 0f 125W) and the battery is also supplying 90% of the battery contribution during 100% load (90% of 50W). From 50% to 30% of load condition, battery supply is constant to

30W and for 20% and 10%, only PV is supplying to the load. The efficiency of the MR converter is almost same throughout the load range.

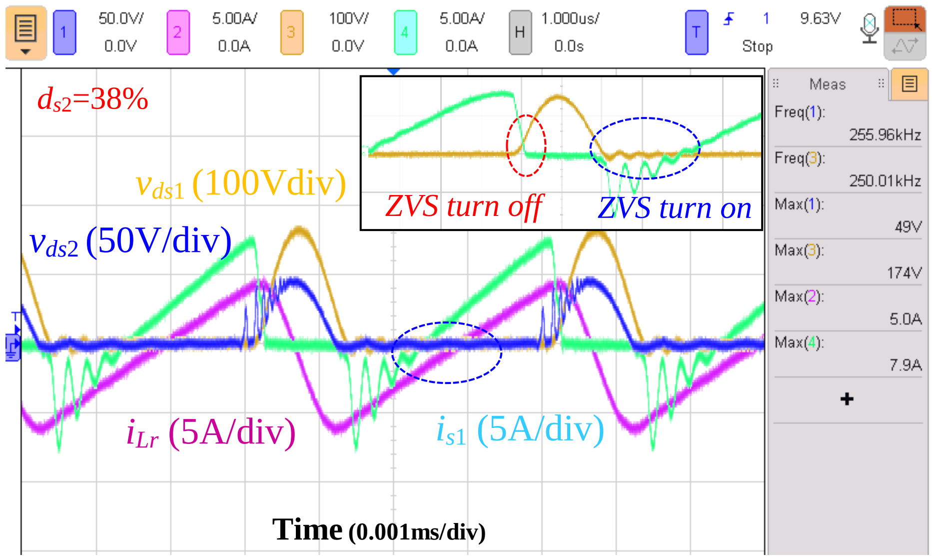

(a) Mode 1

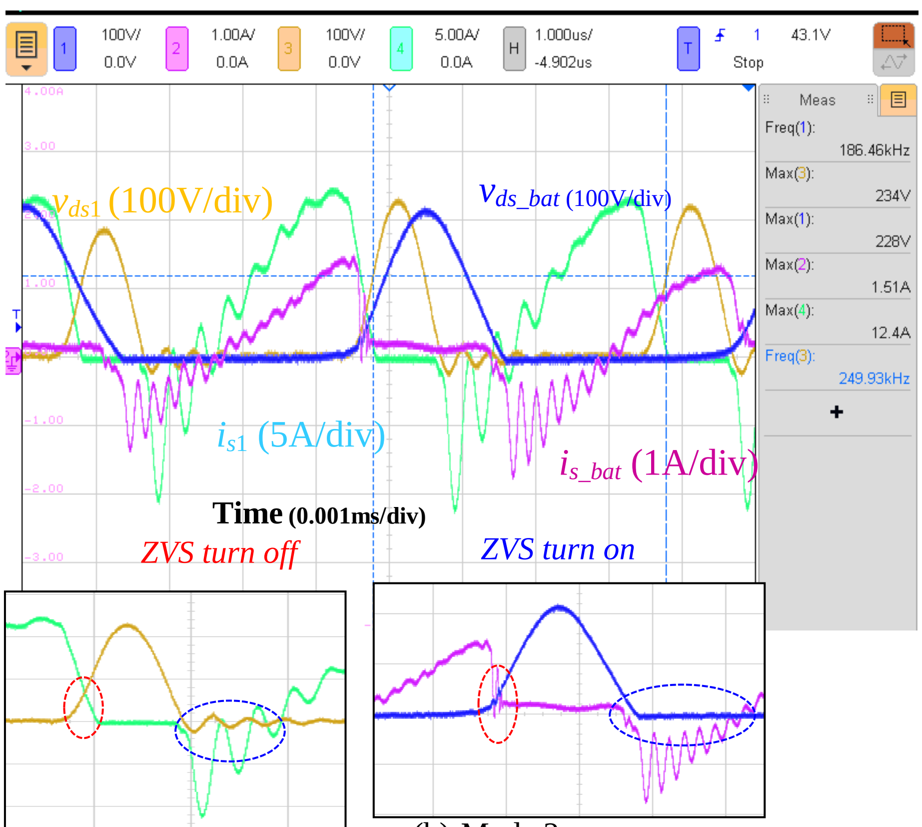

(b) Mode 2

Figure 4-29 Soft switching operations in simultaneous operation (a) mode 1 (b) mode 2

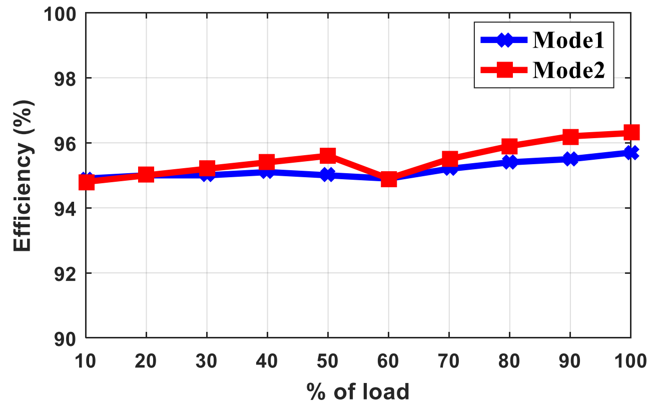

Figure 4-30 Efficiency of the proposed converter in simultaneous mode 1 and 2

The loss breakdown of the key components of the proposed converter as a percentage of total loss is shown in Figure 4-31. Loss in the resonant components is negligible as the components are very small as well as their ESR. A comparison between MICs presented in Table 1-2 and converters proposed in Chapter 3 and Chapter 4 are presented in Table 4-3 based on several features. The proposed converters offer better control of the system with fewer active components compared to other MICs. The proposed converters utilize higher switching frequency and achieved soft switching for all the switches. The efficiency of the proposed converters is higher in comparison to other converters.

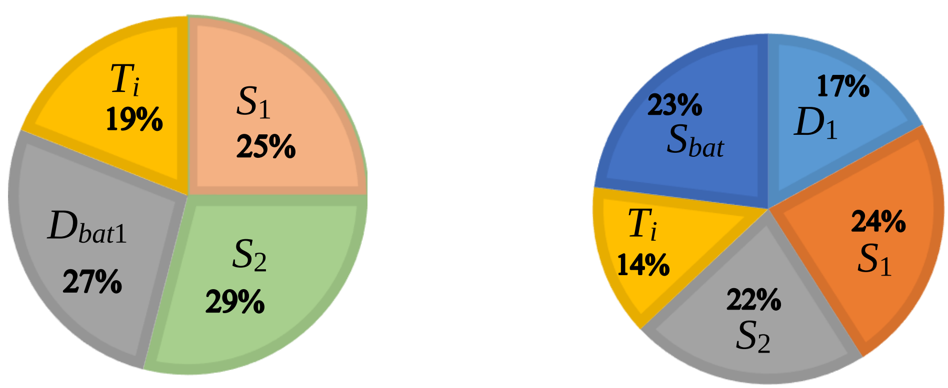

(a) Simultaneous mode 1 (b) Simultaneous mode 2

Figure 4-31 Loss breakdown of the key components in percentage of the total loss

Table 4-3 Comparison of MICs presented in the literature and the proposed MICs for PV-battery system

		[57]	[79]	[80]	[81]	MIC Proposed in Ch.3	MIC Proposed in Ch.4
No. of components	**Switch**	6 (HF)	3 (HF)	4 (HF)	5 (HF)	2 (HF) 1(LF)	3 (HF) 1(LF)
	Diode	4	5	5	-	3	2
	Inductor	3	1	-	2	4	3
	Capacitor	8	3	9	2	4	3
	Coupled Inductor	-	1 (2W)	2 (2W)	1 (4W)	1 (2W)	1 (2W)
Soft-switching		No	No	Yes	Yes	Yes	Yes
MPPT for all operating modes		No	No	Control mechanism not reported	No	No	Yes
Rated power		150W	300W	150W	200W	175W	175W
Switching frequency		100kHz	50kHz	50kHz	50kHz	300kHz	350kHz
Double power process issue of the battery circuit		Yes	Yes	No	Yes	No	No
Efficiency		87%	94.3%	95.8%	90.1%	97.1%	96.2%
* W- no. of winding, HF- high frequency, LF- low frequency ** No filter (input and output) components are counted *** MICs comprise of 1 PV module and 1 battery module							

4.7 Chapter Summary

In this chapter, an integrated battery storage for the PV system with output voltage regulation is presented. The battery charging circuit (ZVS-QR flyback converter) is integrated at the front end of the PV power optimizer (ZVS-MR boost converter). The battery discharge (ZVS-QR buck-boost converter) circuit shares the output filter of the power optimizer. The proposed converter integrates the soft-switched converters with minimum active and passive components. Hence, the proposed system becomes efficient. The operating principle and the analysis of the proposed converter are explained. Then the controller for the proposed converter is discussed in detail. The simulation results of the proposed converter with the controller are presented to highlight the features with the change of load, light intensity and battery conditions. The experimental results are presented at the end of the chapter to further support the performance of the converter.

Chapter 5 Conclusions

The power generation from renewable resources has been increased in the past decade to meet the growing energy demand without causing more green house gas emission. In general, renewable resources are intermittent in nature. Therefore, using multiple resources together in the system provides a more reliable power solutions for renewable power generation system. Power electronics interface plays a vital role in energy harvesting from renewable resources. It is responsible for converting the captured power from the dedicated renewable resources to usable power. Key functions of the power converter interface of renewable systems include: (1) providing MPPT; (2) providing input PFC when the power converter interfaces with renewable generation unit that outputs an AC voltage. In addition, when battery storage is also considered in the power electronics interfaces for renewable energy system, several other key functions need to be provided, including: (1) providing charging and discharging paths of the battery (or any energy storage devices); (2) following the battery charging profile for battery system; and (3) regulating output voltage.

In conventional renewable energy systems, individual converter is used for interfacing with each energy source. Therefore, the overall converter system requires a large number of circuit components. Multi-input converter (MIC) configuration provides a more compact and efficient approach when multiple energy sources are utilized as the MIC circuit is able to share several common components. However, existing MICs reported for renewable energy systems are not able to either achieve all the required features or perform all the existing features efficiently. The motivation of this research stems from the challenges of the existing power converter structures for the renewable energy systems. In particular, MICs presented in this thesis utilize minimal active and passive components while at the same time, all the aforementioned system features are able to be achieved.

5.1 Contributions

The contributions of this thesis research are summarized below:

1. A family of soft-switched DC-DC unidirectional MIC topologies have been proposed, in each of these topologies, only one switch is required in each input module.
2. Several three-phase AC-DC PFC circuits have been investigated to integrate with one of the modules of the devised DC-DC MICs without adding additional switches. In the presented topologies that consist of input module works with AC input, soft switching condition has shown to be achieved with high PF maintained at the input.
3. The battery charging circuit has been integrated at the input side of the module-connected PV power optimizer through high frequency AC link, whereas the battery discharging circuit has been incorporated at the output side of the PV power optimizer. The power flow through the whole system is unidirectional. Therefore, the double power process issue of the battery circuit cased by the bidirectional converter has been overcome. The number of components of the proposed converter has been reduced by integrating the PV power optimizer, and the battery charging and discharging circuit.
4. An alternative PV power optimizer circuit structure with an integrated battery system power interface and output voltage regulation has been presented. The operating principles of the complete control mechanism for the devised PV-battery system have also been presented.

5. The operating principles and the steady state analysis of all the devised MIC circuit topologies have been presented and discussed in details.
6. Small signal analysis of the proposed converters for PV-battery system has been presented.
7. The performance of all the developed MIC topologies has been verified by Powersim simulation results, as well as experimental results on proof-of-concept hardware prototypes. The design procedure of each MIC topology presented in this thesis has also been described in details.

5.2 Future Works

Some future works related to the research presented in this thesis are as follows:

1. The experimental work is performed in the laboratory environment with a PV emulator. However, the outside environment is more dynamic. A battery equivalent resistor is used rather than a practical battery. Therefore, it is worthwhile to test the proposed MIC converter system in a more realistic testing environment.
2. The MPPT presented in this thesis focused only on the power conversion for PV system. Since one of the proposed MIC circuits involved interfacing with three-phase AC input voltage (such as the wind turbine generator output), it is important to also investigate and to develop the MPPT controller that can be used for wind system to extract the maximum power. A general controller that supports the devised MIC circuit to support both DC and AC input sources will also be studied and investigated.
3. The controller that performed output voltage regulation for the proposed system presented in Chapter 4 is developed to demonstrate the functionality of the proposed

MIC circuit. However, the controller is not optimized. Further tuning of the controller is required for the optimum performance.

List of Publications

<u>Journal Publications</u>:

1. S. Moury and J. Lam, " A Soft-switched, Multiport Photovoltaic Power Optimizer with Integrated Storage Interface and Output Voltage Regulation," in *IEEE Transactions on Industrial Electronics*. (Accepted, March 2020)

2. S. Moury and J. Lam, "A Soft-Switched Power Module with Integrated Battery Interface for Photovoltaic-Battery Power Architecture," in *IEEE Journal of Emerging and Selected Topics in Power Electronics*. (Early access, Accepted May 2019)

<u>Conference Publications</u>:

1. S. Moury and J. Lam, "An Integrated PV-Battery Soft-switched Power Converter with MPPT and Voltage Regulation," *2019 IEEE Energy Conversion Congress and Exposition (ECCE)*, Baltimore, MD, USA, 2019, pp. 3433-3440.

2. S. Moury and J. Lam, "A Novel Soft-Switched Power Converter Architecture with an Integrated Energy Storage Interface Compatible with DC and AC Energy Sources," *2018 IEEE Energy Conversion Congress and Exposition (ECCE)*, Portland, OR, 2018, pp. 6660-6667.

3. K. Kanathipan, S. Moury and J. Lam, "A fast and accurate maximum power point tracker for a multi-input converter with wide range of soft-switching operation for solar energy systems," *2017 IEEE Applied Power Electronics Conference and Exposition (APEC)*, Tampa, FL, 2017, pp. 2076-2083.

4. S. Moury and J. Lam, "New soft-switched high frequency multi-input step-up/down converters for high voltage DC-distributed hybrid renewable systems," *2017 IEEE Energy Conversion Congress and Exposition (ECCE)*, Cincinnati, OH, 2017, pp. 5537-5544.

5. S. Moury, J. Lam, V. Srivastava and R. Church, "A novel multi-input converter using soft-switched single-switch input modules with integrated power factor correction capability for hybrid renewable energy systems," *2016 IEEE Applied Power Electronics Conference and Exposition (APEC)*, Long Beach, CA, 2016, pp. 786-793.

6. S. Moury, J. Lam, V. Srivastava and R. Church, "New soft-switched multi-input converters with integrated active power factor correction for hybrid renewable energy applications," *2016 IEEE Energy Conversion Congress and Exposition (ECCE)*, Milwaukee, WI, 2016, pp. 1-8.

Bibliography

[1] Enerdata 2019. (2019) Global energy statistical yearbook. [Online]. https://yearbook.enerdata.net/

[2] "Renewable energy statistics 2019," International Renewable Energy Agency (IREA), AbuDhabi, ISBN 978-92-9260-137-9, 2019.

[3] Ran Fu, Timothy Remo, and Robert Margolis, "2018 U.S. Utility-Scale Photovoltaics-Plus-Energy Storage System Costs Benchmark," National Renewable Energy Laboratory, NREL/TP-6A20-71714, November 2018.

[4] Harold Anuta, Pablo Ralon, and Michael Taylor, "Renewable power generation costs in 2018," International Renewable Energy Agency (IRENA), Abu Dhabi, ISBN 978-92-9260-126-3, May, 2019.

[5] Florida solar energy center. [Online]. www.fsec.ucf.edu/en/consumer/solar_electricity/basics/cells_modules_arrays.htm

[6] M. Pucci and M. Cirrincione, "Neural MPPT Control of Wind Generators With Induction Machines Without Speed Sensors," *IEEE Transactions on Industrial Electronics*, vol. 58, no. 1, pp. 37-47, Jan. 2011.

[7] T. Bogaraj, J. Kanakaraj, and J. Chelladurai, "Modeling and simulation of stand-alone hybrid power system with fuzzy MPPT for remote load application," *Archives of Electrical Engineering*, vol. 64, no. 3, pp. 487–504, 2015.

[8] "Handbook on battery energy storage system," Assian Development Bank (ADB),

Metro Manila, Philippines, ISBN 978-92-9261-471-3, December, 2018.

[9] A. Affanni, A. Bellini, G. Franceschini, P. Guglielmi, and C. Tassoni, "Battery choice and management for new-generation electric vehicles," *IEEE Transactions on Industrial Electronics*, vol. 52, no. 5, pp. 1343-1349, Oct. 2005.

[10] N. Shafiei, M. Ordonez, M. A. Saket Tokaldani, and S. A. Arefifar, "PV Battery Charger Using an L3C Resonant Converter for Electric Vehicle Applications," *IEEE Transactions on Transportation Electrification*, vol. 4, no. 1, pp. 108-121, March 2018.

[11] F. Musavi, M. Craciun, D. S. Gautam, W. Eberle, and W. G. Dunford, "An LLC Resonant DC–DC Converter for Wide Output Voltage Range Battery Charging Applications," *IEEE Transactions on Power Electronics*, vol. 28, no. 12, pp. 5437-5445, Dec. 2013.

[12] T. Cleveland and S. Dearborn, "Developing affordable mixed-signal power systems for battery charger applications," Microchip Technology Inc., 2006.

[13] S. B. Kjaer, J. K. Pedersen, and F. Blaabjerg, "A review of single-phase grid-connected inverters for photovoltaic modules," *IEEE Transactions on Industry Applications*, vol. 41, no. 5, pp. 1292-1306, Oct. 2005.

[14] G. R. Walker and P. C. Sernia, "Cascaded DC-DC converter connection of photovoltaic modules," *IEEE Transactions on Power Electronics*, vol. 19, no. 4, pp. 1130-1139, July 2004.

[15] A. Chub, D. Vinnikov, R. Kosenko, and E. Liivik, "Wide input voltage range

photovoltaic microconverter with reconfigurable buck–boost switching stage," *IEEE Transactions on Industrial Electronics*, vol. 64, no. 7, pp. 5974-5983, July 2017.

[16] C. Jain and B. Singh, "An adjustable DC link voltage-based control of multifunctional grid interfaced solar PV system," *IEEE Journal of Emerging and Selected Topics in Power Electronics*, vol. 5, no. 2, pp. 651-660, June 2017.

[17] A. J. Hanson, C. A. Deline, S. M. MacAlpine, J. T. Stauth, and C. R. Sullivan, "Partial-Shading Assessment of Photovoltaic Installations via Module-Level Monitoring," *IEEE Journal of Photovoltaics*, vol. 4, no. 6, pp. 1618-1624, Nov. 2014.

[18] Y. Li and Y. Han, "A Module-Integrated Distributed Battery Energy Storage and Management System," *IEEE Transactions on Power Electronics*, vol. 31, no. 12, pp. 8260-8270, Dec. 2016.

[19] V. Karthikeyan and R. Gupta, "Multiple-Input Configuration of Isolated Bidirectional DC–DC Converter for Power Flow Control in Combinational Battery Storage," *IEEE Transactions on Industrial Informatics*, vol. 14, no. 1, pp. 2-11, Jan. 2018.

[20] G. Hua and F. C. Lee, "Soft-switching techniques in PWM converters," *IEEE Transactions on Industrial Electronics*, vol. 42, no. 6, pp. 595-603, Dec. 1995.

[21] N Mohan, W. P. Robbins, and T. M. Undeland, *Power Electronics: Converters, Applications, and Design*, 3rd ed.: John Wiley & Sons, Inc, 1989.

[22] W. Xiao, A. Elnosh, V. Khadkikar, and H. Zeineldin, "Overview of maximum power point tracking technologies for photovoltaic power systems," in *IECON 2011 - 37th*

Annual Conference of the IEEE Industrial Electronics Society, Melbourne, 2011, pp. 3900-3905.

[23] T. Esram and P. L. Chapman, "Comparison of Photovoltaic Array Maximum Power Point Tracking Techniques," *IEEE Transactions on Energy Conversion*, vol. 22, no. 2, pp. 439-449, June 2007.

[24] N. Femia, G. Petrone, G. Spagnuolo, and M. Vitelli, "Optimization of perturb and observe maximum power point tracking method," *EEE Transactions on Power Electronics*, vol. 20, no. 4, pp. 963-973, July 2005.

[25] S. Jain and V. Agarwal, "A new algorithm for rapid tracking of approximate maximum power point in photovoltaic systems," *IEEE Power Electronics Letters*, vol. 2, no. 1, pp. 16-19, March 2004.

[26] W. Xiao, W. G. Dunford, P. R. Palmer , and A. Capel, "Application of Centered Differentiation and Steepest Descent to Maximum Power Point Tracking," *EEE Transactions on Industrial Electronics*, vol. 54, no. 5, pp. 2539-2549, Oct. 2007.

[27] Yeong-Chau Kuo, Tsorng-Juu Liang, and Jiann-Fuh Chen, "Novel maximum-power-point-tracking controller for photovoltaic energy conversion system," *IEEE Transactions on Industrial Electronics*, vol. 48, no. 3, pp. 594-601, June 2001.

[28] Chung-Yuen Won, Duk-Heon Kim, Sei-Chan Kim, Won-Sam Kim, and Hack-Sung Kim, "A new maximum power point tracker of photovoltaic arrays using fuzzy controller," in *1994 Power Electronics Specialist Conference - PESC'94*, Taipei,

Taiwan, 1994, pp. 396-403.

[29] T. Hiyama, S. Kouzuma, and T. Imakubo, "Identification of optimal operating point of PV modules using neural network for real time maximum power tracking control," *IEEE Transactions on Energy Conversion*, vol. 10, no. 2, pp. 360-367, June 1995.

[30] M. Veerachary, T. Senjyu, and K. Uezato, "Neural-network-based maximum-power-point tracking of coupled-inductor interleaved-boost-converter-supplied PV system using fuzzy controller," *IEEE Transactions on Industrial Electronics*, vol. 50, no. 4, pp. 749-758, Aug. 2003.

[31] F. Caricchi, F. Crescimbini, F. G. Capponi, and L. Solero, "Study of bi-directional buck-boost converter topologies for application in electrical vehicle motor drives," in *Applied Power Electronics Conference and Exposition, 1998 (APEC '98)*, Anaheim, CA, 1998, pp. 287-293.

[32] A. M. O. Haruni, M. Negnevitsky, M. E. Haque, and A. Gargoom, "A Novel Operation and Control Strategy for a Standalone Hybrid Renewable Power System," *IEEE Transactions on Sustainable Energy*, vol. 4, no. 2, pp. 402-413, April 2013.

[33] Y. Zhang, X. Cheng, C. Yin, and S. Cheng, "Analysis and Research of a Soft-Switching Bidirectional DC–DC Converter Without Auxiliary Switches," *IEEE Transactions on Industrial Electronics*, vol. 65, no. 2, pp. 1196-1204, Feb 2018.

[34] H. Do, "Nonisolated Bidirectional Zero-Voltage-Switching DC–DC Converter," *IEEE Transactions on Power Electronics*, vol. 26, no. 9, pp. 2563-2569, Sept. 2011.

[35] R. W. A. A. De Doncker, D. M. Divan, and M. H. Kheraluwala, "A three-phase soft-switched high-power-density DC/DC converter for high-power applications," *IEEE Transactions on Industry Applications*, vol. 27, no. 1, pp. 63-73, Jan.-Feb. 1991.

[36] F. Z. Peng, Hui Li, Gui-jia Su, and J. S. Lawler, "A new ZVS bidirectional DC-DC converter for fuel cell and battery application," *IEEE Transactions on Power Electronics*, vol. 19, no. 1, pp. 54-65, Jan. 2004.

[37] H. Tao, J. L. Duarte, and M. A. M. Hendrix, "Three-Port Triple-Half-Bridge Bidirectional Converter With Zero-Voltage Switching," *IEEE Transactions on Power Electronics*, vol. 23, no. 2, pp. 782-792, March 2008.

[38] J. W. Kolar and T. Friedli, "The essence of three-phase PFC rectifier systems – Part I," *IEEE Trans. Power Electronics*, vol. 28, no. 1, pp. 176-198, Jan. 2013.

[39] K. Yao, X. Ruan, C. Zou, and Z. Ye, "Three-phase single-switch boost power factor correction converter with high input power factor," *IET Power Electronics*, vol. 5, no. 7, pp. 1095-1103, Aug. 2012.

[40] E. Ismail and R. W. Erickson, "A single transistor three phase resonant switch for high quality rectification," in *23rd Annual IEEE Power Electronics Specialists Conference*, Toledo, Spain, 1992, pp. 1341-1351.

[41] M. Marchesoni and C. Vacca, "New DC–DC Converter for Energy Storage System Interfacing in Fuel Cell Hybrid Electric Vehicles," *IEEE Transactions on Power Electronics*, vol. 22, no. 1, pp. 301-308, Jan. 2007.

[42] K. P. Yalamanchili, M. Ferdowsi, and K. Corzine, "New Double Input DC-DC Converters for Automotive Applications," in *2006 IEEE Vehicle Power and Propulsion Conference*, Windsor, 2006, pp. 1-6.

[43] S. Khwan-on and K. Kongkanjana, "The control of a multi-input boost converter for renewable energy system applications," in *2017 International Electrical Engineering Congress (iEECON)*, Pattaya, 2017, pp. 1-4.

[44] Y.-M. Chen, Y.-C Liu, and S.-H. Lin, "Double-input PWM DC/DC converter for high/low-voltage sources," *IEEE Transactions on Industrial Electronics*, vol. 53, no. 5, pp. 1538–1545, Oct. 2006.

[45] M. Veerachary , "Two-loop controlled buck–SEPIC converter for input source power management," *IEEE Transactions on Industrial Electronics*, vol. 59, no. 11, pp. 4075–4087, Nov. 2012.

[46] R. Wai, C. Lin, J. Liaw, and Y. Chang, "Newly Designed ZVS Multi-Input Converter," *IEEE Transactions on Industrial Electronics*, vol. 58, no. 2, pp. 555-566, Feb. 2011.

[47] Z. Rehman, I. Al-Bahadly , and S. Mukhopadhyay, "Multiinput DC–DC converters in renewable energy applications–An overview," *journal of Renewable and Sustainable Energy Reviews*, vol. 41, pp. 521–539, Jan. 2015.

[48] J. Wang, M. Reinhard, F. Z. Peng, and Z. Qian, "Design guideline of the isolated DC-DC converter in green power applications," in *4th International Power Electronics and Motion Control Conference (IPEMC 2004)*, 2004, pp. 1756-1761.

[49] Yaow-Ming Chen, Yuan-Chuan Liu , and Feng-Yu Wu, "Multi-input DC/DC converter based on the multiwinding transformer for renewable energy applications," *IEEE Transactions on Industry Applications*, vol. 38, no. 4, pp. 1096-1104, July-Aug. 2002.

[50] Y. C. Liu and Y. M. Chen, "A Systematic Approach to Synthesizing Multi-Input DC-DC Converters," *IEEE Transactions on Power Electronics*, vol. 24, no. 1, pp. 116-127, Jan 2009.

[51] A. Kwasinski, "Identification of Feasible Topologies for Multiple-Input DC–DC Converters," *IEEE Trans. on Power Electronics*, vol. 24, no. 3, pp. 856-861, March 2009.

[52] Y Li, D. Ruan, F. Liu, and C. K. Tse, "Synthesis of Multiple-Input DC-DC Converters," *IEEE Trans. on Power Electronics*, vol. 25, no. 9, pp. 2372-2385, Sept. 2010.

[53] S. Y. Yu and A. Kwasinski, "Multiple-input soft-switching converters in renewable energy applications," in *2012 IEEE Energy Conversion Congress and Exposition (ECCE)*, Raleigh, NC, 2012, pp. 1711-1718.

[54] H. Wu, K. Sun, H. Hu, and Y. Xing, "Full-Bridge Three-Port Converters With Wide Input Voltage Range for Renewable Power Systems," *IEEE Trans. on Power Electronics*, vol. 27, no. 9, pp. 3965-3974, Sept. 2012.

[55] M. R. Ramteke, H. M. Suryawanshi, K. Kothapalli and S. P. Gawande N. K. Reddi, "An Isolated Multi-Input ZCS DC–DC Front-End-Converter Based Multilevel Inverter

for the Integration of Renewable Energy Sources," *IEEE Transactions on Industry Applications*, vol. 54, no. 1, pp. 494-504, Jan.-Feb. 2018.

[56] S. Dusmez, X. Li, and B. Akin, "A New Multiinput Three-Level DC/DC Converter," *IEEE Transactions on Power Electronics*, vol. 31, no. 2, pp. 1230-1240, Feb. 2016.

[57] M. Uno and K. Sugiyama, "Switched Capacitor Converter Based Multiport Converter Integrating Bidirectional PWM and Series-Resonant Converters for Standalone Photovoltaic Systems," *IEEE Transactions on Power Electronics*, vol. 33, no. 12, pp. 1394-1406, Feb. 2019.

[58] F. Kardan, R. Alizadeh, and R. Banaei, "A New Three Input DC/DC Converter for Hybrid PV/FC/Battery Applications," *IEEE Journal of Emerging and Selected Topics in Power Electronics*, vol. 5, no. 4, pp. 1771-1778, Dec. 2017.

[59] B. Mangu, S. Akshatha, D. Suryanarayana, and B. G. Fernandes, "Grid-Connected PV-Wind-Battery-Based Multi-Input Transformer-Coupled Bidirectional DC-DC Converter for Household Applications," *IEEE Journal of Emerging and Selected Topics in Power Electronics*, vol. 4, no. 3, pp. 1086-1095, Sept. 2016.

[60] Yaow-Ming Chen, Chung-Shen Cheng, and Hsu-Chin Wu, "Grid-connected hybrid PV/wind power generation system with improved DC bus voltage regulation strategy," in *Twenty-First Annual IEEE Applied Power Electronics Conference and Exposition, 2006. APEC '06.*, Dallas, TX, 2006, pp. 1088-1094.

[61] C. Chen, C. Liao, K. Chen, and Y. Chen, "Modeling and Controller Design of a

Semiisolated Multiinput Converter for a Hybrid PV/Wind Power Charger System," *IEEE Transactions on Power Electronics*, vol. 30, no. 9, pp. 4843-4853, Sept. 2015.

[62] N. K. Reddi, M. R. Ramteke, H. M. Suryawanshi, K. Kothapalli, and S. P. Gawande, "An Isolated Multi-Input ZCS DC–DC Front-End-Converter Based Multilevel Inverter for the Integration of Renewable Energy Sources," *IEEE Transactions on Industry Applications*, vol. 54, no. 1, pp. 494-504, Jan.-Feb. 2018.

[63] Y. Chen, Y. Liu, S. Hung, and C. Cheng, "Multi-Input Inverter for Grid-Connected Hybrid PV/Wind Power System," *IEEE Transactions on Power Electronics*, vol. 22, no. 3, pp. 1070-1077, May 2007.

[64] Y. Chen, Y. Liu, F. Wu, and Y. Wu, "Multi-input converter with power factor correction and maximum power point tracking features," in *APEC. Seventeenth Annual IEEE Applied Power Electronics Conference and Exposition*, Dallas, TX, USA, 2002, pp. 490-496.

[65] A. Deihimi and M. E. S. Mahmoodeih, "Analysis and control of battery-integrated DC/DC converters for renewable energy applications," *IET Power Electronics*, vol. 10, no. 14, pp. 1819-1831, Nov 2017.

[66] Z. Yi, W. Dong, and A. H. Etemadi, "A unified control and power management scheme for PV-battery based hybrid microgrids for both grid-connected and islanded modes," *IEEE Transactions on Smart Grid*, vol. 9, no. 6, pp. 5975-5985, Nov. 2018.

[67] N. Kim and B. Parkhideh, "PV-Battery Series Inverter Architecture: A Solar Inverter

for Seamless Battery Integration With Partial-Power DC–DC Optimizer," *IEEE Transactions on Energy Conversion*, vol. 34, no. 1, pp. 478-485, March 2019.

[68] S. M. Chen, T. J. Liang, and K. R. Hu, "Design, analysis, and implementation of solar power optimizer for DC distribution system," *IEEE Transactions on Power Electronics*, vol. 28, no. 4, pp. 1764-1772, April 2013.

[69] A. Deihimi and M. E. S. Mahmoodieh, "Analysis and control of battery-integrated DC/DC converters for renewable energy applications," *IET Power Electronics*, vol. 10, no. 14, pp. 1819-1831, Nov. 2017.

[70] J. Zeng, T. Kim, and V. Winsread, "A Soft-switched Four-port DC-DC Converter for Renewable Energy Integration," in *2018 IEEE Energy Conversion Congress and Exposition (ECCE)*, 2018, pp. 5851-5856.

[71] L. Callegaro, M. Ciobotaru, D. J. Pagano, and J. E. Fletcher, "Control Design for Photovoltaic Power Optimizers Using Bootstrap Circuit," *IEEE Transactions on Energy Conversion*, vol. 34, no. 1, pp. 232-242, Maarch 2019.

[72] A. I, S. Senthilkumar, D. Biswas, and Kaliamoorthy M., "Dynamic Power Management System Employing a Single-Stage Power Converter for Standalone Solar PV Applications," *IEEE Transactions on Power Electronics*, vol. 33, no. 12, pp. 10352-10362, Dec 2018.

[73] H. Zhu, D. Zhang, H. S. Athab, B. Wu, and Y. Gu, "PV isolated three-port converter and energy-balancing control method for pv-battery power supply applications," *IEEE*

Transactions on Industrial Electronics, vol. 62, no. 6, pp. 3595-3606, June 2015.

[74] H. Lee and J. Yun, "Quasi-resonant voltage doubler with snubber capacitor for boost half-bridge DC-DC converter in photovoltaic micro-inverter," *IEEE Transactions on Power Electronics.*, p. (early access).

[75] A. Chub, D. Vinnikov, R. Kosenko, and E. Liivik, "Wide input voltage range photovoltaic microconverter with reconfigurable buck–boost switching stage," *IEEE Transactions on Industrial Electronics*, vol. 64, no. 7, pp. 5974-5983, July 2017.

[76] S. Sathyan, H. M. Suryawanshi, A. B. Shitole, M. S. Ballal, and V. B. Borghate, "Soft-switched interleaved DC/DC converter as front-end of multi-inverter structure for micro grid applications," *IEEE Transactions on Power Electronics*, vol. 33, no. 9, pp. 7645-7655, Sept. 2018.

[77] F. C. Melo et al., "Proposal of a photovoltaic AC-module with a single-stage transformerless grid-connected boost microinverter," *IEEE Transactions on Industrial Electronics*, vol. 65, no. 3, pp. 2289-2301, March 2018.

[78] H. Zhu, D. Zhang, B. Zhang, and Z. Zhou, "A Nonisolated Three-Port DC–DC Converter and Three-Domain Control Method for PV-Battery Power Systems," *IEEE Transactions on Industrial Electronics*, vol. 62, no. 8, pp. 4937-4947, Aug. 2015.

[79] L. Chien, C. Chen , J. Chen, and Y. Hseih, "Novel Three-Port Converter With High-Voltage Gain," *IEEE Transactions on Power Electronics*, vol. 29, no. 9, pp. 4693-4703, Sept. 2014.

[80] R. Faraji and H. Farzanehfard, "Soft-Switched Nonisolated High Step-Up Three-Port DC–DC Converter for Hybrid Energy Systems," *IEEE Transactions on Power Electronics*, vol. 33, no. 12, pp. 10101-10111, Dec. 2018.

[81] Y. Chen, A. Q. Huang, and X. Yu, "A High Step-Up Three-Port DC–DC Converter for Stand-Alone PV/Battery Power Systems," *IEEE Transactions on Power Electronics*, vol. 28, no. 11, pp. 5049-5062, Nov. 2013.

[82] M.K. Kazimierczuk, "Class-E DC/DC converters with a capacitive impedance inverter," *IEEE Transactions on Industrial Electronics*, vol. 36, no. 3, pp. 425-433, Aug 1989.

[83] K. -. Liu and F. C. Y. Lee, "Zero-voltage switching technique in DC/DC converters," *IEEE Transactions on Power Electronics*, vol. 5, no. 3, pp. 293-304, Jul 1990.

[84] Marian Kazimierczuk and Dariusz Czarkowski, "Quasiresonant and Multiresonant DC-DC Power Converters," in *Resonant power converters*, second edition ed., N.J. Hoboken, Ed.: IEEE: Wiley, 2011, ch. 22.

[85] B. W. Williams, "DC-to-DC Converters With Continuous Input and Output Power," *IEEE Transactions on Power Electronics*, vol. 28, no. 5, pp. 2307-2316, May 2013.

[86] S. Freeland and R. D. Middlebrook, "A unified analysis of converters with resonant switches," in *1987 IEEE Power Electronics Specialists Conference*, Blacksburg, VA, 1987, pp. 20-30.

[87] V. Vorperian, R. Tymerski, and F. C. Y. Lee, "Equivalent circuit models for resonant

and PWM switches," *IEEE Transactions on Power Electronics*, vol. 4, no. 2, pp. 205-214, April 1989.

[88] S. Moury, J. Lam, V. Srivastava, and R. Church, "A novel multi-input converter using soft-switched single-switch input modules with integrated power factor correction capability for hybrid renewable energy systems," in *2016 IEEE Applied Power Electronics Conference and Exposition (APEC)*, Long Beach, CA, 2016, pp. 786-793.

[89] S. Schacham and A. Kuperman M. Sitbon, "Disturbance Observer-Based Voltage Regulation of Current-Mode-Boost-Converter-Interfaced Photovoltaic Generator," *IEEE Transactions on Industrial Electronics*, vol. 62, no. 9, pp. 5776-5785, Sept. 2015.

[90] A. F. Witulski and R. W. Erickson, "Extension of state-space averaging to resonant switches and beyond," *IEEE Transactions on Power Electronics*, vol. 5, no. 1, pp. 98-109, Jan. 1990.

[91] J. M. F. D. Costa and M. M. Silva, "Small-signal models of quasi-resonant converters," in *IEEE International Symposium on Industrial Electronics*, 1997, pp. 258-262.

[92] V. Vorperian, R. Tymerski, and F. C. Y. Lee, "Equivalent circuit models for resonant and PWM switches," *IEEE Transactions on Power Electronics*, vol. 4, no. 2, pp. 205-214, April 1989.

[93] S. Cuk and R. D. Middlebrook, "A new optimum topology switching DC-to-DC converter," in *1977 IEEE Power Electronics Specialists Conference*, Palo Alto, CA, USA, 1977, pp. 160-179.

[94] "Overall efficiency of grid connected photovoltaic inverters," EN 50530, April, 2010.

[95] S. Moury and J. Lam, "New soft-switched high frequency multi-input step-up/down converters for high voltage DC-distributed hybrid renewable systems," in *IEEE Energy Conversion Congress and Exposition (ECCE)*, Cincinnati, OH, 2017, pp. 5537-5544.

[96] "Design guidelines for off-line flyback converters using Fairchild power switch," Fairchild Semiconductor, App. Note AN4137, 2003.

[97] D. Maksimovic and S. Cuk, "Constant-frequency control of quasi-resonant converters," *IEEE Transactions on Power Electronics*, vol. 6, no. 1, pp. 141-150, Jan 1991.

[98] A. Szabo, M. Kamsara, and E. S. Ward, "A unified method for the small-signal modelling of multi-resonant and quasi-resonant converters," in *IEEE International Symposium on Circuits and Systems (Cat. No.98CH36187)*, 1998, pp. 522-525.

[99] F. Nuno, J. Diaz, J. Sebastian, and J. Lopera, "A unified analysis of multi-resonant converters," in *3rd Annual IEEE Power Electronics Specialists Conference*, Toledo, Spain, 1992, pp. 822-829.

[100] L. S. Yang, T. J. Liang, and J. F. Chen, "Analysis and design of a novel three–phase AC–DC buck–boost converter," *IEEE Trans. on Power Electronics*, vol. 23, no. 2, pp. 707-714, Mar. 2008.

Appendix A: Analysis of Buck Quasi-resonant Converter

The analysis of the four power conversion stages of buck QRC are presented below.

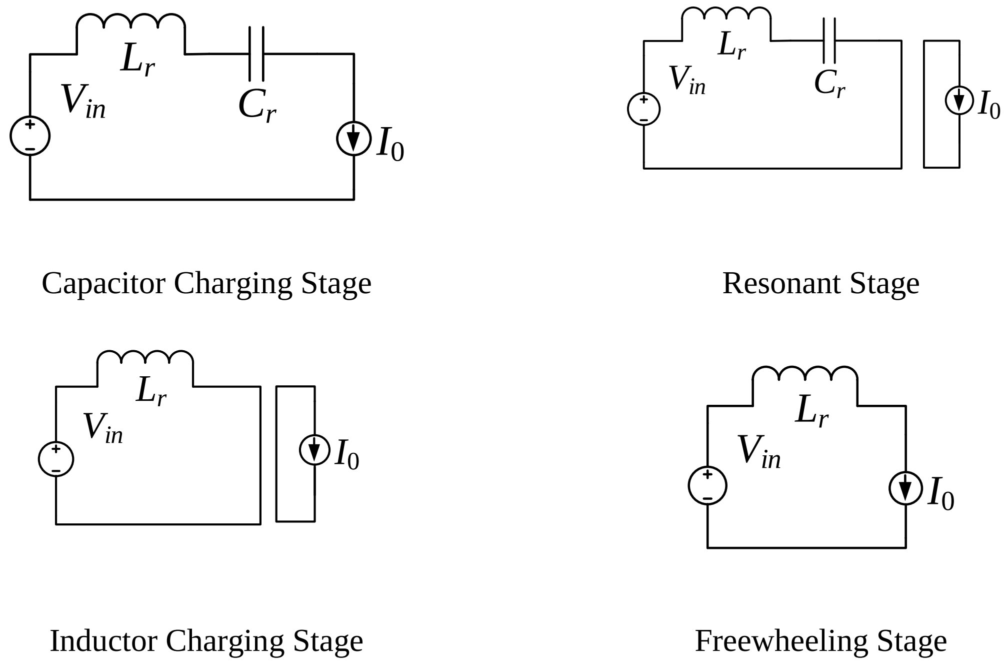

Figure A-1 Analysis of buck QRC

1) *Capacitor charging stage:*

The resonant inductor current is constant throughout this stage and is equal to I_0. The resonant capacitor is in series with the resonant inductor. Therefore, the resonant inductor and capacitor current is shown by Eq. A- 1 and Eq. A- 2.

$$I_{Lr} = I_0 \qquad \text{Eq. A- 1}$$

$$C_r \frac{dv_{Cr}}{dt} = I_0 \qquad \text{Eq. A- 2}$$

Taking the Laplace transform of Eq. A- 2

$$C_r\left[sv_{Cr}(s)-v_{cr}(0)\right]=\frac{I_0}{s} \qquad \text{Eq. A- 3}$$

The initial voltage across the resonant capacitor is zero. Therefore,

$$C_r\left[sv_{Cr}(s)\right]=\frac{I_0}{s} \qquad \text{Eq. A- 4}$$

$$v_{Cr}(s)=\frac{1}{C_r}\frac{I_0}{s^2} \qquad \text{Eq. A- 5}$$

The inverse Laplace transform of Eq. A- 5

$$v_{Cr}(t)=\frac{1}{C_r}I_0 t \qquad \text{Eq. A- 6}$$

This stage ends when the voltage across the resonant capacitor reached to V_{in}. Hence,

$$T_{d1}=C_r\frac{V_{in}}{I_0} \qquad \text{Eq. A- 7}$$

2) *Resonant stage:*

The state equations of the resonant stage are:

$$L_r\frac{di_{Lr}}{dt}=V_{in}-v_{Cr} \qquad \text{Eq. A- 8}$$

$$C_r\frac{dv_{Cr}}{dt}=i_{Lr} \qquad \text{Eq. A- 9}$$

The Laplace transform of Eq. A- 8

$$L_r\left[si_{Lr}(s)-i_{Lr}(0)\right]=\frac{V_{in}}{s}-v_{Cr}(s) \qquad \text{Eq. A- 10}$$

The initial current through the resonant inductor is I_0. Therefore,

$$L_r s i_{Lr}(s) = \frac{V_{in}}{s} + L_r I_0 - v_{Cr}(s) \qquad \text{Eq. A- 11}$$

The Laplace transform of Eq. A- 9

$$C_r \left[s v_{Cr}(s) - v_{Cr}(0) \right] = i_{Lr}(s) \qquad \text{Eq. A- 12}$$

The initial voltage across the resonant capacitor is V_{in}. Therefore,

$$s C_r v_{Cr}(s) = i_{Lr}(s) + C_r \frac{V_{in}}{s} \qquad \text{Eq. A- 13}$$

From Eq. A- 11 and Eq. A- 13

$$v_{Cr}(s)\left[sC_r + \frac{1}{sL_r} \right] = \frac{I_0}{s} + V_{in}\left[C_r - \frac{1}{s^2 L_r} \right] \qquad \text{Eq. A- 14}$$

Where

$$sC_r + \frac{1}{sLr} = C_r \frac{s^2 + \omega_r^2}{s} \qquad \text{Eq. A- 15}$$

$$C_r - \frac{1}{s^2 Lr} = C_r \frac{s^2 + \omega_r^2}{s^2} \qquad \text{Eq. A- 16}$$

Therefore,

$$v_{Cr}(s) = \frac{V_{in}}{s} + \frac{1}{C_r} \frac{I_0}{s^2 + \omega_r^2} \qquad \text{Eq. A- 17}$$

The inverse Laplace transform of Eq. A- 17

$$v_{Cr}(t) = V_{in} + ZI_0 \sin \omega_r t \qquad \text{Eq. A- 18}$$

From Eq. A- 11 and Eq. A- 17

$$L_r s i_{Lr}(s) = L_r I_0 - \frac{1}{C_r} \frac{I_0}{s^2 + \omega_r^2} \qquad \text{Eq. A- 19}$$

$$\begin{aligned} i_{Lr}(s) &= \frac{I_0}{s} - \frac{1}{L_r C_r} \frac{I_0}{s\left(s^2 + \omega_r^2\right)} \\ &= \frac{I_0}{s} - \frac{\omega_r^2}{s\left(s^2 + \omega_r^2\right)} I_0 \end{aligned} \qquad \text{Eq. A- 20}$$

The inverse Laplace transform of Eq. A- 20

$$i_{Lr}(t) = I_0 \cos \omega_r t \qquad \text{Eq. A- 21}$$

The time duration of this stage is

$$T_{d2} = \frac{\alpha}{\omega_r} \qquad \text{Eq. A- 22}$$

$$\alpha = \sin^{-1} \varphi = \sin^{-1} \frac{V_{in}}{ZI_0} \qquad \text{Eq. A- 23}$$

3) Inductor charging stage

The resonant inductor is getting charged with the input voltage.

$$L_r \frac{di_{Lr}}{dt} = V_{in} \qquad \text{Eq. A- 24}$$

The Laplace transform of Eq. A- 24

$$L_r \left[s i_{Lr}(s) - i_{Lr}(0) \right] = \frac{V_{in}}{s} \qquad \text{Eq. A- 25}$$

The initial current through the resonant inductor is $I_0 \cos \omega_r t$. Therefore,

$$sL_r i_{Lr}\left(s\right) - L_r I_0 \cos\alpha = \frac{V_{in}}{s}$$ Eq. A- 26

$$i_{Lr}\left(s\right) = \frac{1}{L_r}\frac{V_{in}}{s^2} + \frac{1}{s} I_0 \cos\alpha$$ Eq. A- 27

The inverse Laplace transform of Eq. A- 27

$$i_{Lr}\left(t\right) = I_0 \cos\alpha + \frac{1}{L_r} V_{in}(t)$$ Eq. A- 28

This stage ends when the current through the resonant inductor reached to I_0. Hence,

$$T_{d3} = L_r \frac{I_0}{V_{in}}\left(1 - \cos\alpha\right)$$ Eq. A- 29

4) *Freewheeling stage*:

The duration of this stage is

$$T_{d4} = T_s - T_{d1} - T_{d2} - T_{d3}$$ Eq. A- 30

<u>DC voltage conversion:</u>

The output energy

Eq. A- 31

$$E_0 = V_0 I_0 T_s$$

The input energy

$$\begin{aligned} E_{in} &= V_{in} I_{in} T_s \\ &= V_{in} \left(\int_0^{Ts} i_{Lr} dt \right) \end{aligned} \qquad \text{Eq. A- 32}$$

The input current can be found by

$$\int_{t_0}^{t_1} i_{Lr} dt = I_0 T_{d1} \qquad \text{Eq. A- 33}$$

$$\begin{aligned} \int_{t_1}^{t_2} i_{Lr} dt &= \int_{t_1}^{t_2} I_0 \cos \alpha dt \\ &= \frac{-I_0}{\omega_0} \end{aligned} \qquad \text{Eq. A- 34}$$

$$\begin{aligned} \int_{t_2}^{t_3} i_{Lr} dt &= \int_{t_1}^{t_2} \left(I_0 \cos \alpha + \frac{V_{in} t}{L_r} \right) dt \\ &= \frac{I_0 \varphi}{2\omega_r} \end{aligned} \qquad \text{Eq. A- 35}$$

$$\int_{t_3}^{t_4} i_{Lr} dt = I_0 T_{d4} \qquad \text{Eq. A- 36}$$

$$\begin{aligned} I_{in} &= I_0 \left(T_s - \frac{\alpha}{\omega_r} - \frac{1-\cos\alpha}{\omega_r \varphi} - \frac{I_0 \varphi}{2\omega_r} - \frac{I_0 \varphi}{\omega_r} \right) \\ &= I_0 T_s \left[1 - \frac{f_s}{2\pi f_r} \left(\alpha + \frac{\varphi}{2} + \frac{1}{\varphi} \left(1 - \cos\alpha \right) \right) \right] \end{aligned} \qquad \text{Eq. A- 37}$$

Therefore, the voltage conversion ratio from Eq. A- 31, Eq. A- 32, and Eq. A- 37

$$\frac{V_0}{V_{in}} = M_v = \left[1 - \frac{f_s}{2\pi f_r} \left(\alpha + \frac{\varphi}{2} + \frac{1}{\varphi} \left(1 - \cos\alpha \right) \right) \right] \qquad \text{Eq. A- 38}$$

Appendix B: Analysis of Cuk Quasi-resonant Converter

The analysis of the four power conversion stages of buck QRC are presented below.

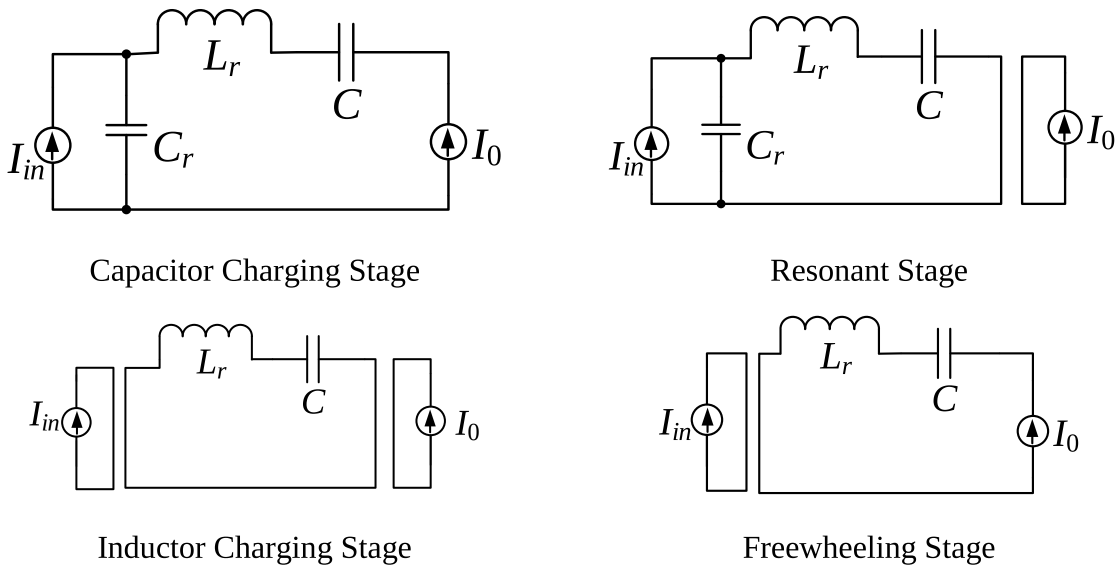

Figure B-1 Analysis of Cuk QRC configuration#1

1) Capacitor charging stage:

The resonant inductor current is constant throughout this stage and is equal to I_0. The resonant capacitor is getting charged with I_{in}+I_0. Therefore, the resonant inductor and capacitor current is shown by Eq. B- 1and Eq. B- 2.

$$I_{Lr} = I_0 \qquad \text{Eq. B- 1}$$

$$C_r \frac{dv_{Cr}}{dt} = I_{in} + I_0 \qquad \text{Eq. B- 2}$$

Taking the Laplace transform of Eq. B- 2

$$C_r \left[s v_{Cr}(s) - v_{cr}(0) \right] = \frac{I_{in} + I_0}{s} \qquad \text{Eq. B- 3}$$

The initial voltage across the resonant capacitor is zero. Therefore,

$$C_r\left[sv_{Cr}(s)\right]=\frac{I_{in}+I_0}{s}$$ Eq. B- 4

$$v_{Cr}(s)=\frac{1}{C_r}\frac{I_{in}+I_0}{s^2}$$ Eq. B- 5

The inverse Laplace transform of Eq. B- 6

$$v_{Cr}(t)=\frac{1}{C_r}\left(I_{in}+I_0\right)t$$ Eq. B- 6

This stage ends when the voltage across the resonant capacitor reached to V_{in}+V_0. Hence,

$$T_{d1}=C_r\frac{V_{in}+V_0}{I_{in}+I_0}$$ Eq. B- 7

2) *Resonant stage:*

The state equations of the resonant stage are:

$$L_r\frac{di_{Lr}}{dt}=V_{in}+V_0-v_{Cr}$$ Eq. B- 8

$$C_r\frac{dv_{Cr}}{dt}=I_{in}+i_{Lr}$$ Eq. B- 9

The Laplace transform of Eq. B- 8

$$L_r\left[si_{Lr}(s)-i_{Lr}(0)\right]=\frac{V_{in}+V_0}{s}-v_{Cr}(s)$$ Eq. B- 10

The initial current through the resonant inductor is I_0. Therefore,

$$L_rsi_{Lr}(s)=\frac{V_{in}+V_0}{s}+L_rI_0-v_{Cr}(s)$$ Eq. B- 11

The Laplace transform of Eq. B- 9

$$C_r\left[sv_{Cr}(s)-v_{Cr}(0)\right]=\frac{I_{in}}{s}+i_{Lr}(s) \quad \text{Eq. B- 12}$$

The initial voltage across the resonant capacitor is V_{in}+V_0. Therefore,

$$sC_r v_{Cr}(s)=i_{Lr}(s)+C_r\frac{V_{in}+V_0}{s} \quad \text{Eq. B- 13}$$

From Eq. B- 11and Eq. B- 14

$$v_{Cr}(s)\left[sC_r+\frac{1}{sL_r}\right]=\frac{I_{in}+I_0}{s}+\left(V_{in}+V_0\right)\left[C_r-\frac{1}{s^2L_r}\right] \quad \text{Eq. B- 14}$$

Therefore from Eq. B- 14, Eq. A- 15, and Eq. A- 16

$$v_{Cr}(s)=\frac{V_{in}+V_0}{s}+\frac{1}{C_r}\frac{I_{in}+I_0}{s^2+\omega_r^2} \quad \text{Eq. B- 15}$$

The inverse Laplace transform of Eq. B- 16

$$v_{Cr}(t)=\left(V_{in}+V_0\right)+Z\left(I_{in}+I_0\right)\sin\omega_r t \quad \text{Eq. B- 16}$$

From Eq. B- 11and Eq. B- 15

$$i_{Lr}(s)=\frac{s}{s^2+\omega_r^2}I_0-\frac{\omega_r^2}{s^2+\omega_r^2}I_{in} \quad \text{Eq. B- 17}$$

$$\begin{aligned} i_{Lr}(s)&=\frac{s}{s^2+\omega_r^2}I_0-\left(\frac{1}{s}+\frac{s}{s^2+\omega_r^2}\right)I_{in} \\ &=\frac{s}{s^2+\omega_r^2}\left(I_0+I_{in}\right)-\frac{1}{s}I_{in} \end{aligned} \quad \text{Eq. B- 18}$$

The inverse Laplace transform of Eq. B- 18

$$i_{Lr}(t)=\left(I_{in}+I_0\right)\cos\omega_r t-I_{in} \quad \text{Eq. B- 19}$$

The time duration of this stage is

$$T_{d2} = \frac{\alpha}{\omega_r} \qquad \text{Eq. B- 20}$$

$$\alpha = \sin^{-1}\varphi = \sin^{-1}\frac{\left(V_{in}+V_0\right)}{Z\left(I_{in}+I_0\right)} \qquad \text{Eq. B- 21}$$

3) Inductor charging stage:

The resonant inductor is getting charged at this stage.

$$L_r \frac{di_{Lr}}{dt} = V_{in} + V_0 \qquad \text{Eq. B- 22}$$

The Laplace transform of Eq. B- 22

$$L_r\left[si_{Lr}\left(s\right) - i_{Lr}\left(0\right)\right] = \frac{V_{in}+V_o}{s} \qquad \text{Eq. B- 23}$$

The initial current through the resonant inductor is $\left[\left(I_{in}+I_0\right)\cos\alpha - I_{in}\right]$. Therefore,

$$i_{Lr}\left(s\right) = \frac{1}{L_r}\frac{V_{in}+V_0}{s^2} + \frac{1}{s}\left[\left(I_{in}+I_0\right)\cos\alpha - I_{in}\right] \qquad \text{Eq. B- 24}$$

The inverse Laplace transform of Eq. B- 24

$$i_{Lr}\left(t\right) = \left[\left(I_{in}+I_0\right)\cos\alpha - I_{in}\right] + \frac{1}{L_r}\left(V_{in}+V_0\right)t \qquad \text{Eq. B- 25}$$

This stage ends when the current through the resonant inductor reached to I_0. Hence,

$$T_{d3} = L_r \frac{I_{in}+I_0}{V_{in}+V_0}\left(1-\cos\alpha\right) \qquad \text{Eq. B- 26}$$

4) Freewheeling stage:

The duration of this stage is

$$T_{d4} = T_s - T_{d1} - T_{d2} - T_{d3}$$ Eq. B- 27

DC voltage conversion:

The time integral of the current through the resonant inductor over a period is zero.

$$\int_0^{T_s} i_{Lr} dt = 0$$ Eq. B- 28

Where

$$\int_{t_0}^{t_1} i_{Lr} dt = \int_{t_0}^{t_1} I_0 dt$$ Eq. B- 29

$$\int_{t_1}^{t_2} i_{Lr} dt = \int_{t_1}^{t_2} i_{Lr} dt + \int_{t_1}^{t_2} \left[\left(I_0 + I_{in} \right) \cos \omega_r t \right] dt + \int_{t_1}^{t_2} I_{in} dt$$ Eq. B- 30

$$\int_{t_2}^{t_3} i_{Lr} dt = \int_{t_2}^{t_3} \frac{1}{L_r} \left(V_{in} + V_0 \right) t dt + \int_{t_2}^{t_3} \left(I_0 + I_{in} \right) \cos \alpha dt + \int_{t_2}^{t_3} I_{in} dt$$ Eq. B- 31

$$\int_{t_3}^{t_4} i_{Lr} dt = \int_{t_3}^{t_4} i_{Lr} dt$$ Eq. B- 32

From Eq. B- 28, Eq. B- 29, Eq. B- 30, Eq. B- 31, and Eq. B- 32

$$\frac{I_0}{I_{in}} = \frac{\frac{f_s}{2\pi f_r} \left(\alpha + \frac{\varphi}{2} + \frac{1 - \cos \alpha}{\varphi} \right)}{1 - \frac{f_s}{2\pi f_r} \left(\alpha + \frac{\varphi}{2} + \frac{1 - \cos \alpha}{\varphi} \right)}$$ Eq. B- 33

Therefore, the voltage conversion ratio from Eq. B- 33

$$\frac{V_0}{V_{in}} = \frac{I_{in}}{I_0} = \frac{1 - \frac{f_s}{2\pi f_r}\left(\alpha + \frac{\varphi}{2} + \frac{1-\cos\alpha}{\varphi}\right)}{\frac{f_s}{2\pi f_r}\left(\alpha + \frac{\varphi}{2} + \frac{1-\cos\alpha}{\varphi}\right)} \qquad \text{Eq. B- 34}$$

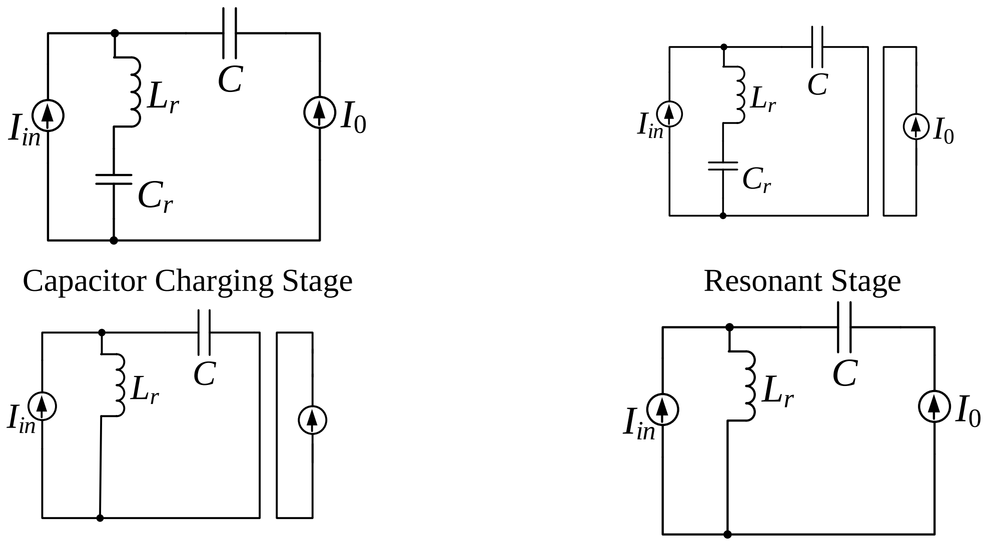

Configuration #2

Figure B-2 Analysis of Cuk QRC configuration#2

The analysis of configuration#2 is similar as configuration#1. The only difference is the resonant inductor is in series with the resonant capacitor rather the storage capacitor. Therefore, during capacitor charging stage, the resonant inductor carries $I_{in}+I_0$ in configuration#2. Whereas, during capacitor charging, the resonant inductor carries I_0 stage in configuration#1. For all other cases the resonant inductor is in the same loop as in configuration#1. Therefore, the analysis is same.

During capacitor charging stage

$$I_{Lr} = I_{in} + I_0 \qquad \text{Eq. B- 35}$$

During resonant stage, the current through the resonant capacitor is

$$C_r \frac{dv_{Cr}}{dt} = I_{in} + i_{Lr} \qquad \text{Eq. B- 36}$$

The initial current through the resonant inductor is I_{in}+I_0. Therefore, all other equations of this stage become same as the configuration#1.

Appendix C: Analysis of Flyback Quasi-resonant Converter

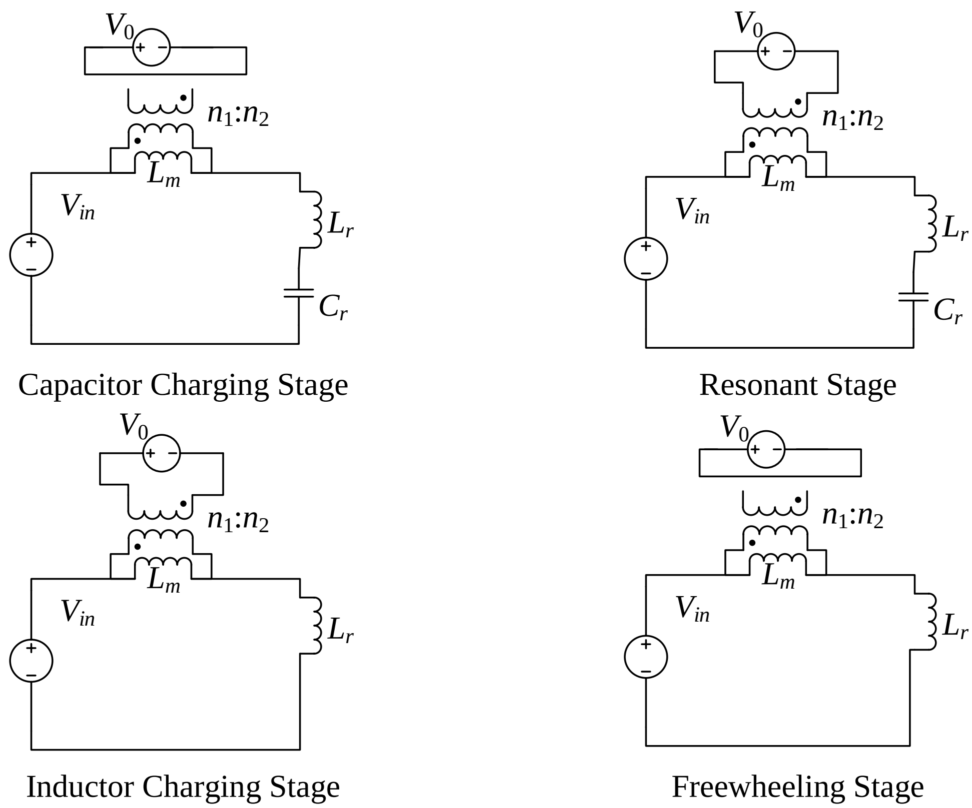

Figure C-1 Analysis of flyback QRC

1) *Capacitor charging stage:*

The resonant inductor current is constant throughout this stage and is equal to I_M. The resonant capacitor is in series with the resonant inductor. Therefore, the resonant inductor and capacitor current is shown by Eq. C- 1 and Eq. C- 2.

$$I_{Lr} = I_M = I_{in} + \frac{1}{N} I_0 \qquad \text{Eq. C- 1}$$

$$C_r \frac{dv_{Cr}}{dt} = I_M \qquad \text{Eq. C- 2}$$

Taking the Laplace transform of Eq. C- 2

$$C_r\left[sv_{Cr}(s)-v_{cr}(0)\right]=\frac{I_M}{s} \quad \text{Eq. C- 3}$$

The initial voltage across the resonant capacitor is zero. Therefore,

$$v_{Cr}(s)=\frac{1}{C_r}\frac{I_M}{s^2} \quad \text{Eq. C- 4}$$

The inverse Laplace transform of Eq. C- 4

$$v_{Cr}(t)=\frac{1}{C_r}I_M t \quad \text{Eq. C- 5}$$

This stage ends when the voltage across the resonant capacitor reached to $V_{in}+V_0$. Hence,

$$T_{d1}=C_r\frac{V_{in}+V_0}{I_M} \quad \text{Eq. C- 6}$$

2) *Resonant stage:*

The state equations of the resonant stage are:

$$L_r\frac{di_{Lr}}{dt}=V_{in}+NV_0-v_{Cr} \quad \text{Eq. C- 7}$$

$$C_r\frac{dv_{Cr}}{dt}=i_{Lr} \quad \text{Eq. C- 8}$$

The Laplace transform of Eq. C- 7

$$L_r\left[si_{Lr}(s)-i_{Lr}(0)\right]=\frac{V_{in}+NV_0}{s}-v_{Cr}(s) \quad \text{Eq. C- 9}$$

The initial current through the resonant inductor is I_M. Therefore,

$$sL_r i_{Lr}(s)=\frac{V_{in}+NV_0}{s}+L_r I_M-v_{Cr}(s) \quad \text{Eq. C- 10}$$

The Laplace transform of Eq. C- 8

$$C_r\left[sv_{Cr}(s)-v_{Cr}(0)\right]=i_{Lr}(s) \quad \text{Eq. C- 11}$$

The initial voltage across the resonant capacitor is $V_{in}+NV_0$. Therefore, from Eq. C- 10 and Eq. C- 11

$$C_r\left[sv_{Cr}(s)-\left(V_{in}+NV_0\right)\right]=\frac{1}{L_r}\frac{V_{in}+NV_0}{s^2}+\frac{I_M}{s}-\frac{1}{L_r}\frac{v_{Cr}(s)}{s} \quad \text{Eq. C- 12}$$

$$v_{Cr}(s)\left[sC_r+\frac{1}{sL_r}\right]=\frac{I_{in}}{s}+\left(V_{in}+NV_0\right)\left[C_r-\frac{1}{s^2L_r}\right] \quad \text{Eq. C- 13}$$

Therefore from Eq. C- 13, Eq. A- 15, and Eq. A- 16

$$v_{Cr}(s)=\frac{V_{in}+NV_0}{s}+\frac{1}{C_r}\frac{I_M}{s^2+\omega_r^2} \quad \text{Eq. C- 14}$$

The inverse Laplace transform of Eq. C- 14

$$v_{Cr}(t)=\left(V_{in}+NV_0\right)+ZI_M\sin\omega_r t \quad \text{Eq. C- 15}$$

From Eq. C- 10 and Eq. C- 14

$$i_{Lr}(s)=\frac{s}{s^2+\omega_r^2}I_M \quad \text{Eq. C- 16}$$

The inverse Laplace transform of Eq. C- 16

$$i_{Lr}(t)=I_M\cos\omega_r t \quad \text{Eq. C- 17}$$

The time duration of this stage is

$$T_{d2}=\frac{\alpha}{\omega_r} \quad \text{Eq. C- 18}$$

$$\alpha = \sin^{-1}\varphi = \sin^{-1}\frac{\left(V_{in} + NV_0\right)}{ZI_M} \qquad \text{Eq. C- 19}$$

3) *Inductor charging stage:*

The resonant inductor is getting charged at this stage.

$$L_r \frac{di_{Lr}}{dt} = V_{in} + NV_0 \qquad \text{Eq. C- 20}$$

The Laplace transform of Eq. B- 22

$$L_r\left[si_{Lr}\left(s\right) - i_{Lr}\left(0\right)\right] = \frac{V_{in} + NV_o}{s} \qquad \text{Eq. C- 21}$$

The initial current through the resonant inductor is $I_M \cos\alpha$. Therefore,

$$i_{Lr}\left(s\right) = \frac{1}{L_r}\frac{V_{in} + NV_0}{s^2} + \frac{1}{s} I_M \cos\alpha \qquad \text{Eq. C- 22}$$

The inverse Laplace transform of Eq. B- 24

$$i_{Lr}\left(t\right) = I_M \cos\alpha + \frac{1}{L_r}\left(V_{in} + NV_0\right)t \qquad \text{Eq. C- 23}$$

This stage ends when the current through the resonant inductor reached to I_0. Hence,

$$T_{d3} = \frac{ZI_M}{\omega_r\left(V_{in} + NV_0\right)}\left(1 - \cos\alpha\right) \qquad \text{Eq. C- 24}$$

4) *Freewheeling stage:*

The duration of this stage is

$$T_{d4} = T_s - T_{d1} - T_{d2} - T_{d3} \qquad \text{Eq. C- 25}$$

DC voltage conversion:

The output energy

$$E_0 = V_0 I_0 T_s \qquad \text{Eq. C- 26}$$

The input energy

$$\begin{aligned} E_{in} &= V_{in} I_{in} T_s \\ &= V_{in} \left(\int_0^{Ts} i_{Lr}\, dt \right) \end{aligned} \qquad \text{Eq. C- 27}$$

The input current can be found by

$$\int_{t_0}^{t_1} i_{Lr}\, dt = I_M T_{d1} \qquad \text{Eq. C- 28}$$

$$\begin{aligned} \int_{t_1}^{t_2} i_{Lr}\, dt &= I_M \frac{\sin \omega_r}{\omega_r} T_{d2} \\ &= \frac{-\varphi}{\omega_0} I_M \end{aligned} \qquad \text{Eq. C- 29}$$

$$\int_{t_2}^{t_3} i_{Lr}\, dt = I_M T_{d3} + \frac{I_M \varphi}{2\omega_r} \qquad \text{Eq. C- 30}$$

$$\int_{t_3}^{t_4} i_{Lr}\, dt = I_0 T_{d4} \qquad \text{Eq. C- 31}$$

$$I_{in} = I_M T_s \left[1 - \frac{f_s}{2\pi f_r} \left(\alpha + \frac{\varphi}{2} + \frac{1}{\varphi} (1 - \cos \alpha) \right) \right] \qquad \text{Eq. C- 32}$$

Therefore, the voltage conversion ratio from Eq. C- 26, Eq. C- 27, and Eq. C- 32

$$\frac{V_0}{V_{in}} = \frac{I_{in}}{I_0} = \frac{1}{N}\frac{1-\frac{f_s}{2\pi f_r}\left(\alpha+\frac{\varphi}{2}+\frac{1-\cos\alpha}{\varphi}\right)}{\frac{f_s}{2\pi f_r}\left(\alpha+\frac{\varphi}{2}+\frac{1-\cos\alpha}{\varphi}\right)} \qquad \text{Eq. C- 33}$$

Appendix D: Analysis of Boost Multi-resonant Converter

The resonant inductor L_r is in a loop with both switch S_1 and S_2 and output voltage. By applying Kirchhoff's Voltage law and and Kirchhoff's Current Law:

$$v_{s1}+v_{s2}+\frac{di_{Lr}}{dt}=1 \qquad \text{Eq. D- 0-1}$$

$$i_{s1}+\frac{dv_{s1}}{dt}+i_{s2}-C_N\frac{dv_{s2}}{dt}=I_0^N \qquad \text{Eq. D- 0-2}$$

Therefore, the state equations are:

$$i_{s1}+\frac{dv_{s1}}{dt}=i_{Lr}+I_x \qquad \text{Eq. D- 0-3}$$

$$i_{Lr}+i_{s2}-C_N\frac{dv_{s2}}{dt}=I_0^N \qquad \text{Eq. D- 0-4}$$

1) *Stage* 11:

The Laplace transform of the state equation Eq. D- 0-5 is shown in Eq. D- 0-6. The time domain state equation of the resonant inductor current is shown in Eq. D- 0-7 by inverse Laplace transform of Eq. D- 0-6.

$$\frac{di_{Lr}^N}{dt}=1 \qquad \text{Eq. D- 0-5}$$

$$si_{Lr}(s)-I_{Lr\_nn}=\frac{1}{s} \qquad \text{Eq. D- 0-6}$$

$$i_{Lr}^N(t)=\omega_r t+I_{Lr\_nn} \qquad \text{Eq. D- 0-7}$$

2) Stage 10:

The Laplace transform of state equations Eq. D- 0-8 and Eq. D- 0-9 are shown by Eq. D- 0-10 and Eq. D- 0-11.

$$\frac{di_{Lr}^{N}}{dt}=1-v_{s2}^{N} \qquad \text{Eq. D- 0-8}$$

$$\frac{dv_{s2}^{N}}{dt}=i_{Lr}^{N} \qquad \text{Eq. D- 0-9}$$

$$si_{Lr}(s)-I_{Lr\_nf}=\frac{1}{s}-v_{s2}(s) \qquad \text{Eq. D- 0-10}$$

$$sv_{s2}(s)-V_{s2\_nf}=i_{Lr}(s) \qquad \text{Eq. D- 0-11}$$

By solving equation Eq. D- 0-10 and Eq. D- 0-11

$$s\left[sv_{s2}(s)-V_{s2\_nf}\right]+v_{s2}(s)=\frac{1}{s}+I_{Lr\_nf} \qquad \text{Eq. D- 0-12}$$

$$v_{s2}(s)=\frac{1}{s}+\frac{I_{Lr\_nf}}{1+s^{2}}+\frac{s}{1+s^{2}}\left(V_{s2\_nf}-1\right) \qquad \text{Eq. D- 0-13}$$

$$si_{Lr}(s)-I_{Lr\_nf}=\frac{1}{s}-\frac{i_{Lr}(s)}{s}-\frac{V_{s2\_nf}}{s} \qquad \text{Eq. D- 0-14}$$

$$i_{Lr}(s)=\frac{1}{\left(1+s^{2}\right)}-\frac{s}{\left(1+s^{2}\right)}I_{Lr\_nf}-\frac{1}{\left(1+s^{2}\right)}V_{s2\_nf} \qquad \text{Eq. D- 0-15}$$

The inverse Laplace transform of Eq. D- 0-13 and Eq. D- 0-15

$$i_{Lr}^{N}(t) = I_{Lr\_nf}^{N} \cos\omega_r t + \left(1 - V_{s2\_nf}^{N}\right)\sin\omega_r t \qquad \text{Eq. D- 0-16}$$

$$v_{s2}^{N}(t) = 1 + I_{Lr\_nf}^{N} \sin\omega_r t + \left(V_{s2\_nf}^{N} - 1\right)\cos\omega_r t \qquad \text{Eq. D- 0-17}$$

3) *Stage* 00:

The Laplace transform of the state equations Eq. D- 0-18, Eq. D- 0-19 and Eq. D- 0-20

$$\frac{di_{Lr}^{N}}{dt} = 1 - v_{s1}^{N} - v_{s2}^{N} \qquad \text{Eq. D- 0-18}$$

$$\frac{dv_{s1}^{N}}{dt} = \frac{1}{C_N}\left(i_{Lr}^{N} - I_{0}^{N}\right) \qquad \text{Eq. D- 0-19}$$

$$\frac{dv_{s2}^{N}}{dt} = i_{Lr}^{N} \qquad \text{Eq. D- 0-20}$$

$$s i_{Lr}(s) - I_{Lr\_ff} = \frac{1}{s} - v_{s1}(s) - v_{s2}(s) \qquad \text{Eq. D- 0-21}$$

$$s v_{s1}(s) - V_{s1\_ff} = \frac{1}{C_N}\left[i_{Lr}(s) - \frac{I_0^N}{s}\right] \qquad \text{Eq. D- 0-22}$$

$$s v_{s2}(s) - V_{s2\_ff} = i_{Lr}(s) \qquad \text{Eq. D- 0-23}$$

By solving equation Eq. D- 0-21, Eq. D- 0-22 and Eq. D- 0-23

$$s i_{Lr}(s) - I_{Lr\_ff} = \frac{1}{s} - \frac{1}{C_N s}\left[i_{Lr}(s) - \frac{I_0^N}{s}\right] - \frac{V_{s1\_ff}}{s} - \frac{1}{s} i_{Lr}(s) - \frac{V_{s2\_ff}}{s} \qquad \text{Eq. D- 0-24}$$

$$i_{Lr}(s)\left[s+\frac{1}{C_N s}+\frac{1}{s}\right]=\frac{1}{s}\left[1-V_{s1\_ff}-V_{s2\_ff}\right]+\frac{1}{C_N s^2}I_0^N+I_{Lr\_ff} \qquad \text{Eq. D- 0-25}$$

Where

$$\begin{aligned} s+\frac{1}{C_N s}+\frac{1}{s} &= s\left[1+\frac{1+C_N}{C_N}\frac{1}{s^2}\right] \\ &= s\left[1+\frac{\chi}{s^2}\right] \end{aligned} \qquad \text{Eq. D- 0-26}$$

$$i_{Lr}(s)=\frac{1}{s^2+\chi}\left[1-V_{s1\_ff}-V_{s2\_ff}\right]+\frac{1}{C_N}\frac{1}{s\left(s^2+\chi\right)}I_0^N+\frac{s}{s^2+\chi}I_{Lr\_ff} \qquad \text{Eq. D- 0-27}$$

The inverse Laplace transform of Eq. D- 0-25

$$\begin{aligned} i_{Lr}^N(t) &= \frac{I_0^N}{1+C_N}\left(1-\cos\sqrt{\frac{1+C_N}{C_N}}\omega_r t\right) \\ &\quad +I_{Lr\_ff}^N\cos\sqrt{\frac{1+C_N}{C_N}}\omega_r t \\ &\quad +\sqrt{\frac{C_N}{1+C_N}}\left(1-v_{s1\_ff}^N-v_{s2\_ff}^N\right)\sin\sqrt{\frac{1+C_N}{C_N}}\omega_r t \end{aligned} \qquad \text{Eq. D- 0-28}$$

Appendix E: MPPT Control Code

```
#include <Stdlib.h>
#include <String.h>
#include <math.h>
#include <Psim.h>

// PLACE GLOBAL VARIABLES OR USER FUNCTIONS HERE...

double v;
double oldv;
double dv;

double p;
double oldp;
double dp;

double counter;  // frequency
double light;

double outputcounter = 100; //no of steps during ON time

double max = 400;//Maximum switching frequency
double min = 150;//Minimum switching frequency

double x = 0.2;
double a = 0;
double d=0.5; // d is the duty ratio



// FUNCTION: SimulationStep
//   This function runs at every time step.
//double t: (read only) time
//double delt: (read only) time step as in Simulation control
//double *in: (read only) zero based array of input values. in[0] is the first node, in[1] second
input...
//double *out: (write only) zero based array of output values. out[0] is the first node, out[1]
second output...
//int *pnError: (write only)  assign  *pnError = 1;  if there is an error and set the error message in
szErrorMsg
//    strcpy(szErrorMsg, "Error message here...");
// DO NOT CHANGE THE NAME OR PARAMETERS OF THIS FUNCTION
void SimulationStep(
                    double t, double delt, double *in, double *out,
                     int *pnError, char * szErrorMsg,
                     void ** reserved_UserData, int reserved_ThreadIndex, void * reserved_AppPtr)
{
```

```
v = in[0]; // Read in PV voltage
i = in[1]; // Read in PV current
if (outputcounter >= a)
{
p = v*i; // Calculate PV power
oldp = oldv*oldi; // Calculate PV power from previous cycle
dp = (p-oldp); // Calculate the change in PV power
dv = (v-oldv); // Calculate the change in PV voltage

if (p > oldp)
{
if( (p - oldp) < p/(counter*100))
{
counter = counter;
outputcounter = 1;
}
else
if (dv>0)
{
if (counter >=max)
counter = max; // set switching frequency to allowable maximum limit
else
counter = counter + x;
}
else
{
if (counter <= min)
counter = min;  // set switching frequency to allowable minimum limit
else
counter = counter - x;
}
outputcounter = 1;
}
else
{
if( (oldp - p) < p/(counter*100))
{
counter = counter;
outputcounter = 1;
}
else
if (dv<0)
{
if (counter >= max)
counter = max;// set switching frequency to allowable maximum limit
else
counter = counter + x;
}
else
```

```
{
if (counter <= min)
counter = min;// set switching frequency to allowable minimum limit
else
counter = counter - x;
}
outputcounter = 1;
}
outputcounter = 1;
out[0]=1;
out[2]=counter;
a = (1/((counter)*1000))/(0.01/(10*10*10*10*10*10));//convert switching frequency to time
steps
oldv = v;//save state voltage for next cycle
oldi = i;//save state current for next cycle
}
else
{
d=1-(toff*/(1/((counter)*1000)));//calculate duty ratio for constant off time
if(outputcounter <= a*d)
out[0] = 1;//output signal
else
out[0] = 0;//output signal
outputcounter = outputcounter+1;
out[2] = counter;
}
}
```

Appendix F: Printed Circuit Board (PCB) Layout from Altium

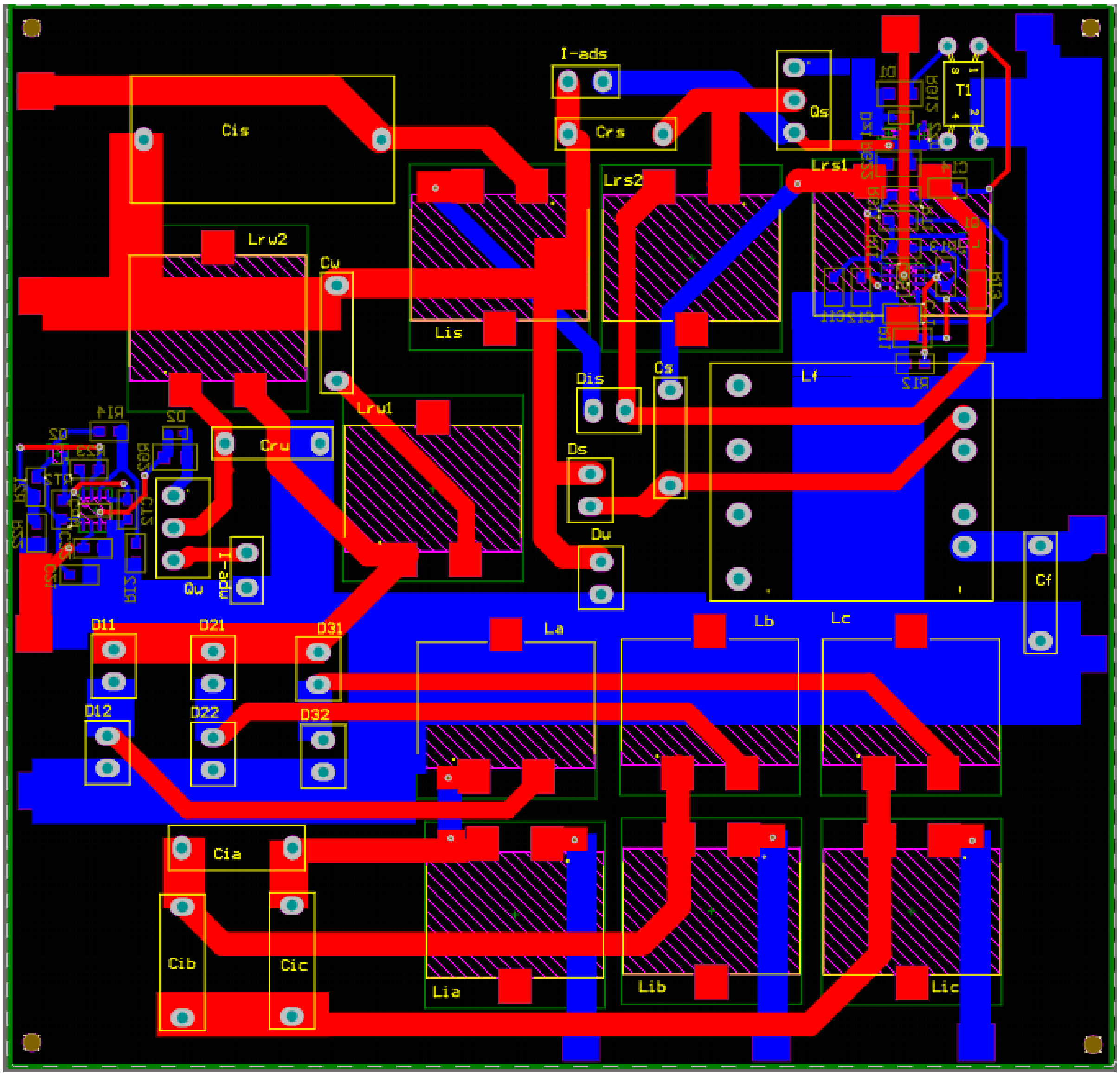

Figure E-1 PCB layout for ZVS-QR Cuk-Cuk converter

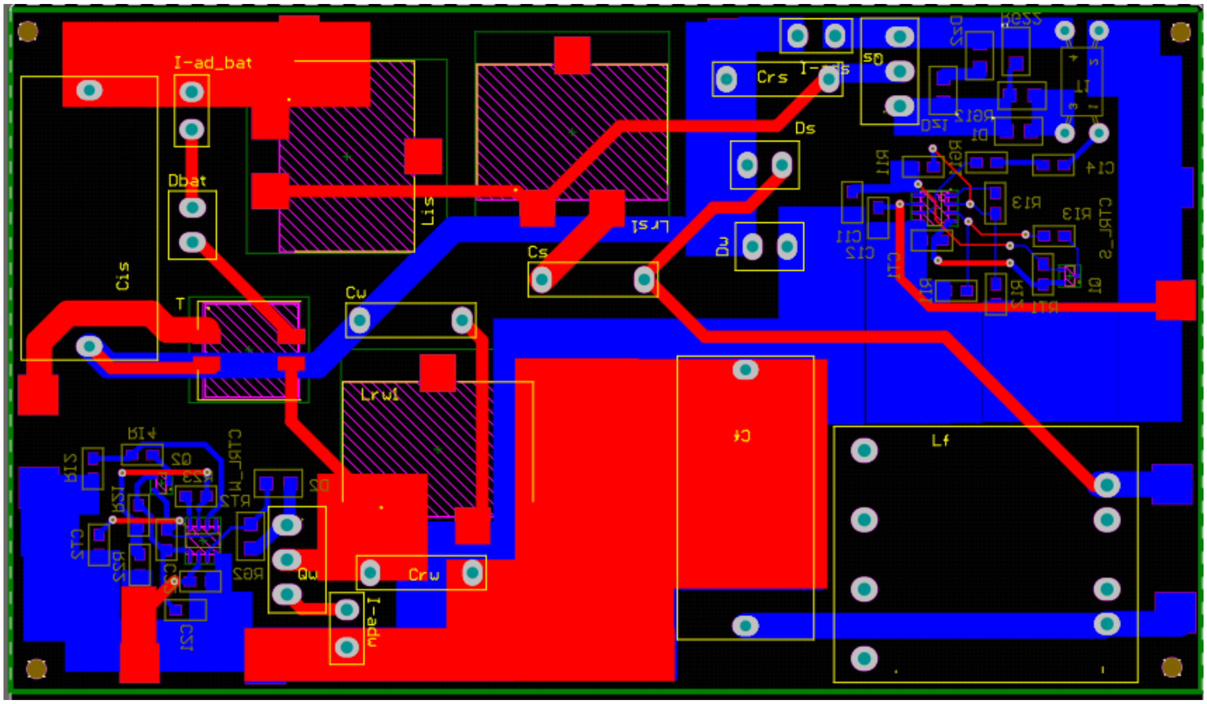

Figure F-2 PCB layout for PV-battery integrated converter for regulated grid

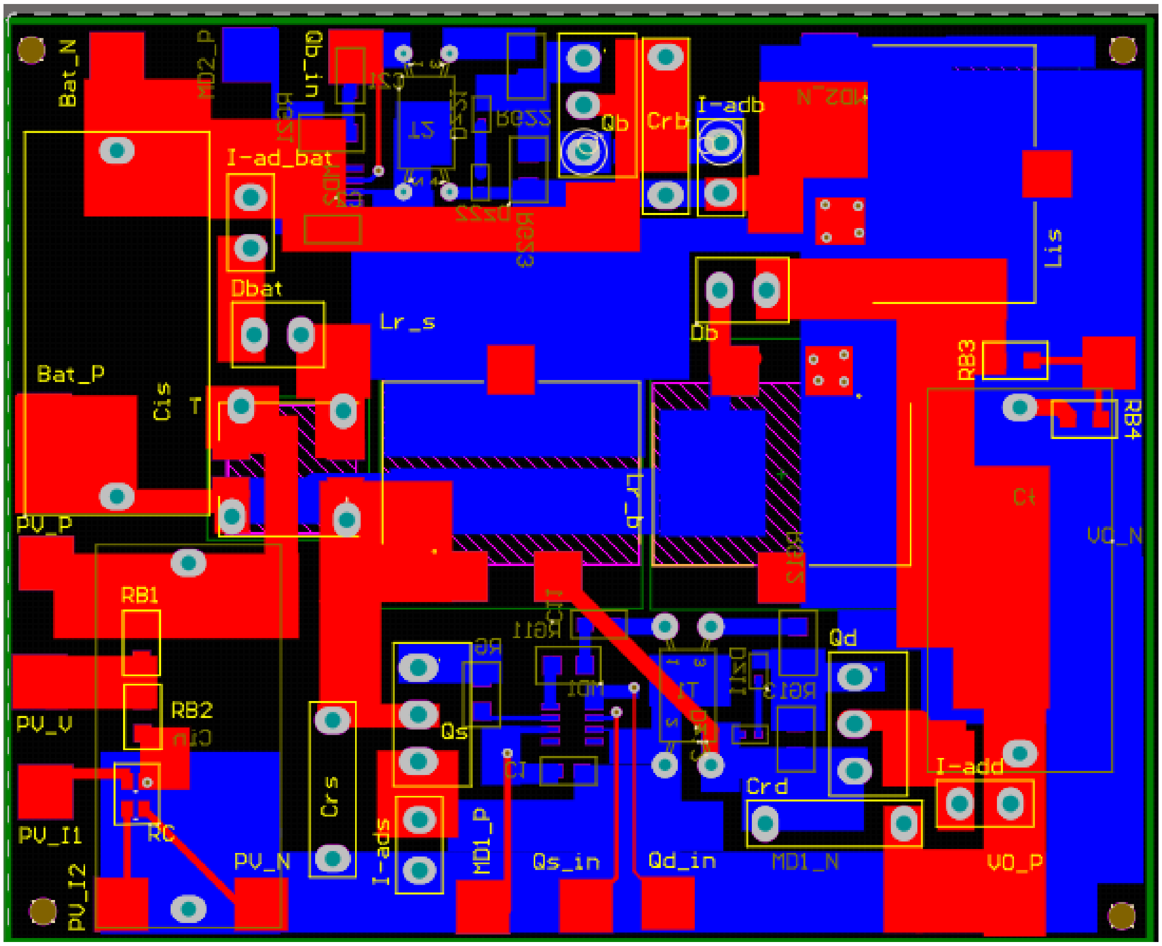

Figure F-3 PCB layout for PV-battery integrated converter for unregulated grid

Appendix G: Experimental Setup

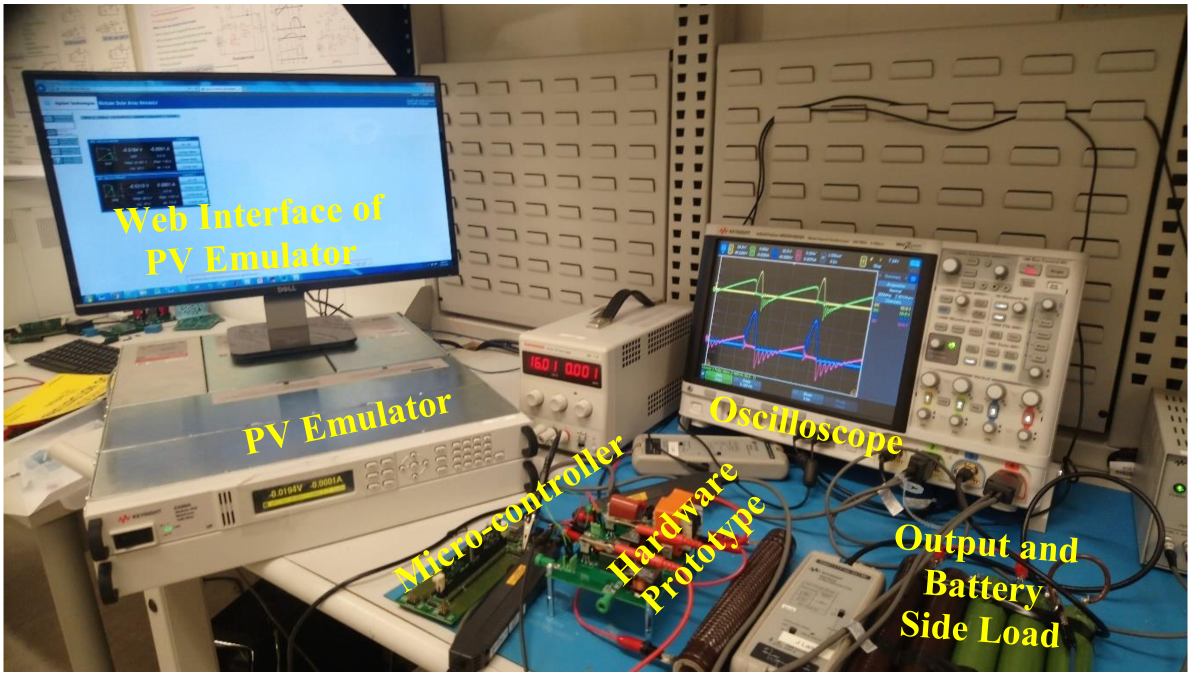

Figure G-1: Experimental setup